Optical Techniques for Fruit Firmness Assessment

A thesis

submitted in fulfilment

of the requirements for the degree

of

Doctor of Philosophy in Electronic Engineering

at

The University of Waikato

by

PHILIP ROWE

THE UNIVERSITY OF
WAIKATO
Te Whare Wānanga o Waikato

2015

Abstract

This thesis describes the design and development of a new high-speed multispectral imaging (MSI) system compatible with a commercial grading line. The purpose of this system was to carry out spatially resolved spectroscopy to assess fruit firmness. Captured images were analysed using diffusion theory and modified Lorentzian models to extract a sample's optical properties (absorption and reduced scattering coefficients) and optical parameters respectively. The high-speed MSI system was designed to capture images of fruit using a high-resolution complementary metal–oxide–semiconductor camera, 12.5 mm lens, and discrete lasers operating at 685, 850, and 904 nm. Each laser illuminates a separate fruit, and the camera captures the interacting light with a single frame encompassing all three fruit. Depending on the size of each fruit the spatial resolution with the 12.5 mm lens ranged from 0.15 to 0.22 mm/pixel.

Initial measurements were made on 200 'Royal Gala' apples to identify the relationships between the optical properties or parameters and either acoustic or the industry standard penetrometer firmness measurements. Performance of the high speed MSI system was poor compared to the results seen in the literature using alternative spatially resolved spectroscopic systems and other apple varieties. Only weak correlations ($R = 0.33$) were found between the individual optical measurements and firmness.

Unsatisfactory performance from the high-speed system led to the development of a static MSI system to measure stationary fruit and the development of an inverse adding-doubling (IAD) system to provide an independent measurement of the samples optical properties. The purpose of these systems was to help understand the measurement, reduce variability, and give an indication of the upper level of performance possible. The static MSI system featured a number of improvements including the addition of a 980 nm laser, the elimination of an asymmetry caused by laser polarisation, improved temperature control, an electronic shutter system, precise location control of the fruit, and a new 25 mm lens improving spatial resolution (0.057mm/pixel).

A second study was carried out using the new MSI and IAD systems on 92 'Royal Gala' apples. Fruit were sliced to expose a flat measurement surface eliminating variation caused by fruit curvature and skin pigments. With these refinements and simplifications the relationships between optical properties or parameters and penetrometer firmness strengthened. As fruit softened and penetrometer firmness fell the reduced scattering coefficient measured by both the IAD and MSI system increased with correlation coefficients ranging from -0.62 to -0.70. The absorption coefficients measured by the two systems showed the expected features related to the absorption of chlorophyll and carotenoid pigments, and water absorption. As the fruit softened chlorophyll absorption decreased as the pigments are broken down and carotenoid absorption increased as new pigments are synthesised. No useful relationships were identified between the optical measurements and acoustic firmness. Multiple linear regression models were formed to predict penetrometer firmness using either the optical properties or modified Lorentzian parameters. The best performing model used a combination of the absorption and scattering coefficients, and had a correlation coefficient of 0.8 and a standard error of 5.87 N.

Acknowledgements

During my doctoral study I have met, and worked with, so many fantastic people who without their guidance and support would have not made this research possible. First, I would like to thank my supervisors, Rainer Kunnemeyer and Sadhana Talele from the University of Waikato, and Andrew McGlone from the New Zealand Institute for Plant and Food Research. They provided guidance, encouragement, enthusiasm, patience, support and a willingness to share their knowledge.

I would also like to thank the New Zealand Institute for Plant and Food Research and the University of Waikato for their financial support through scholarships. My time was mainly spent at Plant and Food's Ruakura campus where everyone I met was more than willing to help and share their enormous wealth of knowledge. I would like to specifically thank the technical staff, Lyn Cate, Murray Ashby, James Pinfold, and Paul Gaastra. They provided essential support for the design and construction of the fruit measurement systems. I would like to thank Peter Schaare, Richard Oliver, and Richard Seelye for their assistance on the main experimental work as well as their thought provoking discussions. I would like to thank Paul Martinsen who has gone above and beyond to provide me with endless support and discussion on preparing publications, software and hardware design, and experimental assistance. I would also like to thank the greater Bio Engineering team who have provided interesting discussion, advice and assistance throughout my research.

Finally I would like to thank my friends and family, who have given me support, patience, and encouragement throughout my studies. I would also like to specifically thank my fiancée Cheryl. Our studies have kept life exciting, and you have handled the difficulties of my long hours and now long distances amazingly.

Table of Contents

List of Tables

List of Figures

List of Abbreviations

NIRS	Near-infrared spectroscopy
SSC	Soluble solids content
CA	Controlled atmosphere
PLS	Partial least squares
MLR	Multiple linear regression
SMLR	Stepwise multiple linear regression
PCR	Principal components regression
SEP	Standard error of prediction
RMSE	Root mean standard error
RMSEP	Root mean standard error of prediction
RMSECV	Root mean standard error of cross-validation
SEV	Standard error of validation
SECV	Standard error of cross-validation
FT	Fourier transform
CCD	Charged coupled detector
SRS	Spatially resolved reflectance spectroscopy
FSI	Full spatial image
LSI	Line spatial image
MLD	Modified Lorentzian distribution
UVE	uninformative variable elimination
SAP	Supervised affinity propagation
LS-SVM	Least squares support vector machine
TRS	Time resolved reflectance spectroscopy
SFDI	Spatial frequency domain imaging
DMD	Digital micromirror device
ADC	Analog to digital
CMOS	Complementary metal-oxide-semiconductor
PID	proportional-integral-derivative
CAD	Computer aided design
TEC	Thermoelectric cooling
RH	Relative humidity
AFS	Acoustic firmness sensor
FWHM	Full width half maximum
PCB	Printed circuit board

LED	Light emitting diode
MOSFET	Metal-oxide-semiconductor field-effect transistor
GUI	Graphical user interface
AD	Adding-doubling
IAD	Inverse adding-doubling
MSI	Multispectral imaging
NA	Not available
TEM	Transmission electron microscopy

1. Introduction

The fresh fruit industry is one of the most important in New Zealand with exports of approximately NZ 1.5 billion dollars in 2013. The largest portion of this market is made up of kiwifruit (62%), followed by apples (31%), avocados (2%), and the combination of other fruit types (5%) (The New Zealand Institute for Plant and Food Research, 2013). It is important that this industry continues to thrive and grow. This puts pressure on the suppliers to make sure that they have plenty of fruit, the fruit can be supplied over a long period, and that the fruit is of a high quality. These requirements mean that the fruit need to be measured not only for external properties visible to the consumer such as size or shape but also for internal and physiological properties such as taste, texture, and maturity. Results from these measurements can then be combined to sort fruit based on its present state and its expected performance in storage. The poor storing fruit can be sent to market quickly, and the rest can be stored and sold over time at premium prices.

To meet the requirements of fruit processors complex fruit grading and sorting systems have been developed. These systems handle huge numbers of fruit by running them over large conveyor systems and past automated inspection points at high speed (e.g. apples at ten fruit per second). These modern systems are currently capable of a large number of non-destructive measurements including weight, size, colour, shape, and external defects. Near-infrared spectroscopy has also provided a measurement for some types of internal defects and fruit quality parameters such as dry matter. While these modern capabilities have already revolutionised the industry, one quality parameter that remains difficult to measure at high speed, non-destructively is firmness. Currently, the industry standard for firmness measurement is a penetrometer. This is a destructive approach in which a metal plunger is driven into the fruit flesh, and the resisting force is measured. The penetrometer is well accepted by the horticultural industry because of it's correlations with consumer preference as found in sensory trials (Harker et al., 2002; Abbott, 1994; Mehinagic et al., 2004; Plocharski & Konopacka, 1999).

Three mechanical approaches have been commercialised in an attempt to replace the penetrometer. These include the AWETA acoustic firmness sensor, the Sinclair IQ firmness tester, and the Greefa Intelligent Firmness Detector. All three require physical

contact with the fruit, which risks damage such as bruising and limits their operating speed due to mechanical inertia. This speed limitation not only affects the measurement itself, but also the whole grading line reducing overall throughput. These and other deficiencies have meant adoption of the systems by industry remains limited. This has left open the opportunity for a non-contact, non-destructive, and high speed optical firmness measurement system to be developed which would pose no risk to the fruit and not be encumbered by mechanical inertia.

Researchers working in this area have demonstrated several promising optical approaches which have been used to investigate how light interacts with fruit tissue as it matures and softens and to develop predictive models for firmness and other quality parameters. These approaches include near-infrared spectroscopy, spatially resolved and time-resolved reflectance spectroscopy, and spatial frequency-domain imaging. The majority of this research has been carried out on stationary fruit. Spatially resolved reflectance spectroscopy is a promising approach where both the absorption and scattering properties of the fruit flesh are interrogated and, through modelling, can be separated. The absorption information is used to investigate the chemical composition such as sugar content while the scattering information provides detail on structural properties such as texture and firmness. Measurements commonly involve illuminating a fruit sample using a spot source and then capturing the interaction of light with the sample using an imaging system. Through the use of modern imaging systems and high-power laser sources, new high-speed systems designs are made possible.

This thesis covers design and development of a high-speed multispectral imaging system to carry out spatially resolved reflectance spectroscopy on ‘Royal Gala’ apples and investigate its potential as a high-speed, non-destructive fruit firmness measurement. Images captured by the system will be analysed using modified Lorentzian and diffusion theory models to extract out optical parameters and properties. The relationships between the industry standard penetrometer and acoustic firmness measurements and these optical parameters and properties will be identified. These relationships will be used to develop predictive models for firmness. The thesis also covers the development of a semi-automated inverse adding-doubling system which provides an independent measurement of the apple sample’s optical properties.

In addition to the main body of work developing a firmness measurement system, a small study was carried out to measure the thermal stability of Intralipid, a highly scattering fatty emulsion commonly used in optical phantoms. This study was published in the Journal of Applied Spectroscopy; further detail can be found in Appendix 1.

1.1. Thesis Outline

This thesis is divided into nine chapters, the first being this introduction to the thesis. The next three chapters give an introduction to the background material. Chapter 2 introduces fruit grading covering the physiology of apples as well as the various properties and attributes of fruit that affect consumer satisfaction. Also introduced in Chapter 2 are the various fruit grading measurements and technologies currently used by industry. This includes a discussion on the mechanical approaches used to measure fruit firmness but does not detail the optical approaches. These are covered in subsequent chapters.

Chapter 3 describes light propagation inside fruit. It introduces the optical properties used to characterise how light is absorbed and scattered through interactions with the fruit tissue. This chapter also introduces some of the models used to describe light transport inside the fruit including radiative transport theory, diffusion theory, and Monte Carlo simulation. Chapter 4 completes the background material by introducing the different optical measurement approaches researchers have used to try and estimate fruit firmness. These include spatial-frequency domain imaging and near-infrared, spatially-resolved and time-resolved spectroscopy.

Chapter 5 outlines specifications for the design of a high-speed multispectral imaging system. These specifications were developed from the background information discussed in Chapter 4 and the requirements for practical, high speed, online fruit grading systems. The specifications were used to guide the detailed design of the imaging system, light sources, physical arrangement, and software used to collect multispectral images presented in the second part of this chapter.

The high-speed multispectral imaging system was evaluated by measuring 200 'Royal Gala' apples on a mock-up commercial fruit grader running at 1m/s. This experiment is described in Chapter 6 along with analysis of the data using modified Lorentzian and diffusion theory models. The optical properties and parameters from these models

are compared to reference data found in the literature and the relationships between these and reference firmness measurements, either acoustic or penetrometer, are investigated. These parameters were also used to develop firmness prediction models using multiple linear regression, and the performance of these models is evaluated.

The high-speed system didn't perform as well as expected from the literature on slower and static systems. So, Chapter 7 describes a number of refinements to improve confidence in the measurement and help identify issues that need to be resolved. These refinements include transitioning the system to one where fruit are stationary, improvements to the laser sources and imaging systems, the addition of an electronically controlled shutter and accurate fruit location controller, and refinements to the software. Chapter 7 also describes the design of the inverse adding-doubling system which provides an independent measurement of a sample's optical properties.

Chapter 8 discusses the experimental validation of the refined multispectral imaging and new inverse adding-doubling systems. Measurements are made on four liquid optical phantoms with increasing concentrations of Intralipid, a scattering medium. This simulated a wide range of scattering coefficients in excess of the range measured in the literature on a number of apple varieties.

Chapter 9 presents the data from a final experiment carried out using the now static multispectral imaging and inverse adding-doubling systems on 92 'Royal Gala' apples. In addition to the improvements of the multispectral imaging system, fruit variation caused by skin and shape effects was eliminated by slicing the fruit samples so that a flat measurement surface was exposed. These simplifications allowed us to identify an upper limit on performance. Imaging data was analysed again using modified Lorentzian and diffusion theory models. Relationships between reference firmness measurements and the modified Lorentzian parameters or optical properties from the multispectral imaging and inverse adding-doubling systems were identified. Again predictive models were formed from these optical properties and parameters to estimate firmness and their performance evaluated.

Finally, in Chapter 10 the work is concluded and possible directions for further work in the future are discussed.

Appendix 1 discusses the small study on the thermal stability of Intralipid based optical phantoms and Appendix 2 provides further detail on the software used to

control the high-speed and static multispectral imaging systems, and the shutter controller.

1.2. Contributions

Original contributions from this research include:

- The optical properties of 'Royal Gala' apples have been measured using the multispectral imaging system at 685, 850, 904, and 980 nm and the inverse adding-doubling system between 400 and 1050 nm.
- The relationships between penetrometer firmness in 'Royal Gala' apples and either carotenoid or chlorophyll pigment absorption has been identified, quantified, and reported in a peer-reviewed journal.
- A Multispectral imaging system that can operate at high speed and with stationary fruit has been designed, built and tested.
- A Semi-automated Inverse adding-doubling system has been developed, validated, and the limitations reported.
- A comparison between the inverse adding-doubling and multispectral imaging approaches has been made on Intralipid and 'Royal Gala' apple samples.
- The thermal stability of Intralipid, a common liquid phantom for diffuse optical measurements, has been quantified and reported in the Journal of Applied Spectroscopy.

The following peer-reviewed journal papers have arisen from this work:

- Rowe, PI, Künnemeyer, R, McGlone, A, Talele, S, Martinsen, P & Oliver, R 2013, "Thermal Stability of Intralipid Optical Phantoms," *Applied Spectroscopy*, vol. 67, no. 8, pp. 993–996.
- Rowe, PI, Künnemeyer, R, McGlone, A, Talele, S, Martinsen, P & Seelye, R 2014, "Relationship between tissue firmness and optical properties of 'Royal Gala' apples from 400 to 1050nm," *Postharvest Biology and Technology*, vol. 94, pp. 89–96.

In addition, the following oral and poster presentations have arisen from this work:

- IEEE Instrumentation and Measurement Society, 4th Annual Workshop on Smart Sensors, Measurements, and Instrumentation: Applications to agricultural and environmental monitoring. April 2012, Lincoln, New Zealand. Oral presentation titled "Development of a Laser Based Fruit Firmness Sensor".
- 15th ANISG/NZNIRSS Conference, Queenstown, New Zealand, April 2012. Oral presentation titled "Transmission NIRS of a Fatty Emulsion (Intralipid) at Elevated Temperatures" (Student Presentation Award).
- Conference on Optics, Atoms, and Laser Applications (IONS-KOALA), Brisbane, Australia, December 2012. Poster titled "An Optical Fruit Firmness Measurement System".
- IEEE Instrumentation and Measurement Society, 5th Annual Workshop on Smart Sensors – Instrumentation and Measurement. February 2013, Hamilton, New Zealand. Oral presentation titled "Optically Sensing Fruit Firmness".

2. Introduction to Fruit Grading

How would you like to sort billions of apples by hand? In 2005 the United States apple industry picked, graded, and packed billions of fruit into 234.9 million cartons (University of Illinois Extension, 2007). This is an impossible request and has lead to the development of a large fresh fruit processing industry. The industry relies on fruit grading and sorting systems that must be carefully designed to meet the requirements of fruit growers, processors (pack-houses), and consumers. Growers and processors are after high throughput, consistent performance, low cost, market premiums, and efficiency gains (Londhe et al., 2013; Ruiz-Altisent et al., 2010). Customers want fresh, high quality, defect free fruit, and a consistent experience from both the external and internal properties of the fruit (Studman, 2001; García-Ramos et al., 2005; Ruiz-Altisent et al., 2010).

This chapter introduces the relevant physiology of apple, the primary fruit investigated in this thesis, and the various properties and attributes that contribute to customer and industry satisfaction. Also described are the fruit grading measurements and technologies currently used, including both destructive and non-destructive approaches. Details on how some of these measurements have been implemented by grading companies for high-speed measurement are also presented.

2.1. Fruit Physiology

2.1.1 Apples

Apples (Malus domestica) are one of the most widely cultivated fruits in the world. They originated in the Middle East over 4,000 years ago growing on small flowering deciduous trees (Institute of Food Research, 2009; Cook et al., 1998). There are more than 7,500 different cultivars growing worldwide bred for different applications including cider production, general fresh eating (dessert apples), and cooking (Elzebroek & Wind, 2008).

Apples have a complex developmental cycle. They are not suitable for tropical climates, requiring cold winter temperatures to blossom effectively. This blossoming usually occurs in early spring and pollination is typically carried out using bees (Levetin & McMahon, 2008). Once pollinated the fruit grows by exponential cell division for approximately one week, after this the fruit then begin to grow both

through cell division and cell expansion for a further 4 to 5 weeks. Finally for the remainder of the growth cycle only cell expansion takes place (Lakso & Goffinet, 2013). Modern commercial orchards tend to use dwarf rootstocks which limit the tree size to approximately two meters. This makes the orchard much easier to manage (Levetin & McMahon, 2008).

The core of an apple fruit is a five-carpeled ovary with seeds. Figure 2-1 (D) shows a typical break down of the internal features of an apple. A fine greenish boundary (Exocarp) indicates the extent of the ovary with a parchment like material surrounding the seeds (endocarp). The skin is made up of cuticle, epidermal, and hypodermal layers with lenticels that allow gas diffusion (Watkins et al., 2004). A ripe apple is composed of 87% water, 12% sugar, 1% fibre, and negligible amounts of fat and protein (Levetin & McMahon, 2008).

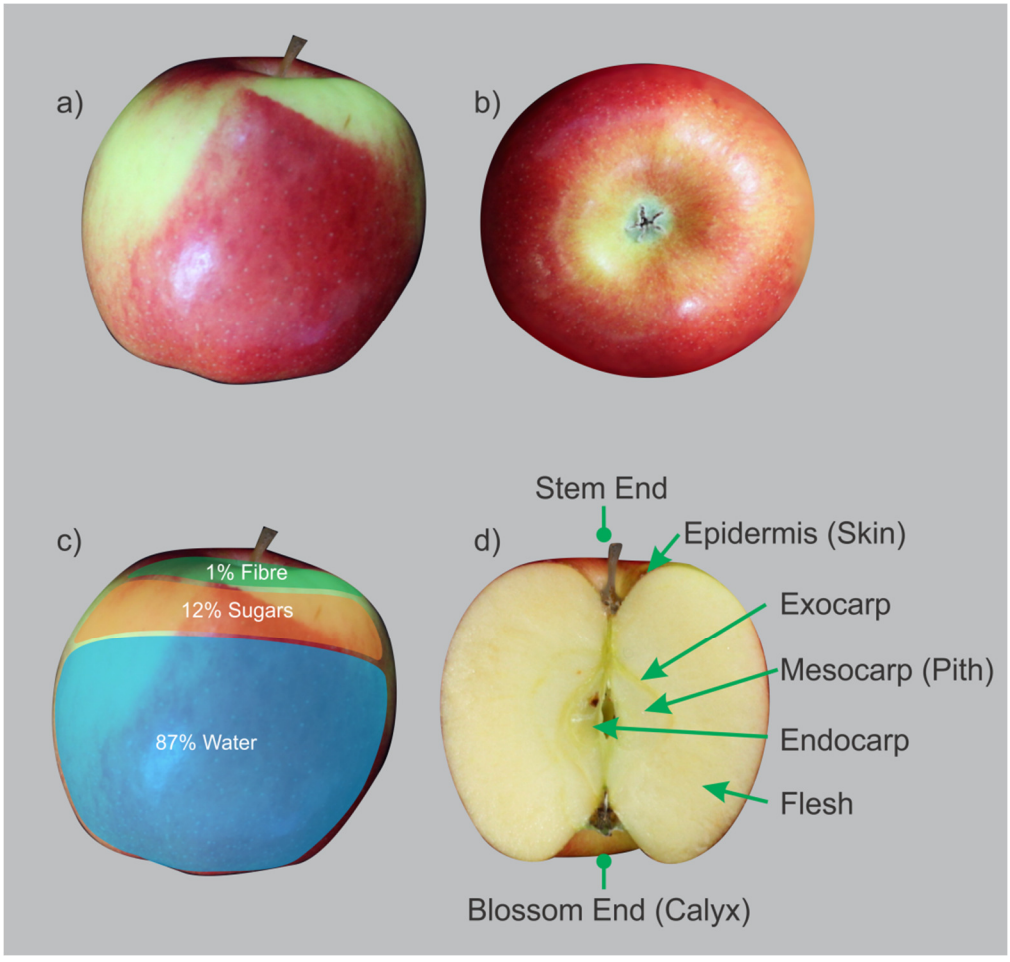

Figure 2-1. Photographs and illustrations of a Pink Lady apple showing important internal and external features. (a) Side view of the apple with the stem at the top and the calyx at the bottom. (b) View looking from the calyx end. (c) Composition of a typical apple (Levetin & McMahon, 2008). (d) Section along the fruits axis showing different features.

Figure 2-2 shows the cell structure of a young apple and a 'Royal Gala' apple after 16 weeks in storage. It demonstrates the complicated arrangement of cells whose density and size change as one traverses away from the skin layer towards the centre of the fruit (Bain & Robertson, 1951). Typical cell sizes for skin range from 67 to 85 µm and for the flesh from 160 to 235 µm (Mohsenin, 1986).

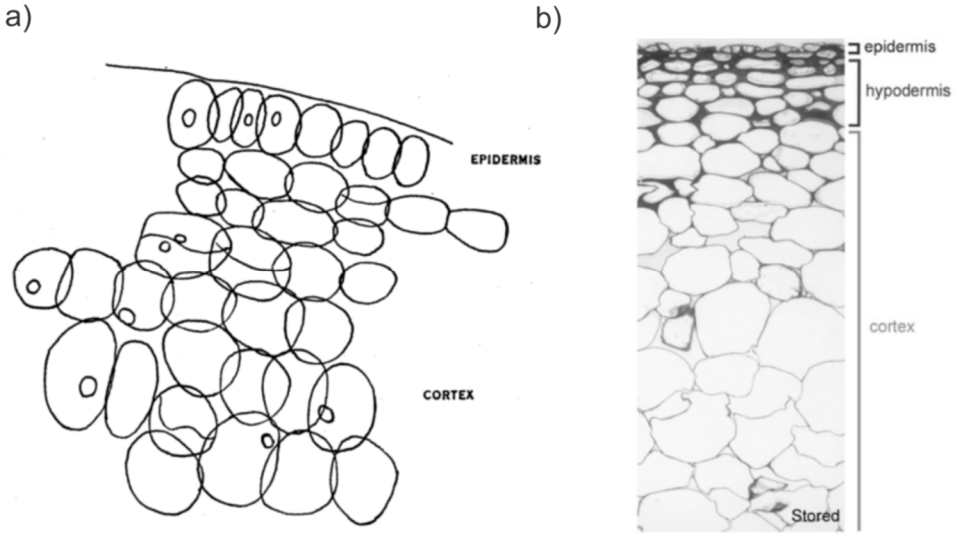

Figure 2-2. (a) Typical appearance of newly divided cells inside of a young apple (Bain & Robertson, 1951). (b) Toluidine blue stained sections from 'Royal Gala' apples after 16 weeks in storage (Atkinson et al., 2012).

Commercial breeding worldwide has produced thousands of different cultivars. This thesis focuses on 'Royal Gala' apples as they make up the largest percentage (33% by weight in 2012) of apple fruit exported from New Zealand (The New Zealand Institute for Plant and Food Research, 2013).

2.2. Consumer Requirements

The endpoint for the fruit industry is the consumer, and if their expectations are not met the consequences are significant. Batt & Sadler (1998) questioned 260 customers about their eating experiences with apples. They found if the consumer has a bad eating experience then 58% will change cultivars, 31% will purchase fewer apples, 24% will switch to other fruit, 17% will stop buying for a while, 10% will switch to higher priced fruit, and 5% will switch brands.

As consumer demands shift and evolve the fruit processors (pack-houses) have to adjust. They put pressure on the grading system companies to develop new and

innovative technologies. Consumer requirements that affect the sales of fresh fruit and vegetables cover a broad spectrum. Key fruit requirements include, in no particular order: price, skin colour, size, shape, visible defects, internal defects, seediness, labelling, pesticide usage, and eating quality (Manalo, 1990; Baker, 1998; Campbell et al., 2004; Batt & Sadler, 1998).

Requirements particularly relevant to fruit processors are the colour, size, shape, visible defects, internal defects, and eating quality. The industry currently has high-speed grading solutions for many of these, but there is a significant push to be able to grade based on eating quality. In apples for example, studies suggest that textural characteristics (part of the overall eating quality) such as crispness and firmness rank high on consumers' minds followed by taste, shape, and colour (Manalo, 1990; Harker, 2001).

Eating quality is made up of textural and taste characteristics. Textural characteristics are based on the mechanical properties of the flesh, its firmness, how it feels in the mouth, and its juiciness. Taste characteristics include sweetness, acidity and astringency. Requirements around shape and colour are usually about maintaining consistency which is a common theme throughout the literature for not only shape and colour, but all the characteristics previously mentioned.

2.3. Fruit Grading Technologies and Measurements

Many different types of measurements have been developed in the fruit industry for gauging the quality of fruit in response to the consumer requirements covered in the previous section. Routine measurements currently include weight, size, colour, shape, external defect identification, and density. More advanced measurements are also possible. These allow the internal quality to be evaluated by identifying defects or estimating eating quality parameters such as dry matter, soluble solids, and firmness. These measurements include both destructive and non destructive types. Destructive measurements mean that the fruit are tested in such a way that afterwards they are no longer useful and must be thrown away. This is wasteful and means only a subsample can be tested. Care must be taken to make sure this subsample is representative of the population. Non-destructive measurements, on the other hand, allow the fruit to remain part of the saleable population. It also allows every single fruit to be tested

online (on the grader line) at high speed, and fruit can be tracked and measured multiple times throughout the process reducing uncertainty (Studman, 2001).

2.3.1 Weight

Weight is commonly calculated using a set of load cells and digital electronics. This is essentially how digital kitchen scales work. At high speed this technique can also be used. Compac Sorting Equipment has a system of special fruit carriers that slide over a load cell platform where measurements are made. Averaging is used to reduce noise. Weights as precise as ±1g are achievable (Compac Sorting Equipment, 2013).

2.3.2 Size, Shape, Density, Colour, and External Defects

Size, shape, and density measurements can be made using standard equipment such as digital callipers. At high speed, these measurements can be made using camera based vision systems. One example, is that developed by AWETA called Powervision-3D that uses colour cameras to capture images of the fruit. These images are processed to extract colour information, fruit diameter or size, and fruit shape. These vision systems can also use intelligent algorithms, such as neural networks, to identify blemishes and visible surface defects which can then be placed in a lower grade or rejected (AWETA America, 2013).

Figure 2-3. AWETA Powervision-3D lighting and camera system as seen from below (AWETA America, 2013).

2.3.3 Dry Matter

Dry matter of a fruit sample is the non-water component and is measured as the ratio of dry weight to wet weight. It is a measure of the solid fraction of the total fruit weight including carbohydrates, fats, proteins, vitamins, minerals, and antioxidants.

Dry matter has been proven in some types of fruit, including kiwifruit and apples, to be a strong indicator of consumer preference (Palmer et al., 2010; Burdon et al., 2004).

The higher the dry matter, the more likely the fruit is to be accepted by the consumer. Dry matter is traditionally measured by destructively removing a section of fruit. This section is then weighed, dried using a heated chamber to remove all moisture, and then weighed again. The ratio of wet to dry weight is then used to calculate dry matter, commonly reported in percent.

Dry matter can also be estimated non-destructively using optical measurements such as near-infrared spectroscopy, Fourier transform infrared spectroscopy, and hyperspectral backscatter imaging (McGlone & Kawano, 1998; McGlone et al., 2002; Walsh et al., 2004; Ying et al., 2005; Zude et al., 2006; Peng & Lu, 2008; Liu et al., 2008; Lu et al., 2009).

The main technique employed by online grading systems is near-infrared spectroscopy (NIRS). Figure 2-4 shows the Taste Technologies Ltd T1 system. This illuminates the sample with high intensity broadband light. A spectrometer is used to collect the light signals (spectra) at a number of wavelengths at high speed. Taste Technologies has collected spectra on many fruit as well as reference data from destructive techniques. They use this data to build calibration models that can be applied to future fruit for an online estimate of their dry matter.

Figure 2-4. Taste Technologies Ltd T1 system, capable of measuring the reflected and transmitted light using the built in spectrometer (Taste Technologies, 2013).

2.3.4 Soluble Solids Content

Soluble solids content is a measure of the amount of soluble solid matter in a fruit. It is generally stated as a ratio or percentage of fruit weight. Fruit sugars dominate the

measure and it is often used as a proxy for sweetness, a key component of taste and highly important for consumer satisfaction. As apples ripen, there is an increase in sugars that occur as insoluble starch is converted into simple sugars. The soluble solids content (SSC) reaches a maximum once the fruit reaches a level of ripeness suitable for eating. A refractometer is used to measure the concentration of sugar from a sample of fruit juice (in units of % or degrees Brix) and this is approximately equal to the SSC. Hoehn et al. (2003) have identified minimum SSC requirements for various apple varieties based on consumer expectations.

Soluble solids can be measured non-destructively and at high speed using the same near-infrared spectroscopy systems as those used for dry matter measurements. Mathematical calibration models are developed using reference measurements (refractometer) and a calibration set of fruit. These models are then used to estimate soluble solids content at high-speed.

2.3.5 Internal Defects

A number of techniques have been developed for the identification of internal defects in fruit. Some examples of internal defects include bruising, insect damage, browning, and rots. Tollner et al. (1992) used x-ray images to identify watercore and bruising in apples (Figure 2-5a). Chen et al. (1989) looked at apples using nuclear magnetic resonance imaging (Figure 2-5b). They were able to get high resolution images and identify various internal defects including bruises, dry regions, and worm damage.

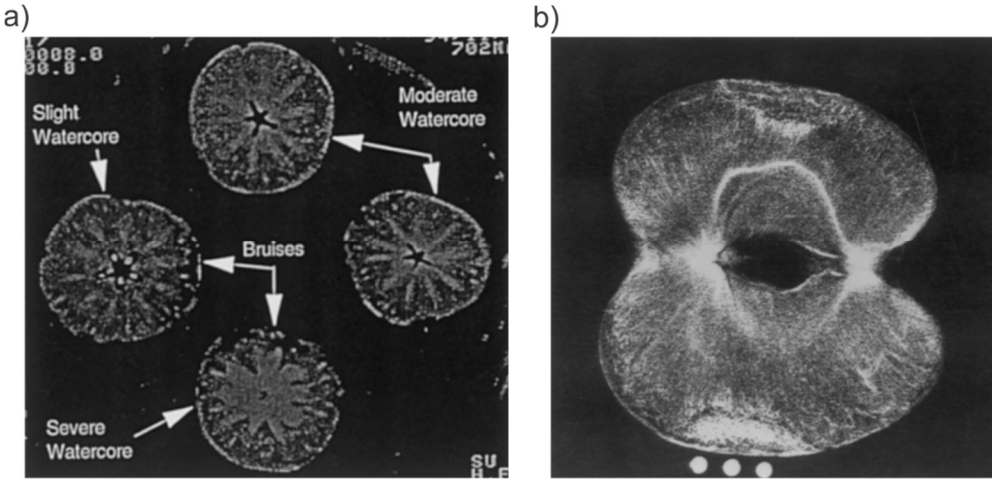

Figure 2-5. (a) X-ray tomography images of an apple showing watercore and bruses (Tollner et al., 1992). (b) Magnetic resonance images of intact 'Delicious' apples. Three one hour old bruses are visible (Chen et al., 1989).

Of all the technologies investigated for identifying internal defects, near-infrared spectroscopy is the only technology with any significant adoption from the fruit grading industry. Han et al. (2006) used the transmission of near-infrared light to identify brown core. They were able to correctly classify pears into either slight, moderate, and severe classes. Clark et al. (2003) used near-infrared spectroscopy to identify brown heart in 'Braeburn' apples.

Taste Technologies Ltd has developed their T1 system (Figure 2-4) to be able to identify some internal defects. Intelligent multivariate algorithms have been developed to identify defects based on their unique spectral signatures. They claim it can identify core rot, internal browning, water core in apples, and various other disorders present in different types of fruit (Taste Technologies Ltd, 2013). Decisions can then be made to reject these fruit or send them on for further investigation.

2.3.6 Fruit Maturity

Maturity at harvest time is an important parameter that determines post harvest storage, marketability, and taste (Kviklienė & Valiuškaitė, 2009; Kader, 1997; Ferguson et al., 1999). Immature fruit can be more susceptible to shrivelling and mechanical damage as well as suffer from poorer flavour quality (Kader, 1997). Generally fruit reach their best eating quality when allowed to ripen on the tree (Kader, 1997). Unfortunately by this stage the fruit is ready to be eaten, and the time it takes to ship it to consumers would mean that it would likely spoil. Many types of fruit also tend to soften as they ripen. This makes them far more likely to be mechanically damaged. A balancing act must be struck that allows for the best tasting fruit possible to make it to market while still subjecting them to conventional post harvest approaches such as high-speed sorting, storage, and long distance transport.

Maturity is typically estimated using maturity indices, which help guide the grower to select the best time for harvest. An example of this is the Streif Index, SI, commonly used on apples. It is defined as:

$$SI = \frac{F}{SSC \times ST} \quad ,$$

where F is the firmness, SSC is the soluble solids content, and ST is the starch index (Delong et al., 1999). It has been used successfully to estimate the optimum harvest time for different apple cultivars around the world and has been shown to be independent of orchard influences and climate conditions.

Current measurement approaches for maturity are limited because they are destructive, slow, and require careful sub-sampling to make sure the results are representative. These disadvantages mean fruit processors tend to err on the side of caution and side with a longer shelf life rather than the highest eating quality. Newer non-destructive and fast technologies could replace the current approaches so that maturity can be estimated both infield and inside the pack houses. This will allow better management of fruit, maximizing profits for growers, and a higher quality product for the consumer.

2.3.7 Firmness

Fruit firmness is an important characteristic that helps gauge the quality and maturity of fruit. It is related to the mechanical and structural properties of the fruit's flesh. This depends on many factors including the fruit's water status, climate and storage conditions, fruit maturity and variety, cell size and cell density, and the adhesive strength of the intercellular bonding (Rizzolo et al., 2010). To quantify these mechanical properties approaches similar to those used in materials engineering have been developed (Abbott, 1999). These look at fundamental properties such as the shear strength, Young's modulus (elastic region before irreversible damage), compressive strength, yield points, tensile strength, and hardness (Abbott, 1999).

Destructive (Mechanical)

To measure the material properties on fruit, a number of destructive mechanical devices and measurement schemes have been developed. The most common measurements include puncture (penetrometer), compression, and tension testing (Abbott & Harker, 2004).

The most common firmness measurement is a puncture test, also known as a penetrometer test. This has eveloved over the years to become accepted as the industry standard because of its relationship with consumer preference as found in sensory trials on apples and other fruit (Harker et al., 2002; Abbott, 1994; Mehinagic et al., 2004; Plocharski & Konopacka, 1999). A device named the Magness-Taylor pressure tester (Figure 2-6a) was the first instrument developed to carry out penetrometer measurements on fruit. This device is rather cumbersome, and adaptations of this original idea have been built which are much more compact such as the Effe-gi tester (Figure 2-6b). A penetrometer measurement is made on a region of fruit where the skin is first removed. A metal plunger (with a particular geometry) is driven into the fruit

flesh simultaneously measuring its compression, rupture, and shear properties (Nicolaï et al., 2006). The measurement device records the maximum force encountered on a gauge which is read off after the measurement and should be reported in pounds force (lbf) or Newtons (N) (Abbott & Harker, 2004).

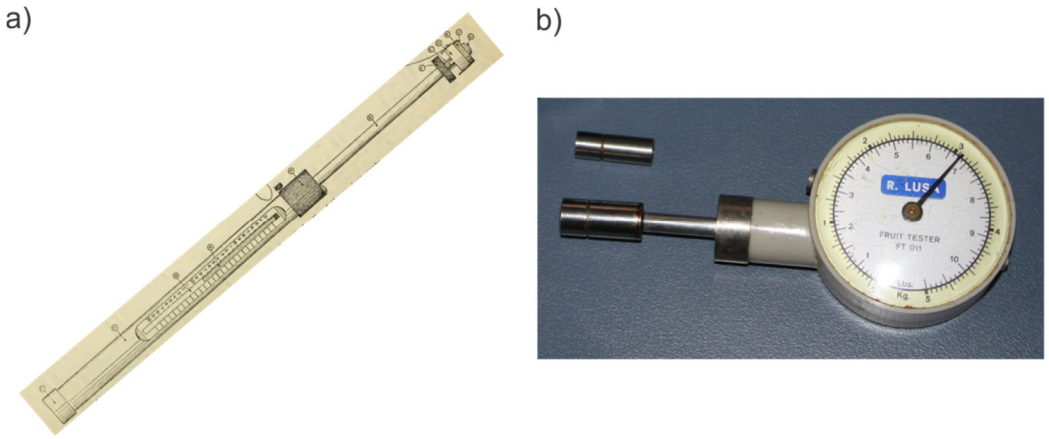

Figure 2-6. (a) Magness-Taylor pressure tester. The metal plunger shown on the right hand side penetrates the fruit flesh and the force is measured using the central gauge (Magness & Taylor, 1925). (b) An alternative compact penetrometer called the Effe-gi tester.

More recently computerised texture analysers have been developed that can carry out penetrometer measurements in a more consistent, and controlled fashion. The GUSS Fruit Texture Analyser (GS-20, GUSS Manufacturing Limited, South Africa) is one example. It has electronically controlled motors that drive a metal plunger into the fruit flesh at a constant speed and measure the resulting force using a load cell. Figure 2-7

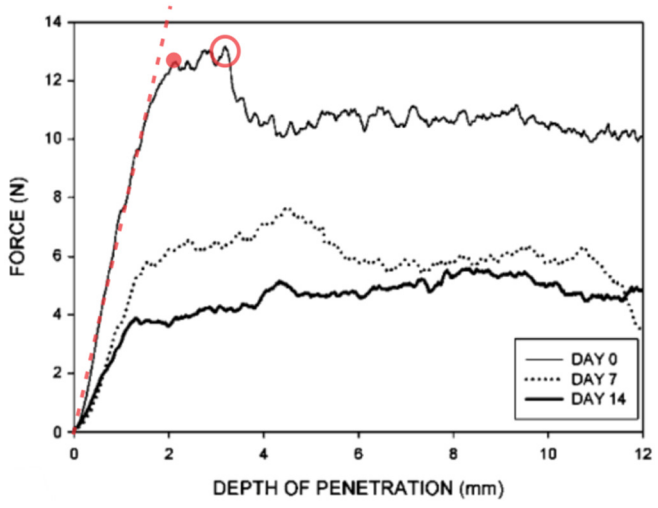

Figure 2-7. Force deformation profile from an automated penetrometer tester (Varela et al., 2007).

shows a typical force deformation profile for an automated tester. The dashed red line indicates the elastic deformation region where the elastic properties of the flesh are measured. The red dot indicates the bio-yield point where the slope significantly deviates from its value in the elastic region. Finally, the red open circle indicates the maximum force recorded throughout the whole profile (Abbott & Harker, 2004; Kilcast, 2013). The maximum force recorded is equivalent to the result from a manual penetrometer.

Another common materials test is compressive strength. Figure 2-8 (a) shows a TA.XT2i Texture Analyser (GA-XT2i/25, Texture Technologies Limited, USA) commonly used for compression testing. A cylindrical shaped sample is removed from the fruit being tested. The texture analyser then squeezes the sample using flat parallel plates and records the force as it does so. Figure 2-8b shows the force profile captured from a compression tester on apple flesh. Similar parameters to the penetrometer can be found: stiffness, modulus of elasticity, Poisson's ratio, force and deformation. Stiffness describes how a material resists deformation; the modulus of elasticity describes the stiffness of an elastic material; and Poisson's ratio describes the tendency of an object to expand in directions perpendicular to a compressive force.

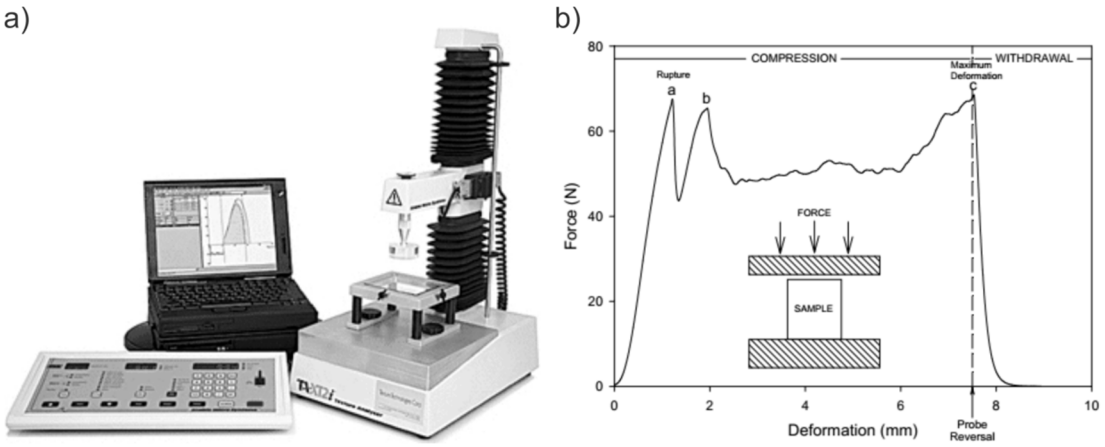

Figure 2-8. (a) TA.XT2i Texture analyser and (b) a typical compression profile showing the different features (Abbott & Harker, 2004)

The last mechanical measurement is tensile strength, which is the maximum stress that a material can withstand before failure while being stretched. Tensile testing machines are very similar to the texture analysers mentioned earlier except they run in reverse. Samples are removed from the fruit, gripped at both ends, and a machine slowly pulls them apart recording how much force is required using a load cell (Alamar et al., 2008).

Non-destructive (Mechanical)

Considerable work has been carried out developing non-destructive approaches to replace the penetrometer and the other destructive techniques. Often these new systems end up being calibrated to match the old approaches they are replacing. This improves their chances of gaining industry acceptance and eliminates the time and expense required in carrying out new sensory trials. The main approaches investigated are based on force-deformation, impact response, and acoustic response (García-Ramos et al., 2005).

Force-deformation is typically measured by applying a small force to the surface of the fruit and measuring the resulting deformation. Steinmetz et al. (1996) used a device developed by the French National Center of Agricultural Machinery, Rural Engineering, Water and Forestry (CEMAGREF) to measure micro-deformation on peaches. A 4 mm diameter micro-sphere protrudes from a reference surface which is pressed against the fruit applying a constant force. The penetration of the sphere into the skin of the fruit is measured. They found good agreement between this penetration and impact firmness (R = 0.93), acoustic firmness (R = 0.82), penetrometer firmness (R = 0.85-0.91), and stiffness (R = 0.76-0.84). Macnish et al. (1997) developed the digital firmness meter shown in Figure 2-9. It consists of a digital displacement gauge with a 12 mm range and a 0.1 mm resolution. The gauge is zeroed at the fruit surface, and a

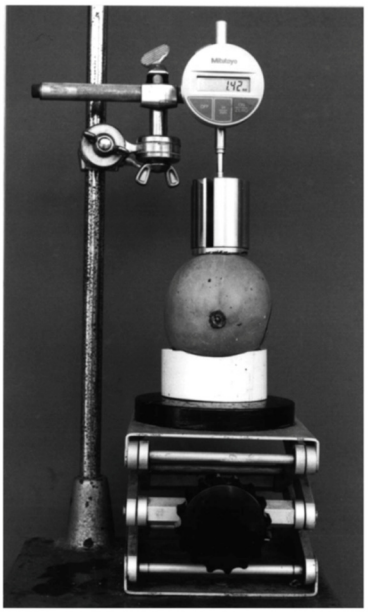

Figure 2-9. Digital firmness meter consisting of an electronic indicator gauge, laboratory jack, and a 500 g weight (Macnish et al., 1997).

500 g weight is used to deform the fruit and after 30 seconds the amount of deformation is recorded. Measurements with this system correlated strongly (R = 0.96) with a subjective hand pressure measurement where panellists rated fruit from 1 to 5 (firm to soft).

Impact response measurements are carried out by hitting the fruit with a small mass or by dropping the fruit onto a surface. In each case, the kinematics involved in the impact is measured using sensing elements such as an accelerometer. García-Ramos et al. (2005) state in their review that Chen & Ruiz-Altisent (Chen & Ruiz-Altisent, 1996) found impact force and its duration are directly related to fruit firmness. Figure 2-10 shows the impact response system used by Lien et al. (2009) to measure tomato maturity. Fruit were dropped from 15 mm because it provided adequate signal while not visibly bruising the fruit. Fruit were grouped based on penetrometer firmness using a cluster analysis and then classified using the impact response indices. A regression analysis showed they could classify the correct maturity with an accuracy of 79.2%.

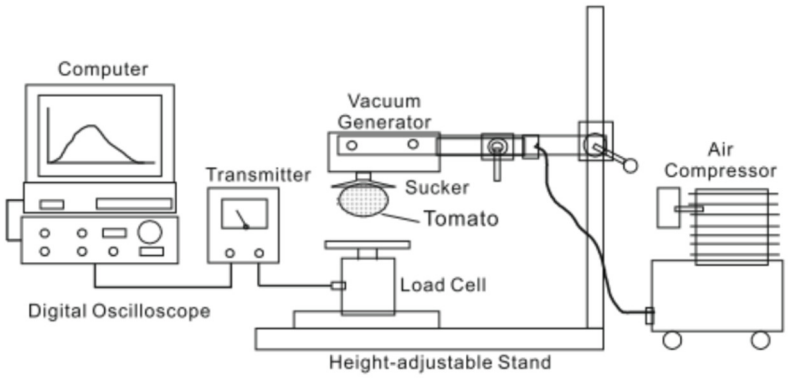

Figure 2-10. Impact response system by Lien et al. (2009).

Commercially impact response has been used in the Sinclair IQ firmness tester (Sinclair Systems International, United States) and the Greefa Intelligent Firmness Detector (iFD, Greefa, Geldermalsen, Netherlands). The Sinclair firmness tester uses air driven bellows which cause a mass at one end to impact the fruit. The impact is measured using an accelerometer, and firmness is calculated from an empirical model. Howarth & Ioannides (2002) found that it was able to predict penetrometer firmness for nectarines (R = 0.95), avocados (R = 0.84), and kiwifruit (R = 0.92) but was not able to predict firmness in apples. Their website suggests that it is currently being used for avocado and kiwifruit only and active marketing of the device has ceased (Sinclair,

2007). The Greefa iFD carries out a similar measurement. A large wheel equipped with multiple sensors rotates impacting each fruit multiple times and can operate at speeds up to 7 fruit per second (Kilcast, 2013). Greefa has very little information available on the iFD and no longer appears to be marketing the firmness sensing system on their website (Greefa, 2014).

Acoustic firmness, thought of as a whole fruit measurement, involves subjecting the fruit to an impact or other excitation force to make the fruit vibrate (García-Ramos et al., 2005). This vibration signal is captured using a microphone or other sensing element, and the resonant frequency is extracted using a fast Fourier transform (Baerdemaeker et al., 1982). The resonant frequency of the fruit depends on its geometry, mass, and modulus of elasticity (Duprat et al., 1997). As fruit matures and softens the modulus of elasticity decreases which is believed to be a good indicator of the mechanical properties of the fruit tissue (Duprat et al., 1997).

Yamamoto et al. (1980) developed a system for measuring the natural frequency of fruit and tested it on apples and watermelons. A pendulum is swung into the fruit and the vibration signal captured with a microphone. They found poor correlations between natural frequency and penetrometer firmness for watermelons. For 'Starking Delicious' and 'Golden Delicious' apples correlations improved ($R = 0.65$-0.77). Shmulevich et al. (1996) developed the Firmalon firmness tester based on acoustic firmness. They used a mechanical impulse to excite the fruit and measured the vibration signal using a piezoelectric film sensor. They found the technique fast, simple, and repeatable. The Firmalon device was used to continuously monitor fruit in controlled atmosphere (CA) storage and showed a steady decrease in acoustic firmness as the fruit softened, however, there was no correlation between this and Magness-Taylor firmness measurements (Shmulevich et al., 2002). Cen et al. (2013) used a commercial bench top acoustic firmness sensor (AFS, AWETA, Nootdorp, Netherlands) to non-destructively monitor 'Golden Delicious' and 'Granny Smith' apples during storage. They also found a consistent decrease in acoustic firmness over time.

AWETA have a commercial version of their acoustic firmness sensor that can operate in pack houses at high speed (Figure 2-11). As the fruit travel along a small mass taps them, a bellow is used to isolate out background noise, and a microphone captures the resulting vibration signal. They have had some success with uptake by the avocado

industry (Calavo, 2013). However, its practical use in other fields is unknown, and their website no longer markets their acoustic sensors.

Figure 2-11. Mango fruit being measured for acoustic firmness using AWETA's online high-speed acoustic firmness sensor (AFS, AWETA, Nootdorp, Netherlands).

Non-destructive (Optical)

Currently, there is a significant amount of research being carried out on the development of optical systems that can index fruit firmness. Usually fruit samples are illuminated in some way, and the interaction between that light and a sample's tissue is used to estimate firmness. Optical systems would have significant advantages over their mechanical counterparts. They tend to have few or no moving parts minimizing maintenance. They require no mechanical contact with the fruit, reducing any chance of mechanical damage such as bruising. It also means they are not constrained by mechanical inertia and allow for operation at speeds in excess of 10 fruit per second (typical apple grading speeds). The following chapters will go into more detail relavant to optical firmness measurements.

2.4. Summary

There are many types of measurements for quantifying the quality of fruit. Determination of weight, size, shape, density, colour, and external defects has become routine in the fruit grading industry. Measurements for eating quality are far less common but are of great importance to consumer satisfaction. The requirement for non-destructive, high-speed measurements (ten fruit per second) has limited which approaches can be successfully applied. In terms of eating quality, the main commercial technology adopted has been near-infrared spectroscopy, used to estimate dry matter, soluble solids content and some internal defects.

Firmness, as one of the main characteristics of eating quality and maturity, remains one of the most difficult to measure non-destructively. The industry wide reliance on the penetrometer firmness measurement has meant gaining traction with new technologies

is difficult, and many remain in bench-top form only. A few exceptions to this are the devices built by AWETA, Greefa, and Sinclair. These companies have taken their firmness measurement technologies onto high-speed grading lines, however, all three technologies are limited to particular fruit types, still require physical contact with the fruit limiting their operational speed, and risking physical damage to the fruit.

There remains an opportunity for the development of a more effective firmness sensing system that is non-destructive, capable of operating at high speeds, and suitable for other fruit types. In light of this opportunity, there has been a number of optical based firmness measurements investigated. The following chapters introduce light transport through fruit samples and discuss various optical approaches currently being investigated for measuring firmness.

3. Optical Properties and Light Transport

In order to discuss the optical approaches used for measuring firmness non-destructively in fruit (Chapter 4) it is important to understand how light propagates inside the fruit samples. This chapter gives a brief overview of the optical properties that characterise photon propagation in biological tissue. This includes the refractive index, absorption and scattering coefficients, and the anisotropy factor. This chapter also introduces the basic models commonly used for describing light transport inside these samples including radiation transport theory and the diffusion approximation.

3.1. Optical Properties

In a homogenous medium light travels in well defined paths, and the absorption of light that occurs as it propagates can be adequately described by the Beer-Lambert Law. Once the medium contains in-homogeneities that cause the light to undergo multiple scattering it is known as turbid, and more sophisticated models are required.

Figure 3-1a demonstrates some of the basic effects that take place as light interacts with a turbid sample. On the immediate boundary a small portion of the light is reflected based on the refractive index mismatch between the two media (n_1 and n_2). The remaining portion enters the material where it propagates and is occasionally scattered (μ_s) or absorbed (μ_a). Fruit can typically be considered a turbid medium (Figure 3-1b).

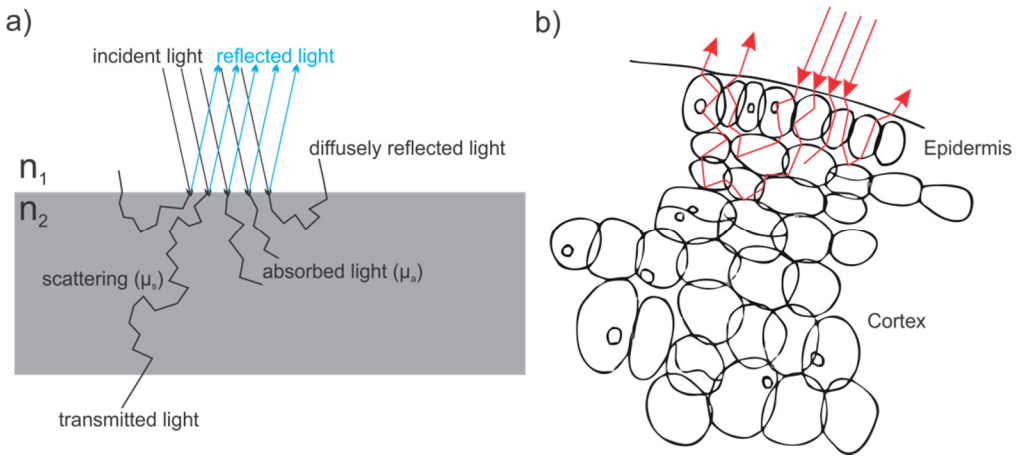

Figure 3-1. (a) Illustration of the optical behaviour as light interacts with a turbid sample. (b) Light interaction inside of an apple. Scattering occurs on cell boundaries and on contents inside each cell (the original diagram of fruit cell structure was taken from Bain & Robertson (1951)).

Inside there are many in-homogeneities including cell wall boundaries, cell membranes, mitochondria, and nuclei (Esau, 1993). This interaction of light with a sample can be described by the sample's refractive index, absorption coefficient, scattering coefficient, and anisotropy factor.

3.1.1 Refractive Index

The refractive index ($n(\lambda)$), is an intrinsic property of all materials that determines the speed of light inside a medium. It is a wavelength dependent function defined as:

$$n(\lambda) = \frac{c}{c_m(\lambda)} \quad ,$$

where c is the speed of light in a vacuum, $c_m(\lambda)$ is the speed of light inside the medium, and λ is the wavelength of light. Changes in refractive index are responsible for scattering, reflection, and refraction. As light encounters an abrupt refractive index change (Figure 3-2) a portion is reflected and the remaining portion is refracted. Reflected light propagates away at the same angle as it arrives, that is $\theta_1 = \theta_2$. The fraction of incident power that is reflected can be calculated using the Fresnel equations and is related to the degree of mismatch in the refractive indices, the polarisation state, and the incident angle. The remaining fraction of light is refracted at an angle based on Snell's law defined as:

$$n_1 \sin\theta_1 = n_3 \sin\theta_3 \quad ,$$

where n_1 and n_3 are the refractive indices of the two media, and θ_1 and θ_3 are the incident and refracted angles respectively (Welch & Gemert, 2010).

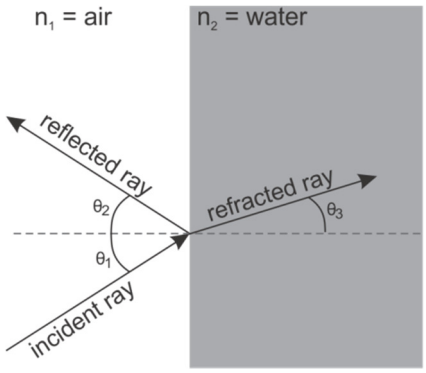

Figure 3-2. Illustration of light encountering an abrupt refractive index change.

3.1.2 Absorption Coefficient

Absorption occurs when atoms and/or molecules take up energy from incident radiation. This raises the absorbing molecule or atom to an excited state. These

transitions correspond to specific energy levels, and hence are found only in specific spectral bands.

Depending on the energy levels (wavelength) of the excitation source there can be a number of absorption processes that take place. These include electronic, vibrational, and rotational. Electronic transitions can occur in both atoms and molecules while vibrational and rotational process can occur only in molecules (Vo-Dinh, 2010). Electronic transition based absorption requires higher energy levels than vibrational and rotational absorption. For this reason UV and visible wavelengths, with their higher energy levels, can induce electronic based absorption while NIR and IR wavelengths typically induce vibrational and rotational absorption (Welch & Gemert, 2010).

Once absorption occurs, and the species is excited to a higher energy state, it will then decay. If the transition is electronic then there could be a re-emission of a photon that corresponds to the energy level difference, or alternatively the decay could present in the form of localised heating, as is the case for the vibrational or rotational processes (Welch & Gemert, 2010). The overall result of this is a reduction in intensity.

To characterise the absorption properties of a certain medium it is common to use the absorption coefficient (μ_a) and absorption cross section (σ_a) (Vo-Dinh, 2010). For a localised absorber the absorption cross section is:

$$\sigma_a = \frac{P_{abs}}{I_0} \quad ,$$

where P_{abs} is the amount of power absorbed, and I_0 is the intensity of the initial uniform plane wave. In a medium with a uniform distribution of the same absorbing particles we get the absorption coefficient:

$$\mu_a = \rho\sigma_a \quad ,$$

where ρ is the number density of absorbers. The absorption coefficient (μ_a) has units of per unit length (usually mm^{-1}). The relationship between absorption and the thickness of a medium is known as the Lambert-Bouguer law:

$$dI = -\mu_a I dz \quad ,$$

where dI is the differential change of intensity for a collimated beam propagating an infinitesimal path dz through the medium. For an incident intensity (I_0), propagating through a sample of a known thickness (z), the transmitted intensity is given by:

$$I = I_0 \exp(-\mu_a z) \quad ,$$

This is known as the Beer-Lambert law (Figure 3-3), also commonly expressed as:

$$I = I_0 \exp(-\varepsilon a z) \quad ,$$

where ε_λ is the molar extinction coefficient, a is the molar concentration of the absorption species, and z is the path length (thickness). To satisfy the Beer-Lambert law the medium must be homogenous, non-scattering, the absorbers must act independently, incident radiation must be parallel rays traversing the same path length, and the radiation should be monochromatic.

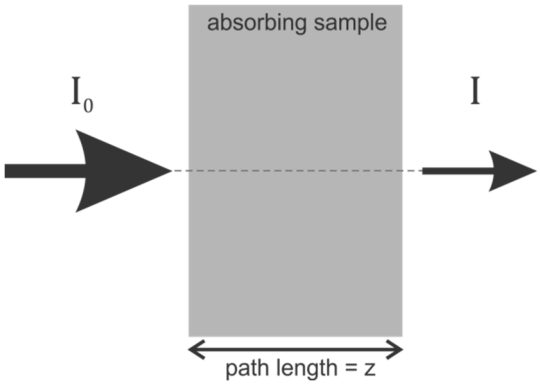

Figure 3-3. Absorption of light by a non-scattering homogenous sample. The Beer-Lambert law can be used to calculate the transmitted intensity based on the absorption coefficient of the sample and the path length.

This relationship between the physical chemistries (atoms and molecules) of the medium and absorption makes it useful for interrogating the chemical composition of a sample. In fruit for example, NIR absorption is mainly caused by the C-H, O-H, and N-H bonds in the compounds which make up the fruit. These compounds include water, sugars, chlorophylls, and carotenoids (Nicolaï et al., 2014). The absorption of light due to these bonds has been widely used in the fruit grading industry for predicting sugar content and dry matter (Chapter 2).

3.1.3 Scattering Coefficient

Light scattering occurs when light travelling in a host medium encounters an obstacle/inhomogeneity in the refractive index. The light is scattered over a range of angles depending on the refractive indices of the host and scatterer materials, the size of the scattering particle, and the wavelength of the light. Scattered light gives useful information about the spatial properties of the medium such as structural detail and density fluctuations. Like absorption, scattering inside a medium can be characterized

by the scattering coefficient (μ_s) and the scattering cross section (σ_s) (Vo-Dinh, 2010). The scattering cross section is:

$$\sigma_s = \frac{P_{scatt}}{I_0} \quad ,$$

where I_0 is the intensity of a monochromatic plane wave encountering a scattering object, and P_{scatt} is the power that gets redirected by the scattering object. The scattering coefficient is:

$$\mu_s = \rho\sigma_s \quad ,$$

where, this time, ρ is the number density of the scattering particles. As with the absorption coefficient the units are in per unit length (mm^{-1}) and the reciprocal of the scattering coefficient is known as the mean free path between scattering events.

The scattering phenomenon is divided into three domains based on the size of the scattering particle relative to the wavelength of light. The first is Rayleigh scattering where the size of the scatterer is small compared to the wavelength of the incident light. Rayleigh scattering is considered elastic because the energy of the scattered photon is the same as that of the incident photon. Rayleigh scattering is the main mechanism responsible for the blue colour in the sky. This is due to the strong $1/\lambda^4$ relationship; blue wavelengths are strongly scattered compared to red wavelengths. The second domain covers the region where the size of the scatterers is similar to the wavelength of light. This is commonly known as Mie theory. Gustav Mie developed a solution to describe both absorption and scattering by spherical particles of arbitrary radius and refractive index (Mie, 1976). It is important to note that this is a general solution which can also be used, with increased complexity, in the Rayleigh scattering region. The third scattering domain covers the region where the wavelength of light is small compared to the size of the scatterers. In this case, standard geometric optics can be applied (reflection and refraction).

In fruit, the complex tissue structure made up of cells, their internal components, and intercellular air spaces introduces refractive index mismatches that cause light to scatter (Nicolaï et al., 2014). Apples for example consist of a fleshy tissue made up of parenchyma cells permeated with vascular tissue and intercellular air spaces (Rizzolo et al., 2010). The geometric properties of these cells, presence of a middle lamella, water content, and subcellular features such as mitochondria and nuclei all influence how light scatters within the sample (Rizzolo et al., 2010). Measurement of this interaction

provides a way to interrogate the structural and textural composition of the fruit sample leading to the possible measurement of quality parameters like firmness, mealiness, and crunchiness.

3.1.4 Anisotropy Factor and Scattering Phase Function

In relation to scattering, another important property is the scattering phase function ($p(\hat{s}, \widehat{s'})$). This describes the angular distribution of scattered light. That is, the probability that a photon travelling in its original direction ($\hat{s}$), is scattered emerging with a new direction ($\widehat{s'}$). If the scattering is symmetric with respect to the incident direction then the phase function only depends on the angle between the two directions ($\hat{s}$ and $\widehat{s'}$). If the scattering particles are randomly distributed throughout the medium then the phase function can be normalised to unity (Boas et al., 2012). The normalised phase function is defined as:

$$\int_{4\pi} p(\hat{s}, \widehat{s'})\, d\Omega' = 2\pi \int_0^{\pi} p(\theta) \sin\theta \, d\theta = 1 \quad ,$$

where $d\Omega'$ is the cone of solid angle originating at the scatterer and θ is the scattering angle. The phase function is usually approximated using the Henyey-Greenstein function. This was developed to describe the angular dependence of light scattering by small particles while studying the diffuse radiation from interstellar dust clouds. It has also been proven experimentally to be a good approximate scattering phase function for describing optical transport in the Mie scattering region (Vo-Dinh, 2010). It is defined as:

$$P_{HG}(\cos\theta) = \frac{4\pi\sigma_s}{\sigma_a + \sigma_s} \frac{1 - g^2}{(1 + g^2 - 2g\cos\theta)^{3/2}} \quad ,$$

where g is the anisotropy factor, σ_a is the absorption cross section, and σ_s is the scattering cross section. The anisotropy factor (g), represents the mean cosine of the scattering angle, defined as:

$$\mathrm{g} = \langle \cos\theta \rangle = 2\pi \int_0^{\pi} \cos\theta \, p(\theta) \sin\theta \, d\theta$$

Figure 3-4 illustrates the effect of the anisotropy factor in the scattering phase function. It can range from -1 for highly backward scattering (Figure 3-4a) to +1 for highly forward scattering (Figure 3-4c). In between (g = 0) the scattering is considered isotropic (Figure 3-4b).

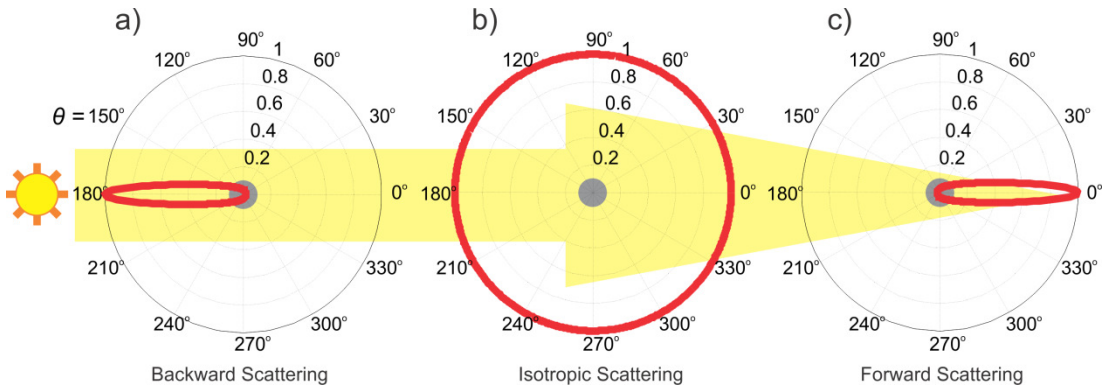

Figure 3-4. The effect of the anisotropy factor on the scattering phase function (red line). (a) Backward scattering with an anisotropy factor of -0.9, (b) isotropic scattering with an anisotropy factor of 0, and (c) forward scattering with an anisotropy factor of +0.9.

By combining the scattering coefficient (μ_s) and anisotropy factor (g) we get a third optical property commonly called the reduced (or transport) scattering coefficient (μ_s'), defined as:

$$\mu_s' = \mu_s(1 - g)\,.$$

This represents the number of isotropic scattering events that occur per unit length and is used in diffusion theory for modelling light transport in turbid media. The inverse of the reduced scattering coefficient is the reduced mean free path which corresponds to the distance a photon must travel before it's scattering is considered isotropic. The purpose of the reduced scattering coefficient is to describe the propagation of photons as they randomly walk with a step size equal to the reduced scattering mean free path ($1/\mu_s'$). Each of these steps corresponds to an equivalent isotropic scattering step that is made up of a number of small anisotropic steps ($1/\mu_s$). Figure 3-5 illustrates this. With an anisotropy factor of 0.9 scattering is in the forward direction with an average deflection angle of 26°. It would take 10 scattering events before reaching an equivalent point where the light scatter is now considered isotropic.

3.2. Modelling Light Propagation in Turbid Media

There are two main theories that have been developed to model the propagation of light where multiple scattering occurs (turbid media). The first is called the analytical theory (or multiple scattering theory) and is based on Maxwell's equations. It is mathematically rigorous accounting for all effects including polarisation, diffraction, and interference (Martelli et al., 2009). This high level of complexity makes the

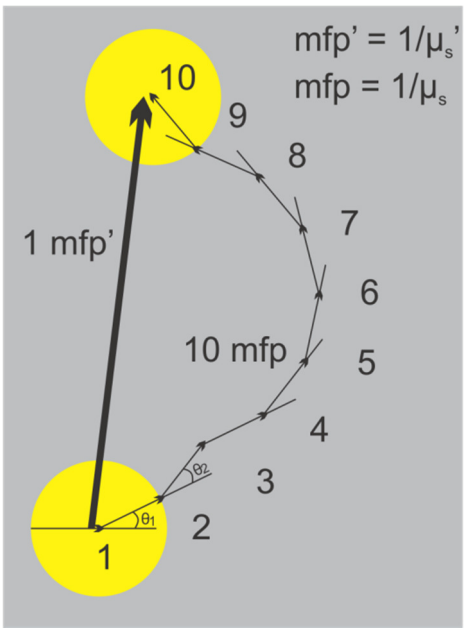

Figure 3-5. Example comparison between the reduced scattering mean free path and the standard scattering mean free path (Jacques, 2007).

analytical approach difficult for use in practical situations. The second is radiative transport theory. This is a phenomenological and heuristic theory which describes the flow of energy through a scattering medium (Martelli et al., 2009). While it is not mathematically rigorous it has been used, with simplifying assumptions, to develop useful models for practical situations such as atmospheric scattering and light propagation inside biological tissue (Derya & Ilan, 2013). The following sections discuss radiative transport theory and some of its applications.

3.2.1 Radiative Transport Theory

Radiative transport theory describes the flow of energy within the medium ignoring the wavelike nature of light. It only considers the transport of individual photons that can either be absorbed or scattered. This is described mathematically using the radiative transport equation (Boltzmann equation) where light is treated as a localized incoherent packet of photons. If that packet of energy is located at $\boldsymbol{r}(t)$ and is propagating in the $\hat{\boldsymbol{s}}$ direction then over a time interval dt there are losses due to absorption and scattering out of the $\hat{\boldsymbol{s}}$ direction, and gains from light scattered from other directions into the $\hat{\boldsymbol{s}}$ direction (Vo-Dinh, 2010). The radiative transport equation provides a relationship between the radiance $I(\boldsymbol{r}(t), \hat{\boldsymbol{s}}, t)$, at position $\boldsymbol{r}(t)$, in the direction $\hat{\boldsymbol{s}}$, and these gains or losses. It is defined as:

$$\frac{1}{c_m}\frac{\partial I(\boldsymbol{r},\hat{\boldsymbol{s}},t)}{\partial t} = -\hat{\boldsymbol{s}}\cdot\vec{\nabla}I(\boldsymbol{r},\hat{\boldsymbol{s}},t) - (\mu_a+\mu_s)I(\boldsymbol{r},\hat{\boldsymbol{s}},t) + \frac{(\mu_a+\mu_s)}{4\pi}\int_{4\pi} p(\hat{\boldsymbol{s}},\hat{\boldsymbol{s}}')\,I(\boldsymbol{r},\hat{\boldsymbol{s}},t)d\Omega' + Q(\boldsymbol{r},\hat{\boldsymbol{s}},t) \quad ,$$

Where c_m is the speed of light in the medium, μ_a is the absorption coefficient, μ_s is the scattering coefficient, p is the phase function, and Q is the source term where the radiation originates from.

3.2.2 Diffusion Approximation

The radiative transport equation is well accepted. However, no analytical solutions are available (Martelli et al., 2009). Further assumptions are required to generate simpler approximate models. The Diffusion Approximation (P1 approximation) is an approximate solution to the radiative transport equation based on diffusion theory and the assumptions that inside the medium light scattering is the main method of transport ($\mu_s' \gg \mu_a$). This scattering is approximately isotropic, and the source is an isotropic point source. The time dependent diffusion equation is (Vo-Dinh, 2010):

$$\frac{\partial}{\partial t}\Phi_d(\boldsymbol{r},t) = D\nabla^2\Phi_d(\boldsymbol{r},t) - \mu_a c_m \Phi_d(\boldsymbol{r},t) + Q_c + Q_s \quad ,$$

where Φ_d is the fluence rate, or the amount of energy that intersects a unit area in a specific time interval (Figure 3-6), Q_c and Q_s are the coherent and local sources, and D is the diffusion constant defined as:

$$D = \frac{c_m}{3(\mu_a + (1-g)\mu_s)} \quad .$$

When applying diffusion theory care must be taken to avoid boundary effects, and ensure illumination sources are sufficiently far from the detectors.

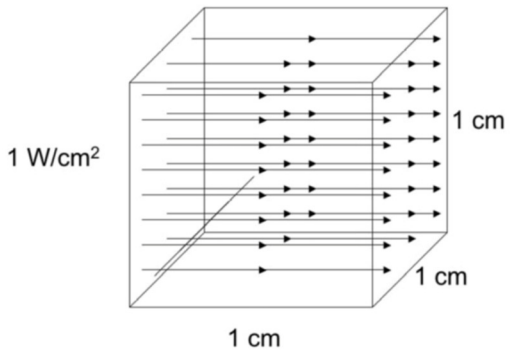

Figure 3-6. Illustration of a fluence rate equal to 1W/cm² (Jacques & Pogue, 2008).

Solutions to the Diffusion Approximation

Work carried out in this thesis and some of the work discussed in the optical techniques for predicting firmness chapter (Chapter 4) involves steady state, spatially-resolved measurements. This section introduces two commonly used steady state solutions to the diffusion approximation.

The first, developed by Farrell et al. (1992), describes the reflectance (R) at a radial distance (ρ) from an infinitely small beam, illuminating a semi-inifinite, homogenous, turbid sample (Figure 3-7). This solution assumes that the resulting reflectance originates from an isotropic source located one transport mean free path ($1/\mu_s'$) inside the sample below the incident point. It is defined as:

$$R(\rho) = \frac{a'}{4\pi}\left[\frac{1}{\mu_t'}\left(\mu_{eff} + \frac{1}{r_1}\right)\frac{\exp\left(-\mu_{eff} r_1\right)}{\mathrm{r}_1^2} + \left(\frac{1}{\mu_t'} + \frac{4A}{3\mu_t'}\right)\left(\mu_{eff} + \frac{1}{r_2}\right)\frac{\exp\left(-\mu_{eff} r_2\right)}{\mathrm{r}_2^2}\right] \quad ,$$

where a' is the transport albedo ($a' = \mu_s'/(\mu_a + \mu_s')$), μ_t' is the total interaction coefficient ($\mu_t' = \mu_a + \mu_s'$), μ_{eff} is the effective attenuation coefficient ($\mu_{eff} = \left(3\mu_a(\mu_a + \mu_s')\right)^{1/2}$), r_1 and r_2 are the distances from the observation point at the interface to the isotropic source and the image source defined as (Qin & Lu, 2005):

$$r_1 = \left[\left(\frac{1}{\mu_t'}\right)^2 + r^2\right]^{1/2}$$

$$r_2 = \left[\left(\frac{1}{\mu_t'} + \frac{4A}{3\mu_t'}\right)^2 + r^2\right]^{1/2} \quad .$$

A is related to the surface reflection and can be derived from the Fresnel reflection coefficients or through the use of an alternative empirical approach developed by Groenhuis et al. (1983):

$$A = \frac{1 + r_d}{1 - r_d} \quad ,$$

where

$$r_d = -1.440 n_{rel}^{-2} + 0.710 n_{rel}^{-1} + 0.668 + 0.0636 n_{rel} \quad .$$

n_{rel} is the relative refractive index ($n_{rel} = n_{tissue}/n_{air}$).

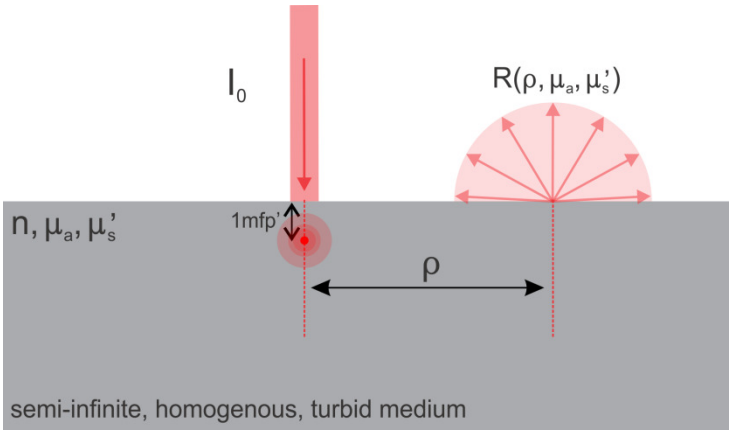

Figure 3-7. The solution developed by Farrell et al. (1992) describes the reflectance from an infinitely small beam illuminating a turbid medium.

The second model is an improved solution to the stead-state diffusion equation developed by Kienle & Patterson (1997). They calculated reflectance from the integral of the reflected radiance and not from the gradient of the fluence rate, an approach originally presented by Haskell et al. (1994) in the frequency domain. This leads to a model where the steady-state spatially resolved diffuse reflectance ($R(r)$) can be expressed as the sum of the scaled isotropic fluence rate at the surface, and the scaled diffuse reflectance calculated as flux (Cen et al., 2010):

$$R(r) = C_1\Phi(r, z = 0) + C_2 R_{flux}(r)\,,$$

where Φ is the fluence defined as:

$$\Phi(r, z = 0) = \frac{1}{4\pi D}\left[\frac{\exp(-\mu_{eff} r_1)}{r_1} - \frac{\exp(-\mu_{eff} r_2)}{r_2}\right] \quad ,$$

and $R_{flux}(r)$ is the flux defined as:

$$R_{flux}(r) = \frac{a'}{4\pi}\left[\frac{1}{\mu_t'}\left(\mu_{eff} + \frac{1}{r_1}\right)\frac{\exp(-\mu_{eff} r_1)}{r_1^2} + \left(\frac{1}{\mu_t'} + \frac{4A}{3\mu_t'}\right)\left(\mu_{eff} + \frac{1}{r_2}\right)\frac{\exp(-\mu_{eff} r_2)}{r_2^2}\right] \quad .$$

The flux term is the same as the solution provided for reflectance by Farrell et al. (1992). The scale terms (C_1 and C_2) are constants determined by the relative refractive index mismatch at the tissue-air interface (Cen et al., 2010):

$$C_1 = \frac{1}{4\pi}\int_{2\pi}\left[1 - R_{fres}(\theta)\right]\cos\theta \, d\Omega$$

$$C_2 = \frac{3}{4\pi}\int_{2\pi}\left[1 - R_{fres}(\theta)\right]\cos^2\theta \, d\Omega \quad ,$$

where $R_{fres}(\theta)$ is the Fresnel reflection coefficient for a photon with an incident angle of θ (Kienle & Patterson, 1997). For a refractive index of 1.4, C_1 is equal to 0.118 and C_2

is equal to 0.306. For biological samples such as fruit, a refractive index of 1.35 is commonly used, resulting in a C_1 equal to 0.1277 and C_2 equal to 0.3269 (Cen et al., 2011).

Both the solution developed by Farrell et al. (1992) and the improved solution by Kienle & Patterson (1997) have been used to measure the optical properties of fruit and form predictive models for fruit quality attributes (Lu et al., 2009, 2006; Qin et al., 2009; Cen et al., 2011).

3.2.3 Monte Carlo

Another approach that makes use of radiative transport theory is the Monte Carlo method. This is a stochastic approach where simulation is used to model the path of photons inside a medium. The path these photons take depends on the probability that the photons are absorbed or scattered. Photons are injected into the sample where they propagate in straight lines through a number of discrete interactions. At each interaction, a decision is made as to whether the photon is scattered or absorbed. Once the photon is scattered out of the region of interest or it is permanently absorbed then the simulation stops. Monte Carlo has been widely used because of its simple implementation, its ability to handle very complex geometries, and its accurate results. It is not limited by the assumptions of the Diffusion Approximation ($\mu_s' \gg \mu_a$) and results can be accurate near boundaries. The main disadvantage is that Monte Carlo modelling is computationally intensive. Photons are governed by Poisson statistics so the signal-to-noise ratio of the sampled distribution only increases with the square root of the number of photons in the simulation (Schmidt, 1999).

4. Optical Techniques for Predicting Fruit Firmness

Of the many parameters used to characterise fresh fruit, firmness remains one of the more elusive for online grading. Traditionally it is measured using a penetrometer (Chapter 2) which has a relationship to sensory data and is generally accepted by industry. Penetrometer measurements are however destructive making them unsuitable for online, high-speed sorting.

Building on the optical properties of samples discussed in the previous chapter we now look at the results described in the literature for optical firmness measurement. Optical approaches have significant advantages over their mechanical counterparts; they are non-destructive, require no mechanical contact with the fruit (not constrained by mechanical inertia), and they can operate at high speed.

This chapter describes a number of optical firmness measurements that fall under the broad category of near-infrared spectroscopy (NIRS). NIRS is any measurement where a sample is illuminated with near-infrared radiation and the light that interacts with the sample is measured using various detection schemes. Figure 4-1 shows the electromagnetic spectrum. The near infrared region encompasses the wavelength range from 780 nm to 2500 nm (Nicolaï et al., 2007). This region also covers most of the therapeutic window (600 nm to 1300 nm); an important region for biological samples because light propagation tends to be dominated by scattering, and absorption tends to be low enough for light to probe several mm or more below the surface (Fraser et al.,

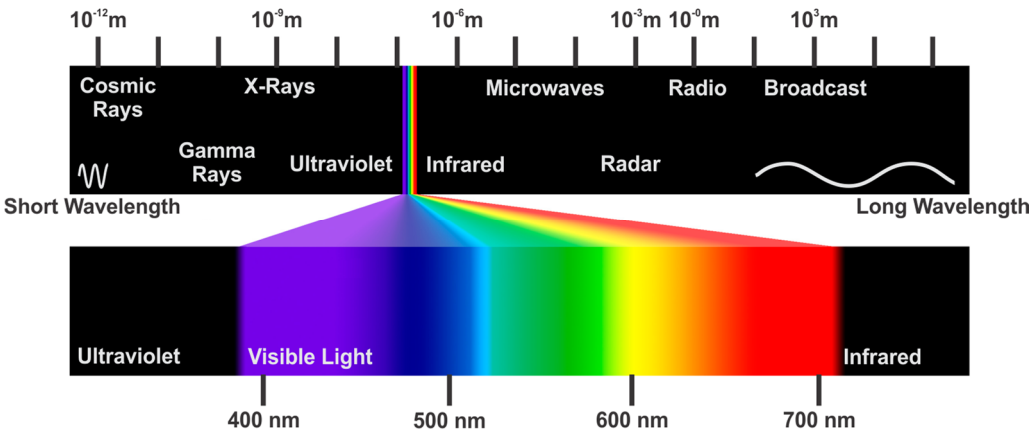

Figure 4-1. The electromagnetic spectrum.

2001). Often wavelengths below 780 nm are also included as these regions contain valuable information on absorbing pigments within the fruit flesh and skin (Merzlyak et al., 2003).

As light propagates in a sample it is affected both by absorption (chemical) and scattering (structural properties). Once the resulting spectra are measured a number of approaches are used to build models that relate the spectra to destructive reference measurements (dry matter, penetrometer firmness, soluble solids content). This is typically done using chemometric multivariate analysis tools which build the models using a number of regression methods including partial least squares regression (PLS), multiple linear regression (MLR), and principal components regression (PCR). The generated models can then be used on further fruit to predict the destructive measurement results non-destructively (Lammertyn et al., 1998; Peirs et al., 2002; McGlone et al., 2002; Ventura et al., 1998).

4.1. Near Infrared Spectroscopy

Near-infrared spectroscopy, the measurement, describes an approach where a broadband source is used to illuminate a sample and the light that interacts with the sample is measured using a spectrometer or scanning detector. Near-infrared spectroscopy in the horticultural field was initially used to measure dry matter on onions, soluble solids content in apples, and water content in mushrooms (Nicolaï et al., 2007). Today it has been applied to a wide variety of horticultural and agricultural problems including measuring the quality of grains, vegetables, fruits, dairy products, and eggs (Ozaki et al., 2006; Workman et al., 2007).

Three common measurement configurations are illustrated in Figure 4-2. The first is a reflectance measurement where the sample is illuminated from above and a detector measures light that is reflected back. The second is transmittance where the sample is illuminated from one side and a detector measures light on the other. This approach ensures that all of the light measured has interacted with the sample. It is often difficult to make transmittance measurements due to the exponential attenuation of light as it travels through the sample. The final configuration is interactance where light from a source illuminates the sample and a barrier is used to block surface reflections from reaching the detector. Light must first travel through the fruit where it is scattered in the direction of the detector and measured. In all cases the illuminated area is typically

large compared with the sample size, both for simplicity (often a tungsten halogen lamp is used which can be difficult to focus to a small area), to get plenty of light in to the sample (reducing measurement time), and to reduce the effect small variances in the fruit have on the measurement.

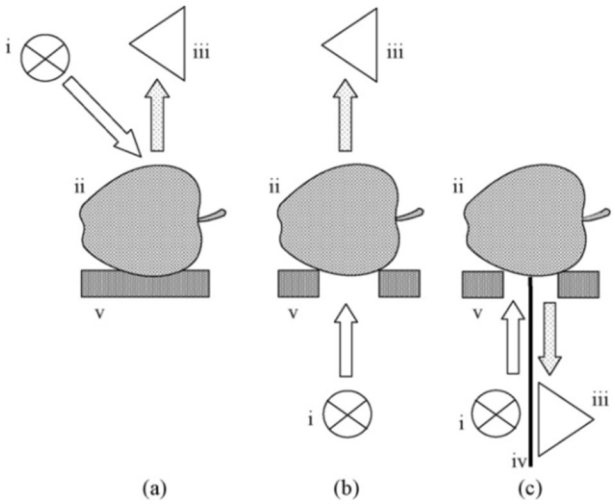

Figure 4-2. Different acquisition schemes for near infrared spectroscopy measurements. (a) reflectance, (b) transmittance, and (c) interactance. (i) is the light source, (ii) is the sample, (iii) is the detector, (iv) is a light barrier, and (v) is a mechanical support (Nicolaï et al., 2007).

Lammertyn et al. (1998) used near-infrared spectroscopy on 210 'Jonagold' apples to non-destructively measure acidity, soluble solids, and firmness. Their system consisted of a 100 W tungsten halogen lamp and a scanning spectrophotometer (380 to 1650 nm). Fruit reflectance measurements were made in four positions an equal distance apart around the equator. Principal component regression and partial least squares regression techniques were used to develop prediction models. They found good to excellent prediction performance with a standard error of prediction (SEP) of 0.54 to 0.67 °Bx (R=0.79 to 0.87) for soluble solids, SEP of 0.062 to 0.079 pH (R=0.90 to 0.94) for acidity, and a SEP of 0.27 to 3.24 N/mm (R=0.73 to 0.75) for predicting the slope of the force deformation curve. The units of degrees brix (°Bx) is the percentage of sugar content in an aqueous solution.

Peirs et al. (2002) compared Fourier transform (FT) NIR spectroscopy to traditional NIRS approaches. Their NIRS system consisted of a tungsten halogen lamp with a fibre bundle to deliver light to the sample. A detection fibre is placed at an angle of 45° from the incident spot which delivers light to a monochromator and two detectors, a silicon detector (380 to 1080 nm) and and InGaAs detector (1080 to 2000 nm). The second FT

system consisted of a Fourier transform interferometer operating from 1000 to 2500 nm. They found that the accuracy based on PLS modelling when measuring quality characteristics in 4 different cultivars was comparable between the two systems. They found their models could predict soluble solids and firmness well with an SEP for soluble solids ranging from 0.66 to 0.88°Bx and SEP for firmness ranging from 8.26 to 12.06 N.

Ventura et al. (1998) utilized an interactance style probe consisting of a commercial spectrophotometer (350 to 999 nm) and a halogen lamp to predict soluble solids on 190 'Golden Delicious' and 150 'Jonagold' apples. Six 200 µm fibres are bundled together with a collection fibre in the middle. A plastic standoff is used to keep the probe at a 45° angle 6 mm from the fruit, and a rubber ring ensures only light reflecting from the fruit reaches the detector. They were able to build multi-linear regression models to predict soluble solids with a SEP ranging from 1.05 to 1.18°Bx (R=0.65 to 0.75). Peirs et al. (2001) similarly used an interactance method to find the Sterif index (a maturity index based on firmness, soluble solids, and starch). They found models using partial least squares regression (PLS) that could predict firmness with an SEP ranging from 0.9 to 1.13 kg (8.82 to 11.1 N, R=0.77 to 0.81) and soluble solids content with an SEP of 0.59 to 0.86°Bx (R=0.73 to 0.89).

McGlone et al. (2002) used the setup shown in Figure 4-3 to measure quality parameters on 'Royal Gala' apples. They used a 50 W halogen lamp to illuminate the sample and captured interacted light using an optical fibre and a Zeiss photodiode array based spectrometer. They carried out PLS modelling and found a root mean square standard error of prediction (RMSEP) of 0.72°Bx (R=0.79) for soluble solids content and a RMSEP of 7 N (R=0.79) for penetrometer firmness. They also concluded that for firmness the best results were found using the wavelength range of 500 to 750 nm indicating that the prediction is heavily dependent on the chlorophyll absorbance peak rather than actual textural changes.

Kavdir et al. (2007) used an interactance system similar to Figure 4-3. A charge coupled detector (CCD) spectrometer was used to measure from 550 to 1100 nm with light delivered from a quartz tungsten halogen source via a fibre optic ring. They used the system to measure the quality of pickling cucumbers and found good correlations with penetrometer area (area under the force displacement profile) and slope (R=0.84 and

R=0.82 respectively) however penetrometer maximum force had a poorer correlation (R=0.72).

Sirisomboon et al. (2012) used a fibre optic interactance probe to capture spectra from 1100 to 2500 nm of 'Momotaro' tomatoes and predict maturity and textural properties. They found a strong correlation (R=0.95) when predicting the bioyield point (point where the slope changes after the elastic region of the force deformation profile) using normalized spectra between 1100 and 1800 nm.

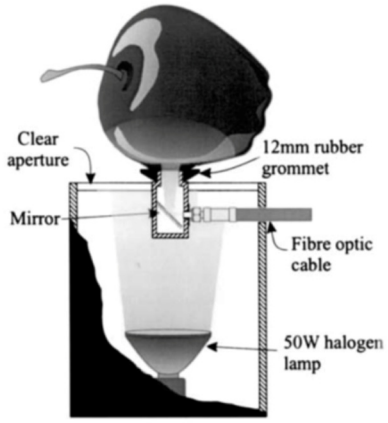

Figure 4-3. Experimental Visible/NIR system used to measure quality indices on 'Royal Gala' apples (McGlone et al., 2002)..

4.2. Spatially Resolved Reflectance Spectroscopy (SRS)

In the previous section, each approach treats the measured light as a bulk signal, a combination of the effects of scattering and absorption. Spatially resolved reflectance spectroscopy is an approach where samples are irradiated, and measurements are made that gather both spectral as well as spatial information. This extra spatial information can allow for the mapping of sample properties spatially (across the samples surface) and in some measurement geometries allows for the absorption and scattering properties to be separated. The absorption information, related to the chemical composition can then be used for identifying sugar content and taste parameters while the scattering information, related to the microstructure of the tissue can be used for identifying textural parameters such as firmness.

4.2.1 Hyperspectral Imaging

Hyperspectral imaging is a technique traditionally used to collect spatially resolved reflectance spectra. This is a natural extension to colour imagery where instead of just three colours a complete spectrum is captured for every point in the image. There are

two types of systems generally discussed (Lu & Chen, 1999). The first is a full spatial image (FSI) system where a tunable filter is used to capture full images at each wavelength band. The second is a line spatial image (LSI) system where light that interacts with the samples enters a thin slit where a diffraction grating spreads it onto a CCD or similar sensor array. An example image from an LSI system is shown in Figure 4-4. The spatial dimension across the slit is on the x-axis and wavelength is on the y-axis. Because this approach only gathers spatial information across the thin slit, the camera or sample must be scanned to construct a full image set.

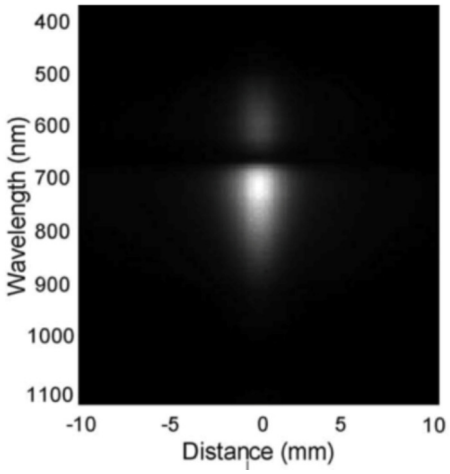

Figure 4-4. An example hyperspectral image captured using a line spatial image system on an apple sample illuminated with a broadband source (Mendoza et al., 2011).

Hyperspectral imaging has been successfully used for a number of horticultural applications including mapping sugar content in kiwifruit (Martinsen & Schaare, 1998), and detecting fungal contamination and bruising (Kim et al., 2001). Lu & Peng (2006) developed a novel approach where they use a LSI hyperspectral imaging system to capture images of spot illumination. This allows them to simultaneously measure intensity at different distances from the source over a broad wavelength range. Their system is illustrated in Figure 4-5. Light is delivered from a quartz tungsten halogen lamp via an optical fibre to the surface of the fruit sample (1.6mm beam size). A back-illuminated CCD camera and imaging spectrograph is used to capture the hyperspectral images from 500 to 1000 nm. The authors record the intensity profile (intensity vs. displacement) at each wavelength and fit a Lorentzian distribution function to it. This provides them with two parameters (a and b) which describe the profile. These parameters are then used on their own or in combination to model firmness using multi-linear regression. They found that using the two parameters as independent variables gave the best result for predicting penetrometer firmness with

correlation coefficients equal to 0.88 and 0.76 and standard error of validations (SEV) equal to 14.2 N and 19.1 N for 'Red Haven' and 'Coral Star' peaches, respectively.

Lu (2007) used the same system to measure the firmness and soluble solids content for 'Golden Delicious' and 'Red Delicious' apples. They extracted mean and standard deviation spectra (average and standard deviation of intensity over a 25mm distance). These were then used in a neural network to predict penetrometer firmness and soluble solids content. They found good predictions with an SEP equal to 6.2 N (R=0.87) and 0.72 °Bx (R=0.89) for 'Golden Delicious' and for 'Red Delicious' an SEP of 6.1 N (R=0.74) and 0.81 °Bx (R=0.80).

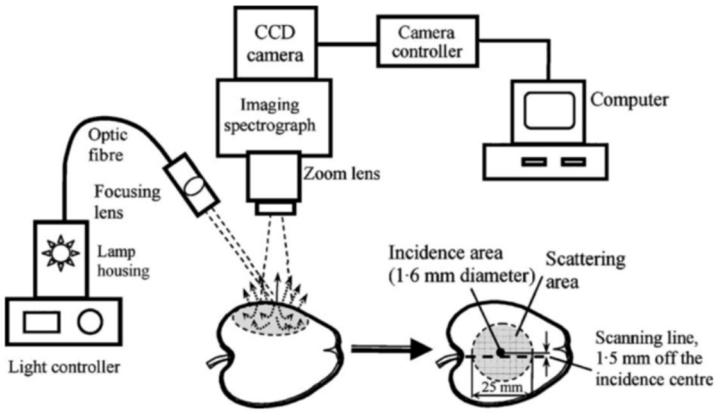

Figure 4-5. Hyperspectral imaging system developed by Lu & Peng (2006).

Noh & Lu (2007) used a modified version of the same system to capture hyperspectral fluorescence images. The modified system used a 430 nm laser diode as the excitation source and a similar CCD based imaging system to capture the broadband fluorescence signal. They found that fluorescence decreased steadily during the initial three minutes of illumination but was stable by five minutes. They found their predictions of fruit quality parameters were comparable to those of the near infrared systems with an SEP of 8.57 N (R=0.75) for penetrometer firmness, 1.19°Bx (R=0.66) for soluble solids content, 0.8 g/L (R=0.57) for titratable acidity, and 0.03 radian (R = 0.93) for skin hue.

Peng & Lu (2008) applied correction schemes on 'Golden Delicious' apple intensity profiles to account for fruit size and for the Lambertian cosine response. They then fitted ten modified Lorentzian distribution (MLD) models to parameterise the curves and carried out multiple linear regressions with those parameters and destructive measurements to predict fruit quality. They found that their analysis was sensitive to what modified Lorentzian function was used with a maximum 19% difference in correlation coefficient values and a 26% difference in standard error of cross validation

(SECV). The MLD-32 and MLD-41 (Table 4-1) functions were the best performing modified Lorentzian functions for both firmness and soluble solids content. However Peng & Lu (2008) persued the MLD-32 function further because it requires fewer terms (3 instead of 4) and uses wavelengths from more suitable locations. Models could predict penetrometer firmness with an SEP of 6.14 N (R=0.894) and soluble solids content with an SEP of 0.73% (R=0.883).

Function Designation	Equation
MLD-41	$R = a + \frac{b}{1 + (z/c)^d}$
MLD-31	$R = a + \frac{b}{1 + (z/c)^2}$
MLD-32	$R = \frac{b}{1 + (z/c)^d}$
MLD-33	$R = a + \frac{1 - a}{1 + (z/c)^d}$
MLD-34	$R = a + \frac{R_{max} - a}{1 + (z/c)^d}$
MLD-21	$R = \frac{b}{1 + (z/c)^2}$
MLD-22	$R = \frac{1}{1 + (z/c)^d}$
MLD-23	$R = \frac{R_{max}}{1 + (z/c)^d}$
MLD-24	$R = a + \frac{1 - a}{1 + (z/c)^2}$
MLD-25	$R = a + \frac{R_{max} - a}{1 + (z/c)^2}$

Table 4-1. Modified Lorentzian functions investigated by Peng & Lu (2008).

Huang & Lu (2010) used a hyperspectral imaging system to detect apple mealiness (a combination of the elastic properties of the fruit and juiciness). This was based on the same approach presented by Lu (2007). They collected a hyperspectral image of 'Red Delicious' apples spot illuminated with a broadband source. These images were processed and the average (mean) reflectance over a 10mm range from the incident point was calculated. They used the mean reflectance values to carry out PLS modelling to predict hardness and juiciness. Hardness was measured using an automated texture analyser and juiciness was measured by squeezing juice onto filter paper and then measuring the area that it consumed. They were able to predict hardness with an SEP of 12.61 kN/m (R=0.689) and juiciness with an SEP of 1.31 cm^2 (R=0.524) using a pooled dataset (cool stored and recently picked fruit). They also carried out a partial least squares discriminant analysis and found relatively good classification between mealy and non-mealy apples with 75% of the fruit correctly classified.

Wang et al. (2012) used the same approach as Huang & Lu (2010) to capture mean reflectance values on 600 'Golden Delicious' apples. This time they looked at identifying key wavelengths using uninformative variable elimination (UVE) and supervised affinity propagation (SAP). They also investigated the fusion of these approaches through a back propagation neural network to improve the overall prediction. They did find that predictions were improved when the UVE PLS and SAP PLS models were combined giving an SEP of 5.53 N (R=0.83).

4.2.2 Single or Multispectral Imaging

Single or multispectral imaging is very similar to the hyperspectral approaches mentioned above, but the number of wavelengths explored is significantly lower, typically 1-7. These key wavelengths are usually chosen based on previous near infrared reflectance spectroscopy or hyperspectral measurements. The advantages of single or multispectral imaging systems are reduced system complexity and often expense, a reduction in data handling, a potential improvement in illumination power density through the use of LEDs or lasers, and the potential to run at higher speeds.

Cho & Han (1999) looked at characterising the firmness of 'Tsugaru' and 'Fuji' apples using laser light scatter imaging. Their system consisted of two helium neon lasers emitting light at 632.8 nm and 543.5 nm which are used to illuminate the samples. Images of the laser scatter are captured on a colour CCD camera. They used their cameras saturation point to segment the three colour channels and from that counted the number of pixels in each segmented region. The number of pixels in each region was then used in ratios to provide a level of self referencing. They found strong correlations between their parameters and a number of texture analysis features (Chapter 2, Section 2.3.7) including bio-yield deformation, bio-yield force ('Tsugaru' onlys), rupture deformation ('Fiji' only), rupture force, initial slope, and secant slope. They also found that the 632.8 nm red laser consistently performed better than the green laser.

In parallel with their hyperspectral imaging systems Lu (Lu, 2003) presented a new measurement system (Figure 4-6) to make multispectral spatial measurements. In this case, a 250 W quartz tungsten source is delivered via an optical fibre and is focused to a spot (0.8mm) on the fruit samples surface (550 'Red Delicious' apples). Light propagates inside the fruit tissue and a portion is backscattered out towards a CCD camera. In front of the camera was an optical filter wheel with five filters installed

(10 nm bandwidth). This limits only a particular wavelength range of light to transmit on to the detector. In this study, they used 680 nm because of its relationship with chlorophyll in fruit, 880 nm and 905 nm because of their ability to predict soluble solids content, 940 nm because it had been shown to predict firmness, and finally 1060 nm because it had also been used to predict soluble solids content. Each image was radially averaged so that a simple intensity versus displacement profile was found. They feed these profiles and combinations of profiles (ratios) into a neural network to predict penetrometer firmness. They found that the inclusion of data closer than 1.5 mm to the centre of the intensity profile harmed predictions and therefore chose to exclude this from the modelling. The best predictions for firmness were found using three ratio combinations (680/940 nm, 880/905 nm, and 905/940 nm) giving an SEP of 5.8 N (R=0.87). For soluble solids they found that a two ratio combination (880/905 nm and 905/940 nm) gave the best prediction with an SEP of 0.78% (R=0.77).

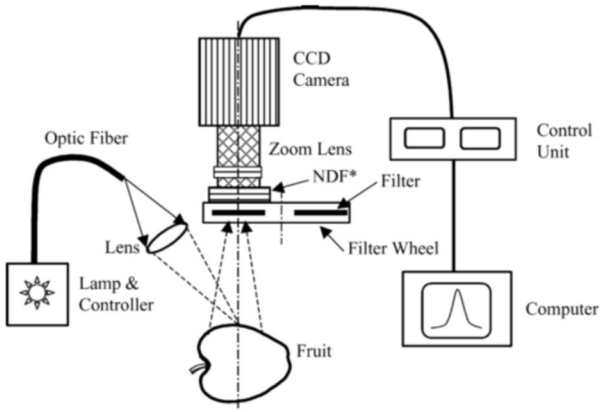

Figure 4-6. Multispectral imaging system for measuring the firmness and soluble solids of apples (Lu, 2003).

Lu (2004) developed his system further replacing the filter wheel approach with a new system comprising of beam splitters capable of simultaneously acquiring scattering images at four discrete wavelengths. The system still requires filters to do the actual wavelength selection and in this study the target wavelengths were 680, 880, 904, and 940 nm each with a 10 nm bandwidth. Measurements this time were made on 585 'Red Delicious' and 480 'Golden Delicious' apples. Prediction of firmness and soluble solids were carried out in a similar way using a backpropagation neural network. They were able to predict firmness of 'Red Delicious' apples with an SEP of 6.2 N (R=0.76) and 'Golden Delicious' with an SEP of 8.9 N (R=0.73).

Peng & Lu (2004) developed yet another adaptation of this multispectral imaging system. This time utilizing a liquid crystal tunable filter placed in front of a CCD camera. This allowed them to select wavelengths between 650 and 1100 nm on the fly to help select the best combination. They captured these multispectral images on 180 'Red Delicious' apples where they then radially averaged the result ending up with a set of intensity values at different distances from the incident point. A MLD model with four parameters was then fitted to the intensity profile. The four parameter modified Lorentzian model is:

$$I(x) = a + \frac{b}{1 + \left(\frac{|x|}{c}\right)^{d}} \quad ,$$

where x is the distance from the illumination point expressed in pixels, I is the intensity measured from the camera, a is the asymptotic value, b is the peak value at saturation, c is the full scattering width at half the maximum intensity, and d is related to the slope of the falling intensity profile. These four parameters (a, b, c, and d) were used to construct prediction models for firmness. They found seven optimum wavelengths (690, 770, 790, 810, 920, 980, and 1000 nm) and developed a model for firmness using multiple linear regression. Their validation set had an SEP of 6.64 N (R=0.82).

Peng & Lu (2005) investigated the performance of firmness prediction models based on parameters extracted by fitting Lorentzian, exponential, and Gaussian distribution functions to light scattering profiles. Data on 'Red Delicious' apples came from two multispectral systems, the first presented by Lu (Lu, 2003) and the second by Lu (2004). Peng & Lu (2005) found the Lorentzian distribution function was the best at describing the scattering profiles. Multi-linear models were used on the extracted parameters to predict penetrometer firmness. Their SEV was 6.39 N (R=0.82) using the first experimental system and 6.01 N (R=0.76) for the second system.

Lu & Peng (2005) presented another adaptation of their multispectral systems. This time, instead of a broadband light source they used four solid state laser diodes that matched the four filters (680, 880, 905, and 940 nm). These were coupled to an optical fibre and focused on the surface of 'Golden Delicious' and 'Red Delicious' apples. Corrections were applied to the intensity accounting for the Lambertian cosine response and the curvature of the fruit assuming a fixed fruit size (median). A

modified Lorentzian function was then fitted to the corrected intensity profiles and four parameters were extracted at each wavelength. Multi-linear regression was performed on the extracted parameters to predict penetrometer firmness. They were able to predict firmness of 'Golden Delicious' apples with an SEV equal to 7.7 N (R=0.85) and for 'Red Delicious' apples an SEV of 7.6 N (R=0.86).

Peng & Lu (2006) refined their multispectral system further. In this study, they incorporated a light intensity controller to improve the stability of the broadband light source. They also filtered out noise signals such as bright and dark spots and accounted for intensity variations due to fruit size and shape. They validated these changes on 572 'Red Delicious' apples and 547 'Golden Delicious' apples again by fitting a modified Lorentzian distribution function and carrying out multi-linear regression to predict penetrometer firmness. This improved system and data handling gave results comparable to their earlier studies (Peng & Lu, 2005, 2004). Prediction models were developed with an SEV equal to 6.41 N (R=0.898) for the 'Red Delicious' apples and 6.14 N (R=0.897) for the 'Golden Delicious' apples.

Lu & Peng (2007) developed their laser system further targeting it for use at online grading speeds. They also refined the fruit size and cosine corrections to account for the acceptance angle of the imaging system. This lead to firmness predictions with an SEP of 6.86 N (R=0.86) for 'Golden Delicious apples and an SEP of 7.24 N (R=0.86) for 'Red Delicious' apples, comparable with their earlier studies. The maximum speed of this system was about two fruit per second, still below that of typical commercial grading lines (10 fruit per second).

Peng & Lu (2007) investigated individual fruit size corrections for both cosine response and displacement (previously the median value was used). They also utilized a white reference tile to reduce the affect of light source variation. They found that a modified Gompertz function with three parameters did a better job at predicting fruit firmness compared to the modified Lorentzian function. A four parameter modified Gompertz function was also better at predicting soluble solids content. The multi-linear regression models for firmness using the extracted parameters gave firmness predictions with an SEP of 6.5 N (R=0.896) and soluble solids predictions with an SEP of 0.92% (R=0.816).

Qing et al. (2007) developed a different analysis approach trying to non-destructively measure the firmness and soluble solids content of 560 'Elstar' and 'Pinova' apples.

They still illuminated a spot on the sample using a laser diode source emitting light at 680, 780, 880, 940, and 980 nm. A colour CCD camera was used to capture backscatter images at each of the wavelengths. Each image was then converted to monochrome, and a number of threshold algorithms were used to separate the laser light scattering section of the images from the background. They also applied corrections for the Lambertian cosine response and fruit size effects. For each fruit, they collected soluble solids content and penetrometer firmness which were then used along with the optical data to build prediction models using partial least squares. Two forms of optical data were used, the first was the backscatter region size (number of illuminated pixels, 5 wavelengths x 420 samples) and the second was an intensity histogram (65 bins x 420 samples). They found the histogram data using a first inflection threshold algorithm provided the best prediction results for firmness with an SECV of 4.71 N/cm² (4.47 N) and a correlation coefficient of 0.91. For soluble solids, an iterative arithmetic threshold provided better results with an SECV of 0.68 °Bx (R=0.90).

Qing et al. (2008) used the same setup to investigate 'Elstar' and 'Pinova' apples. The apples were harvested and measured in quantities of 40 per week over two months. One half were from a drought stress zone, and the other half were from a well irrigated zone. They used the first inflection point from a bimodal histogram to threshold the images separating the background from the backscattered light. The remaining backscatter histogram was used to build up prediction models using PLS regression, stepwise multiple linear regression, and PCR. For 'Elstar' apples the best soluble solids content model was found using PLS regression with an RMSECV of 0.73°Bx (R=0.89). The PLSR model also performed the best at predicting firmness with an RMSECV of 5.48 N/cm² (R=0.89). For 'Pinova' apples it was the same; the PLS regression models achieved an RMSECV of 0.82°Bx (R=0.88) for soluble solids content and 4.71 N/cm² (R=0.91) for firmness.

Lleó et al. (2009) used a custom multispectral system to classify peaches into four groups each with similar properties. Their multispectral system used a custom CCD camera with three sensors each filtered using a different 20 nm bandpass filter (800 nm, 675 nm, and 450 nm). A 670/800 nm ratio was used to avoid fruit shape affects on light reflectance. As fruit matured their histograms increased in intensity. They also found firmness decreased while reflectance at 680 nm increased due to a breakdown of chlorophyll. This appears to be a common basis for optical firmness measurement.

There might be a secondary correlation between chlorophyll and some combination of firmness and fruit maturity.

Mollazade et al. (2013) carried out measurements on plums, apples, tomato, and mushrooms. Fruit were housed in chambers to maintain temperature and humidity. A measurement set was removed from storage every 13, 3, 7, and 3 days for apple, plum, tomato, and mushrooms respectively. Backscatter measurements were made first, followed by compression testing. Backscatter images were gathered using a monochrome CCD camera and a 660 nm solid state laser diode. The laser beam had a diameter of 1 mm and was incident at 15°. Images were segmented removing saturated pixels and separating the backscattered region from the background signal. The threshold used was adaptive and was based on neighbouring pixel values. They tested four statistical techniques to predict firmness including an image histogram, a gray level co-occurrence matrix, gray level run length matrix, and a local binary pattern. They also investigated six space-domain techniques including the total number of backscatter pixels, statistical features (min, max, mean, etc,), radial averaging, modified Lorentzian function, modified Gompertz function, and Farrell's diffusion theory function. They found that the wavelet transform and modified Lorentzian function were the best at predicting firmness.

4.2.3 Optical Property Extraction

Spatially resolved reflectance spectroscopy can also be used to measure a sample's absorption and reduced scattering coefficients (optical properties). This typically involves fitting a model to measurements of light intensity at a range of distances from the illumination source. The optical properties are used as fitting parameters and can be taken directly from the fit result.

Several researchers have used this approach to find the optical properties of fruit samples and relate them to measurable fruit quality parameters including firmness. In 2006, a system (Figure 4-7) was presented that utilized a hyperspectral imaging system to measure the optical properties of 'Golden Delicious' apples with the purpose of assessing fruit quality (Qin & Lu, 2006; Lu et al., 2006). Qin & Lu (2006) introduced their system which consists of a high performance CCD camera, imaging spectrograph, and a feedback controlled broadband light source. They used an inverse algorithm where a diffusion approximation model provided by Farrell et al. (1992) is fitted to the

hyperspectral scattering profiles using a trust-region nonlinear least-squares fit. The absorption and reduced scattering coefficient are parameters of the model.

Validation of this approach was carried out on liquid samples made up of Intralipid and a mixture of dyes. Reference absorption of non-scattering samples was measured using a standard 10 mm path length cell and a commercial spectrometer. Scattering was calculated using the empirical equations developed by van Staveren et al. (1991). They found that the absorption coefficient was within 18% and the reduced scattering coefficient was within 11% of the reference measurements. Qin & Lu (2006) also looked at simple correlations between the optical properties and either soluble solids or penetrometer firmness. This was carried out on 15 'Golden Delicious' apple samples over a wavelength range from 600 to 950 nm. They found a maximum correlation coefficient of -0.77 for soluble solids at 690 nm and a maximum correlation coefficient of -0.7 for penetrometer firmness at 780 nm.

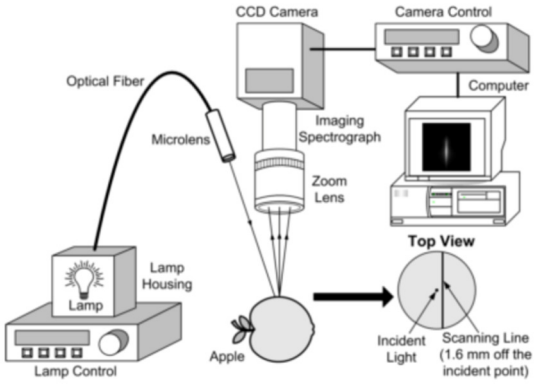

Figure 4-7. Hyperspectral imaging system used to extract out the optical properties of liquid turbid samples (Qin & Lu, 2005).

Lu et al. (2006) used this system to carry out measurements on 650 'Golden Delicious' apples. They also collected destructive reference measurements including penetrometer firmness and soluble solids content. Each hyperspectral image was corrected for fruit size, and non-linear instrument effects caused by imperfections in the optical components. Examples of the extracted absorption and reduced scattering coefficient spectra can be seen in Figure 4-8. The reduced scattering coefficient was mostly featureless, decreasing slightly as wavelength increases as expected; at 600 nm the measurements varied from about 13.5 to 18 cm^{-1}. The absorption spectra, however, had an absorption peak at 675 nm due to chlorophyll absorption. Lu et al. (2006) took these spectra (530 to 950 nm) and applied a multi-linear regression modelling

technique with a leave one out cross validation to predict soluble solids and fruit firmness. For firmness, they found an SEP of 10.17 N (R=0.66) and for soluble solids they got an SEP of 1.3% (R=0.48). Prediction errors were higher and correlations lower compared to their previous work where the optical properties were not separated. They attributed this to high fitting errors for the absorption coefficient and aim to improve their imaging system and non-linear search algorithm to improve these fits.

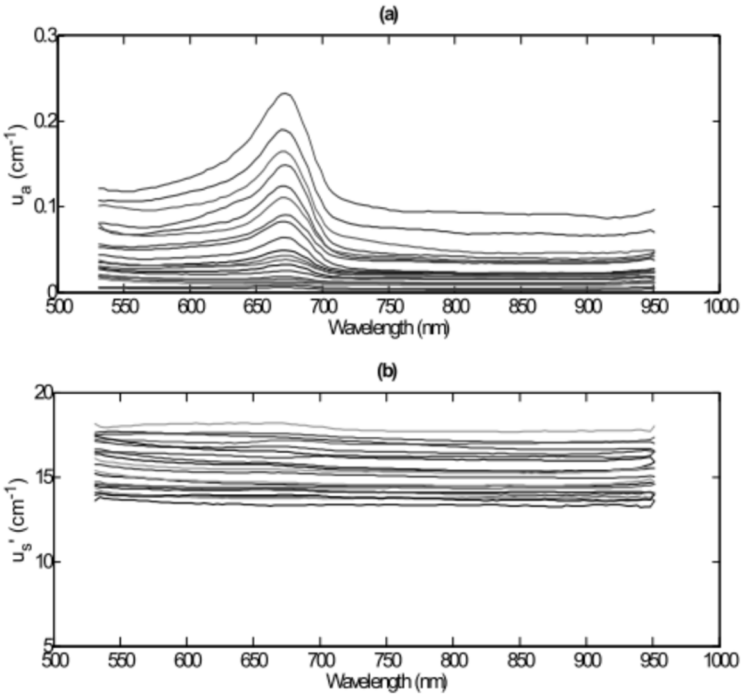

Figure 4-8. (a) Absorption and (b) reduced scattering spectra extracted from intensity profiles by fitting a diffusion approximation based model (Lu et al., 2006).

Qin et al. (2007) continued work on the hyperspectral system and added an electronically controlled positioning system. This allowed them to accurately control the height of the samples and move them horizontally for multiple scans. They validated this on 600 'Golden Delicious' apples again predicting firmness and soluble solids content. Images are initially corrected for spectral, geometrical and non-uniform instrumental effects. Intensity profiles are then extracted and corrected for fruit size using a correction that accounts for curvature (assuming spherical fruit). Finally they use non-linear curve fitting with a diffusion theory model to extract the optical properties. The authors identified three groups of wavelengths that help predict fruit firmness. These are the carotenoid pigment region (500 to 550 nm), the chlorophyll pigment region (625 to 700 nm), and the water absorption region (900 to 990 nm). Best predictions were found by combining the absorption and reduced scattering

coefficients in a multi-linear regression model. For firmness they got an SEP of 5.66 N (R=0.88) and for soluble solids they got an SEP of 0.75% (R=0.82).

Qin et al. (2009) used the same system and compared the approach of extracting the optical properties with the technique of using relative mean spectra (average reflectance over a 10 mm distance divided by Teflon disk average reflectance). They found correlation coefficients of 0.857 and 0.704 for firmness and soluble-solids content respectively when forming models based on absorption and reduced scattering spectra. Models performed with an SEP of 6.07 N and 0.9%. When they used relative mean spectra to predict firmness they got a comparable result (R=0.844, SEP=6.62 N) and an improved result for soluble solids content (R=0.864, SEP=0.69%).

Cen et al. (2011) carried out hyperspectral image measurements from 515 to 1000 nm on 'Redstar' peaches to measure the optical properties and use them to predict penetrometer firmness, acoustic firmness, soluble solids content, and skin and flesh colour properties. In this study, a modified approach was used to extract the optical properties from scattering intensity profiles. This is illustrated in Figure 4-9. They first extract a spatial profile at each wavelength from the hyperspectral image. A curve based on a model developed by Kienle & Patterson (1997) is fitted to each profile in three steps. For the first step, both absorption and reduced scattering are free parameters in the model. In the second step a power model ($a\lambda^{-b}$) is fitted to the reduced scattering coefficient. Finally, the curve fit to the original intensity profiles is repeated, this time using the modelled reduced scattering coefficient with the absorption coefficient as the free parameter.

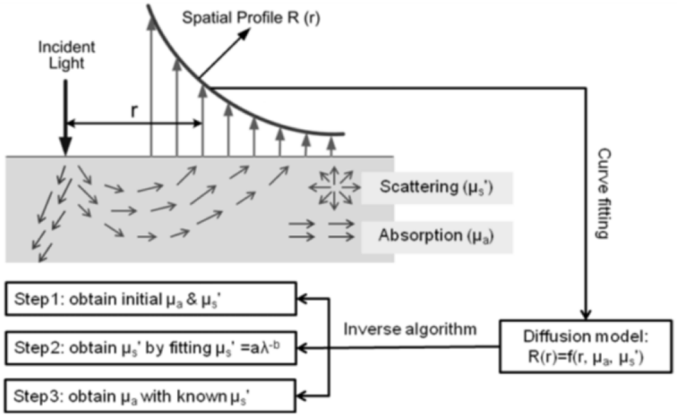

Figure 4-9. Approach used to extract out the optical properties of peach fruit using hyperspectral scattering profiles (Cen et al., 2011).

They carried out measurements on 500 peaches and developed prediction models using PLS and a least squares support vector machine (LS-SVM). LS-SVM is a statistical learning theory that uses a structural risk minimization principle rather than an empirical risk minimization principle (Cen et al., 2011). For firmness, the LS-SVM approach found the best prediction with an SEP of 17.39 N (R=0.749). This error is considerably higher when compared to their earlier experiments on apples, for example, Qin et al. (2007) got an SEP of 5.66 N (R=0.88) for 'Golden Delicious' apples.

Cen et al. (2013) sought to establish a relationship between optical properties and the structural and mechanical properties of apples. They captured hyperspectral images from 500 to 1000 nm of 'Golden Delicious' and 'Granny Smith' apples and extracted their optical properties using a diffusion model (Kienle & Patterson, 1997). They also measured tissue elasticity, acoustic/impact firmness, and quantified the morphological features of cells. The absorption spectra showed clear peaks in the chlorophyll (675 nm) and water (980 nm) regions. Chlorophyll tended to decrease over the measurement period (30 days). The reduced scattering coefficient was smooth and tended to decrease over the measurement period as well, with softer fruit having a lower scattering coefficient than firm fruit. This was in contrast with earlier studies where the reduced scattering coefficient was higher for soft fruit (Qin & Lu, 2006). During this period, there was also a decrease in acoustic/impact firmness, Young's modulus, cell area, and equivalent cell diameter. They suggested their results show that optical properties can be useful for the understanding of mechanical properties and micro-structural changes as fruit soften and mature. They did not attempt to predict the mechanical properties from their optical measurements.

4.3. Time Resolved Reflectance Spectroscopy

Time resolved reflectance spectroscopy is a non-invasive method used to measure the absorption and scattering properties of turbid samples. The technique is based on measuring the time delay and broadening of a short laser pulse travelling through a sample. This delay and broadening can then be de-convolved to extract the optical properties of the sample (Nicolaï et al., 2008). A typical geometry for this measurement is two fibre optic probes placed a fixed distance apart in contact with the surface of a sample (Figure 4-10).

Cubeddu et al. (2000) carried out some of the earliest work using this technique on fruit samples. Their system consisted of a synchronously pumped mode-locked dye laser that delivered pulses less than 20 ps long. It was tunable from 610 to 700 nm with an average output power of 10 mW. Light was delivered and collected from fibre optic probes each with a 1 mm core that were separated by 1.5 cm on the fruits surface. Detecting these types of signals requires a technique called time correlated single photon counting. Carefully timed measurements are made over a series of excitation pulses. After many of these excitation and measurement cycles the final temporal profile is constructed (Zude, 2010). The extraction of optical properties from these temporal profiles is done using a diffusion approximation to the transport equation provided by Patterson et al. (1989). This function was fitted to the profile using a Levenberg–Marquardt iterative procedure, and the absorption and reduced scattering properties are found directly as fit parameters. They were able to identify the chlorophyll peak consistent with other work. They were also able to demonstrate that the skin has very little influence on the measurement.

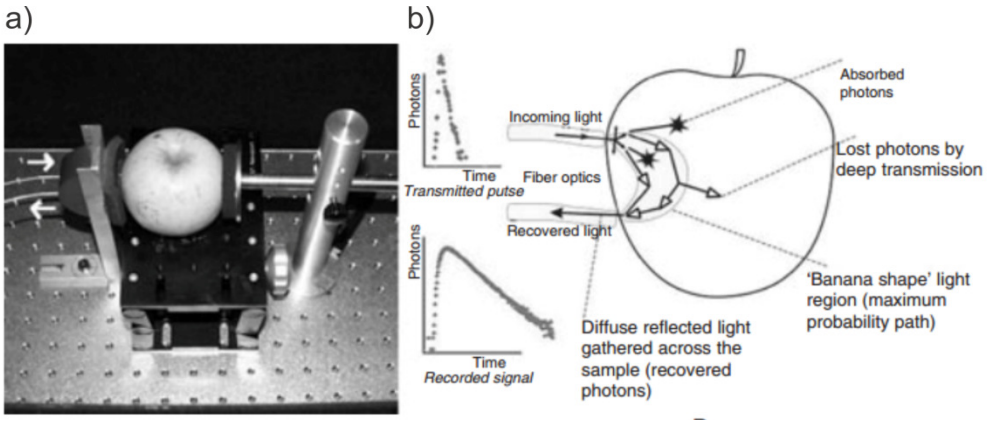

Figure 4-10. Outline of a time resolved reflectance spectroscopy system. The image on the left (a) shows an apple sample mounted on an optical bench in a way that the optical fibre probes are in contact with the fruit a fixed distance from each other. The image on the right (b) shows an outline of the measurement. Light enters the fruit and is scattered and absorbed. Eventually, a portion of the light reaches the measurement probe where it is analysed to extract out the optical properties (Valero & Barreiro, 2005).

Zerbini & Grassi (2004) used time resolved reflectance spectroscopy at 630 nm to investigate the usefulness of the absorption coefficient from 300 'Jonagored' apples. Fruit were ranked based on their absorption from high to low and separated into three maturity classes. The fruit were then subjected to different storage schemes before measurements were carried out. Fruit property measurements included skin colour, flesh firmness, soluble solids, and titratable acidity. Fruit were also classified using a

sensory analysis from 10 semi-trained people evaluating firmness, crispness, mealiness, juiciness, sweetness, sourness, and aroma. As expected from earlier work, they found that the absorption was higher for early picked fruit. They found that the absorption affected fruit mass, skin colour, and acidity at harvest as well as soluble solids content, background colour, percent juice, and sensory attributes after storage. They suggest this means that time resolved reflectance spectroscopy can help select good quality fruit. They do note, however, that firmness was not affected by the maturity classification and was only affected by storage atmosphere, shelf-life, and harvest date.

Valero & Barreiro (2005) measured 50 'Golden Delicious' and 40 'Cox's Orange Pippin' using their time resolved reflectance system. They investigated a number of wavelengths including 572, 750, and 818 nm through the use of individual laser diodes, and from 900 to 1000 nm in 10 nm steps using a tunable laser. Firmness was measured using a texture analyser where hardness was found using the slope of the force deformation curve during loading (N/mm). Juiciness was measured by collecting any juice during the texture analysis onto filter paper. The area which the juice spreads over the paper indicates juiciness (mm^2). Fruit were considered "not firm" when hardness was less than 20, and "firm" otherwise. Fruit are considered "nonjuicy" when the juice area is less than 4 cm^2 and considered "juicy" above this. A fruit is considered mealy when it is both "not firm" and "nonjuicy" at the same time. They found linear relationships between destructive and non-destructive (optical) parameters were poor ($R<0.4$). However, they did find that a classification approach worked well, and they were able to discriminate mealy from non-mealy fruit. They suggest that the technique shows promise and that an online system should be constructed to allow for large numbers of fruit to be measured, allowing them to build better models.

Nicolaï et al. (2008) carried out measurements on 'Conference' pear fruit using a time resolved reflectance spectroscopy (TRS) system and a continuous wave near infrared spectroscopy system. Their NIRS system operated over a wavelength range from 780 to 1700 nm, samples were illuminated using an external 100 W halogen lamp, and light was collected at a 45° angle to avoid specular reflection. Their TRS system consisted of an actively mode-locked Titanium:Sapphire laser capable of providing light from 875 to 1030 nm with 5 nm increments at 100 MHz. Glass fibres (1 mm) were used to deliver and collect light and were positioned 1.5 cm apart. Figure 4-11 shows a typical TRS signal as measured using their system. Along with TRS measurements they also

collected firmness using a universal testing machine (texture analyser) and soluble solids content. They were able to predict soluble solids using standard continuous wave near-infrared spectroscopy (SEP = 0.44°Bx, R=0.77) however were not able to get a significant model for soluble solids using the TRS absorption coefficient spectra. This was attributed to the limited wavelength range of the TRS system. They found firmness decreased in an exponential fashion over the measurement period leaving a residual firmness of about 15 N, however, they were unable to get satisfactory predictions for firmness based on either NIRS or TRS measurements.

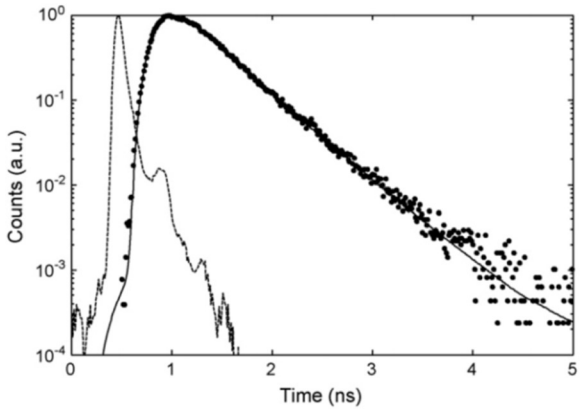

Figure 4-11. Typical time resolved reflectance spectroscopy profile. The dashed line represents the response of the system without the sample. The solid line indicates the line of best fit found while extracting the optical properties using a diffusion approximation model (Nicolaï et al., 2008).

Rizzolo et al. (2010) reports further on their data set collected in 2002. They explore the optical properties at 630, 670, 750, and 780 nm for 'Jonagored' apples and relate these to quality characteristics and sensory data. Fruit in this study was limited to the seven day shelf life set, earlier publications have already reported on the six month and at harvest data. They found that the optical properties were best at classifying fruit at both extremes (low and high) when classifying based on firmness and crispness. They were able to correctly classify over 80% in the low class and above 70% in the high class. They suggested that further work is needed to better understand the microscopic structural features of apple tissue.

Vanoli et al. (2011) collected time resolved reflectance spectra on 60 'Pink Lady' apples at 670 nm and over the spectral range from 740 to 1100 nm. The apples were first ordered based on decreasing absorption at 670 nm and randomised into six batches corresponding to six measurement cycles at harvest, 7, 15, 29, 66, and 91 days. During each measurement cycle firmness, intercellular-space volume, soluble-solids content,

and starch was measured. They found a high correlation coefficient (R>0.8) between the absorption between 920 and 1100 nm and firmness, Sterif index, and intercellular-space volume. They also found a low correlation coefficient (R<0.4) between absorption and soluble-solids content and between the reduced scattering coefficient and all quality parameters. They were able to combine the absorption and reduced scattering coefficient to improve their partial least squares regression predictions of intercellular space volume, Streif index (described in Chapter 2), and firmness (correlation coefficients of 0.87, 0.81, and 0.88 respectively).

4.4. Spatial Frequency Domain Imaging

Spatial frequency-domain imaging (SFDI) is a relatively recent approach that can perform both optical tomography (see inside the sample) and map out the optical properties over a large measurement area. SFDI systems operate by illuminating a sample with a periodic pattern and then capturing the resulting interaction using an imaging system. This illumination signal propagates inside the sample where it is absorbed and scattered. From the captured images of this interaction, the optical properties can be extracted.

Anderson et al. (2006) used their SFDI system (Figure 4-12) to make non-contact optical property measurements on 'Golden Delicious', 'Granny Smith', and 'Red Delicious' apples. Their system consists of a halogen lamp that evenly illuminates a digital micromirror device (DMD). The DMD is controlled by a computer to project different spatial patterns on to the sample. A CCD camera was used to capture the resulting interaction. Care was taken to avoid specular reflection and a Spectralon reflectance standard was used to calibrate for intensity and to correct for non-uniform illumination. They used a liquid crystal tunable filter to capture measurements from 650 to 980 nm. Their first experiment involved looking at the optical properties of bruised tissue. They found that the reduced scattering coefficient was dramatically lower in bruised fruit. Following this they looked at the relationship with their optical property measurements and penetrometer firmness. They found that the reduced scattering coefficients decreased as firmness decreased. They also found the absorption coefficient in the chlorophyll region (680 nm) was particularly sensitive to fruit firmness.

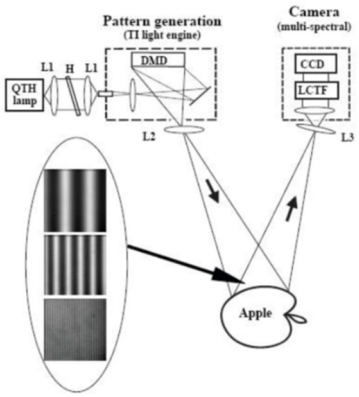

Figure 4-12. Spatial frequency domain imaging system used to measure the optical properties on apple tissue for bruise detection and firmness measurement (Anderson et al., 2007).

Current implementations of this system require images of multiple spatial frequencies as well as discrete wavelength filtering. This limits the acquisition time and makes it less suited for high speed online grading.

4.5. Summary

There have been a significant number of novel optical approaches for measuring fruit firmness and other quality parameters. None of these approaches have been accepted by industry for either low speed or high speed measurements. NIRS systems have arguably been the most successful technology so far because they have proven themselves effective at predicting taste parameters such as soluble-solids and dry matter. Because of this adoption fruit grader manufacturers have also marketed these systems as being able to predict firmness under certain circumstances. The literature does support this idea. NIRS can provide an indication of fruit firmness, however, prediction errors are higher than from other techniques and are erratic (7 to 13.7N).

More recently improvements in firmness estimation have been achieved by using spatially resolved reflectance systems. These approaches involved illuminating fruit with a spot source and characterising how that light interacts either by quantifying parameters like the scatter area or by fitting various models such as the modified Lorentzian. These parameters are then used with reference data and regression techniques to build prediction models with reduced errors (4.48 to 8.57 N).

Both the NIRS and these initial spatially resolved approaches did not attempt to separate the optical properties of the samples. There is an argument that correct separation of the optical properties would improve both chemical and textural analyses

(Cubeddu et al., 2000). The separated absorption coefficient could be used to better model chemical constituents such as chlorophyll, soluble-solids content, dry matter, and water concentration. The scattering or reduced scattering coefficient on the other hand would correspond better to the physical properties of the sample and could improve estimation of firmness. Initial work in this area has shown prediction errors ranging from 5.66 to 10.17 N. There are still opportunities in this field to develop a high-speed system that can more accurately measure firmness and is compatible with commercial fruit grading lines.

5. High-Speed Multispectral Imaging System Design

An experimental multispectral imaging system was developed to collect high-speed laser backscatter images of fruit. The design has been guided by practical considerations for online fruit grading systems developed by Compac Sorting Equipment Limited. The two main constraints of the fruit grading system are the high fruit conveyor speeds (1m/s) and the physical arrangement of fruit on their carriers (97mm between each fruit). The first constraint limits the exposure time the multispectral imaging system can operate at, and the second limits the number of fruit that can fit into a single image frame while still maintaining a suitable spatial resolution.

In this chapter, a set of specifications are developed for the high-speed multispectral imaging system. The design of this system is then discussed including optical throughput calculations, the selection of different hardware elements, and the software used for gathering image data.

5.1. Specifications

The experimental system (Figure 5-1) consisted of a set of discrete lasers that illuminated separate fruit samples and a camera that captured images of the

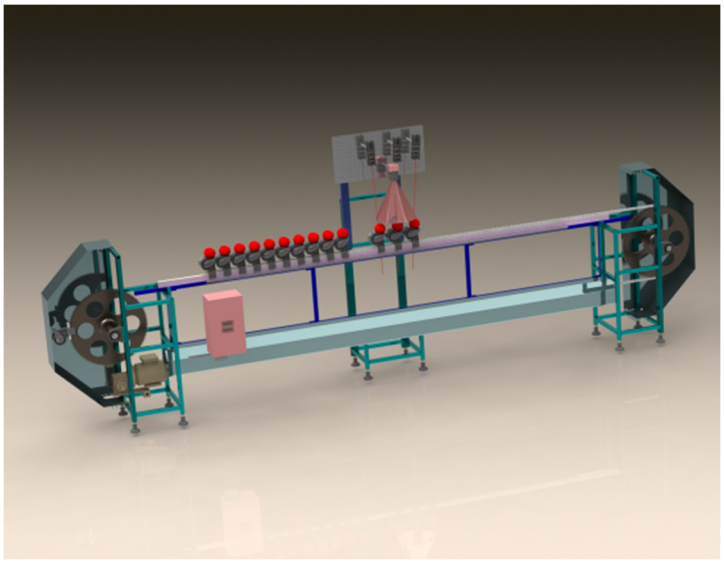

Figure 5-1. Computer aided design model of the high-speed grading system for making multispectral image measurements on fruit at speeds up to 1m/s.

interacting light. This system will be mounted on a rigid measurement station located in the centre of a fruit conveyor. The conveyor system is based on the design of a commercial online grader developed by Compac Sorting Equipment Limited. Fruit begin at one end (in this case the left side) of the grader and accelerate up to speed before reaching the multispectral imaging station. Images are captured, and the fruit decelerates until stopping at the other end. The fruit then travel backward to their original starting position so that replicate measurements can be made.

The choice of camera and lens for the system depends on the required pixel resolution, dynamic range, frame rate, and the intensity resolution (bit depth). In the literature on multispectral imaging (Chapter 4) there are a number of different cameras utilized including a 16bit PixelVision CCD camera with a resolution of 512x512 pixels (Lu & Chen, 1999; Kim et al., 2001), a 12-16bit Hamamatsu CCD camera with 512x512 pixels and a frame rate of 7fps (Lu, 2007; Noh & Lu, 2007; Peng & Lu, 2008; Wang et al., 2012), and a UNIQ CCD camera with a resolution of 768x494 pixels (Peng & Lu, 2004).

Table 5-1 shows the proposed set of specifications targeted for the camera and lens combination selected. The first is a spatial resolution greater than 0.25 mm/pixel. Cen & Lu (2010) investigated a range of spatial resolutions from 0.07 to 0.25 mm/pixel while determining the optical properties of samples. They concluded that errors were insignificant over that range (0.53% for absorption and 0.36% for reduced scattering). The proposed high-speed system will simultaneously capture multiple fruit in the same frame, each illuminated by different wavelength lasers. The fruit conveyor system has fixed spacing between fruit carriers (97 mm). This limits the number of fruit that can fit in a single image and still maintain a suitable spatial resolution. The cameras available during this investigation had horizontal resolutions of from 1312 to 1392 pixels. Assuming a suitable lens is available, and that we need a spatial resolution of 0.25 mm/pixel then we can fit three fruit in each frame.

The second requirement is the ability for the camera to capture at least 10 raw images per second and for the exposure time to be as short as possible. The minimum frame rate allows it to keep up with typical fruit grading speeds of 10 fruit per second. The short exposure time is needed because fruit travel at speeds of 1 m/s. This means that every millisecond of exposure corresponds to a millimetre of movement by the fruit. This will not cause blurring because the fruit is moving and not the laser source, but it

does mean that the proportion of fruit flesh being interrogated changes during exposure.

The third specification is an intensity bit depth of at least 12 bits. The bit depth is the number of colour or grey levels that a camera can measure. For example, an 8bit monochrome camera can only represent an image with 256 intensity levels ($2^8 = 256$) whereas a 12bit camera can represent it with 4096 levels.

The fourth specification is the quantum efficiently, which describes how efficient the sensor is at converting photons into electrons. The quantum efficiency is highly dependent on the detector technology used. Silicon based detectors are more efficient in the visible wavelengths and taper off around 900 nm. Indium gallium arsenide detectors, on the other hand, tend to be highly efficient from about 1000 nm up to about 1600 nm. The camera detector type will be selected based on the wavelengths selected.

Camera Parameter	Desired Specification
Spatial Resolution	<0.2 mm/pixel (Cen & Lu, 2010)
Frame Rate	>10 fps, short exposure time
Bit Depth	12-16 bits
Quantum Efficiency	Sensitive at the target wavelengths

Table 5-1. Specifications for the camera and lens system.

The second major component in the multispectral imaging system is the light source/sources. In a multispectral imaging system specific wavelengths are selected to illuminate the samples. This usually involves taking a broadband light source and filtering it with discrete band pass filters (Lu, 2004). In this particular design lasers were chosen because they provide monochromatic light eliminating the need for filters. They can also have high power densities which improves the signal to noise ratio at greater depths in the sample (Mollazade et al., 2012). It is important to choose the laser wavelengths to get targeted absorption information on different chemical constituents inside the fruit that can provide the most useful quality information. Figure 5-2 shows the different wavelengths used in previous research and what fruit parameters they were measuring. In Chapter 4, there was evidence that the scattering behaviour of light is most useful for characterising the mechanical characteristics of the fruit as these interactions relate to the physical structure of the sample (Cen et al., 2013). The reduced scattering coefficient of turbid biological samples typically follow a smooth monotonically decreasing curve as wavelength increases (Simpson et al., 1998). The

scattering coefficients across wavelengths also tend to be highly correlated (Cen et al., 2013; Qin et al., 2009; Lu et al., 2006). This means that the selection of a specific wavelength for measuring the scattering coefficient is not critical. A good option would be to choose a wavelength in a region where absorption is minimal. This means the light will propagate deeply into the fruit flesh interrogating larger and more representatively relevant regions for firmness assessment.

Using previously published work and the available laser diodes from Thorlabs as a guide (Figure 5-2), three laser wavelengths were selected. The first at 685 nm, which, depending on fruit condition and type, is at or near the chlorophyll absorption peak, providing an indication of the chlorophyll content in fruit (Cen et al., 2013). Chlorophyll has been used as an indicator for maturity and other quality parameters (Kingston, 1992; Song et al., 1997; Noh & Lu, 2007). The second laser chosen was at 850 nm. This is a convenient wavelength inside the therapeutic window (diagnostic window) where absorption is low and light can propagate deep into the sample. The final wavelength selected was 904 nm; this wavelength has been shown to be useful for predicting firmness and soluble solids content in apples and other fruit (Lu, 2003, 2004; Peng & Lu, 2008).

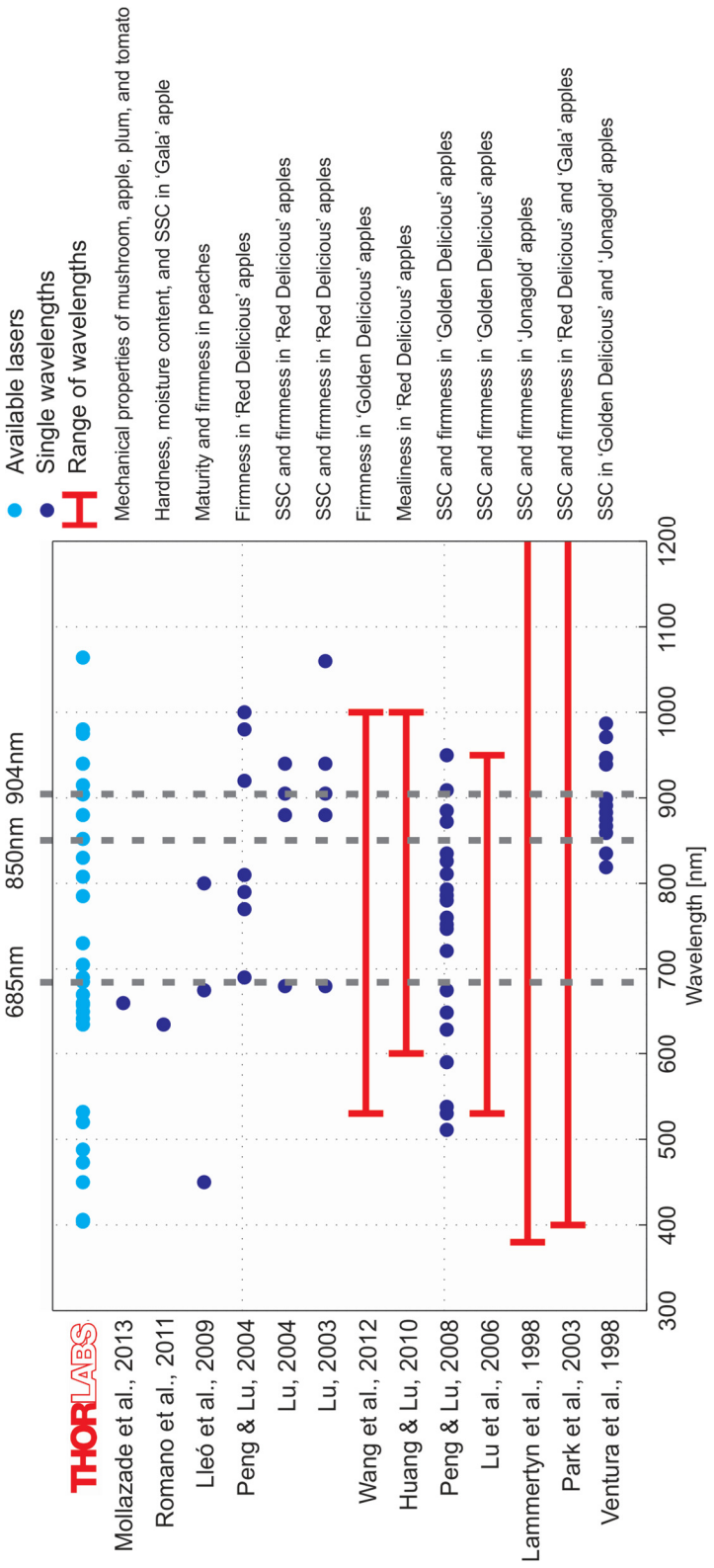

Figure 5-2. Individual wavelengths and wavelength ranges used in other studies to estimate fruit firmness. Laser availability from Thorlabs is shown in light blue(Thorlabs, 2013). Grey dashed lines indicate selected laser wavelengths (Mollazade et al., 2013; Romano et al., 2011; Lleó et al., 2009; Peng & Lu, 2004; Lu, 2004, 2003; Wang et al., 2012; Huang & Lu, 2010; Peng & Lu, 2008; Lu et al., 2006; Lammertyn et al., 1998; Park et al., 2003; Thorlabs, 2013).

5.2. Design

5.2.1 Optical Throughput

High-speed measurements place a number of constraints on the optical system. Fundamentally, the goal is to fill the camera's silicon detectors (pixels) with electrons as this will maximize the signal to noise. Traditionally this is achieved by increasing the exposure time to integrate more light. However, with online measurement where fruit are moving quickly this is not possible. To ensure sufficient light is available for high-speed measurement the optical throughput for the system is modelled. Figure 5-3 illustrates the scenario and Table 5-2 lists the calculation parameters. A 904 nm laser is used to illuminate a turbid sample that has relevant fruit optical properties. Light is then collected using a camera with a silicon-based detector. In this example the details

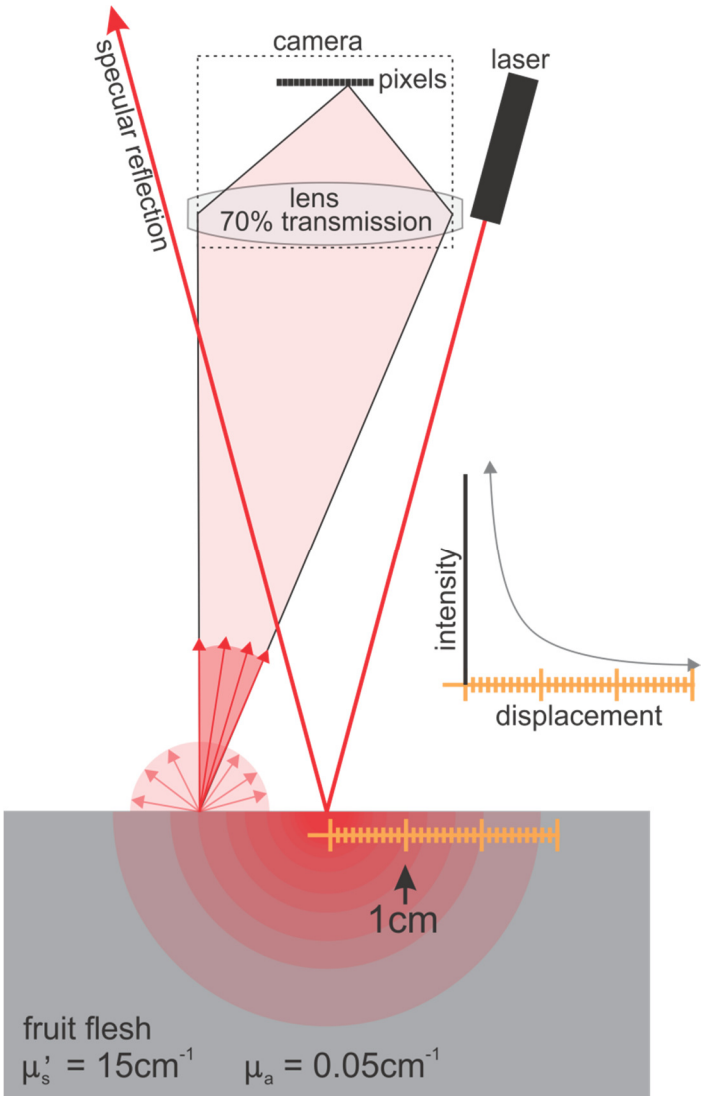

Figure 5-3. Outline of the optical throughput scenario.

of the camera come from the datasheet for the MV1-D1312I-160-CL camera manufactured by Photonfocus. The example source is a readily available (Thorlabs) 30 mW, 904 nm laser. A diffusion theory model found in the study by Cen et al. (2010) is used to describe the behaviour inside the turbid sample with an example set of optical properties found for 'Golden Delicious' apples by Lu et al. (2006). That is an absorption coefficient of 0.05 cm^{-1} and a reduced scattering coefficient of 15 cm^{-1}.

For illustrative purposes, a distance of 1 cm from the source is used along with the diffusion model giving a reflectance of 270 m^{-2}. We then calculate the numerical aperture (NA_{lens}), acceptance angle (θ), and solid angle of the lens (Ω_{lens}). This is done using the following formulae (Katz, 2002; Schubert, 2002):

$$NA_{lens} = \frac{1}{2 \cdot F_{lens}} \quad ,$$

$$\theta = \sin^{-1}(NA_{lens}) \quad ,$$

$$\Omega_{lens} = 2 \cdot \pi \cdot (1 - \cos(\theta)) \quad .$$

With an F number of 1.3 (a suitable lens for this application) this evaluates to a solid angle of 0.483. If we assume light is scattered from the sample in a hemisphere then the fraction of power that the lens collects is:

$$P_{collected}(r) = \frac{\Omega_{lens}}{2 \cdot \pi} \cdot R(r) \cdot P_{laser} \cdot T_{lens} \quad ,$$

where $P_{collected}(r)$ is the irradiance or the power collected by the imaging system at distance r, Ω_{lens} is the solid angle of the lens, $R(r)$ is the reflectance from the diffusion model, P_{laser} is the power of the laser source, and T_{lens} is the transmission of the camera lens.

At 1 cm the irradiance is 0.437 Wm^{-2}. This is then multiplied by the pixel area (6.4×10^{-11} m) giving 28 pW of collected power. Converting this to photons using the Planck–Einstein relation gives 1.273×10^{8} photons per second. The quantum efficiency of a silicon detector is 20% at 904 nm which gives 2.5×10^{7} electrons per second. The full well depth of the Photonfocus camera is 100,000 electrons, and the bit depth is 12 bit. If we use an exposure time of 1 ms the camera captures 25,000 electrons which when converted to the analog to digital (ADC) scale gives a count of 1023 out of a full scale 4095. This indicates that there should be sufficient light at 1cm. Figure 5-4 demonstrates this further by plotting the expected intensity from 0 to 3 cm. The y-axis

is limited to the range of the camera indicating that significant saturation near the incident point should occur.

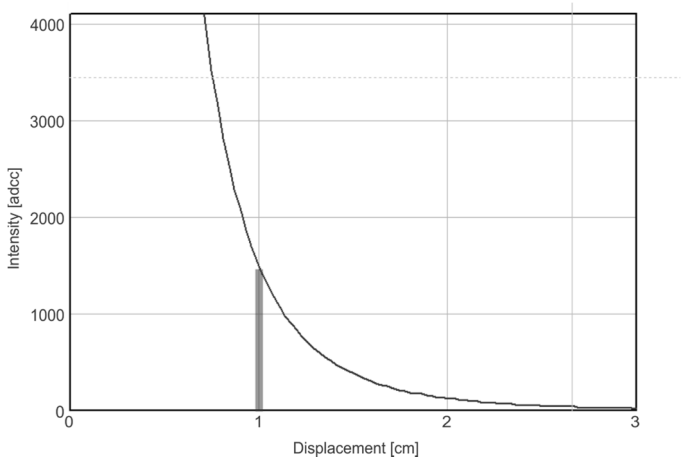

Figure 5-4. Optical throughput using a 980 nm laser diode.

Optical Throughput Parameters	Example
Laser Power (L904P030)	30 mW, 904 nm (Thorlabs, 2010)
Lens Transmission	70% (conservative estimate)
Camera Quantum Efficiency (silicon detector)	20% at 904 nm (Photonfocus, 2010)
Lens F Number	1.3
Full Well Depth	100,000 electrons (Photonfocus, 2010)
Pixel Area	8 µm x 8 µm (Photonfocus, 2010)
Estimated Absorption and Reduced Scattering	0.03 and 10 per cm respectively (Lu et al., 2006)
Diffusion Theory Model	Model presented by Cen et al. (2010)

Table 5-2. Example parameters used in the optical throughput calculation.

5.2.2 Imaging System

A Photonfocus camera (Figure 5-5a, MV1-D1312I-160-CL, Photonfocus, Switzerland) coupled with a Dalsa frame-grabber (x64 Xcelera-CL PX4 Camera Link, Teledyne Dalsa, Waterloo, Canada) was selected for use in the multispectral imaging system. This camera features a high resolution complementary metal-oxide-semiconductor (CMOS) detector with 1312x1082 pixels. It can operate at high speeds (110 frames per second), features 12 bits of greyscale resolution, a full well depth of 100,000 electrons, a signal to noise of 300:1, and has an exposure range from 10 µs – 410 ms. Based on preliminary optical throughput calculations in the last section this camera appears to be suitable in terms of quantum efficiency with greater than 20% conversion from 370 to 910 nm (Figure 5-5b). There is some flexibility in the quantum efficiency requirements due to the availability of a range of power levels for the lasers. This means the laser power can be adjusted to get comparable responses between lasers. In

unpublished internal reports at Plant and Food Research this camera was compared to others in terms of signal to noise. The total noise within an imaging system is made up of photon noise, dark noise, and readout noise. Photon noise is generated by the statistical nature of the arrival times between photons, dark noise arises from electrons thermally generated within the optical sensor, and readout noise is generated by the electronics when converting the optical signal to an electronic one. The Photonfocus camera outperformed an Allied Vision Marlin, an Allied Vision Stingray, a QI Imaging QICam, and a QI Imaging Rolera-XR. At 650 nm the overall signal-to-noise ratio was twice that of the second best camera. At 950 nm it was four times higher. This means the Photonfocus camera showed significantly less noise (photon, dark, and readout noise) compared to the other cameras investigated.

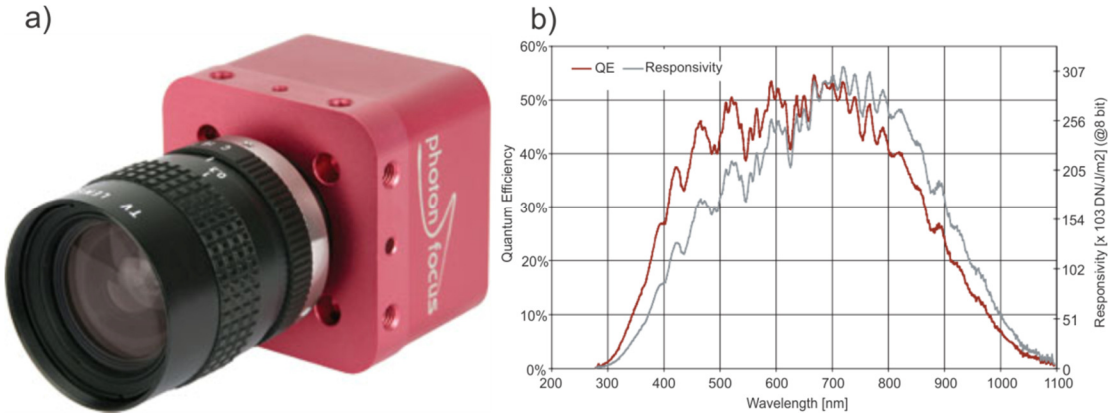

Figure 5-5. (a) Photonfocus MV1-D1312I-160-CL high performance CMOS camera and its (b) quantum efficiency curve (Photonfocus, 2010).

Historically CCD cameras have been chosen for this application due to their increased sensitivity and uniformity; however, modern CMOS technologies (used by the Photonfocus camera) have advanced to a level where their performance is comparable and even in some scenarios offer advantages over CCD technologies. The main advantages include speed and anti-blooming capabilities. CMOS imaging systems tend to be faster than CCD because their construction allows for electrical paths carrying signal and power to be very short. This minimizes inductance and capacitance and hence reduces propagation delays (Litwiller, 2001). The speed advantage is also aided by the massively parallel nature of CMOS, every pixel handles itself, and this includes amplification, noise-correction, and digitization (Litwiller, 2001; Russ, 2011). On the other hand CCD sensors tend to have an analog bottleneck where a row of pixels need to be read by the same charge to voltage converter and digitizer significantly limiting its operating speed (Kiessling & Pichler, 2010).

The second advantage is anti-blooming capabilities (Klinger, 2003; Nixon & Aguado, 2008). Figure 5-6 illustrates this. On the left (a) is an outline of a CCD camera, the bright sun in the image quickly fills up the CCD detectors bin capacity (capacity to accept photons). Once this limit is reached accumulated charge begins to overflow into neighbouring bins. This process continues and can seriously degrade the image. Most of the detail around the trees is washed out by the blooming effect. Some CCD cameras do have anti-blooming features, but these can reduce the sensitivity of the detector. Figure 5-6b shows an image captured with a CMOS camera. CMOS sensors convert charge to voltage directly using circuitry contained in every single pixel. This limits the possible interaction between pixels. This is ideal for a laser based multispectral imaging system as the sample will be illuminated by a very intense laser source which will likely saturate our detector. CMOS technology will allow the signal outside of this high intensity region to remain untainted.

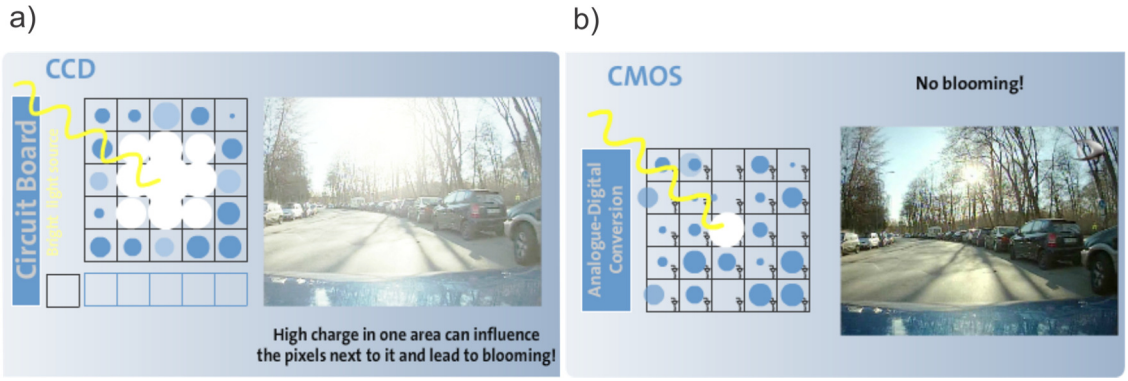

Figure 5-6. A significant advantage of CMOS cameras is their anti-blooming capability. The left image (a) shows how a CCD camera performs when a bright sun is present in the shot. The right image (b) shows a CMOS camera in the same situation (Dallmeier, 2014).

5.2.2.1 Field Of View

The Photonfocus camera was coupled with a 12.5 mm, F1.3, Goyo lens (GMHR412513MCN). This lens is targeted towards high resolution cameras used in machine vision applications. The field of view (FOV) for a camera, can be calculated, (Kruegle, 2011):

$$FOV = \frac{SS}{f} D \quad ,$$

where SS is the sensor size (in the dimension of interest), f is the focal length of the lens, and D is the working distance. At a working distance of 300 mm from the grader (a suitable working distance), the 12.5 mm Goyo lens and Photonfocus camera with a

horizontal sensor size of 10.48 mm will have a horizontal field of view equal to 251.5 mm, suitable for three fruit to be in a frame side by side (Figure 5-7).

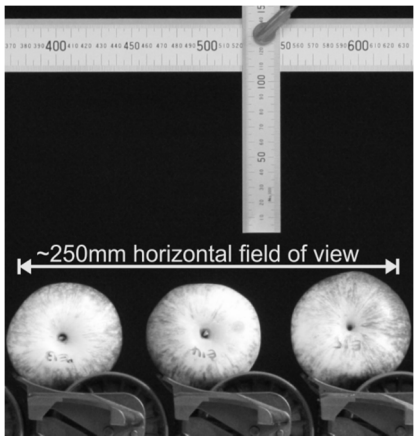

Figure 5-7. Expected field of view using the Photonfocus camera and Goyo lens shows that it should be capable of capturing three fruit side by side on Compac Sorting Equipment fruit carriers.

5.2.2.2 Spatial Resolution

Because the high-speed multispectral imaging system utilizes a conveyer to transport fruit, there is no control over fruit height. This means that the surface of large fruit will appear closer to the camera compared to small fruit. This is a problem because analysis of these images requires knowledge of the distance between the illuminated spot and each pixel in the image. To overcome this issue, a model is needed to convert fruit height into spatial resolution.

To generate this model a metal ruler (Toledo, Australia) was placed in the camera frame at a distance from the camera ranging from 200 to 300 mm in 10 mm increments (Figure 5-8a). The spatial resolution changes linearly as distance changes. Figure 5-8b shows the spatial resolution measured at each of the 11 distances from the camera. The resulting model is:

$$SR = 0.00064 \times D_{sample} + 0.0257 \quad ,$$

where SR is the spatial resolution in mm per pixel, and D_{sample} is the distance between camera and sample. This is used along with the distance from the fruit to the camera to come up with a spatial resolution specific for each fruit.

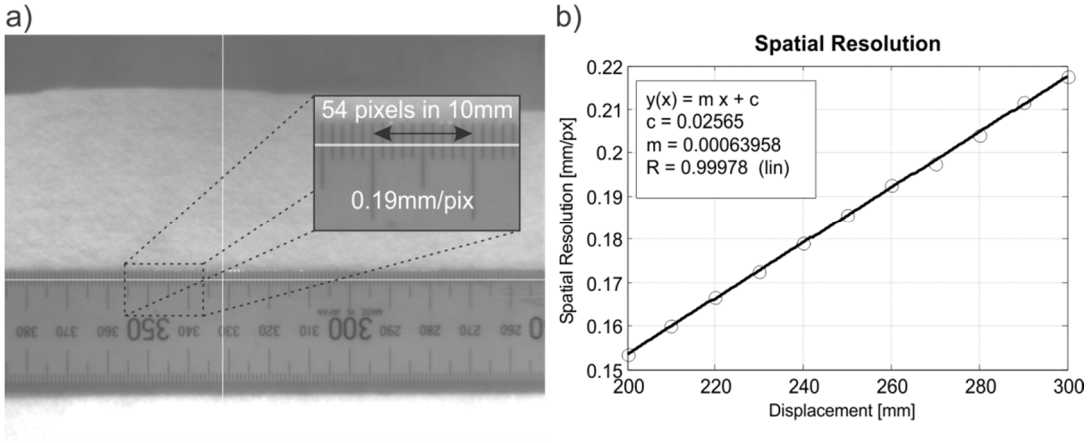

Figure 5-8. (a) Shows a section of the images used to measure spatial resolution for the multispectral imaging system. (b) Shows the spatial resolution at different distances from the camera. Blue indicates the measured values, black indicates the best fit linear line used to model the resolution for different sized fruit.

The 100 mm range investigated sees the spatial resolution reduce from 0.15 to 0.22 mm/pixel. Cen & Lu (2010) discuss their hyperspectral imaging system and the effects of different spatial resolutions. Their investigation showed that spatial resolutions ranging from 0.07 to 0.25 mm/pixel introduce insignificant error when extracting the optical properties of a sample (0.53% for their absorption coefficient and 0.36% for their reduced scattering coefficient). This suggests that the change in spatial resolution we see over a 100 mm range should not introduce significant error.

5.2.2.3 Background Lighting

The high-speed multispectral imaging system was operated in an open lab with fluorescent lighting. To minimize the background lighting captured by the system two precautions were taken. The first was to use a 665 nm long pass filter. Figure 5-9a shows spectra from a fluorescent lamp in the lab. The black line indicates the transmission of the 665 nm glass filter (FGL665S, Thorlabs, New Jersey, USA) used, and the red line shows the resulting light after being filtered. This filter blocks the majority of the fluorescent light leaving only a small insignificant component at 700 nm. The second precaution was to block as much of the room lighting as possible using a physical box constructed with wood and blackout material. This can be seen in Figure 5-9b; it also helps keep the system safe by reducing the opportunity for people to be exposed to the laser beams.

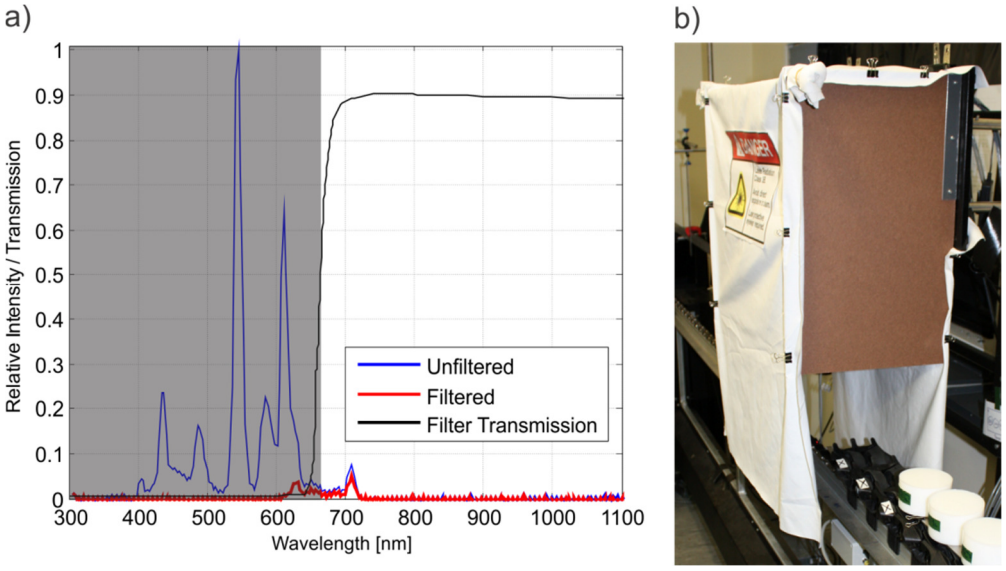

Figure 5-9. (a) A 665 nm long pass filter is used to block the majority of the fluorescent lighting in the lab where the multispectral imaging system is housed. (b) Physical box arrangement using wood and blackout material to further block background lighting.

5.2.2.4 Distortion Correction

The multispectral imaging system is utilizing the full frame of the camera to capture the three fruit side by side. The disadvantage of this is that distortion tends to get larger further away from the centre of the image. The easiest way to visualise distortion is to capture an image of a grid. Ideally the image should have straight lines in both the horizontal and vertical directions. Unfortunately because of distortion this is not normally the case. Figure 5-10 demonstrates the three types of distortion that typically occur. The first is barrel distortion (Figure 5-10a) where the lines bow outward. This occurs because the image magnification decreases from the centre of the image outward. The second is pincushion distortion (Figure 5-10b) where the lines bow

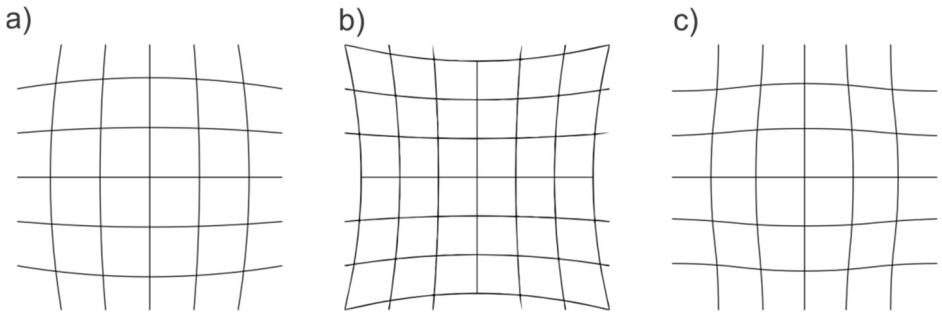

Figure 5-10. Three examples of radial distortion, (a) barrel distortion, (b) pin cushion distortion, and (c) moustache distortion.

inward. This time magnification increases from the centre of the image outward. The final type is known as moustache distortion (Figure 5-10c). This is a combination of both the barrel and pincushion distortion effects. Typically these distortions are symmetric and depend on the lens used.

A camera calibration toolbox for Matlab was used to correct for these distortions on the collected images (Bouguet, 2013). The toolbox requires the collection of about 20 reference images captured using the system you want to calibrate (Figure 5-11). Each image needs to contain a black and white grid held in a different orientation each time. The toolbox uses these to calculate the intrinsic properties of the camera including the focal length, principal point, skew coefficient, and radial and tangential distortions. These properties are then used to correct for the distortions in the multispectral images

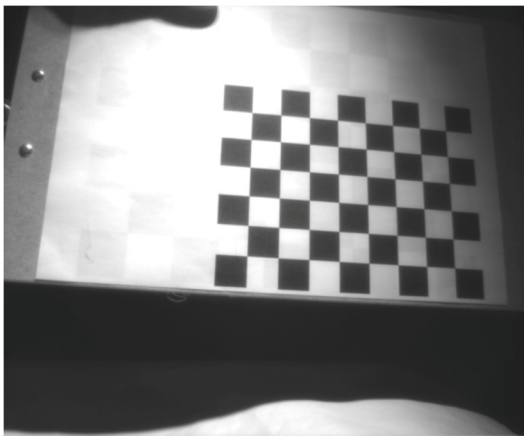

Figure 5-11. Reference grid image used to calibrate the camera and remove distortions from multispectral images. Each black and white box is two by two centimetres.

5.2.3 Light Source

Laser diodes were chosen for this design because they are compact, operate at a versatile range of wavelengths, have a high power density, and are reasonably priced. They are well suited for a multispectral imaging system as they emit light over tight wavelength bands (monochromatic) eliminating the need for discrete filters. The light they emit is also coherent and strongly directional making it simpler to collimate and direct onto a sample.

Laser diodes (Figure 5-12a) are made of semiconductor materials, commonly consisting of elements from columns III and V or II and VI in the periodic table (Zappe, 2003). The different materials and combinations of materials allow different wavelengths of light to be emitted. The output wavelength is determined by the energy level differences between conduction and valence band electrons in the semiconductor (Renk, 2012).

Modern laser diodes are available over a large range, from about 400 nm to 9550 nm in the infrared band (Thorlabs, 2013).

Figure 5-12b shows the layout of a simple semiconductor laser diode. It consists of a p-n junction semiconductor cleaved and coated so that the cut edges form mirrors, in this case the emitting side has a reflectance of about 10% (so light can come out) and the opposite side has a reflectance of about 99%. This laser is known as a Fabry-Perot laser diode due to the Fabry-Perot resonator formed by the two mirrors (Sun, 2012). The p-n junction is forward biased causing electrons and holes to be injected from opposite sides of the junction into the depletion region. Spontaneous emission occurs when one of these electrons and holes recombine (Maini, 2013). If the lasing threshold current is met then these spontaneous emissions will cause other electron pairs to recombine. This recombination releases a stimulated photon with the same wavelength, phase, and polarisation as the photon that caused its recombination (Maini, 2013). These photons reflect back and forth in the gain medium (between the mirrors) stimulating more and more photons. As this stimulation is taking place, there is also a portion of the photons exiting at the low reflectance end of the crystal (emitting end) resulting in a steady state laser output.

Laser diodes typically emit light that is highly divergent and elliptical (Sun, 2012). The elliptical nature of the beam is due to the elongated geometry of the exit aperture as pictured in Figure 5-12b and leads to different divergence angles for light perpendicular and parallel to the active region. If these divergence angles are traced

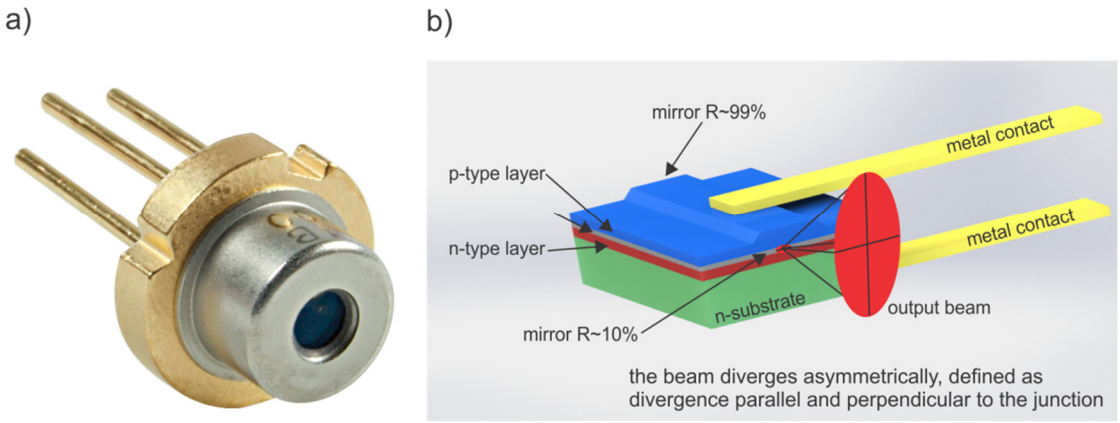

Figure 5-12. (a) Packaged laser diode in hermetically sealed 5.6 mm package. (b) Laser diode chip overview showing the substrate layer, the n-doped silicon layer, the active region, the p doped silicon layer and the metal contacts. Laser diode chips are typically 300 x 300 x 100 µm (Zappe, 2003).

back inside the laser to an imaginary point source the parallel and perpendicular beams will not converge to the same point. This difference is known as the laser's astigmatism.

5.2.3.1 Laser Diodes

The laser diodes for this design were selected based on previous literature to highlight the relevant regions for fruit firmness and quality measurement. Table 5-3 shows details on the final selected laser diodes. Three wavelengths were selected, 685 nm targeting chlorophyll absorption in fruit (maturity indicator), 850 nm because it is in a low absorption region for maximum penetration into the fruit flesh, and 904 nm because it has been shown to be useful for predicting firmness and soluble solids content (Peng & Lu, 2008; Lu, 2004; Noh & Lu, 2007; Song et al., 1997).

Manufacturer Name	Wavelength	Power	Package	Supplier	Measured Wavelength
HL6750MG	685 nm	50 mW	5.6 mm	Thorlabs	690 nm
L850P030	850 nm	30 mW	5.6 mm	Thorlabs	852 nm
L904P030	904 nm	30 mW	5.6 mm	Thorlabs	898 nm

Table 5-3. Laser diodes selected for the multispectral imaging system.

The manufacturing tolerances in lasers can be quite large. This means that for any particular laser diode purchased the wavelength it emits could vary by about ±5 nm (Sun, 2012). To check the wavelength of the lasers purchased a calibrated Zeiss MMS-1 spectrometer was used. Each laser showed up as a peak on the spectrometer. The last column of Table 5-3 shows the actual measured values found using a simple peak finding algorithm. In the following sections of this thesis, the lasers are referred to by their manufacturer specified values.

The safety precautions which must be taken when working with these types of lasers are worth mentioning. All three are class 3B lasers and are considered dangerous to human vision, especially the 850 and 904 nm lasers which are not visible to the naked eye. Appropriate safety measures must be taken, including proper training, the use of protective eyewear, correct signage, and an interlock system to disable the lasers in dangerous situations.

5.2.3.2 Laser Driver and Temperature Control

Each laser is mounted in a Thorlabs LDM21 laser diode housing (Figure 5-13b) and driven using a Thorlabs ITC102 laser diode driver and temperature controller (Figure 5-13a). The controller features configurable laser currents and proportional-integral-

derivative (PID) temperature control. The settings used for each laser are given in Table 5-4. The current was set to be about 90 to 95% of the maximum value possible for each laser. This kept the lasers in a safe operating range while maximising light output. The laser temperature was set to 15 °C to prolong life and maintain the laser in a stable state.

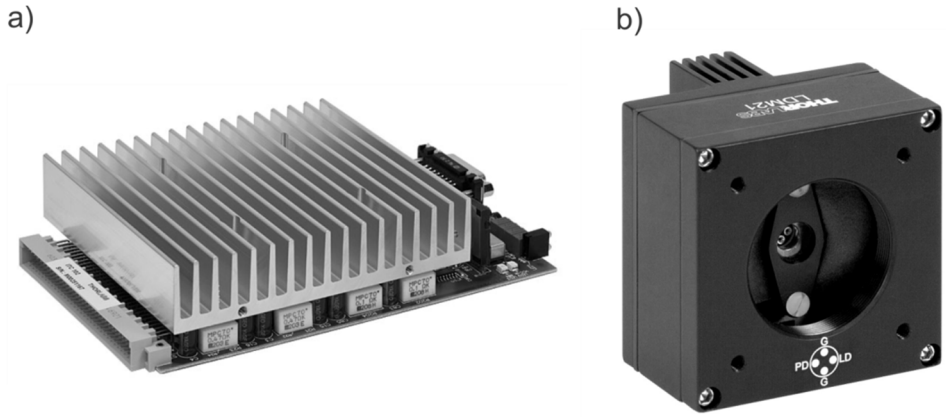

Figure 5-13. (a) ITC102 OEM laser diode driver and temperature controller. (b) LDM21 laser diode housing with thermoelectric cooling unit.

Manufacturer Name	Wavelength	Current [mA]	Temperature Set Point [°C]	Price [$US]
HL6750MG	685 nm	116.2 (120 max)	15	89
L850P030	850 nm	89.5 (95 max)	15	85
L904P030	904 nm	139.9 (150 max)	15	85

Table 5-4. Configuration for each laser diode.

5.2.3.3 Beam Characteristics and Corrections

The laser beam emitted directly from a laser diode is not useful for most applications. The light is highly divergent, and the beam is elliptically shaped making it less suitable for radial averaging, a technique we hope to utilize when extracting out intensity profiles from images. Optical elements are required to minimize this elliptical shape and to either collimate or focus the beam onto the desired target. This can be achieved a number of ways including the use of cylindrical lenses, spatial filtering, anamorphic prism pairs, micro lenses, and optical fibres (Sun, 2012; Gu, 1999).

In this study, spatial filtering was used. Spatial filtering not only helps remove the elliptical shape of the beam but also helps remove any extraneous light that is scattered due to imperfections in the system such as dirty or damaged optics. A spatial filter typically consists of a focusing lens which focuses the beam down to a spot, a pinhole aperture located near the focus to block any undesired light, and a second lens to collimate or focus the clean beam onto the target (Figure 5-14a). The disadvantages of

spatial filters are their sensitivity to pinhole position making alignment difficult, and the loss in power due to the pinhole aperture blocking a portion of the light.

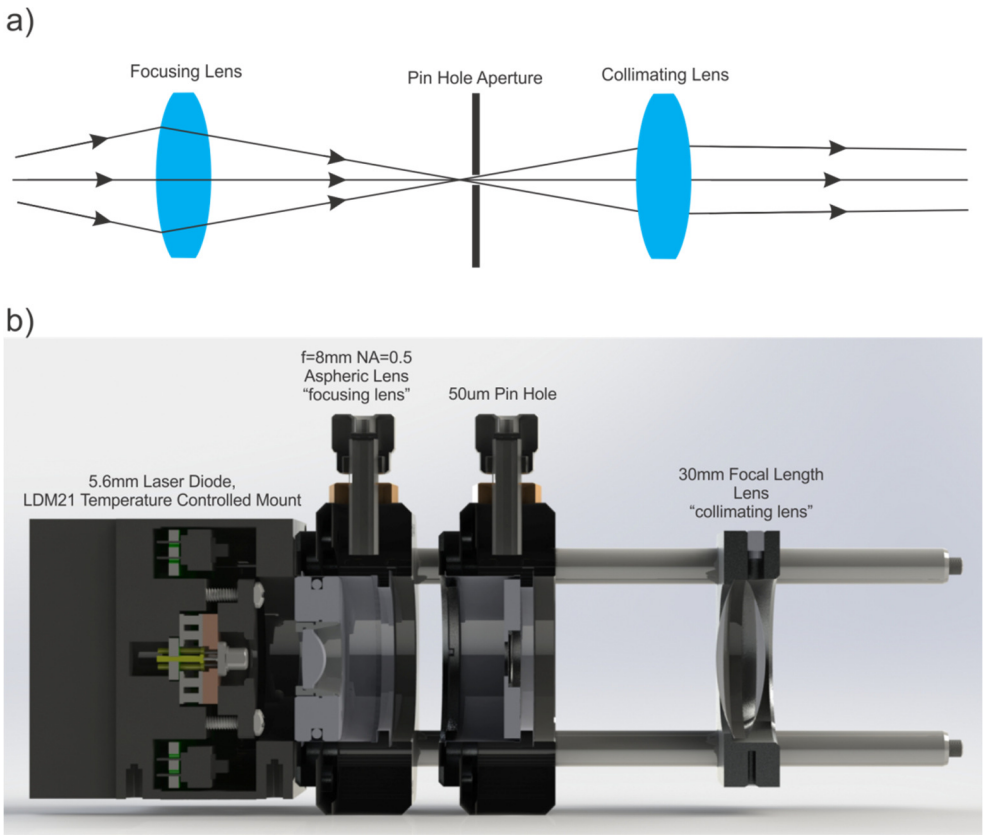

Figure 5-14. (a) Typical layout for a spatial filter. (b) Thorlabs gear arranged to spatially filter light from the solid state laser diodes.

Table 5-5 lists the components used for each laser in the multispectral imaging system. Figure 5-14b shows the arrangement of these components modelled in a computer aided design package (CAD). On the far left is a laser diode mounted in an LDM21 temperature controlled housing. Continuing right is the aspheric focusing lens

Component	Part Number	Supplier
Laser Diode Housing with TEC Cooling	LDM21	Thorlabs
XY Translation Stage	CXY1	Thorlabs
Mounted Geltech Aspheric Lens	C240TME-B	Thorlabs
Pinhole Apertures	50 µm, 56-282, 850 nm 30 µm, 84-065, 690 nm and 904 nm 20 µm, 56-279, 980 nm	Edmond Optics
Collimating lens	30mm focal length, LB1757-B	Thorlabs
Lens Cage Plate	CP02	Thorlabs
4" Metal Cage System Rods	ER4	Thorlabs

Table 5-5. Spatial filter components.

mounted in an X-Y translation stage. This lens focuses the light down to the pinhole aperture also mounted in an X-Y translation stage. Alignment is critical for producing a clean beam and these translation stages allow for precise location control. Finally on the right is a collimating lens mounted in a lens cage plate, this is used to focus the clean beam onto the surface of the fruit samples. All components are rigidly attached to a 30 mm steel rod cage system.

To gain confidence in the setup of each laser they were characterised to find their beam sizes in both the horizontal and vertical directions (Figure 5-15a). This can be done using a number of techniques including commercial beam analysers, optical choppers, and a scanning knife blade (Grigoropoulos, 2009; Suzaki & Tachibana, 1975). For this design an optical chopper was used (Model 75152, Newport Corporation, United States). Each laser beam was focused to a working distance of 300 mm. The chopper was positioned at this working distance, and a large photo-detector (FDS100, Thorlabs, New Jersey, USA) was positioned behind the chopper to measure the light signal. The chopper's blade rotates modulating the light output. The signal from the photo-detector was amplified (DLPCA-200, Femto, Berlin, Germany) and captured using a Tektronix oscilloscope with data logging capabilities. The signal measured is described by the following function:

$$P_d(x) = \int_x^{+\infty} \int_{-\infty}^{+\infty} I_{pk} e^{-\frac{2(x^2+y^2)}{w^2}} dx\, dy = \frac{P_1}{2} \operatorname{erfc}\left(\frac{\sqrt{2}x}{w}\right) \quad ,$$

where P_1 is the laser power, w is the $1/e^2$ radius, and x is the displacement (Miller & Haglund, 1997; Marshall & Stutz, 2011). Matlab (Mathworks, Massachusetts, United States) was used to fit this function to the experimental data. This is demonstrated in Figure 5-15b, the blue line shows the measured data and the red line shows fitted result. Table 5-6 summarises the laser beam diameters as measured using this technique.

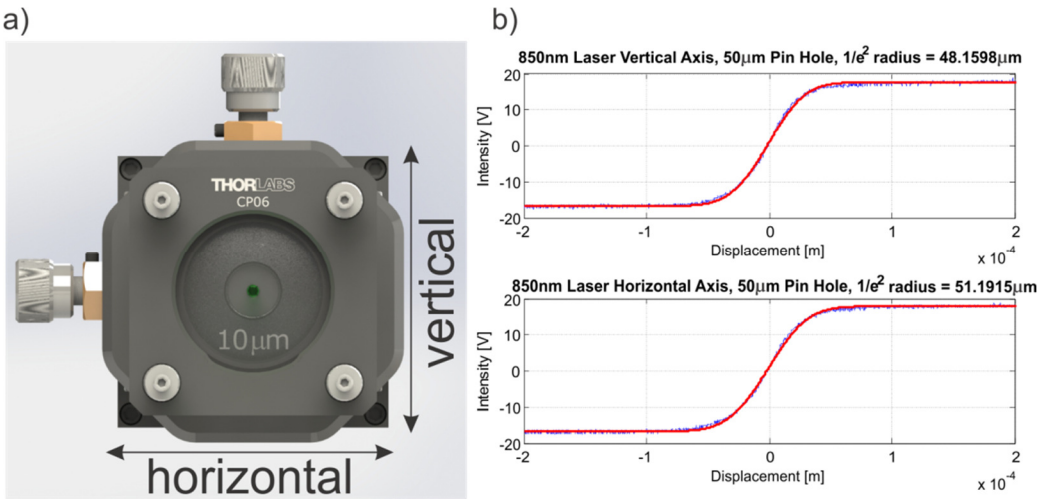

Figure 5-15. (a) Front view of the laser assembly showing the direction of laser beam profile measurements. (b) Example beam profile for 850 nm laser beam with 50 µm pinhole, aspheric lens, and collimating lens.

Laser	Horizontal Diameter	Vertical Diameter
HL6750MG, 685 nm	106.4 µm	115.6 µm
L850P030, 850 nm	102.4 µm	96.4 µm
L904P030 904 nm	140.2 µm	178.4 µm

Table 5-6. Measured laser beam sizes focused to a working distance of 300 mm.

5.2.4 Physical Arrangement

The camera and three lasers were mounted on an optical breadboard then attached to a metal upright frame designed in-house. This frame was designed for maximum rigidity to prevent any movement in the system. It was positioned in the centre of a three meter fruit conveyer system pictured in Figure 5-16a. This position was chosen so that the fruit were up to speed by the time they reached the measurement station. The camera and laser modules were mounted out from the breadboard so that they were aligned with the centre of the fruit travelling along the conveyor (Figure 5-16b). The 904 nm laser was mounted on the left, the 850 nm laser in the middle and the 685 nm laser on the right. The incident angles on the fruit samples were 6°, 13°, and 9° respectively. These were chosen to fit the measurement geometry and to avoid specular reflections (red lines) reaching the camera (Figure 5-16b).

The conveyor system used plastic fruit carriers (Compac Sorting Equipment, Auckland, New Zealand) and was designed to transport up to 12 fruit in both directions. The system allowed for any speed ranging from stationary up to about 1.5 m/s. Care was taken not to accelerate too quickly ensuring that the fruit had settled into the carriers when measurements took place. Each plastic carrier had an extra metal

tab attached to trigger an opto-interrupt that in turn triggered the image acquisition system.

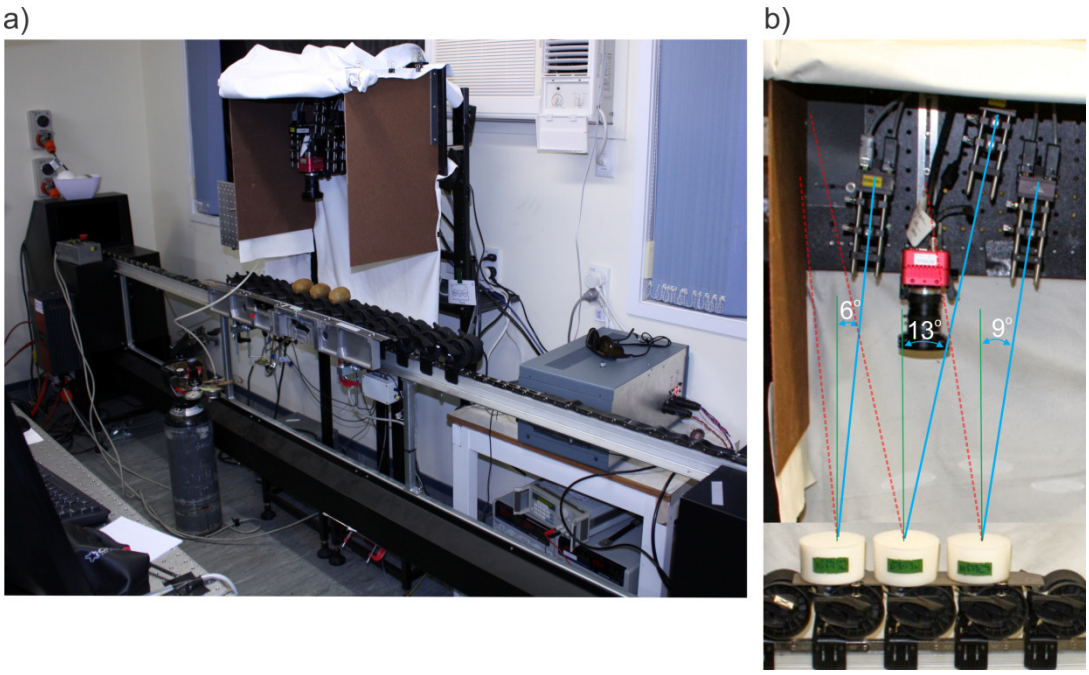

Figure 5-16. (a)Physical design of the in-house fruit grader with the multispectral imaging system mounted in the middle. (b) Lasers and camera were mounted on a vertical breadboard so that they were in line with fruit on the conveyer.

5.2.5 Fruit Size Measurement

A method was needed to measure the size of the fruit. This allows us to calculate the distance between the camera and the samples surface, necessary for calculating the spatial resolution. A second camera (Canon Rebel T3, Canon Inc, Toyko, Japan) with a 50 mm lens was used to capture images of the apples at the left hand end of the grader before they move along under the multispectral imaging system.

Figure 5-17a shows the camera positioned 3 metres from the fruit. In the frame is 10 fruit, a one metre ruler mounted horizontally, a 300 mm ruler mounted vertically, and a black cloth as a backdrop. The black cloth provides a uniform background with clear fruit boundaries. The rulers provide the spatial resolution (mm/pixel) along the horizontal and vertical axis.

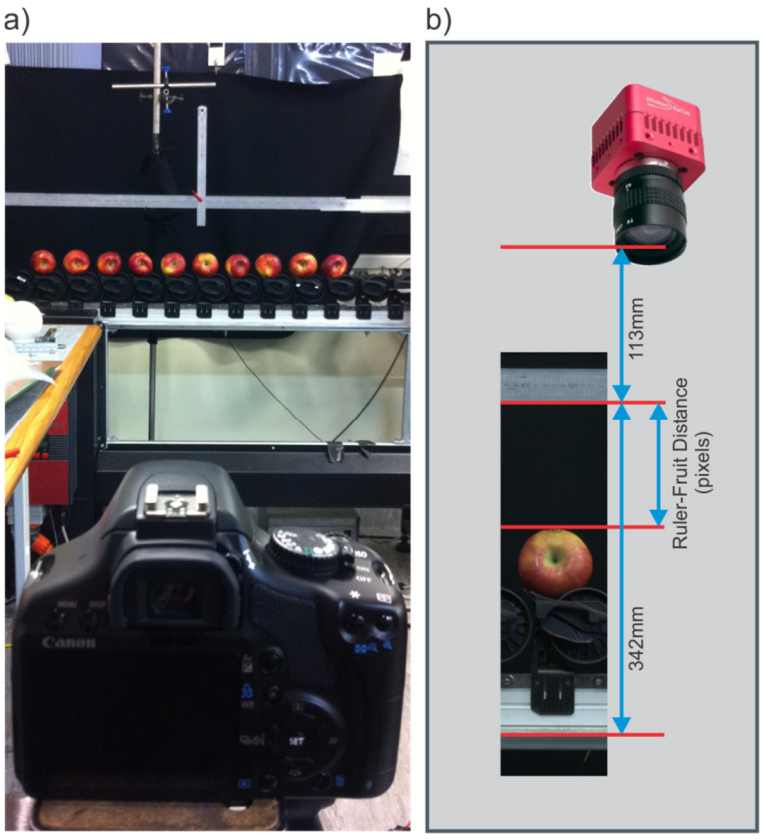

Figure 5-17. (a) Colour camera used to capture images of the fruit at the far left of the grader. Images are processed for fruit size and the distance between fruit and camera lens. (b) Imaging processing extracts out the number of pixels between the ruler and fruit. This is converted to physical distance using the spatial resolution (pixels per mm) of the colour camera.

Fruit size and camera height was extracted using an image processing algorithm developed in Matlab with functions from the Image Processing Toolbox (Mathworks, Massachusetts, United States). Figure 5-18 shows the various steps in the process. The first step is to take the raw colour image (Figure 5-18a) and separate out the red colour channel. This channel was selected because it provides the best contrast between the fruit and the black background. The image is then cropped so that no rogue objects are identified leaving only the fruit and the black background (top of Figure 5-18b). A simple threshold is then used to convert the image to black and white (middle of Figure 5-18b). A simple morphological filter is then applied which does an erosion followed by a dilation of the image. This removes small objects from the foreground. A connected components analysis is run on the remaining black and white image. This finds all the separate white objects in the image. All the objects less than 10,000 pixels were then removed leaving only the fruit objects. A bounding box around each fruit was found. This provided the horizontal and vertical size (in pixels) of each fruit as well as the vertical coordinate for the top of each fruit. The ruler was also identified in

the image and the distance in pixels between the top of the fruit and the ruler was calculated. All pixel amounts were converted to millimetres using the spatial resolution (mm/pixel) calculated from the horizontal and vertical rulers.

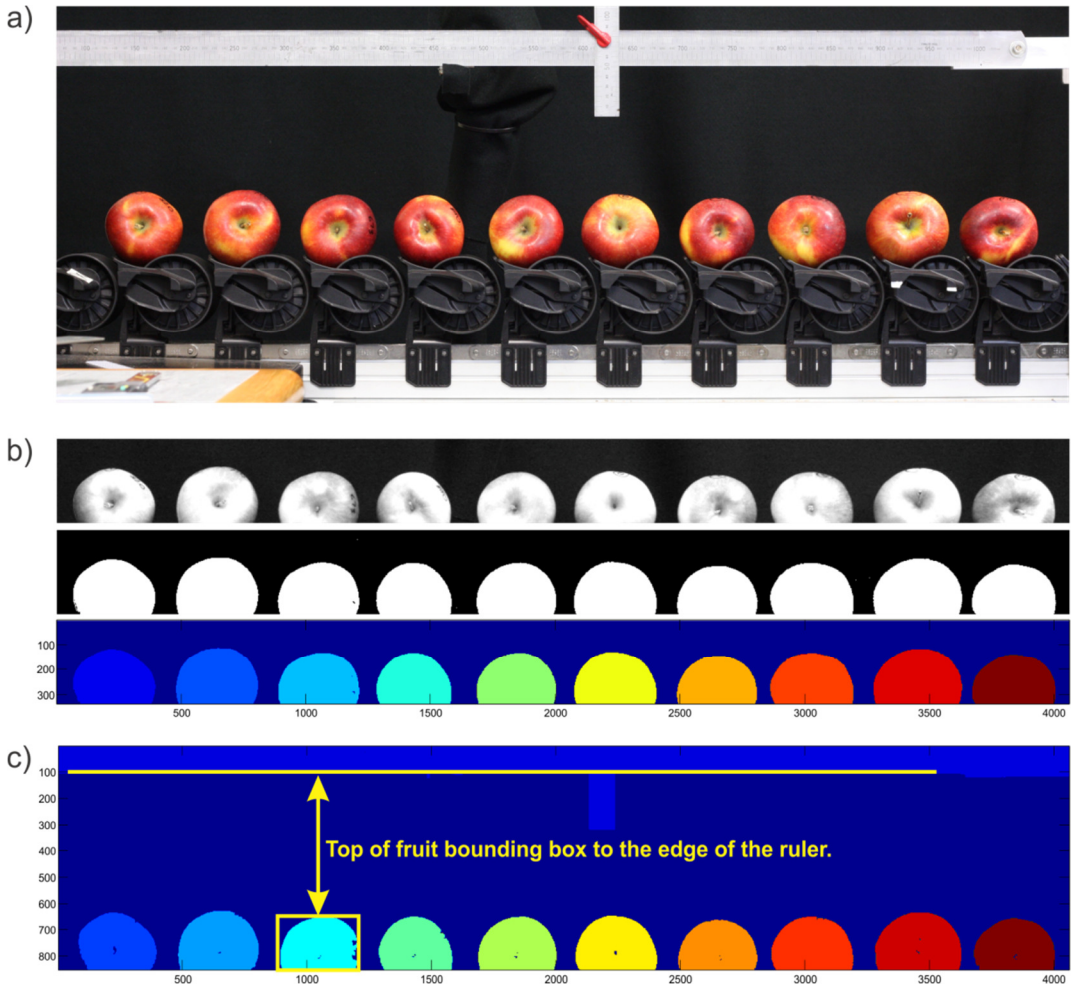

Figure 5-18. Process for extracting the size and camera-fruit displacement. (a) Shows the raw colour image, note the long ruler in the horizontal direction and a short ruler in the vertical direction. (b) Shows the different steps in segmenting each fruit. (c) For each fruit object (indicated by a different colour) there is a bounding box telling us the fruits horizontal and vertical dimensions.

Two sources of error for this measurement were explored. The first error arises from the divergent point of view of the camera (Figure 5-19a). In this situation, we would underestimate the radius of the sample (r). The following equations describe the situation:

$$z^2 = d^2 - r^2 \quad ,$$

$$\theta = \sin^{-1}\left(\frac{r}{d}\right) \quad ,$$

$$x = z \sin\theta \quad ,$$

where z is the distance to the visible edge of the sample, d is the distance to the centre of the sample, r is the true radius of the sample, and x is the displacement the camera sees to the edge of the sample. By rearranging these we find:

$$x = \frac{r}{d}\sqrt{d^2 - r^2} \quad .$$

The consequence of this is that in the limiting case where d gets very large then x approaches r. This indicates that the further the camera is out from the sample the more accurate the measurement of fruit radius will be.

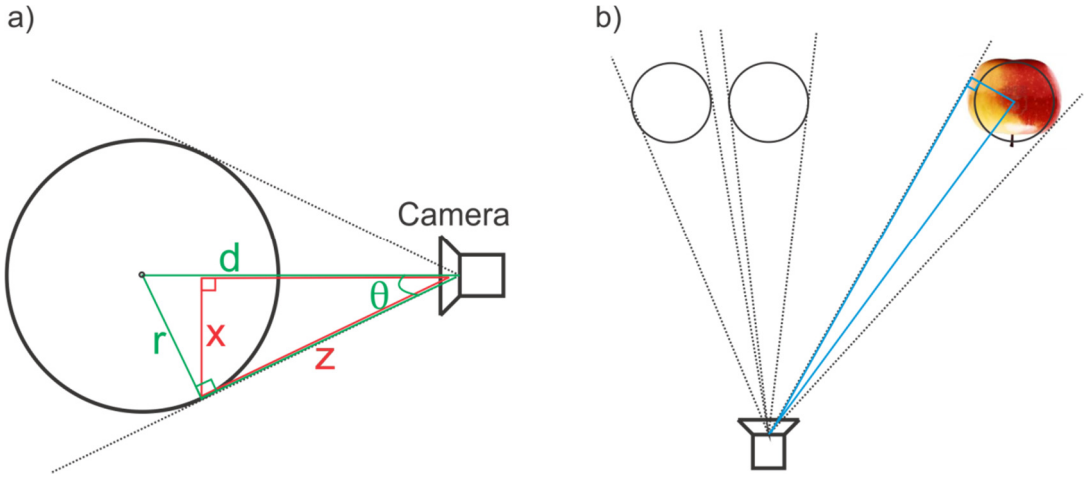

Figure 5-19. (a) The camera is never able to see the exact edge of the sample. (b) Because the fruit samples are not spherical there will be higher errors for fruit that are off the central axis of the camera.

The second source of error is related to the fruit shape. Figure 5-19b demonstrates this. Fruit samples off the central axis will be viewed from a different perspective, more side on. This means that the fruit size measurement error will increase the further out the fruit is. Like the previous source of error, this can be minimized by moving the camera back as far as possible.

The camera was placed three metres from the fruit to minimize these errors. This was as far back as possible given the constraints for the laboratory where the experiment took place. For a white Teflon sphere with a diameter of 80 mm, the measurement system had an average error of 0.22 mm (0.28%) across the 10 fruit positions. On a test set of 10 fruit with an average diameter of 77 mm, an average error of 0.56 mm (0.73%) was found.

5.2.6 Software

A custom software program was developed in C# (Microsoft, Redmond, Washington) to collect data from the high-speed multispectral imaging system. The software interface is pictured in Figure 5-20. Some of the important features incorporated include hardware triggering, a filmstrip interface, camera settings, automated file naming, histogram contrast enhancement, and data integrity protection.

Hardware triggering utilizes an opto-interrupt circuit which when triggered sends a signal to the Camera Link card which in turn grabs an image from the Photon Focus camera. This was important because it means images can be gathered at precisely the right time as the fruit are transported along the conveyor.

The filmstrip interface seen at the top of Figure 5-21 allows the user to quickly review the last set of images. Each time a new run is done this strip begins empty, as fruit travel past the measurement stage images are collected filling the 12 thumbnails. This provides a useful tool for the user to visually inspect the collected images ensuring that they make sense and that all 12 images are collected.

On the main interface are a number of controls designed to allow easy adjustment of camera settings. These include exposure time, image zoom (for the main live display), crosshairs, and status line. The exposure time setting communicates with the camera and adjusts its current exposure time (10µs – 410ms). Image zoom adjusts the zoom applied to the main display on the software interface (Figure 5-21). The crosshairs button activates a white crosshair on the screen and is very useful for aligning objects in the frame, especially when centring the laser beams. The status line enables a camera function which overwrites a few pixels at the edge of the frame and puts in information such as exposure time, and frame number. This provides verification that a new frame has been captured and that the exposure time has been correctly set.

The automated file naming system has two features. The first is an auto incrementing number which is appended to the end of each file. The second is the ability to set the filename using a serial communication channel. This feature was added because a separate piece of software was used to drive the fruit grader. This separate software was used to keep filenaming consistent between different grading equipment.

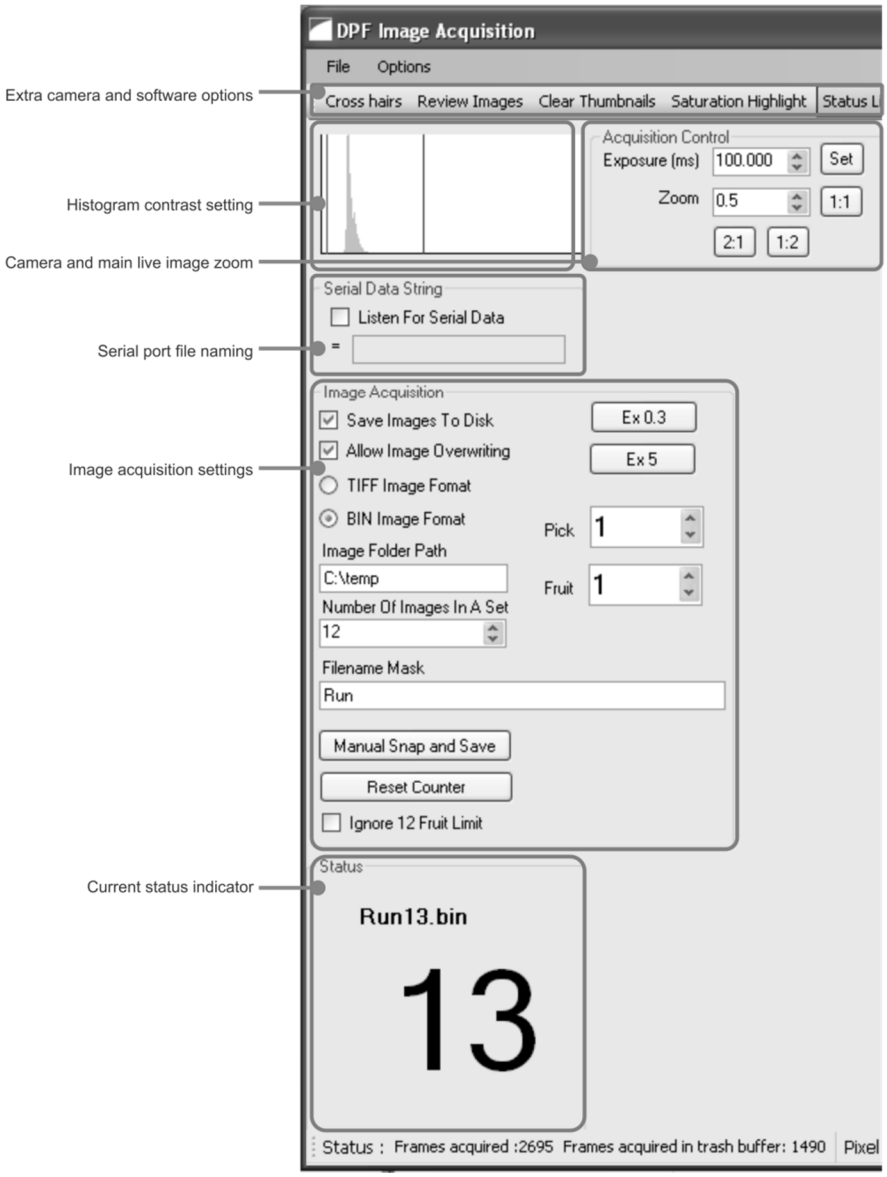

Figure 5-20. Custom software for capturing images using the high-speed multispectral imaging system. Images are captured based on a hardware trigger.

The histogram built into the main user interface lets you adjust the contrast shown on the computer screen. A computer screen can only show a limited number of gray levels, this histogram allows you to rescale those limited levels to different intensify ranges measured by the camera.

The final feature is an option to prevent overwriting images. This was added to maintain data integrity. Once an image is written to the hard disk the software knows not to overwrite it. For example if the central software controlling the filenames fails it could use the same filename twice. This will be detected, overwriting will be blocked, and the user will be notified.

Further detail on the user interface can be found in Appendix 2.

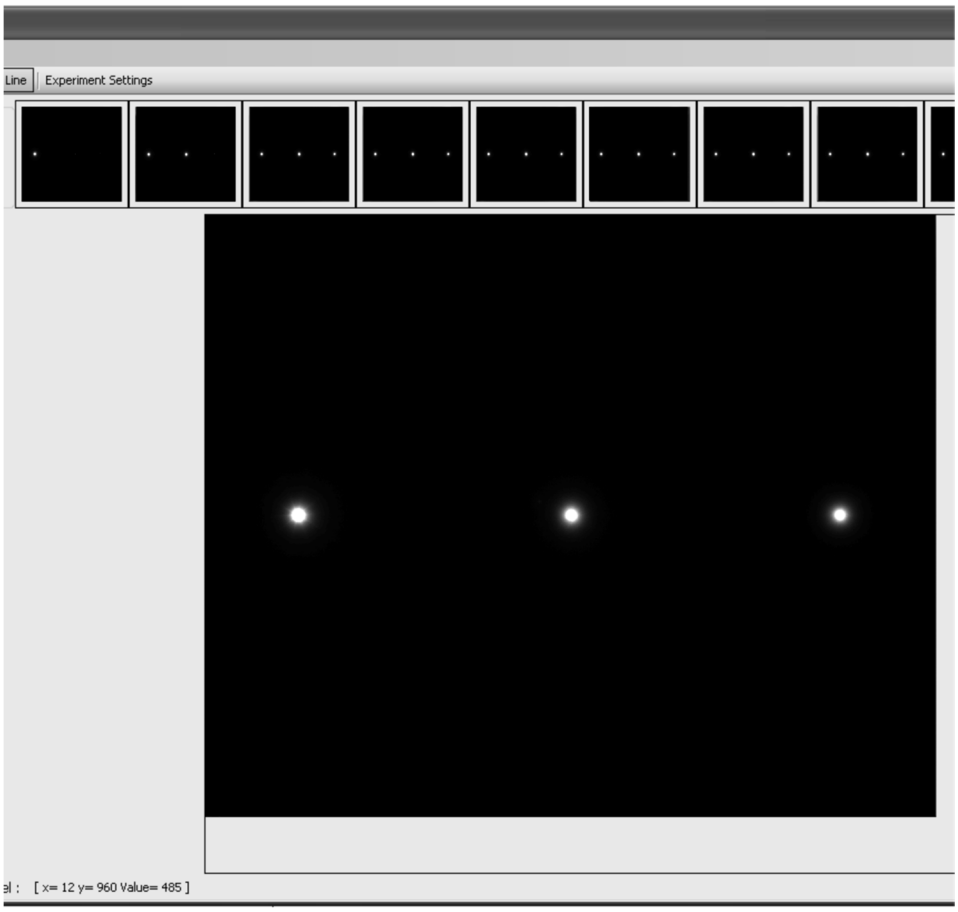

Figure 5-21. Software displaying thumbnails of images collected at the top and an example image in the main display. Note the three bright spots correspond with the three lasers illuminating three different apples.

6. High-Speed Royal Gala Apple Experiment

6.1. Introduction

In Chapter 4, a number of optical approaches for measuring fruit firmness were discussed. That discussion led to the development of a high-speed multispectral imaging system based on a fruit conveyer, discrete lasers, and a CMOS camera. Images captured with the system can then be processed using a number of different techniques with the goal of estimating firmness and other fruit characteristics. These techniques include the measurement of simple parameters like illumination area, spatial profiling of the intensities, curve fitting with different distribution models, and the extraction of optical properties using diffusion theory models. The extracted parameters and optical properties are used along with destructive reference measurements to build models. These models can be used to make non-destructive predictions of the reference measurements on further fruit.

This study seeks to validate the described multispectral imaging system using two approaches presented in the literature. The first is an empirical approach where a modified Lorentzian model is fitted to the intensity profiles (Peng & Lu, 2006a, 2006b), the second attempts to extract optical properties using a diffusion model (Cen, Lu, Mendoza, et al., 2011; Cen, Lu & Mendoza, 2011). Images were captured on 200 'Royal Gala' apples. Two different treatments were used to produce a wide firmness range. Reference measurements including penetrometer and acoustic firmness were taken to build prediction models. These models are compared to those presented in the literature.

6.2. Method

6.2.1 Fruit Samples

Two hundred 'Royal Gala' apples were harvested at commercial maturity from an orchard in New Zealand. This cultivar was chosen (Chapter 2) because it makes up the largest portion of apples exported from New Zealand. Half were housed in a plastic bin with a humidified controlled atmosphere (CA) circulating (2% oxygen and 1% carbon dioxide), and the other half were stored in a similar container but with circulating humidified air. Fruit in these bins were kept at 0.5 °C for a five month

period prior to the beginning of the experiment. These conditions were designed to promote a wide range of fruit firmness relevant to consumer satisfaction, fruit in CA storage remain firmer for longer while air treated fruit should soften (Saftner et al., 2002). For easy access fruit were shifted from these individual storage bins to standard cool-store conditions (-0.5 °C, 80% RH) one week before measurements began.

Twenty fruit from each bin were transported from Auckland to Hamilton (two hour journey) the night before each of the five measurement days where they were housed in a lab at 20 °C to equilibrate overnight. Measurements were made on day 0.5, 1.5, 2.5, 6.5, and 7.5. The 0.5 day fraction in elapsed time is due to the first night (0.5 day) of equilibration. Measurements using the non-destructive multispectral imaging system were carried out each morning. Fruit were then transported back to Auckland where AWETA acoustic firmness and destructive texture analysis was carried out the following day. Figure 6-1 shows the different positions on the fruit where each measurement was carried out. Fruit were numbered prior to any measurements, and this was used as a reference point for fruit orientation. The location of this label was chosen to ensure no visible defects were present in the main measurement locations.

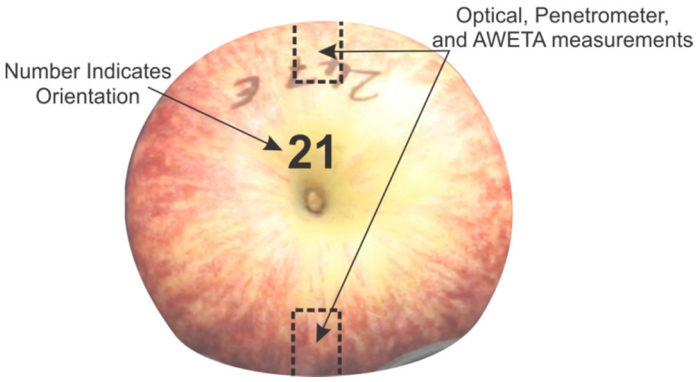

Figure 6-1. Physical measurement locations of the optical, penetrometer, and acoustic firmness measurements.

6.2.2 Texture Analysis

An automated fruit texture analyser (TA.XT*plus*, Stable Micro Systems, Godalming, UK) was used to measure penetrometer firmness on the 'Royal Gala' apple samples (Figure 6-2b). This simultaneously interrogates the compression, shear, and rupture properties of the fruit tissue (Nicolaï et al., 2006). A thin (approximately 2 mm) layer of skin was removed from the measurement site using a mounted razor blade (Figure 6-2a). The texture analyser then measured the force profile required to drive an 11 mm diameter metal Effegi™ probe 9 mm into the sample's flesh at 10 mm s^{-1} (Abbott,

1999). There are many different parameters that can be extracted from these force profiles as discussed in the introductory chapter, however, this study focused on the equivalent measure for penetrometer firmness. That is the maximum force recorded in the displacement cycle. Measurements were carried out in two locations on opposite sides of the fruit (Figure 6-1).

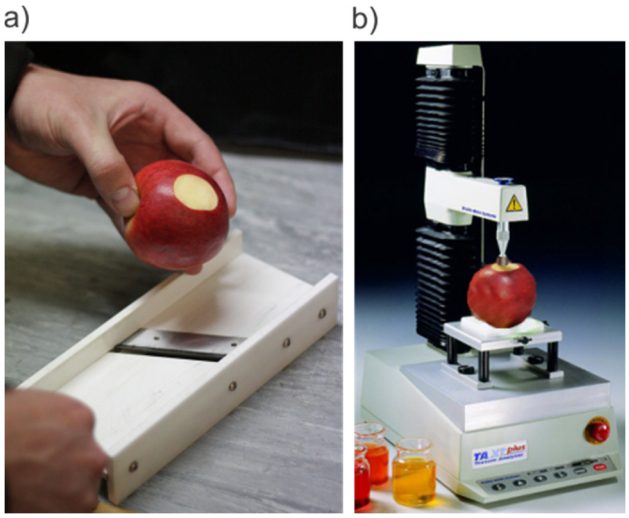

Figure 6-2. (a) Fruit skin is removed using a mounted razor blade. (b) A fruit texture analyser (TA.XT*plus*, Stable Micro Systems, Godalming, UK) is used to measure the penetrometer firmness.

6.2.3 Acoustic Firmness

Acoustic firmness was measured using a commercial desktop acoustic firmness sensor (AFS, AWETA, Netherlands). This system (Figure 6-3a) measures the resonant frequency, a property related the elastic mechanical properties of the fruit tissue

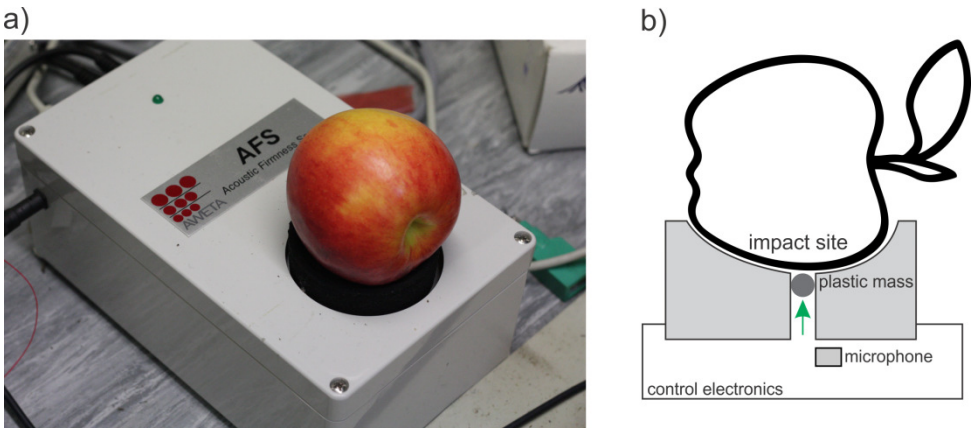

Figure 6-3. (a) AWETA acoustic firmness sensor. (b) Acoustic firmness measurement overview. A small plastic mass impacts the fruit and a microphone is used to record the vibration signal; the fruit weight is also measured using an in-built balance.

(modulus of elasticity)(Duprat et al., 1997; Baerdemaeker et al., 1982). Figure 6-3b illustrates the mechanism. A fruit is placed on a soft foam fruit holder, and once stable a small plastic mass strikes the fruit from underneath and a microphone captures the audible signal. Typically a fast Fourier transform is used to resolve the frequency components of the recorded signal. The first frequency peak is taken to be the resonant frequency of the fruit and used in the firmness calculation. The system also measures fruit mass using an in-built balance. The acoustic firmness index, FI, is calculated from the resonant frequency, f, and the fruit mass, m, measured in grams (Cen et al., 2013):

$$\mathrm{FI} = f^2 \mathrm{m}^{2/3} / 10^6 \quad .$$

Two acoustic firmness measurements were made on each fruit. Measurements were made on the flesh directly adjacent to where the optical measurements were made (Figure 6-1).

6.2.4 Multispectral Image Collection

Multispectral images were gathered using the high-speed system described in Chapter 5. Ten fruit at a time were loaded onto the grader at the left hand end of the conveyer. Care was taken to orient the fruit so that optical measurements were made in the positions relative to their label shown in Figure 6-1.

The fruit size was measured while fruit were in this static left hand position using the system also described in Chapter 5. An example image can be seen in Figure 6-4a. Fruit sizes and camera heights were calculated from this image based on prior knowledge of the ruler position mounted in the same frame.

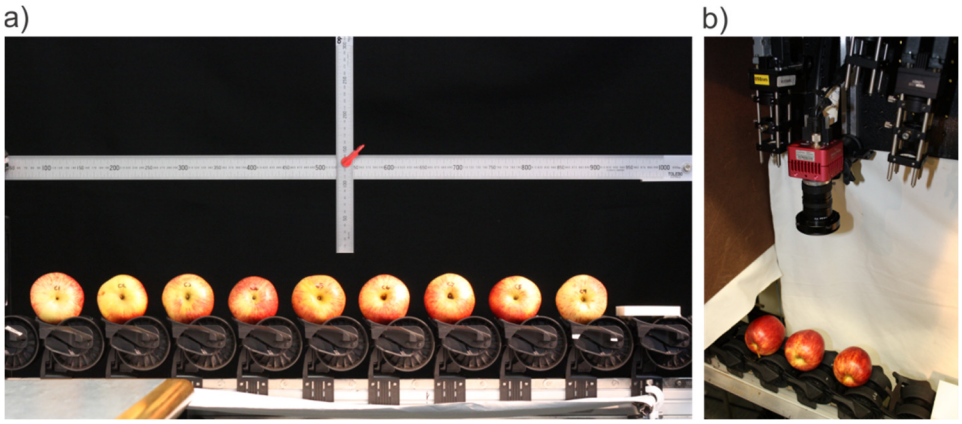

Figure 6-4. (a) Ten fruit lined up at the left hand end of the grader as seen by the colour camera used to measure fruit size and camera height. (b) Fruit passing under the multispectral imaging system.

Fruit were then transported at 1 m/s under the multispectral imaging system where an opto-interrupt trigger was used to initiate the acquisition of each frame. The camera was configured with an f-number of 2 and an exposure time of 1 ms. This corresponds to 1 mm of fruit movement under the laser beam. Each run captures a total of 12 images corresponding to the ten fruit being exposed to the three lasers with three fruit in each frame (except for the leading and trailing fruit). The images are identified by the first fruit number in each set. Two replicate runs were done in each of the two fruit orientations to provide a representative whole fruit measurement and reduce noise. Fruit were then placed back in their box for transport to Auckland where acoustic and texture analysis was carried out. Dark images were obtained at the end of each experimental session and were subtracted from each collected image during analysis.

6.2.5 Multispectral Image Analysis

As fruit move under the multispectral imaging system, it captures a number of frames as illustrated by Figure 6-5. Three consecutive frames are processed to generate a complete set of multispectral images for each fruit. Each image is then corrected to account for dark current. Dark current is related to the temperature of the silicon detector. As temperature increases electrons are freed from valence bands and are measured by the digitization circuitry (Howell, 2000). Dark correction is achieved by subtracting an image with the same exposure time that contains no illumination sources. Images are also corrected for lens distortion as outlined in Chapter 5.

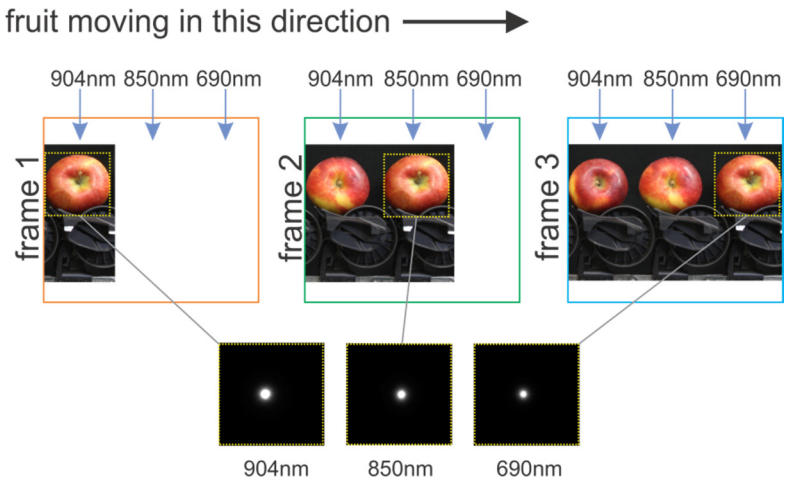

Figure 6-5. Three frames are captured as the fruit move along the conveyor. The first when the first fruit is under the 904 nm laser, then the 850 nm laser, and finally under the 685 nm laser. Images are then segmented to get a full set of multispectral images for each fruit.

Dark and distortion corrected images are then processed using a radial average technique to extract the intensity profiles which will be used for further analysis. This is illustrated in Figure 6-6a. The image is first processed to find the centre of the illuminated regions. A Matlab (Mathworks, Massachusetts, United States) program was constructed that used the image processing toolbox to find the centre of mass for all pixels above a certain intensity threshold (2000 by default). The distance to each pixel is then calculated and rounded to the nearest whole number. All pixels at each of these integer radii were grouped and averaged providing a vector of intensity values that correspond to single pixel rings expanding out from the centre point. The red cross indicates the located centre position; the blue and green crosses indicate the average intensity of rings 11 and 18 pixels from the centre respectively (Figure 6-6b). These intensity profiles are then parameterised using the models presented in the following sections.

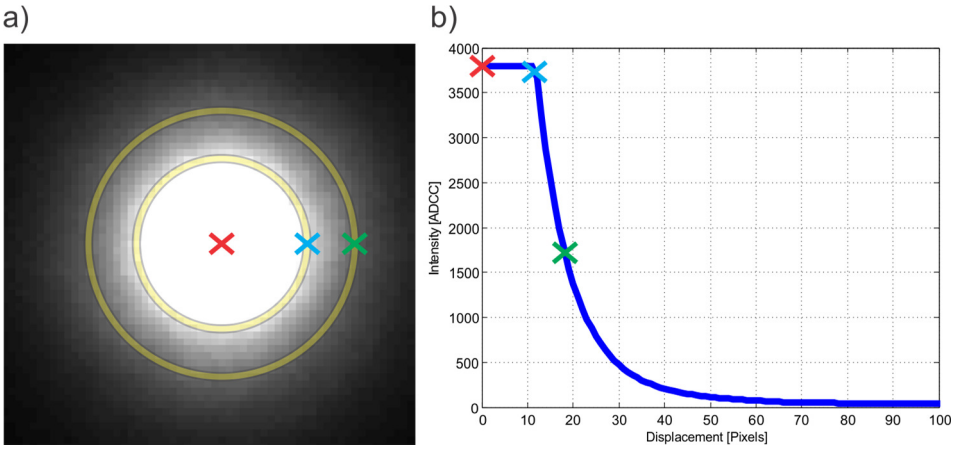

Figure 6-6. Illustration of radially averaging the data to reduce noise. The yellow rings indicate pixels being averaged. Each cross on the intensity profile (b) corresponds with the ring indicated on the image (a).

6.2.5.1 Modified Lorentzian

The first model used to parameterise the intensity profiles is a modified Lorentzian model. Peng & Lu (2005) first investigated the use of fitting a standard Lorentzian function to intensity profiles for the purpose of predicting fruit firmness. More recently Peng & Lu (2006a) modified the Lorentzian function introducing a d term so that it could better handle intensity profiles with saturated central regions, typical with laser illumination. The model they used is:

$$I(x) = a + \frac{b}{1 + \left(\frac{|x|}{c}\right)^{d}} \quad ,$$

where I is the intensity along the intensity profile, a is the asymptotic value of light intensity when x approaches infinity, b is the peak value corresponding with the intensity at the centre of the image, c is the full width half maximum (FWHM) of the intensity profile, and d is related to the slope of the profile in the FWHM region.

Using this model, Peng & Lu (2006b) were able to estimate firmness of 'Red Delicious' and 'Golden Delicious' apples with standard errors (SEV) of 6.64 N and 6.58 N and correlation coefficients of 0.82 and 0.81 respectively. As their experimental method is similar to the approach used in this study, their modified Lorentzian model seemed a good candidate for analysis on the data captured at high speed.

The Matlab Curve Fitting Toolbox (Mathworks, Massachusetts, United State) was used to determine best fits to the intensity profiles. The fitting process used a Levenberg-Marquardt non-linear least squares algorithm (Matlab, 2014) and the data used in the fit was limited from 0 mm to a radius of 10 mm, a similar range to other studies.

6.2.5.2 Optical Property Extraction

The second approach covered in this study is to extract out the optical properties of the sample. As discussed, in Chapter 3, the optical properties are fundamental characteristics of a samples tissue.

To estimate the optical properties of a sample a diffusion approximation model is used. Earlier work in this area utilized a model of reflectance developed by Farrell et al. (1992). Lu et al. (2006) used this model and were able to predict penetrometer firmness with a standard error (SEP) of 10.17 (R = 0.66) for 'Golden Delicious' apples. More recently an improved model was developed and used on 'Delicious' and 'Golden Delicious' apples (Cen, Lu & Mendoza, 2011). The exact form of this model is provided and discussed in Chapter 3. This model requires the refractive index of the sample, in the present study a value of 1.35 was used typical of horticultural products including peaches and apple (Cen, Lu & Mendoza, 2011; Cen et al., 2012). This leads to the constant terms (C_1, C_2) and an effective reflection coefficient (R_{eff}) of 0.1277, 0.3269, and 0.4498 respectively (Cen et al., 2010; Cen, Lu, Mendoza, et al., 2011).

Cen, Lu & Mendoza (2011) used a hyperspectral imaging system for their measurements, however, the model should be compatible with the high-speed measurements made in this study. Again the Matlab Curve Fitting Toolbox (Mathworks, Massachusetts, United States) was used to find the best fit for this model to the intensity profiles, using the Levenberg-Marquardt non-linear least squares

algorithm. The data was first logarithmically transformed, a common variance stabilising transform, to improve the fitting results as suggested by Cen et al. (2010). The data used in the fit was limited to measurements below 3500 ADC counts and up to a radius of 15 mm.

6.2.5.3 Multiple Linear Regression

Multiple linear regression was used to develop firmness prediction models from the modified Lorentzian parameters and optical properties on all 200 'Royal Gala' apples. This has been utilised by many researchers to combine all, or the most relevant data providing more accurate predictions (Qing et al., 2008; Lu et al., 2009; Peng & Lu, 2008). The construction of these models was done using the PLS toolbox for Matlab (Eigenvector Research, Wenatchee, United States). Each model was built using a Venetian blind cross validation with 10 data folds.

6.3. Results and Discussion

6.3.1 Texture Analysis

The distribution of average penetrometer firmness values for the 200 'Royal Gala' apples is shown in Figure 6-7a. The range extends from 27.3 N to 80 N with a combined (treatments) mean firmness of 50.2 N and a standard deviation of 9.6 N. This range is comparable to others found in the literature on the development of optical firmness measurement systems (Lu, 2003). This range is relevant to the New Zealand apple industry with the firmest fruit hitting the highest maturity grade requirement (78.4 N). The range then extends down falling well below the outturn specification (63.7) at which point they would not be exported (Coriolis Research, 2006).

The data is coloured based on the treatment they were subjected to, either humidified air (red), or humidified controlled atmosphere (blue) conditions. The mean firmness for the CA treated fruit was 56 N with a standard deviation of 9.2 N and for humidified air the mean was 44.4 N with a standard deviation of 5.7 N. A significance test ($p = 0.05$) showed that that the results from the two treatments were significantly different at the 5% level. This was expected; CA storage was used to slow the natural processes within the fruit retaining firmness for longer periods than fruit stored in humidified air (Saftner et al., 2002).

The penetrometer measurement was made in two locations on the fruit. Figure 6-7b shows the firmness at first orientation compared to the second, symbol colour

distinguishes the two treatments. There is a significant amount of variation within the fruit as demonstrated by the large amount of spread from one side of the fruit to the other. The standard error of a simple linear regression gives a measure of 'around fruit variability', in this case 5.65 N. This was consistent with other internal studies on kiwifruit in the same firmness range. Generally these two orientations are averaged for an overall firmness measurement within the fruit (Dobrzański et al., 2006).

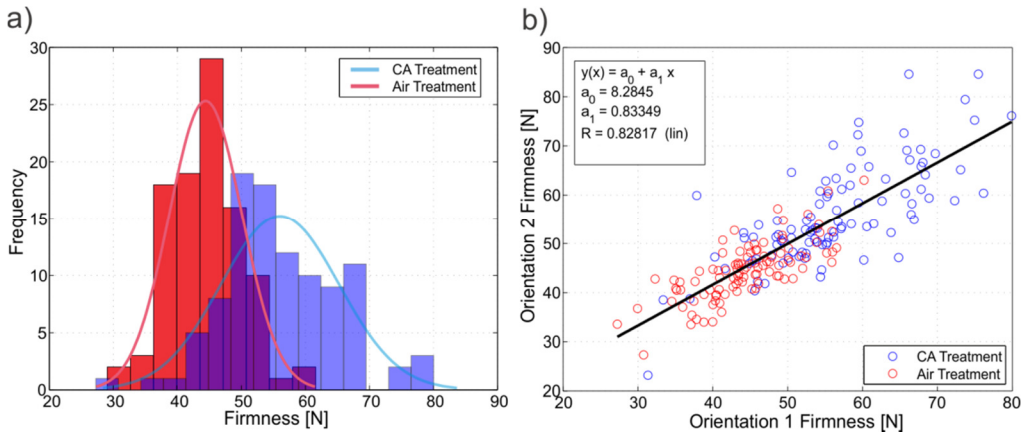

Figure 6-7. (a) Distribution of penetrometer firmness values in 200 'Royal Gala' apples. Humidified air treated fruit are indicated in red and controlled atmosphere treated fruit in blue. (b) Penetrometer firmness in each orientation. Again, colour indicates treatment.

6.3.2 Acoustic Firmness

The distribution of acoustic firmness measurements for the two treatment schemes is shown in Figure 6-8. For this measurement the range extends from 12.6 $Hz^2g^{2/3}$ to 28.7 $Hz^2g^{2/3}$, has a mean of 21.28 $Hz^2g^{2/3}$, and a standard deviation of 2.45 $Hz^2g^{2/3}$.

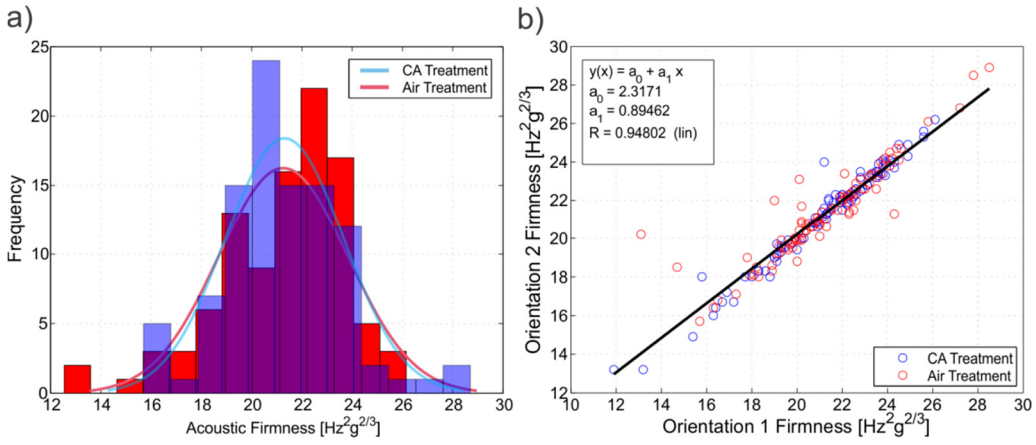

Figure 6-8. (a) Distribution of AWETA acoustic firmness values for 200 'Royal Gala' apples. Humidified air treated fruit are in red and controlled atmosphere treated fruit in blue.

There is no industry standard around acoustic firmness so it is difficult to say if this is a suitable range with commercial relevance. It is, however, comparable with others who have investigated acoustic firmness (Cen et al., 2013; Johnson & Dover, 2005; Molina-Delgado et al., 2009).

Figure 6-8a shows the distribution of acoustic firmness separated by treatment. There was no significant difference ($p = 0.05$) between fruit stored in humidified air and humidified controlled atmosphere conditions (Figure 6-8a). Figure 6-8b shows the acoustic firmness as measured in the two orientations. There were a few visible outliers present. These are likely due to the incorrect identification of the resonant frequency. The algorithm selects the first resonant peak and, in some situations depending on the shape and orientation of the fruit, there are secondary modes of resonance that get incorrectly identified (Lu & Abbott, 1996; Chen & DeBaerdemaeker, 1993). There is a much higher level of agreement between acoustic measurements at each orientation compared to the penetrometer results. This is because the resonance of the whole fruit is being measured.

6.3.3 Acoustic and Penetrometer Firmness Relationship

There was no relationship between the penetrometer firmness and AWETA acoustic firmness (Figure 6-9). This is not unreasonable considering the fundamental difference between the acoustic and penetrometer measurements. Acoustic firmness interrogates the elastic properties only while the penetrometer takes the measurement further inflicting physical damage on the cells and thus gathering insight into the compression, rupture, and shear characteristics (Nicolaï et al., 2006).

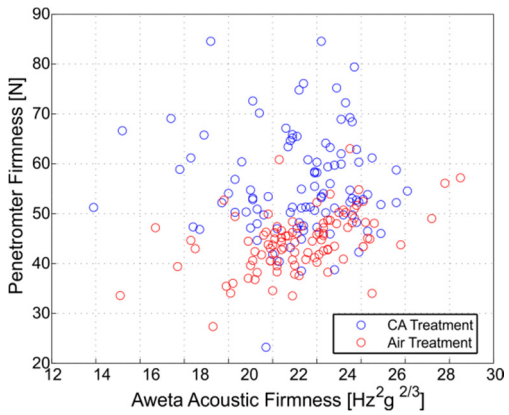

Figure 6-9. The relationship between AWETA acoustic firmness and penetrometer firmness as measured by the texture analyser.

Johnson and Dover (2005) found a poor correlation ($R = 0.51$) for 'Gala' apples, consistent with the results presented, but a strong correlation for the 'Cox's Orange Pippin' cultivar ($R = 0.84$), while Kupferman (2007) found poor correlations for both 'Gala' and 'Red Delicious' apples ($R = 0.14$ and $R = 0.64$ respectively). Acoustic firmness changes have been strongly linked to the water loss in fruit (Landahl, 2007). Researchers have examined different storage conditions, usually varying relative humidity and temperature. This affects the rate at which acoustic firmness changes (Belie et al., 1999; Johnson & Dover, 2005). Fruit in the current study were housed in chambers with either circulated humidified air or controlled atmosphere. This limited water loss and may have slowed the reduction of acoustic firmness and eliminated any correlation between acoustic and penetrometer firmness.

6.3.4 Multispectral Imaging Results

6.3.4.1 Modified Lorentzian

Figure 6-10a shows a typical curve fit of the modified Lorentzian function to the intensity profiles extracted from the multispectral imaging system. There is a distinct region where the modified Lorentzian function does not fit the measured data. This is due both to the sharp transition where the camera saturates and the saturated region itself. Both of these features can not be adequitely described by the form of the modified Lorentzian.

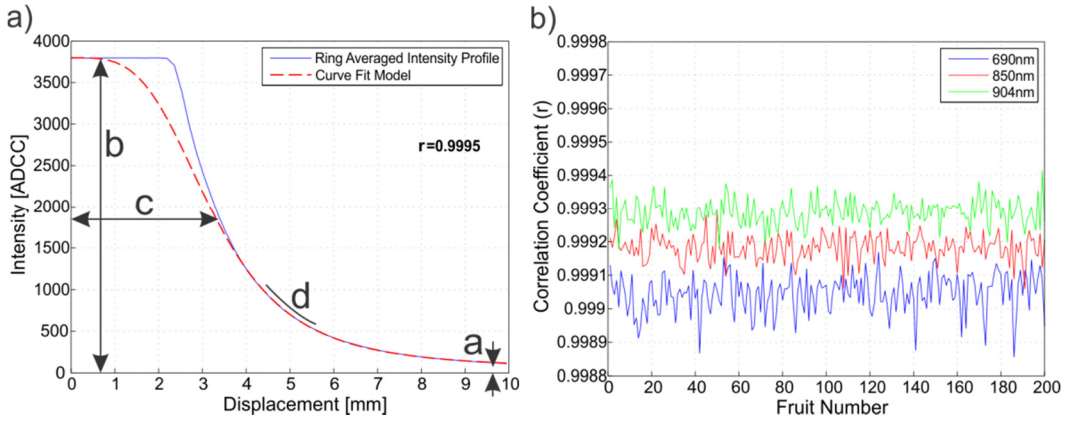

Figure 6-10. (a) Typical curve fit of the modified Lorentzian function to a saturated laser intensity profile. The four parameters of the model are shown next to the features they describe. (b) Shows the correlation coefficients for all 200 curve fits using the modified Lorentzian model.

Peng & Lu (2006b, 2006a) modified the original Lorentzian distribution function to include the 'd' term allowing them to better fit both the profile and the saturated region; the curve fits achieved in our study are consistent with their results. Figure 6-

10b shows the correlation coefficients found for the curve fits on all 200 fruit. An average correlation coefficient of 0.9990, 0.9992, and 0.9993 was found for the 685 nm, 850 nm, and 904 nm laser profiles respectively. This is consistent with the average correlation coefficient of 0.999 reported by Peng & Lu (2006b, 2006a).†

Modified Lorentzian Parameter Values

Figure 6-11 shows the four parameters from the modified Lorentzian curve fits for all 200 'Royal Gala' apples at the three laser wavelengths. Each data point corresponds to the average of two replicates in the first orientation only and is shaded from blue to red illustrating penetrometer firmness from soft to firm respectively. The grey regions in

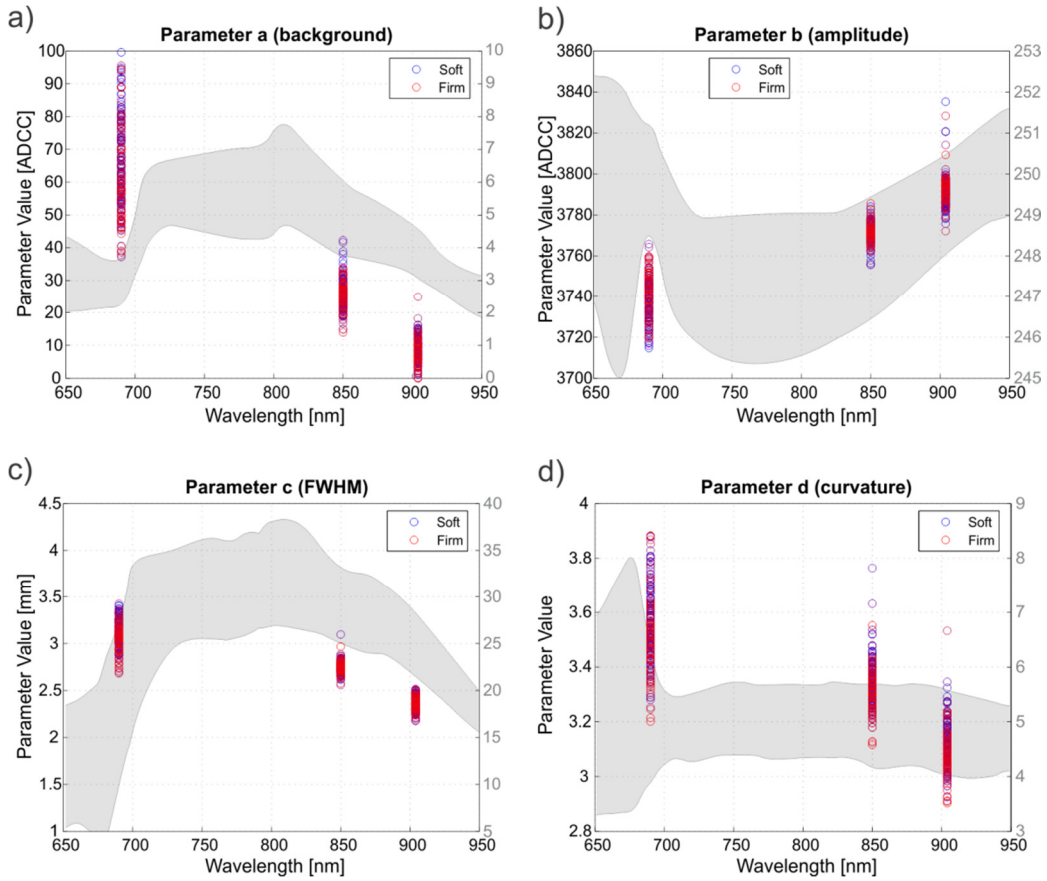

Figure 6-11. Modified Lorentzian parameters for the three laser intensity profiles on 200 'Royal Gala' apples. Grey shaded region shows modified Lorentzian parameters found on 'Red Delicious' apples in a study by Peng & Lu (2006a).

† Correlation coefficients are found by first calculating the coefficient of determination. Strictly speaking the correlation coefficient (R) in the context of non-linear modelling is a poor indicator of fit quality however it was used to contrast our fits with the results presented by Peng & Lu (2006b, 2006a).

each plot represent values extracted for 'Red Delicious' apples in the study carried out by Peng & Lu (2006b, 2006a). Data was extracted from each study using graph digitization software (Blue Leaf Software, 2012).

Figure 6-11a shows all of the extracted values for the 'a' parameter, which corresponds to the background signal or the asymptotic value that the extracted intensity profiles reach at large displacement values. This parameter depends on how effective the dark correction is and will be affected by the range over which data is fit. More variation was observed at 685 nm compared to the parameters found at 850 and 904 nm. This is likely a result of chlorophyll, an absorbing pigment found in apple skin and flesh. This increased variation is not observed in the results of Peng & Lu (2006b, 2006a) on 'Red Delicious' apples. Their results show similar levels of variation at all three wavelengths.

Figure 6-11b shows the 'b' parameter, this corresponds with the amplitude term of the intensity profile. This should always be near the saturation intensity of the camera because we are fitting the model to the flat top saturated intensity profiles. For our camera operating at 12 bits, this gives a maximum value of 4095. However, a dark image is used to correct for dark current giving us an intensity around 3800 analog to digital conversion counts (ADCC). This is consistent with the extracted 'b' parameter with values ranging from 3713 to 3835 ADCC. Peng & Lu (2006b, 2006a) used an 8bit camera which gives them an approximate saturation around 256 ADCC.

Figure 6-11c shows the 'c' parameter corresponding with the FWHM of each intensity profile. Peng & Lu (2007) found that this parameter tends to reflect the changes they visibly observed in their intensity profiles. Peng & Lu (2006b, 2006a) found that soft fruit typically had a higher FWHM compared to firm fruit. In the present study only the 'c' parameters at 685 nm showed a slight sign of soft fruit (blue) having higher FWHM values compared to firm fruit (red). The parameters at 850 and 904 nm show no visible separation. This small signal at 685 nm is consistent with chlorophyll absorption. Chlorophyll breaks down as fruit mature. This would decrease the absorption allowing light to propagate further, increasing the FWHM.

Figure 6-11d shows the 'd' parameter. This describes to the gradient in the FWHM region of the intensity profile (Peng & Lu, 2006a). If we compare our results to the 'Red Delicious' ones, we see that ours tend to trend downward with increasing wavelength whereas theirs remain relatively flat. Peng & Lu (2006b, 2006a) found that firm fruit

had higher 'd' parameters compared to soft fruit. No visible separation was observed in the present study.

There was consistently more variation in the parameters found at 685 nm compared to the other wavelengths. This wavelength was chosen because it corresponds with the chlorophyll absorption in the fruit. As fruit mature and soften chlorophyll tends to break down as part of a process parallel but not directly related to firmness. The fruit investigated was treated to have a large range in firmness and, therefore, is also likely to have a large range in chlorophyll content. This caused significant variation in the intensity profiles which transfers directly into the extracted modified Lorentzian parameters and is consistent with the results presented by Lu & Peng (2007).

Relationship with Fruit Firmness

Figure 6-12 and Figure 6-13 show the relationships between averaged (two replicates) raw extracted parameter values from the modified Lorentzian curve fits and average penetrometer or acoustic firmness respectively. Each figure corresponds to a single wavelength, 685 nm for the penetrometer firmness and 904 nm for the acoustic firmness, and the modified Lorentzian parameters are from the first orientation only. These were chosen because they showed the strongest relationships with their respective reference firmness measurement.

The data points in these plots are coloured based on treatment. For the penetrometer firmness based plots (Figure 6-12) there are visible groupings for each of the treatments. The treatments were designed to create a wide firmness range with air treated fruit filling the soft end of range and CA fruit filling the firm end. Acoustic firmness (Figure 6-13) does not show these groupings. This is consistent with the results shown in Figure 6-8a; acoustic firmness did not respond to the different treatments in the same way penetrometer firmness did.

The correlations coefficients between penetrometer firmness and the extracted modified Lorentzian parameters at 685 nm (Figure 6-12) are all weak ranging from 0.17 to 0.33. The strongest correlation with penetrometer firmness was found to be with the 'c' parameter (FWHM). This is consistent with the views expressed by Peng & Lu (2007) that this parameter best reflects the changes observed between fruit of different firmness. This, however, was not the case at other wavelengths. Table 6-1 summarises the linear regression results for all three lasers. At 850 nm and 904 nm there is no correlation between the 'a', 'b', or 'c' parameters and penetrometer firmness. There is,

however, a correlation of 0.19 (850 nm) and 0.22 (904 nm) for the 'd' parameter and penetrometer firmness. This indicates that the intensity profile shape at these wavelengths in relation to firmness change maybe better described by the 'd' parameter (slope) in the modified Lorentzian model.

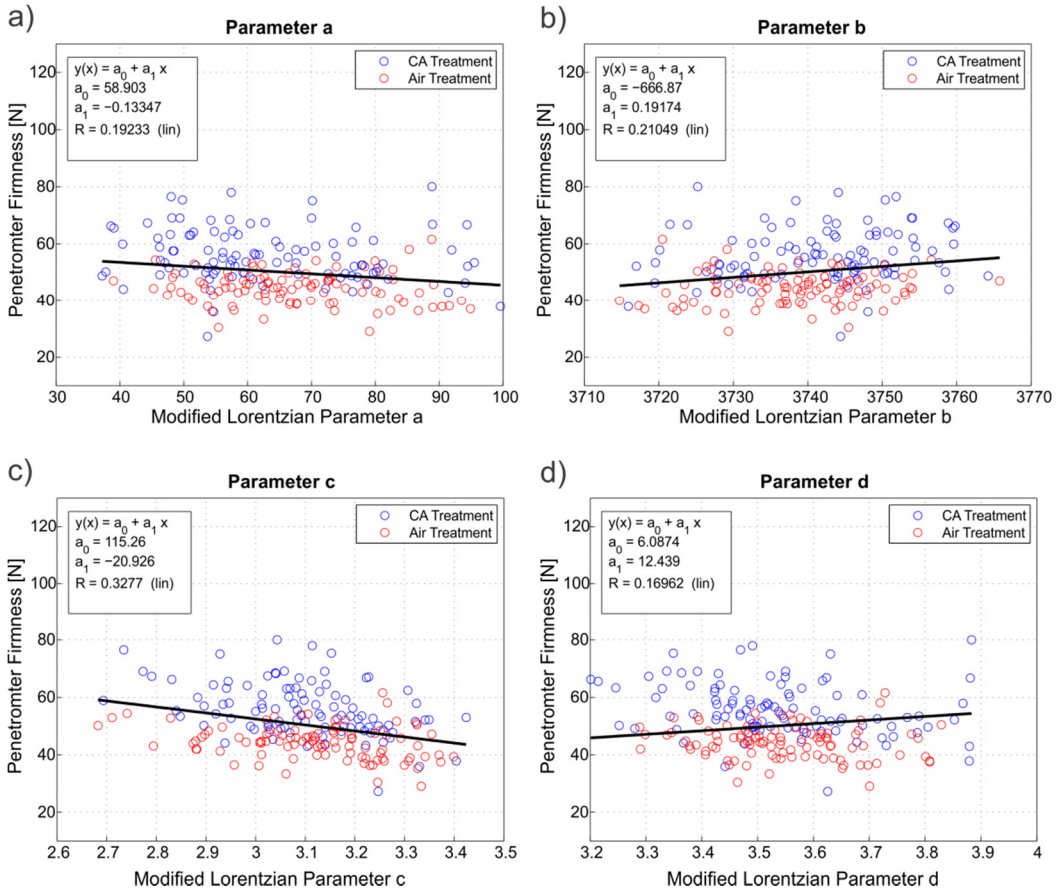

Figure 6-12. The relationships between modified Lorentzian parameters and penetrometer firmness at 685 nm.

Wavelength [nm]	Parameter	Correlation Coefficient	A0	A1
685	a	-0.19	58.90	-0.13
	b	0.21	-666.87	0.19
	c	-0.33	115.26	-20.93
	d	0.17	6.09	12.44
850	a	-0.05	53.20	-0.12
	b	0.006	1.15	0.013
	c	-0.006	52.58	-0.86
	d	-0.19	123.93	-22.11
904	a	0.08	51.93	-0.20
	b	0.05	-176.37	0.060
	c	-0.04	62.434	-5.16
	d	-0.22	126.13	-24.40

Table 6-1. Basic linear regression models for each of the modified Lorentzian parameters and penetrometer firmness. A0 and A1 represent the offset and gradient terms respectively in the model.

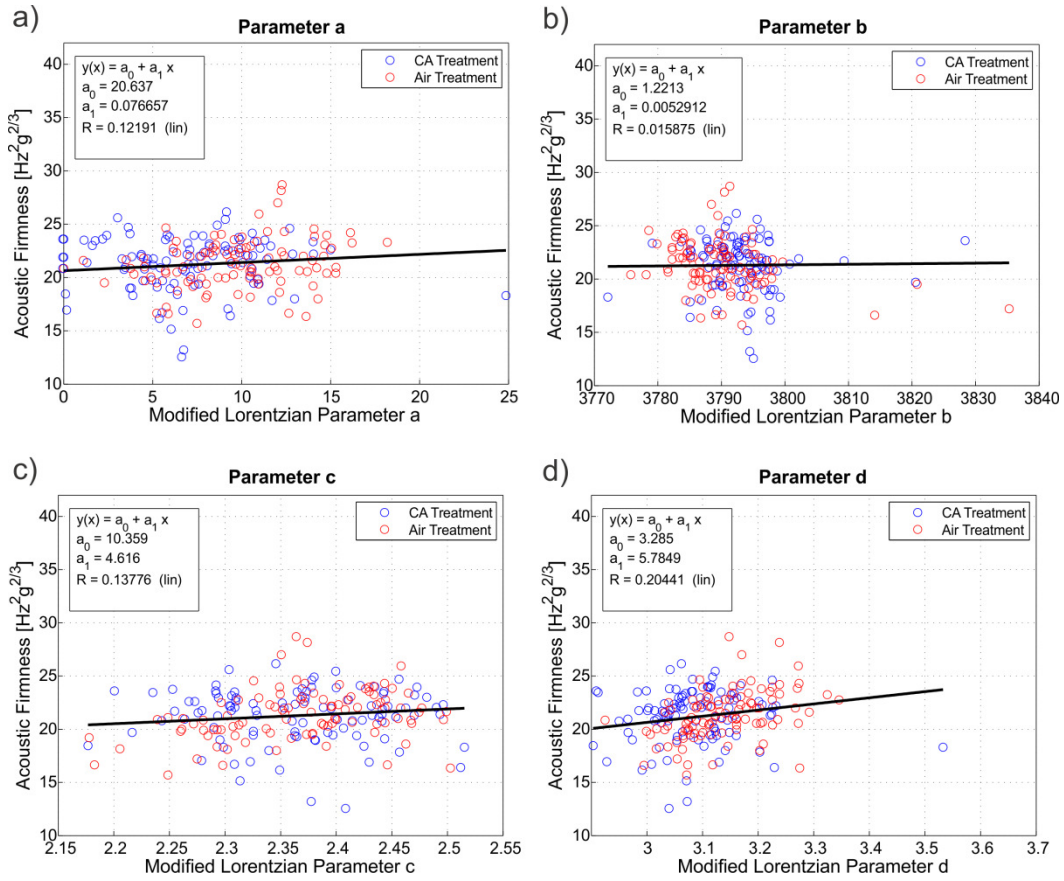

Figure 6-13. The relationship between the modified Lorentzian parameters and AWETA acoustic firmness at 904 nm.

The best correlation found between the 'c' parameter and penetrometer firmness at 685 nm. This is consistent with changes induced in the intensity profiles due to the breakdown in chlorophyll as the fruit mature and soften. This causes a reduction in absorption and leads to an increase in the light levels that propagate inside the fruit and a corresponding increase in the full width half maximum value ('c' parameter). Several studies have used optical systems sensitive to this breakdown in chlorophyll to estimate the maturity of the fruit and other quality characteristics including firmness (Tu et al., 1995, 2006; Duprat et al., 1995; Belie et al., 1999).

The relationships between acoustic firmness and the extracted parameters from the modified Lorentzian function showed even lower correlations than those found with the penetrometer (Table 6-2). Correlations ranged from 0.016 to 0.20 across the different parameters and wavelengths. The highest correlation coefficient of 0.2 was found at 904 nm between the 'd' (profile slope) parameter and acoustic firmness (Figure 6-13d). A correlation at this wavelength is consistent with the acoustic firmness measurement's high sensitivity to water loss (Landahl, 2007; Belie et al., 1999) and the location of the 904 nm laser on the shoulder of the 980 nm water absorption peak (McGlone et al.,

2007). As water evaporates, the absorption in this region would reduce affecting the shape of the intensity profile. The correlation here may have been weakened by our attempts to limit water loss through the humidification of both the air and controlled atmosphere treatments. This would have reduced the rate at which acoustic firmness changed (Belie et al., 1999; Johnson & Dover, 2005).

The correlation coefficient at 685 nm was very low (0.02-0.1). Belie et al. (1999) have shown that the laser backscatter area at (670 and 690 nm) increased as fruit soften so we might have expected the 'c' parameter or 'd' parameter to shows some signal here, however, this was not the case. This may have also been due again to the reduction of water loss, significantly lowering the range over which acoustic firmness decreased (Belie et al., 1999).

Wavelength [nm]	Parameter	Correlation Coefficient	A0	A1
685	a	0.02	21.01	0.0043
	b	0.02	1.22	0.0054
	c	-0.10	26.4	-1.65
	d	0.10	15.107	1.745
850	a	0.07	20.24	0.041
	b	0.01	1.21	0.0053
	c	-0.06	28.07	-2.47
	d	0.16	5.32	4.79
904	a	0.12	20.64	0.077
	b	0.016	1.22	0.0053
	c	0.14	10.36	4.616
	d	0.20	3.29	5.78

Table 6-2. Basic linear regression models for each of the modified Lorentzian parameters and acoustic firmness. A0 and A1 represent the offset and gradient terms respectively in the model.

Multiple Linear Regression Firmness Prediction

Figure 6-14 shows the results from the development of a multiple linear regression model. The model was built using a venetian blind cross-validation with 10 data folds and used all 12 extracted modified Lorentzian parameters (three wavelengths with four parameters at each). Figure 6-14a shows the results of the cross validation, the correlation coefficient for the model was 0.42, and the RMSECV was 8.79 N. Other combinations of parameters were investigated including removing the 'a' (background), and 'b' (amplitude) parameters, however, no improvement was found.

The regression model found compares poorly to those in the literature. Peng & Lu (2006a) used their liquid crystal tunable multispectral imaging system to extract out modified Lorentzian parameters. They found, using single wavelength models (810 and 690 nm), correlations of 0.58 and 0.50, and standard errors of 8.81 N and

8.64 N for 'Red Delicious' and 'Golden Delicious' apples respectively. When they combined seven wavelengths (total of 28 parameters) they got a correlation of 0.82 and a standard error of validation equal to 6.64 N for 'Red Delicious' apples and similar results for 'Golden Delicious' apples. Their wavelength selection included similar wavelengths such as 690, 820, 910 nm. There were, however, differences in wavelength selection between the two cultivars. This may indicate that the wavelengths selected for the high-speed system based on Peng & Lu's (2006a) results, as well as other studies, may not transfer over to the 'Royal Gala' variety.

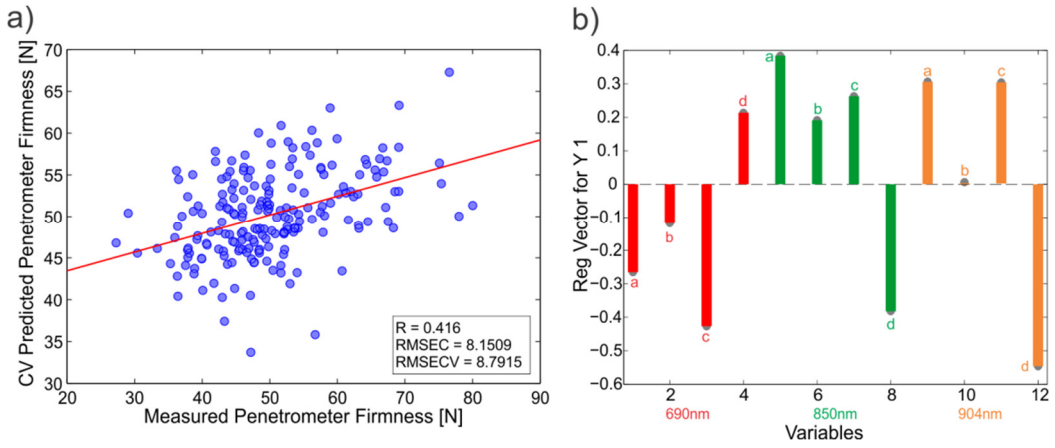

Figure 6-14. (a) Multiple linear regression model for penetrometer firmness using venetian blind cross validation with 10 data splits. (b) Loadings for the different modified Lorentzian parameters.

Figure 6-14b shows the loadings for the multiple linear regression model used to predict penetrometer firmness. There are no clear modified Lorentzian parameters that stand out. This makes sense considering there were no strong correlations found between penetrometer firmness and the individual parameters (Figure 6-12). Table 6-3 summarizes the results from the MLR models both for predicting penetrometer firmness and acoustic firmness. The MLR model for acoustic firmness had a correlation coefficient of only 0.19. This is consistent with the poor correlations between individual modified Lorentzian parameters and acoustic firmness, and indicates that even by combining all of the parameters no suitable prediction model was possible.

Reference Measurement	Correlation Coefficient (R)	Calibration Error (RMSEC)	Cross Validation Error (RMSECV)
Penetrometer Firmness	0.42	8.15 N	8.79 N
Acoustic Firmness	0.19	2.25 $Hz^2g^{2/3}$	2.46 $Hz^2g^{2/3}$

Table 6-3. Results from MLR using all 12 modified Lorentzian parameters.

6.3.4.2 Optical Property Extraction

The second approach investigated in this study was to extract the optical properties from the intensity profiles. This was done in a similar way to the modified Lorentzian parameters by fitting a diffusion theory model (Chapter 3) to the intensity profiles which directly provides the absorption and reduced scattering coefficients. Figure 6-15 shows a typical fit of the diffusion theory model to an intensity profile. The diffusion theory model was not designed to handle saturated regions as was the case of the modified Lorentzian model, so this time the fit was limited from the intensity point closest to 3500 ADC counts out to a distance of 15mm. This upper intensity point was chosen to exclude saturated intensity values (~3800 ADC counts), and the range was consistent with those used in other studies which provided curves that the diffusion model fit well to (Huang et al., 2012; Qin et al., 2007; Qin & Lu, 2008).

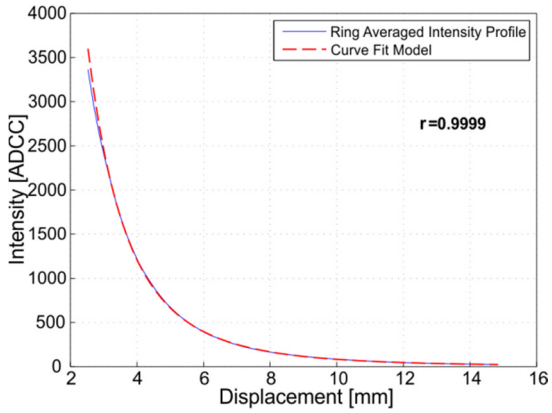

Figure 6-15. Example of a typical intensity profile with the diffusion model fitted to it.

Extracted Optical Properties

Figure 6-16 shows the absorption and reduced scattering coefficients for all 200 'Royal Gala' apples at each of the three laser wavelengths. Each coefficient plotted is the average of the two replicates with fruit in the first orientation, and is coloured from blue to red illustrating penetrometer firmness (soft to firm). The shaded regions illustrate absorption and reduced scattering coefficients from three earlier studies. The first by Qin et al. (2007) on 'Golden Delicious' apples is shown in gray, the second by Cen, Lu & Mendoza (2011) on 'Golden Delicious' and 'Red Delicious' apples is shown in red, and third is a study again on 'Golden Delicious' apples by Cen et al. (2013) shown in blue.

The absorption coefficients extracted from high-speed images (Figure 6-16a) show a trend upwards as wavelength increases. This is consistent with the results found in the other studies on 'Red Delicious' and 'Golden Delicious' apples. However, the

absorption coefficients at 685 nm appear to be lower than what was measured for those studies. About 50% of the points fall within the bounds of the study carried out by Qin et al. (2007), the other half fall outside of the bounds of that study and the others. Cubeddu et al. (2000) found in their study, at 658 nm, absorption coefficients that were more similar to the ones found in this study. Their system was based on time resolved reflectance spectroscopy (TRS) and measured absorption coefficients ranging from 0.003 to 0.007 mm^{-1}, 0.004 to 0.015 mm^{-1}, and 0.005 to 0.012 mm^{-1} for 'Golden Delicious', 'Granny Smith' and 'Starking' apples respectively.

At 850 and 904 nm the majority of the extracted optical properties fall within the bounds of the published studies. The range covered by the absorption coefficients increases as wavelength increased. At 685 nm the absorption ranges from 0.0001 to 0.005 mm^{-1} compared to the 904 nm wavelength where absorption ranges from 0.005 to 0.058 mm^{-1}.

Figure 6-16b show the extracted reduced scattering coefficients. There is a general trend of decreasing scattering as wavelength increases consistent with the earlier studies (Cubeddu et al., 2001; Lu et al., 2009). The range of extracted scattering coefficient values appears similar to those of the grey band representing the 'Golden Delicious' data of Qin et al. (2007). These values are also in the same region of those obtained by Cubeddu et al. (2000) using their time-resolved reflectance spectroscopy system, ranging from 1.3 to 1.5 mm^{-1}, 0.7 to 1.2 mm^{-1}, and 1.4 to 2.0 mm^{-1} for 'Golden Delicious', 'Granny Smith' and 'Starking' apples respectively.

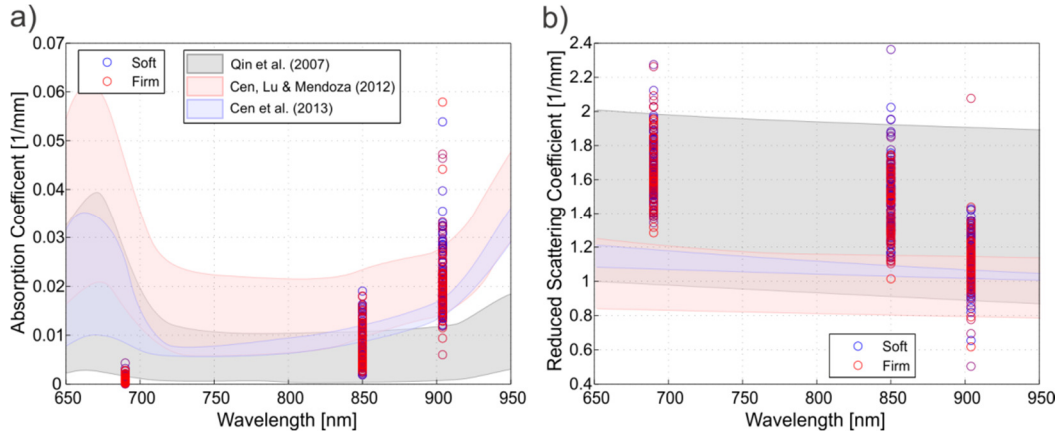

Figure 6-16. (a) Absorption and (b) reduced scattering coefficients of 'Royal Gala' apples plotted at each of the three wavelengths. Grey, red, and blue shaded regions represent data from Qin et al. (2007), Cen, Lu & Mendoza (2011), and Cen et al. (2013) respectively.

Relationship with Fruit Firmness

The plots shown in Figure 6-17 show the relationships between penetrometer firmness and the reduced scattering coefficient at the three wavelengths as measured using the high-speed system. The scattering properties are thought to be related to the textural characteristics of the fruit (Qin et al., 2007; Cen, Lu & Mendoza, 2011). From the results in Figure 6-17 there is no clear relationship between penetrometer firmness and the reduced scattering coefficient. The largest correlation was found at 850 nm but was weak with a correlation coefficient of only -0.11. This is not consistent with what others have reported. Qin & Lu (2006) found a correlation of -0.7 between penetrometer firmness and the reduced scattering coefficient for 'Golden Delicious' apples at 780 nm. They used a hyperspectral imaging system to capture intensity profiles and a diffusion model to extract out the optical properties. Rizzolo et al. (2010) found a correlation of -0.61 at 780 nm and -0.46 at 670 nm for 'Jonagored' apples. They utilized a TRS system for their measurements.

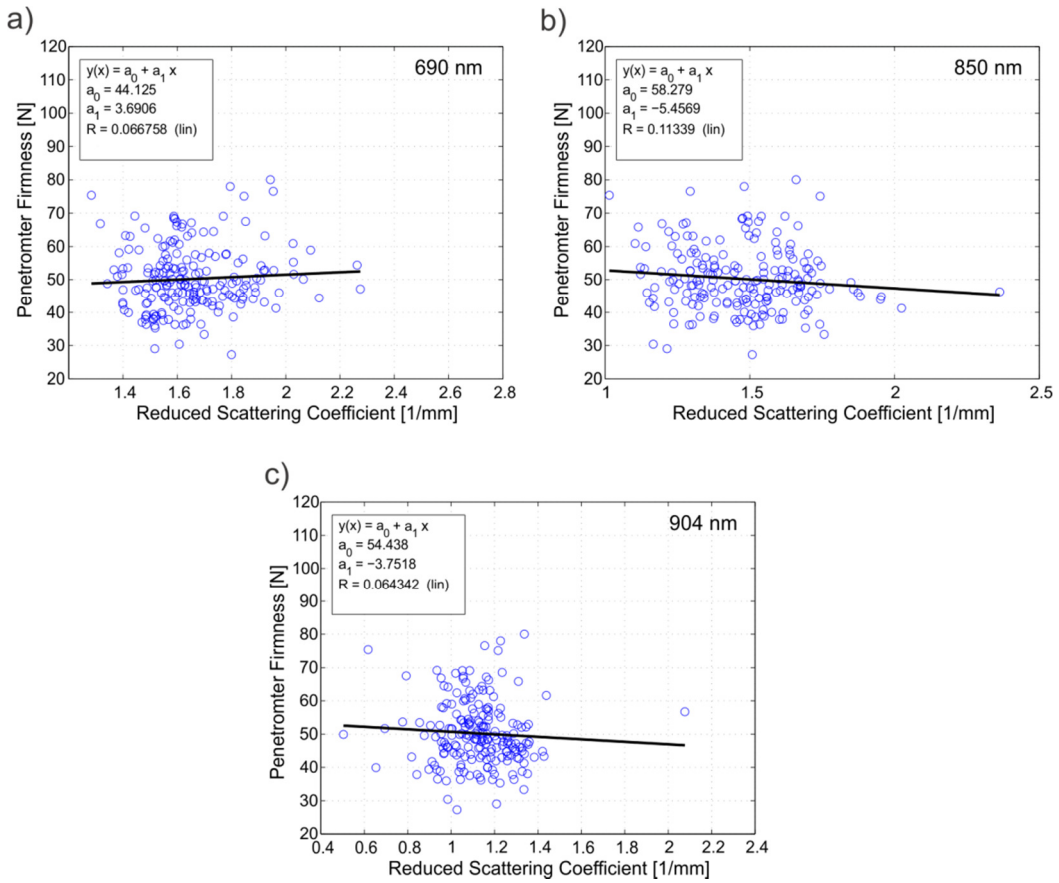

Figure 6-17. The relationship between the extracted reduced scattering coefficient and penetrometer firmness Absorption coefficients at (a) 685 nm, (b) 850 nm, and (c) 904 nm.

Table 6-4 shows the resulting relationships found between the reduced scattering coefficient and both penetrometer (Figure 6-17) and acoustic firmness. The acoustic firmness had a higher correlation with the reduced scattering coefficient at 685 nm compared to the penetrometer result, however, this was still low (R = 0.29). No other wavelengths showed signs of a significant relationship.

Table 6-5 shows a similar result for the relationships between the extracted absorption coefficient and penetrometer or acoustic firmness. Again correlations are all poor ranging with absolute values from 0.02 to 0.18. This is consistent with the hypothesis that absorption is not sensitive to textural information (Valero, 2004; Muhua et al., 2007). A correlation might be expected near the chlorophyll absorption peak (670 nm) which should reduce as fruit mature, however, this was not observed. One factor for this could be the very small absorption range (0.001 to 0.005 mm^{-1}) measured at 685 nm. Earlier studies on 'Red Delicious' and 'Golden Delicious' apples showed a much wider chlorophyll absorption range (Qin et al., 2007; Cen, Lu & Mendoza, 2011; Cen et al., 2013). This could indicate that the 'Royal Gala' cultivar has a weaker chlorophyll absorption signal, or that, as a parallel process it does not correspond to firmness in the same way.

The correlations are similar to those obtained by Rizzolo et al. (2010) who got weak correlation coefficients ranging from 0.03 to 0.25 between penetrometer and absorption at 630, 670, 750, and 780 nm using the time resolved reflectance spectroscopy method on 'Jonagored' apples. Vanoli et al. (2013) demonstrated significant differences between cultivars. For 'Braeburn' apples they found a correlation coefficient of 0.49 between penetrometer firmness and absorption at 690 nm. For 'Cripps Pink' apples at 630 nm they found a poor correlation of only -0.15.

Reference Measurement	Wavelength	Correlation Coefficient (R)	a_0	a_1
Penetrometer Firmness	685	0.07	44.1	3.7
	850	-0.11	58.3	-5.5
	904	-0.06	54.4	-3.8
Acoustic Firmness	685	0.29	14.5	4.1
	850	0.07	20.1	0.8
	904	0.13	19.1	2.0

Table 6-4. Correlation coefficients between the estimated reduced scattering coefficient and either penetrometer firmness or acoustic firmness.

Reference Measurement	Wavelength	Correlation Coefficient (R)	a_0	a_1
Penetrometer Firmness	685	0.04	49.6	612.4
	850	0.02	49.8	56.2
	904	-0.02	50.8	-25.6
Acoustic Firmness	685	-0.18	22.0	-732.3
	850	0.04	21.1	27.1
	904	-0.09	21.9	-27.9

Table 6-5. Correlation coefficients between the estimated absorption coefficient and either penetrometer firmness or acoustic firmness.

Multiple Linear Regression Firmness Prediction

Attempts were made to use the optical property data to generate multiple linear regression models which could predict penetrometer and acoustic firmness. No suitable models were found with all having low correlation coefficients and high prediction errors.

6.3.5 Discussion

Both the modified Lorentzian and diffusion theory models fit the data well. For the modified Lorentzian parameters there was consistently more variation in those extracted at 690 nm compared to the 850 and 904 nm wavelengths.

The optical properties extracted were within the range of those found in earlier studies on 'Golden Delicious' and 'Red Delicious' cultivars. However, relationships between optical properties and penetrometer or acoustic firmness were poor at all wavelengths.

Multiple linear regression models were constructed using both the modified Lorentzian parameters and optical properties. With the modified Lorentzian parameters a correlation of 0.42 was found. This was significantly lower than even the single parameter models found by Peng & Lu (2006a). Using the extracted optical properties for the MLR model saw even poorer results with correlation coefficients below 0.1.

This is the first study utilising the modified Lorentzian and diffusion theory techniques with the 'Royal Gala' apple cultivar to predict fruit firmness. Some studies have demonstrated that there can be significant differences between apple cultivars. Mendoza et al. (2011), for example, used their optical feature extraction approach and got stronger correlations for their firmness predictions on 'Jonagold' apples compared to 'Red Delicious' apples (R = 0.95 and 0.835 respectively). Peng & R Lu (2006b), on the

other hand, showed very similar performance for their prediction models on 'Golden Delicious' and 'Red Delicious' apples (R = 0.82 and 0.81 respectively).

Earlier studies have also demonstrated that specific wavelengths are important for predicting firmness (Figure 2, Chapter 5). The design of the high-speed system was based around studies on mostly 'Golden Delicious' and 'Red Delicious' apples. These specific wavelengths may not be suitable for the 'Royal Gala' cultivar.

The physical arrangement of the system may also be a contributing factor to the poor correlations. The oblique incident angle of each laser means that depending on fruit size, the measurements occur in different positions. The measurements on a single fruit are also not simultaneous occurring over a series of three consecutive frames. This means that if fruit wobble or move as they are transported down the conveyor the system could effectively measure different portions of each fruit. This would have a detrimental effect on the performance of the MLR modelling, which may rely on measurements from the same portion of the fruit for accurate results.

The firmness range used in this study was similar to those found in other studies ranging from 27.3 N to 80 N (penetrometer), however, two independent treatments were necessary to achieve this range. It is possible the different treatments are a confounding factor (through noise introduced by secondary correlations) for optical firmness measurement. A more effective single treatment which can achieve a similar range may be more suitable for this type of study.

One factor not investigated in this study is the use of correction schemes for fruit shape. These have been applied in other studies to improve the correlation between firmness and optical measurements. For example, by correcting for erroneous pixels and fruit shape Peng & Lu (2006c) improved their correlation between measured and predicted firmness. Correlations increased from 0.837 to 0.905 and standard error reduced from 8.27 to 6.38 N. While these corrections are effective the results obtained before corrections are still much higher than anything observed from our high-speed data. These results suggest investigating the performance of the measurement in a more controlled manner is necessary before returning to high-speed measurements. (Cen et al., 2010)

6.4. Conclusion

In this study a high-speed multispectral imaging system was used to gather images of 'Royal Gala' apples illuminated at 685, 850, and 904 nm by point sources. From these images intensity profiles were extracted and parameterised using a modified Lorentzian and diffusion theory models. The relationship between these parameters and acoustic or penetrometer firmness was investigated.

The extracted modified Lorentzian parameters were consistent with earlier studies. In all cases, the 685 nm parameters were more variable than at other wavelengths, indicating that chlorophyll is probably more variable in the fruit used in this study. The optical properties extracted by the diffusion theory model were also consistent with studies on other apple cultivars with absorption coefficients between 0.001 and 0.06 mm^{-1} and scattering coefficients between 0.45 and 2.4 mm^{-1}. While the absorption coefficient is consistent with other studies it is at the low end.

The strongest relationship between penetrometer firmness and a modified Lorentzian parameter was found at 685 nm. Here, a correlation of 0.33 was found between the full-width at half-maximum parameter (c) and penetrometer firmness. This was attributed to the relationship between chlorophyll concentration, fruit maturity and firmness. Acoustic firmness did not correlate well with the measurements at 685 nm. Instead, the best correlation (R = 0.2) was found with the profile slope at 904 nm. Acoustic firmness has been linked to water concentration in the fruit, so this effect might be attributed to the influence of water absorption at 980 nm.

Multiple linear regression models were developed using the modified Lorentzian parameters and the optical properties. The model found using the modified Lorentzian parameters had a correlation coefficient of 0.42 and a standard error of 8.79 N. This was very low compared to other studies. No suitable models were found using the optical properties derived from fitting the diffusion model to the spatial profiles.

These results suggest either an absence of useful optical indicators for firmness in Royal Gala fruit or problems in the measurement system. Further investigation will focus on wavelength selection related to specific cultivars, correctly registered fruit so that consecutive measurements interrogate the same sample areas, a single fruit treatment removing uncertainty due to storage conditions, and the use of fruit shape corrections.

7. Static System; Design and components.

In Chapter 6, the high-speed multispectral imaging system was used make measurements on 'Royal Gala' apples with unsatisfactory results. In this chapter, a set of refinements to the multispectral imaging system is discussed that transitioned it from the high-speed system seen in Chapter 5 to a more controlled static system. With a controlled static system there should be greater confidence in the measurements, which can help identify issues that need to be addressed before the system can operate effectively at high speed. Also discussed is the design of an inverse adding-doubling system which provided an independent measurement of a samples optical properties, and the design of a fruit slicing guillotine which can cut parallel faced slices of fruit, critical to the inverse adding-doubling technique and the multispectral measurements carried out in Chapter 9.

7.1. Static Multispectral Imaging System

A number of changes to the multispectral system were required to transition it from the high-speed arrangement described in Chapter 6 to a system where each fruit is static and precisely located. In the new arrangement, the original concept of multiple fruit per frame was abandoned. Now, a single fruit only is centrally located in each image, and all lasers are aimed at the centre of this sample (Figure 7-1). This simplifies the location control required and allows measurements to be made at higher spatial resolutions (decreased mm/pixel). One consequence of the co-incident lasers is that a single image can no longer capture all wavelengths at once. Because of this, a shutter system was developed providing a robust and simple method for enabling and disabling illumination from each laser independently.

Other refinements to the illumination system include the addition of a fourth laser, the removal of an issue caused by laser polarisation, and improvements to temperature control for each laser module. Outside of the illumination system, a laser displacement sensor and three axis translation stage were added to precisely locate the fruit sample relative to the camera, a new camera lens was added for closer views of each fruit, and new software was developed.

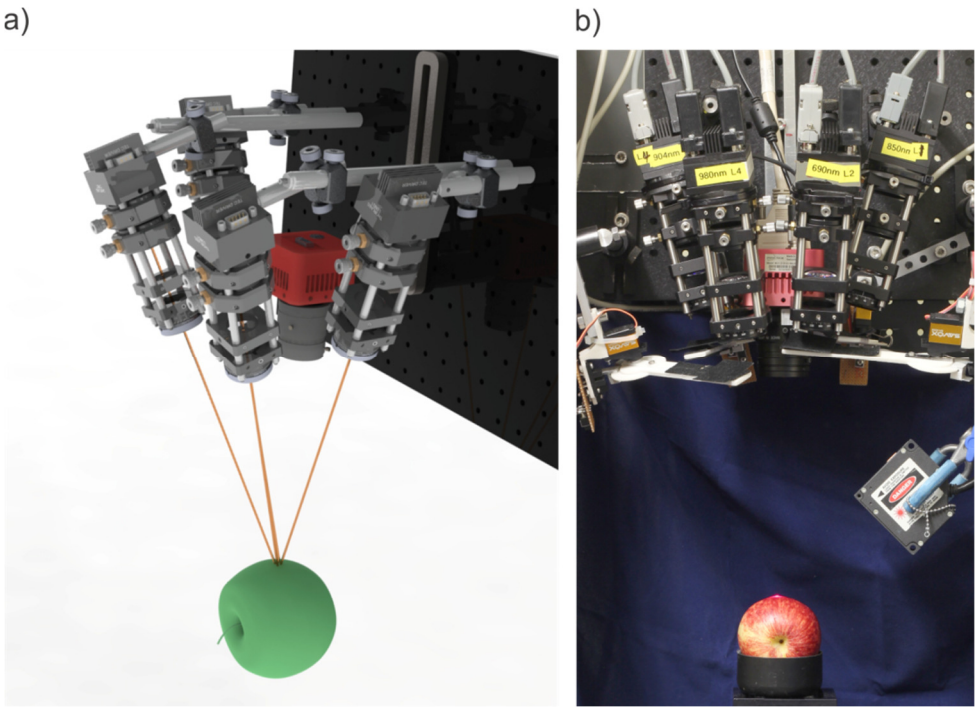

Figure 7-1. (a) Computer aided design model (CAD) of the static multispectral imaging system. (b) Actual implementation of the static system configured with four lasers each with electronically controlled shutters.

7.1.1 Laser Refinements

7.1.1.1 Additional Laser

The high-speed multispectral imaging system contained three discrete lasers operating at 685, 850, and 904 nm. Each of these lasers was chosen for a particular purpose. The 685 nm laser interrogates chlorophyll content within the fruit. The 850 nm laser allowed light to deeply penetrate into the apple sample due to low absorption in this region, and the 904 nm laser has been shown by other researchers to be useful for predicting firmness and soluble solids content in apples. The physical configuration of the static multispectral imaging system allowed for an additional laser which would provide extra information. The laser chosen operated at 980 nm (Table 7-1), corresponding to a water absorption peak. While water content is not directly responsible for fruit softening, a measurement of absorption in this region may offer complementary information about the softening process. This wavelength was included in firmness prediction models by various researchers (Qin et al., 2007; Peirs et al., 2005; Wang et al., 2012). Figure 7-1a illustrates the new arrangement of four lasers using a computer aided design (CAD) model and Figure 7-1b shows the actual implementation of this system including the new laser shutters and the displacement sensor.

Supplier Part Name	Wavelength	Power	Package	Supplier	Measured Wavelength	Incident Angle
HL6750MG	685 nm	50 mW	5.6 mm	Thorlabs	690 nm	19°
L850P030	850 nm	30 mW	5.6 mm	Thorlabs	852 nm	17°
L904P030	904 nm	30 mW	5.6 mm	Thorlabs	898 nm	18°
L980P100	980 nm	100 mW	5.6 mm	Thorlabs	980 nm	19°

Table 7-1. Laser diodes used in the static multispectral imaging system.

7.1.1.2 Polarisation Issue

An issue was identified while imaging low concentration Intralipid® (Fresenius Kabi, Bad Homburg, Germany) solutions which were used as optical phantoms for setup and validation of the optical systems (Chapter 8). Intralipid is a fatty emulsion commonly used as a component in optical phantoms, liquids which are used to simulate the light scattering and absorption properties of biological tissues. Figure 7-2 demonstrates this problem using the 685 nm laser to illuminate 0.5, 1.0, 1.5, and 2.0% Intralipid solutions. We expect that the backscattered light should be radially symmetric, but at 0.5% Intralipid this is not the case. It is also interesting that as Intralipid concentration increased, which corresponds to an increase in the reduced scattering coefficient, the diffuse backscattered light becomes symmetric.

The asymmetry present in the images is a significant problem because the radial averaging technique used to extract the intensity profiles relies on the laser image being symmetric. The problem was investigated, and the laser diode polarisation was found to be the cause. Laser diodes are typically considered linearly polarised with polarisation ratios from 50:1 to 100:1 (Sun, 2012). This scattering asymmetry occurs because Mie scattering is dependent on the polarisation of the light. This polarisation affects the scattering phase function, which defines the angular distribution of light intensity scattered by a particle. For linearly polarised light, this phase function becomes asymmetric (Ramella-Roman et al., 2005). This results in the asymmetric

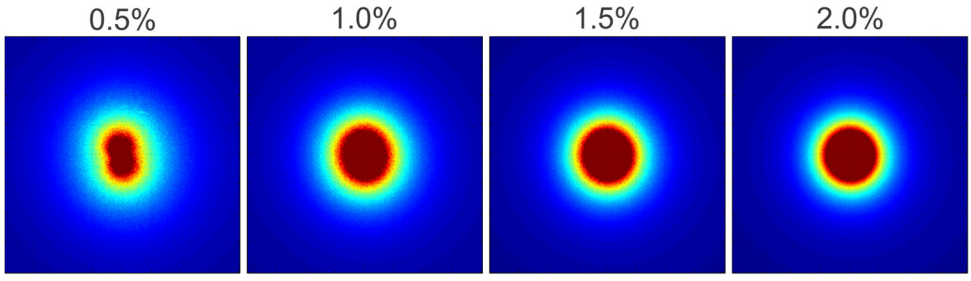

Figure 7-2. Laser images from the 685 nm laser illuminating Intralipid solutions of increasing concentration.

pattern in the backscattered light seen in Figure 7-2. As light scatters this linear polarisation state diminishes. In highly scattering samples this happens quickly which is why the higher Intralipid concentrations mask the effect.

To remove this asymmetry, a quarter wave-plate was installed on each laser assembly to convert the linearly polarised laser light to circularly polarised light (Figure 7-3). A quarter wave plate is a piece of birefringent material that has a slow and fast axis. This means that each axis (x and y) has a different refractive index and therefore light travels at a different speed in each axis. If the incident linear polarisation is oriented at a 45° angle, there is a component in both the slow and fast axis directions (Figure 7-3). These components will travel at different speeds within the material. A quarter wave plate is carefully designed for a certain wavelength to introduce a quarter of a wavelength delay in the slow axis. The resulting waveform that emerges from the quarter wave plate is now circularly polarised. This effectively removes the directionality of the polarisation.

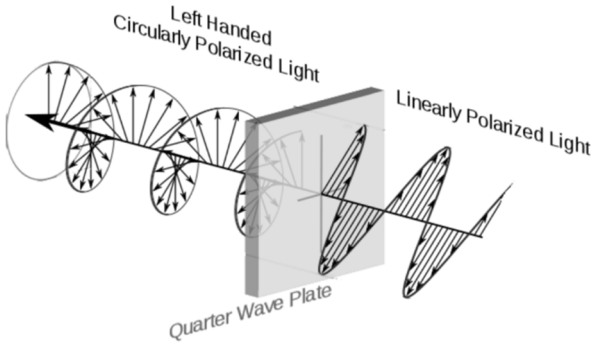

Figure 7-3. Principle of a quarter wave plate used to remove the strong linear polarisation seen in laser diodes (Mainzatnight, 2011).

Figure 7-4 shows the result of a quarter wave plate installed on the 685 nm laser used to illuminate a 0.5% Intralipid sample. Above each image is the angle of the quarter wave plate relative to the linear polarisation direction of the laser. At 0° the light simply passes through the quarter wave plate unaffected. At 10°, 20°, and 30° the light is elliptically polarised and so a portion of the asymmetry remains. At 45° the light leaving the quarter wave plate is circularly polarised, and the asymmetry is eliminated. Table 7-2 shows the quarter wave plates selected for circularly polarising each of the four lasers in the multispectral imaging system. In some situations, an exact quarter wave-plate was not available, so the closest one was selected (850 and 904 nm lasers). This lead to a slight reduction in the retardation of the light, the worst case was at 904 nm (830 nm quarter wave-plate) where the retardation reduced to 0.23 rather than

the ideal 0.25 expected from quarter wave-plates. This meant that the output light will not be perfectly circularly polarised however it was sufficient to minimize the asymmetry.

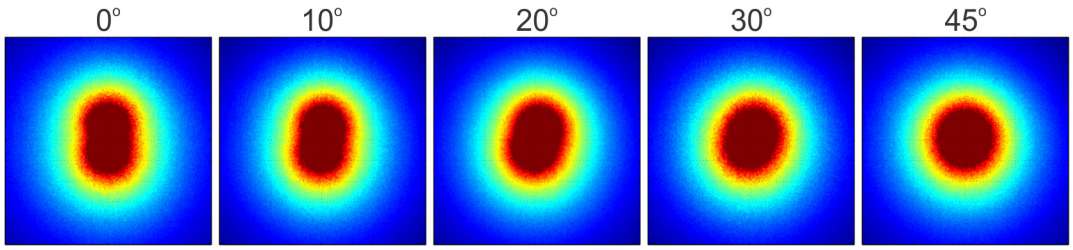

Figure 7-4. Circular polariser applied to the 685 nm laser illuminating a 0.5% Intralipid solution (low reduced scattering coefficient). The quarter wave plate angle is shown above each image.

Manufacturer and Part Name	Quarter Wave Plate Design Wavelength	Laser Wavelength
Thorlabs WPQ05M-670	670 nm	685 nm
Thorlabs WPQ05M-830	830 nm	850 nm
Thorlabs WPQ05M-830	830 nm	904 nm
Thorlabs WPQ05M-980	980 nm	980 nm

Table 7-2. Quarter wave plates used to circularly polarise each diode laser.

7.1.1.3 Temperature Control

In the high-speed multispectral imaging system lasers were configured with a target set point of 15°C to prolong laser life and maximize stability. Further investigation into the temperature controller indicated that this was an inappropriate setting because the on-board thermoelectric cooling unit was not powerful enough to cool to this low set point. For the static multispectral imaging system, all lasers were adjusted to run with a temperature set point of 25°C. This was within the correct operating range for the thermoelectric cooling units and should help maintain stability of the laser units. Table 7-3 reiterates the lasers used and their individual settings now including the new 980 nm laser.

Manufacturer and Part Name	Wavelength	Laser Current [mA]	Temperature Set Point [°C]
Thorlabs HL6750MG	685 nm	116.2 (120 max)	25
Thorlabs L850P030	850 nm	89.5 (95 max)	25
Thorlabs L904P030	904 nm	139.9 (150 max)	25
Thorlabs L980P100	980 nm	199.2 (300 max)	25

Table 7-3. Improved temperature settings for the laser units.

7.1.2 Camera Lens

Each frame of the static multispectral imaging system will contain a single fruit. To utilize more of the pixels in the sensor on each fruit and to allow for fruit to be

positioned closer to the camera a new lens was required. A Navitar 12.5 mm lens (NMV-25M1, Navitar, Rochester, New York) was selected to replace the original 25 mm Goyo lens. With this new lens, the fruit was positioned 160 mm from the camera increasing the spatial resolution to 0.057 mm/pixel (at 160 mm). This is more than 2.6 times the spatial resolution of the high-speed system. With this new lens, the field of view reduces from 251.5 mm to about 67 mm. The background lighting filter was not installed on this lens because the static system was operated in a dark room.

7.1.3 Electronically Controlled Shutter System

In the high-speed multispectral imaging system each frame contained three fruit and each fruit was illuminated by a single laser. This provided a simple approach for gathering a set of multispectral images. A new approach was required for the static system to enable and disable the illumination from each laser independently. A set of electronically controlled mechanical shutters were developed. The system has two main components: the shutter itself and the controller box.

Figure 7-5a shows a CAD model of the mechanical shutter. It consists of a 3D printed arm (green), an electronic servo (black, SH-0256, Savox, Utah, USA), end stop locators (yellow), opto-interrupts (pink, ZD1901, Jaycar Electronics, NSW, Australia), and a 3D printed mechanical mount (blue). Figure 7-5b shows the actual implementation. The 3D printed parts and the metal end-stops were designed and constructed in house at Plant and Food Research. Because the 3D printer uses a white powder that is highly scattering and not completely opaque a piece of black felt was attached to the end of each 3D printed arm. This prevented any light from scattering back and reaching the sample. Also, a piece of electronics prototyping board (veroboard) was attached to the back of each mechanical mount. This provided a common interface for all the electronic components.

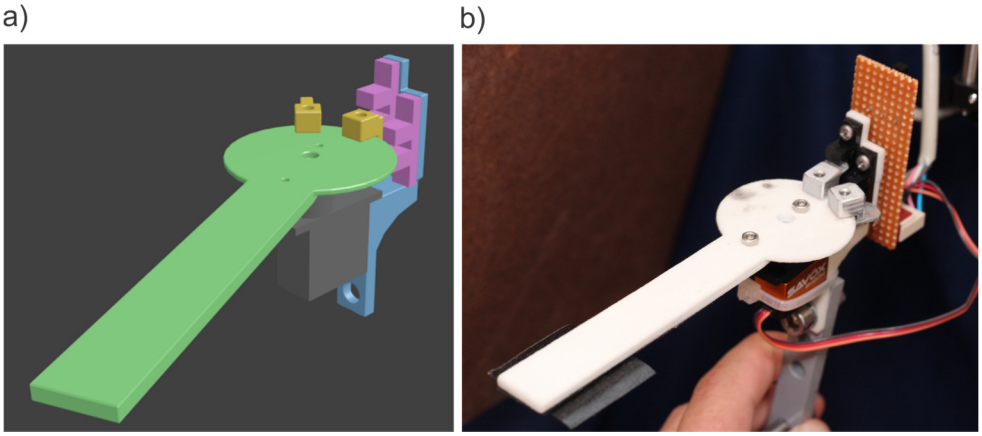

Figure 7-5. (a) CAD model and (b) the actual implemented shutter used to individually enable and disable the illumination from each laser.

Figure 7-6 shows the main controller box which houses the Arduino Mega microcontroller (blue PCB). The Arduino Mega runs custom embedded software written in C++ that controls the servo shutter system interfacing between the computer and each of the separate servos (channel 1 to 4). A copy of the software code can be found in Appendix 2.

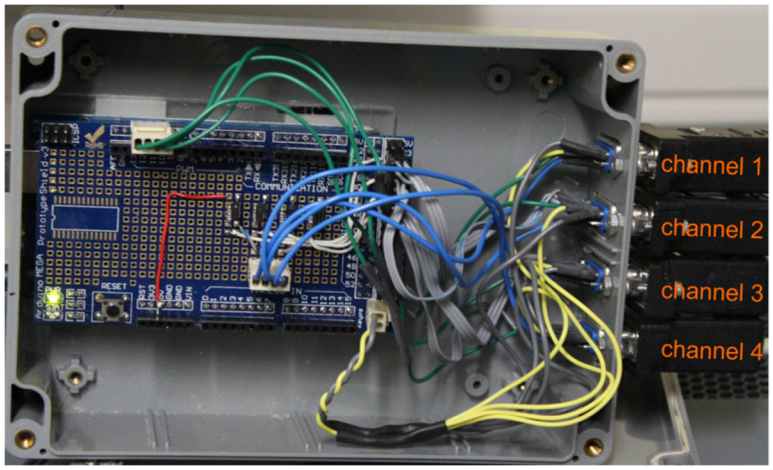

Figure 7-6. Custom shutter controller based on an Arduino microcontroller.

Each of the channel connectors shown in Figure 7-6 connects to a separate shutter. Figure 7-7a shows the circuit schematic for each of the four shutter channels and Figure 7-7b shows the veroboard PCB mounted on each of the shutters that provides an electronic backplane for all of the components to connect to. The main switch on each shutter controls the direction at which the servo moves to open or close the shutter (either clockwise or anti-clockwise). This is important because servos mounted on the right side of the camera need to move clockwise and servos on the left side need to move anti-clockwise.

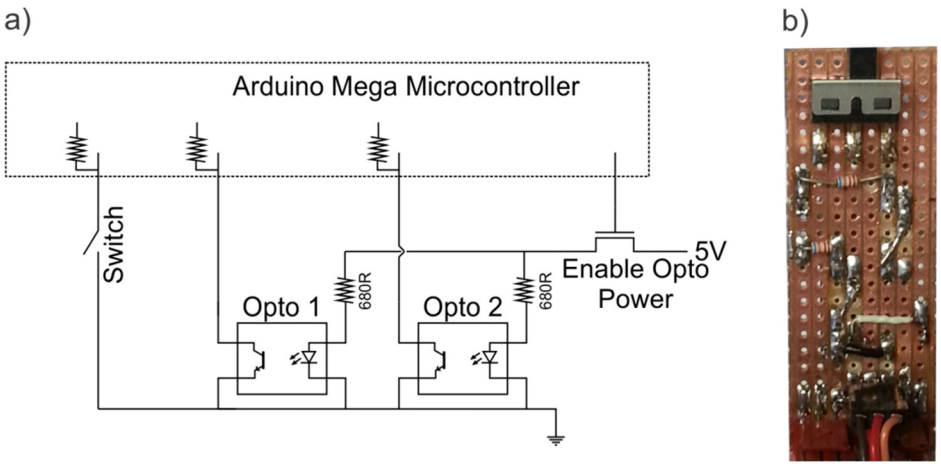

Figure 7-7. (a) Shutter controller circuit diagram. This is replicated for each servo channel (four, one for each laser). (b) Veroboard circuit attached to the back of each servo controller providing an electronic interface.

Each servo also features two opto-interrupters. These are sensors that transmit light from a LED to a phototransistor. When a mechanical end-stop blocks this transmission their output signal switches. The first opto-interrupter is always used to indicate the closed position. This means that when the controller is told to close the shutter, the servo is moved in to the closed position and the opto-interrupter is checked to confirm this move happened. The second opto-interrupter works in a similar fashion but this time confirms if the shutter is open. The final piece of circuitry is a simple p-channel MOSFET to control power to the opto-interrupt's LEDs. This allows the microcontroller to enable the opto-interrupter's LEDs only where they are needed, preventing any stray light from reaching the camera.

7.1.4 Fruit Location Control

A major limitation, while making measurements with the high-speed multispectral imaging system, was that each fruit had a different size and therefore different distance from the illuminated surface to the camera. This required a separate measurement system and a model to define the spatial resolution (mm/pixel) used on each fruit. For the static system more precise control was required so that only a single spatial resolution measurement was needed eliminating a further variable from the measurements. The new system included a translation stage on which the fruit is mounted that allows translation in three dimensions (x, y, and z). A laser displacement sensor accurately locates the top surface of the fruit so that it is always a fixed distance away from the camera lens.

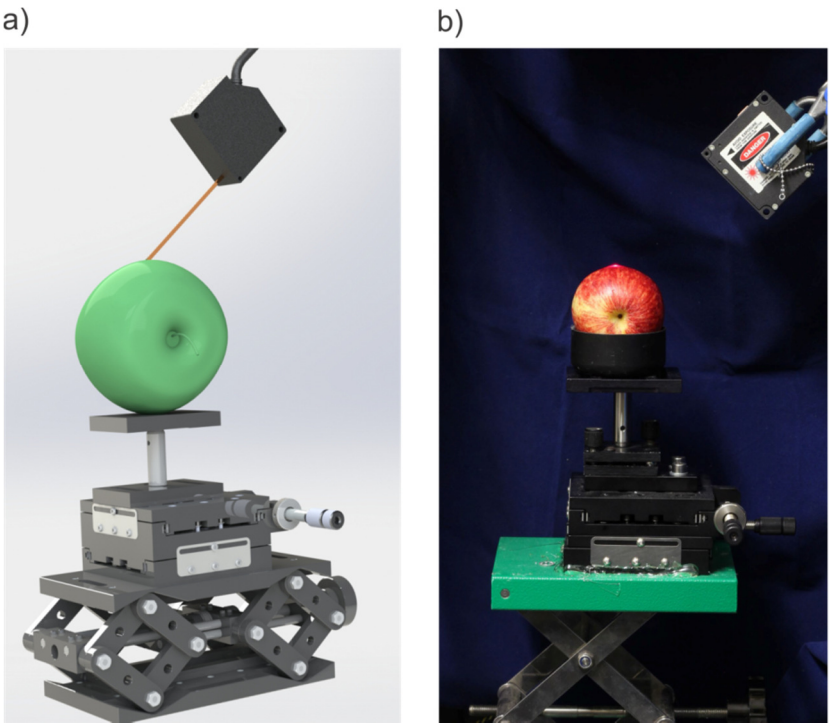

Figure 7-8. (a) CAD model, and (b) the actual implementation of the fruit location system.

Figure 7-8 shows the CAD model and the actual implementation of the fruit location system. The translation stage component consisted of a scissor lab jack (11020, Bochem, Hesse, Germany) for vertical adjustment (z axis) and two linear translation stages (LT1, Thorlabs, New Jersey, USA**)** for adjustment in the x and y axis.

The laser displacement sensor (LB081, Keyance, Osaka, Japan) was mounted approximately 80 mm from the fruit with an incident angle of 45° (Figure 7-8b). This location was selected because the Keyance sensor operates only in a 30 mm region, centred 80 mm from the end of the sensor unit. The readout from the Keyance sensor was configured to display a displacement of 0 mm when the object was at the correct working distance from the lens (160 mm). Each subsequent sample was then placed, and the translation stages adjusted until the sensor again reads 0 mm. To avoid any

Manufacturer and Part Name	Description
Bochem 11020	Scissor Labjack
Thorlabs LT1	Linear translation stage
Keyance RV3-55R	Laser displacement sensor controller unit
Keyance LB1101	Laser displacement sensor amplifier unit
Keyance LB081	Laser displacement sensor head with 8 µm accuracy

Table 7-4. Major components of the fruit location system.

issues with stray light caused by the Keyance laser, which operates at 670 nm, the system is automatically disabled during image collection. Table 7-4 lists the main components used in the final fruit location system.

7.1.5 Software

The software used for the high-speed multispectral imaging system was no longer suitable for use with the static system. Originally images were collected based on a hardware trigger and no shutter system was required. Measurements with the static system require a sequential set of instructions to open and close each shutter, as well as to provide a software trigger to the original acquisition software (Chapter 5) to capture a set of images. For this reason, a Matlab script was created to carry out an experimental run. The script is run from a simple Matlab graphical user interface (GUI) which allows the operator to enter a fruit number and the current orientation of the fruit. These are used to name the image files.

Figure 7-9 illustrates the measurement process the script uses. It first enables the displacement sensor and prompts the operator to load the fruit sample into the holder and adjust the height based on the laser displacement sensor. Once the operator confirms the fruit has been positioned correctly, the laser displacement sensor is disabled and the system begins collecting images. One-by-one each of the laser outputs is enabled by opening the corresponding shutter, and images are collected to complete the set. After the sample images are collected, all lasers are blocked by the shutters and a set of dark images are collected. Finally, if more replicates are required the user is notified and the cycle repeats. If no more replicates are required then the collection is complete, and the operator can move on to the second orientation or next fruit.

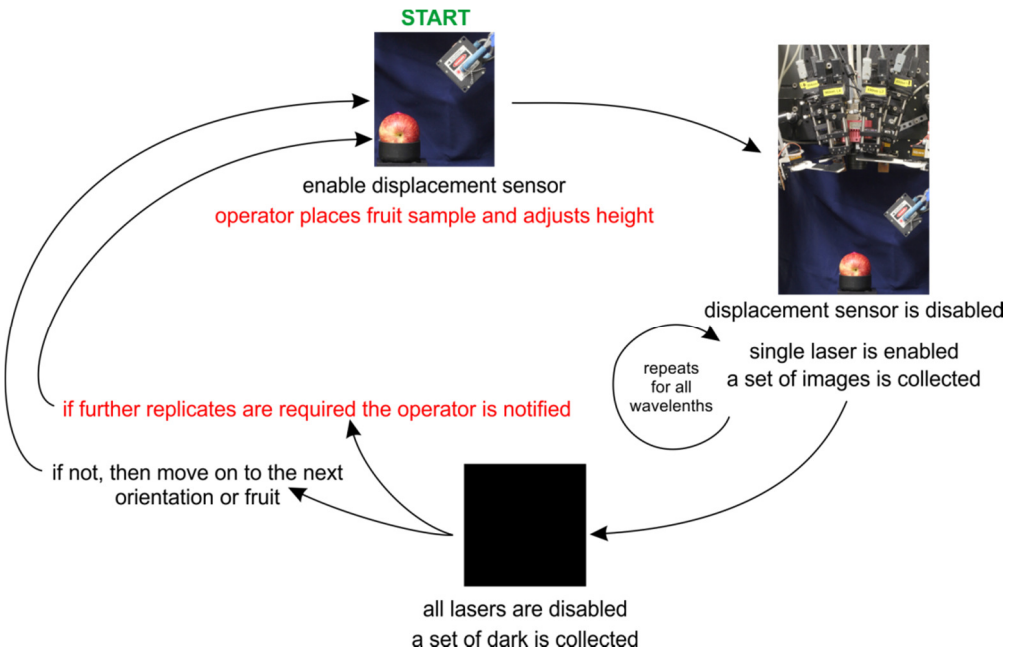

Figure 7-9. Sequential procedure executed using a Matlab script to carry out measurements using the static multispectral imaging system.

7.2. Inverse Adding Doubling System

7.2.1 Introduction

The inverse adding-doubling (IAD) technique was developed by USA scientist Dr Scott Prahl and consists of a method and computer program for calculating the absorption, scattering, and anisotropy properties of turbid samples (Prahl et al., 1993). Prahl (2013) has continued to maintain the software with the latest version (3.9.10) published in April 2013. The IAD algorithm takes the measured reflectance and transmittance of a sample as its input. It then follows an iterative procedure to calculate the samples optical properties. First an initial guess is made for the absorption, reduced scattering and anisotropy properties. The adding-doubling (AD) method is then used to calculate reflectance and transmittance for those initial properties. The AD method first calculates the transmission and reflection for a thin starting slab using single scattering and the initial optical property guess. The slab is then doubled until the desired thickness is reached (Prahl et al., 1993). Improved estimates of the optical properties

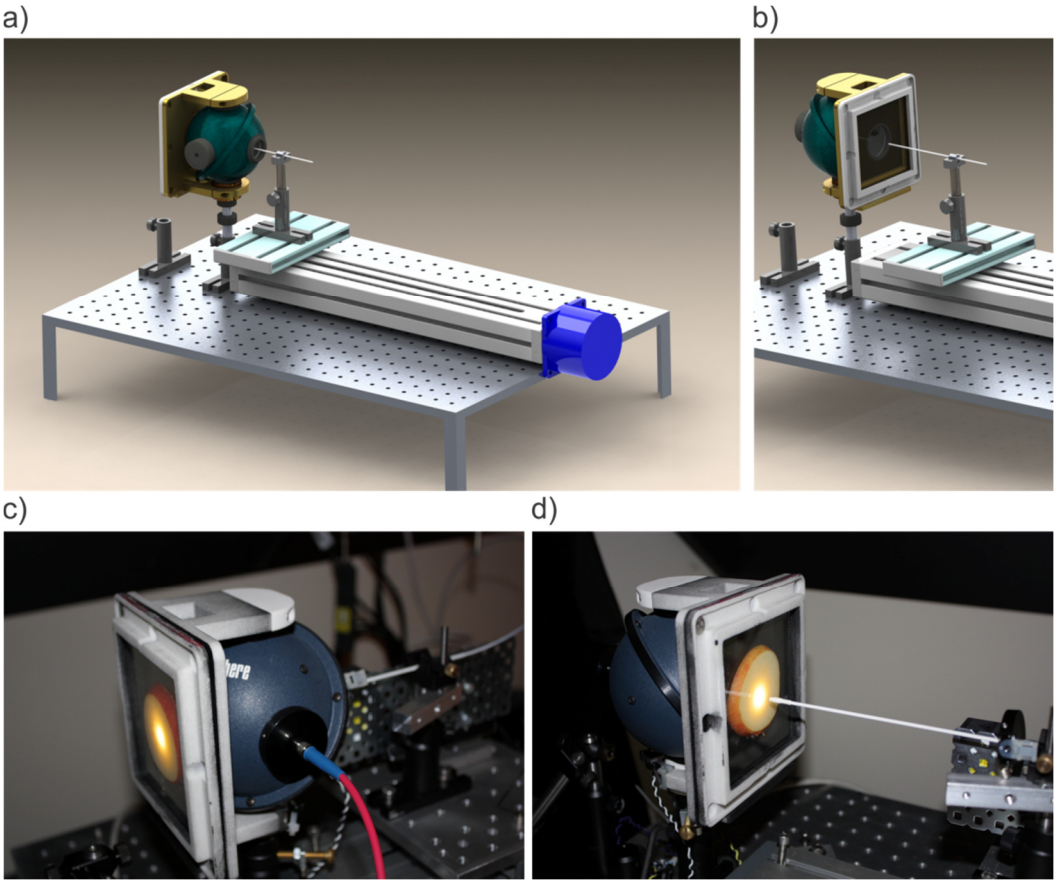

Figure 7-10. CAD model of the semi-automated inverse adding-doubling system in (a) reflectance mode, and (b) transmittance mode. Actual implementation with an apple sample in (c) reflectance and (b) transmittance modes.

are then found by comparing the measured reflectance and transmittance values to the calculated values. The process is then repeated again and continues until there is good agreement of the measured and calculated spectra or an iteration limit is reached. The finally determined optical properties represent those of the measured sample (Prahl et al., 1993).

Figure 7-10 shows the semi-automated inverse adding-doubling system developed for measuring reflectance and transmittance on thin apple samples. All measurements were carried out in a dark room to minimize stray light. Figure 7-11 illustrates the measurement procedure. The system operates in two modes. The first is reflectance mode, where the integrating sphere is oriented with the sample port pointing away from the source probe (Figure 7-10c). Three measurements are made in this orientation. The first is a dark measurement where the probe is transported into its measurement position (8 mm from the sample) with no sample in place (R_0). A black cloth was used to minimize any return signal from the white wall behind. For the second measurement, a 99% reflectance standard is mounted in the sample position. This

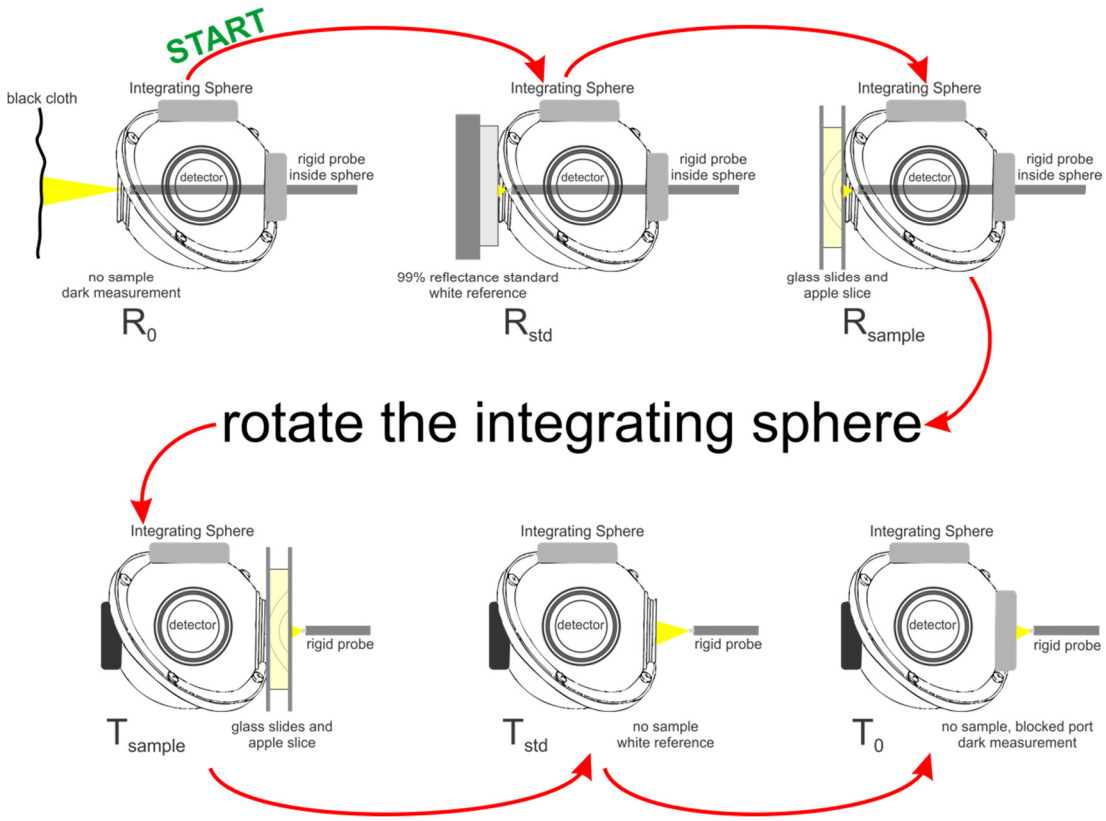

Figure 7-11. Illustration of the six measurements required by the inverse adding-doubling program to resolve the optical properties of fruit samples. The measurements are grouped in two modes, reflectance and transmittance.

provides a measurement of the light source output itself (R_{std}) (white reference). The third measurement is on the fruit sample. A slice of apple flesh is placed between two borosilicate glass slides and then mounted in a 3D printed housing which is magnetically attached to the sample port (R_{sample}).

Following these measurements the system is switched into transmittance mode (Figure 7-10d). Here the integrating sphere is rotated so that the sample port faces the source probe. The fruit sample was left in place from the reflectance measurement. A laser displacement sensor measures the position of the front glass slide and then automatically moves the source probe so that it is 8 mm from the sample. Once the probe is in place the transmittance measurement is made (T_{sample}). A white reference and dark measurement is also required in this orientation. The white reference is measured by replacing the fruit sample and leaving the source probe in place where it directly illuminates the integrating sphere (T_{std}). For the dark measurement, the probe is retracted using a translation stage and a metal cap is placed over the sample port to block any light (T_0). The six measurements are then combined to calculate the total reflectance (R) and total transmittance (T). These are then fed into the IAD algorithm using a Matlab script, and the optical properties are calculated from:

$$R = \mathrm{r}_{std}\frac{R_{sample} - R_0}{R_{std} - R_0} \quad ,$$

$$T = \frac{T_{sample} - T_0}{T_{std} - T_0} \quad .$$

Here r_{std} is the reflectance of the white reference standard. For our system, a 99% Spectralon standard was used (SRS-99, Labsphere, New Hampshire, USA).

7.2.2 Design

Table 7-5 details the major components used in the IAD system. Fruit samples are mounted on a custom 3D printed structure that is attached to the integrating sphere (4P-GPS-033-SL, Labsphere, New Hampshire, USA) (Figure 7-10c). This was designed to allow the sample to be easily mounted using a magnetic attachment scheme and keeps the samples surface flush against the integrating sphere's sample port.

Light was delivered from a 50W quartz tungsten halogen lamp (66884, Newport, Irvine, USA) to the fruit sample via a 1000 µm optical fibre (FT1000EMT, Thorlabs, New Jersey, USA). To increase the rigidity of the fibre, so it could be accurately positioned, the last 210 mm was glued inside a 2.25 mm (outer diameter) stainless steel

tube. The tube was painted white to minimize absorption when the probe is located inside the integrating sphere. Positioning of the probe was controlled by an automated linear translation stage and an Omron laser displacement sensor (ZX2-LD100, Omron, Kyoto, Japan).

Light was collected using a 600 µm optical fibre (BFH48-600, Thorlabs, New Jersey, USA) mounted in the integrating sphere's measurement port. A baffle is present between the sample and measurement ports to prevent any directly reflected light from being measured. Light is delivered from this collection fibre to a Zeiss spectrometer (MMS1, Zeiss, Oberkochen, Germany).

The following sections detail two of the main novel design elements on the IAD system. The first is automated probe positioning, and the second is real-time error checking to help prevent any human errors from affecting the results.

Manufacturer	Model Name	Description
Labsphere	4P-GPS-033-SL	4" integrating sphere, 4 ports, Spectralon coated
Omron	ZX2-LD100	Laser displacement sensor, 100 ± 35 mm, 5 µm resolution
Labjack	U12	General purpose electronic I/O board
Zeiss	MMS-1	Spectrometer, 10 nm bandwidth, 3.3 mm per pixel, 310 to 1100 nm. Thermoelectric cooling (15°C) added in-house.
Thorlabs	FT1000EMT	Source delivery fibre, 1000 µm optical fibre, 0.39 NA
Thorlabs	BFH48-600	Spectrometer feed fibre, 600 µm optical fibre, 0.48 NA
Newport	Bulb:6337, Housing:66884, Power Supply: 69931	Broadband illumination source, Quartz tungsten halogen, 50W
NA	NA	1.1mm x 100 mm x 100 mm borosilicate glass slides. Used to contain fruit slices for the IAD measurement.
NA	NA	Automated linear translation stage, 1.25 µm resolution. 800 steps/mm.
Labsphere	SRS-99-020	99% reflectance standard

Table 7-5. Major components of the inverse adding-doubling system.

7.2.2.1 Probe Positioning

For the IAD technique to work properly, the fibre illumination probe must be positioned at the same distance from the sample in both transmittance and reflectance modes. Reflectance mode is simple because the illuminated surface is always in a fixed location. In transmittance mode, however, the fibre optic probe cannot be placed at a fixed position as the apple slices will vary by small amounts in thickness. To minimize

this positioning error, and to make the system user friendly, an automated probe positioning system was designed.

Figure 7-12 shows the optical fibre probe (white) mounted on a rigid metal base. This base is connected to a linear translation stage which allows automatic movement of the probe with an accuracy of 1.25 µm. Mounted behind the probe, 115 mm from the tip is an Omron laser displacement sensor (yellow). The displacement sensor measures the distance between the glass slide and the fibre probe. This distance is used to shift the translation stage so that the probe is always 8 mm from the glass surface irrespective of the sample thickness.

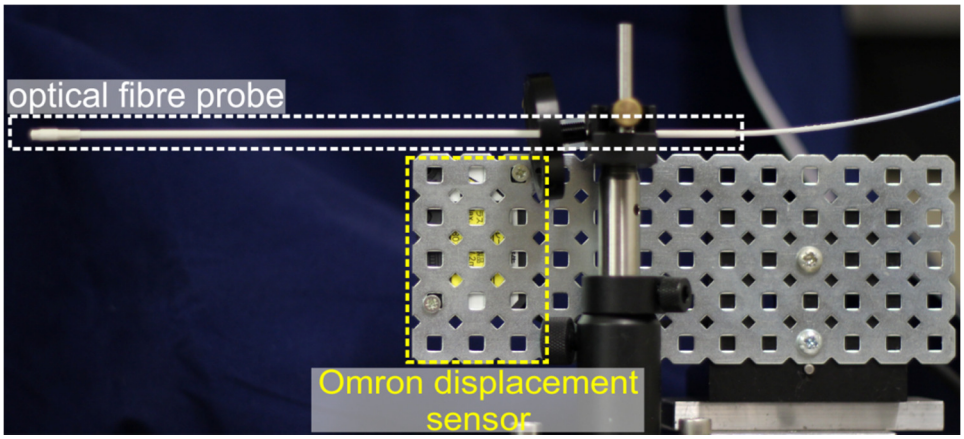

Figure 7-12. Arrangement of the rigid fibre-optic probe and the Omron range sensor (attached in the position indicated on the other side of the frame).

The probe to sample distance of 8 mm was carefully chosen to minimize a problem where light that is reflected from the sample travels straight back down the source fibre. Figure 7-13a illustrates this issue. The dark red line indicates a set of rays that travel out of the source fibre. The rays are diffusely reflected, and a portion of them will be directed back down the fibre and will not be measured by the detector. Figure 7-13b shows the intensity at 720 nm. As the probe to sample displacement increase from 0 to 4 mm, the intensity sharply increases. Above 6 mm, the intensity values stabilise, so a working distance of 8 mm was chosen. The numerical aperture of the fibre was 0.39 providing a beam diameter on the sample of 6.2 mm.

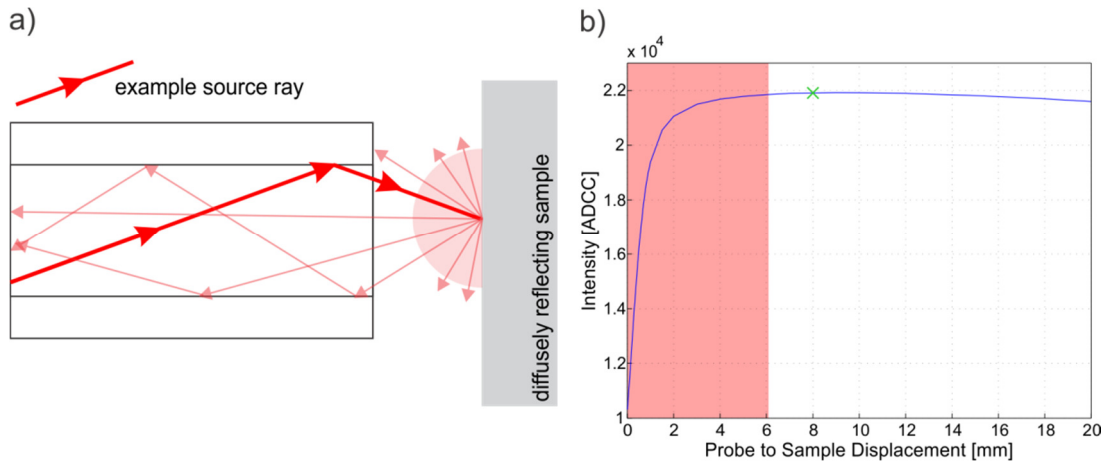

Figure 7-13. (a) A significant amount of light that diffusely reflects off the target sample can travel back down the source fibre if it is too close to the sample. (b) Intensity measured using the rigid fibre probe as the sample to probe distance varies from 0 to 20 mm.

7.2.2.2 Human Error Protection

The inverse adding-doubling system requires a large number of sequential steps for each measurement making it susceptible to high levels of human error. To avoid this, a protection scheme was developed. The system consisted of three magnet and reed switch pairs. A reed switch is a small electronic component with two thin, ferromagnetic contacts. If a magnet field is present, provided by a small magnet, it pulls the contacts together closing the switch. Each of the switches were read using a Labjack data aqusition box (U12, Labjack, Lakewood, USA) by a Matlab program.

Figure 7-14 shows two of the reed switch/magnet pairs. The first (a) is used to indicate what mode the integrating sphere is in. In transmittance mode, this reed switch is activated. A similar one is attached to the other side and indicates when reflectance mode is activated. If neither reed switches are activated it indicates that the sphere is not in either position and measurement is not possible. The second pair shown in Figure 7-14b shows a reed switch attached to the port on the integrating sphere. In reflectance mode, this port is removed so that the probe can pass through. When switched to transmittance mode this port needs to have the cap replaced (an easily forgotten step). This reed switch/magnet pair prevents this, instructing the operator to correctly install the missing port cap.

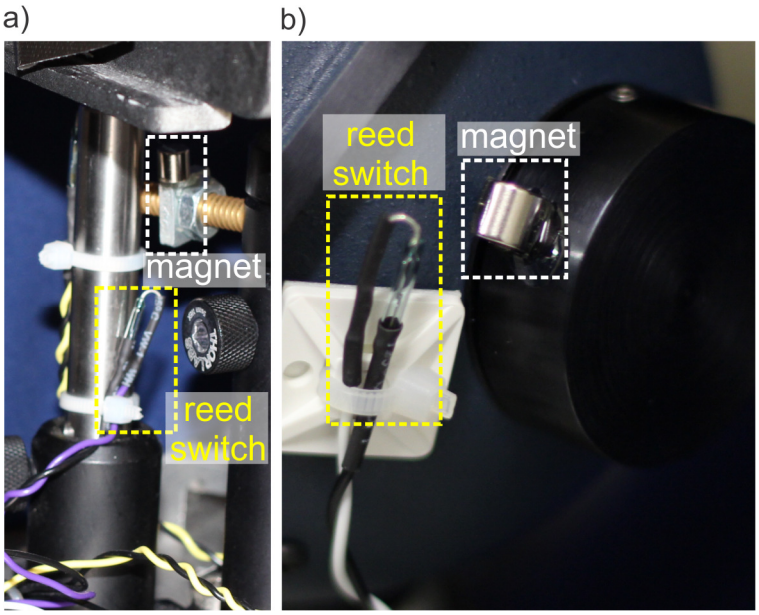

Figure 7-14. Human error protection system implemented with reed switches and permanent magnets. (a) Shows protection on the integrating sphere shaft which indicate what mode it is in. (b) Shows protection on the integrating sphere port cap to ensure it is in place.

7.2.3 System Calibration

For the inverse adding-doubling system to measure the correct optical properties, the sphere wall reflectance is critical. Usually this is not as simple as just using the manufactures measured value for the sphere. The effective sphere wall reflectance can affected by many things including the physical construction of the sphere and components placed inside it such as the optical fibre probe. A calibration step for the sphere reflectance is recommended to avoid systematic errors around the various aspects of the sphere and its components (Prahl, 2012).

Figure 7-15 illustrates the sphere calibration. A separate calibration is required for transmittance and reflectance modes because, in reflectance mode, the sphere contains the optical fibre probe. This is not the case for transmittance mode. The sphere wall is illuminated with broadband light adjacent to the sample port. Two measurements are made, one with a 99% reflectance standard in the sample port and one without. The following formula is used to calculate the system wall reflectance (r_w):

$$\frac{1}{r_w} = a_w + a_d r_d (1 - a_e) + a_s r_{std} (1 - a_e) \frac{R_{std}}{R_{std} - R_0} \quad ,$$

where a_w is the relative area of the sphere wall, a_d is the relative area of the detector, r_d is the reflectance of the detector (assumed to be zero), a_e is the relative area of the

entrance port, a_s is the relative area of the sample port, and r_{std} is the reflectance of the standard. Figure 7-16 shows the calibrated sphere wall reflectance. There is about a 1% drop caused by the probes presence inside the integrating sphere when operating in reflectance mode. The calibrated reflectance values were used for all IAD calculations on fruit.

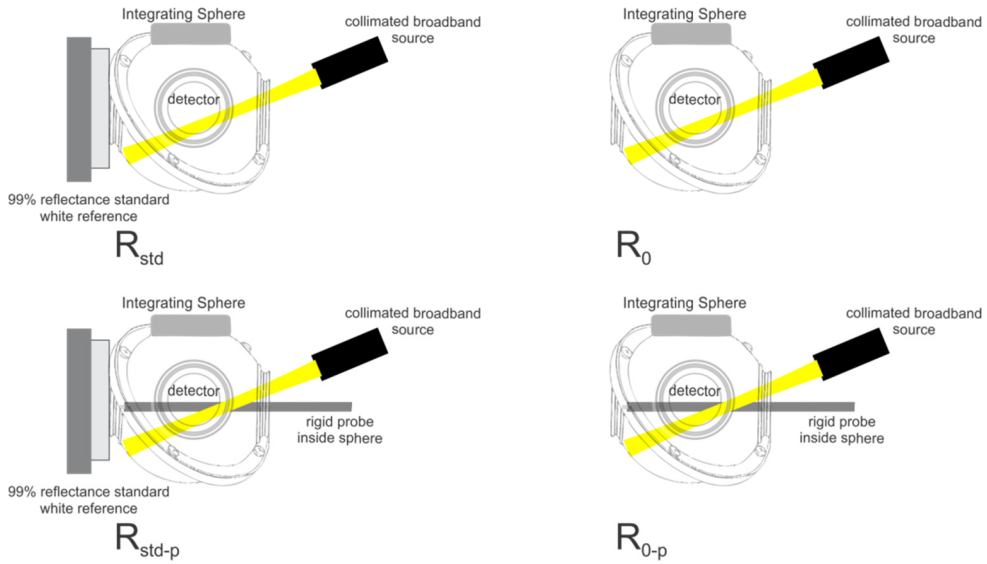

Figure 7-15. Measurements required to calculate system reflectance. Top two measurements provide a calibration for transmittance mode (when the probe is not present), and the bottom two measurements provide a calibration for reflectance mode.

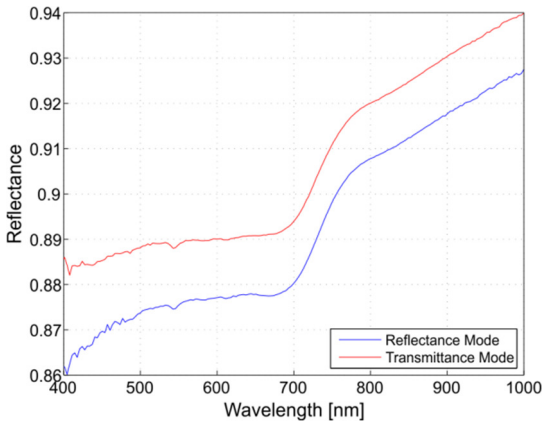

Figure 7-16. Calibrated sphere reflectance.

7.3. Fruit Slicing System

A fruit slicing system was required to cut sections of fruit flesh for use with the IAD system and to create flat sections on fruit for measurement using the static multispectral imaging system (Chapter 9). The measurement configuration of the IAD system requires a thin sample of the fruit flesh to be removed, and placed between glass slides for measurement. Manually slicing samples proved to be a significant

challenge with large errors in thickness across the slice (1 to 2 mm). Figure 7-17 shows the design and implementation of a custom guillotine. The system consists of three main components, a rigid fruit mount, the cutting section, and an adjustable end-stop.

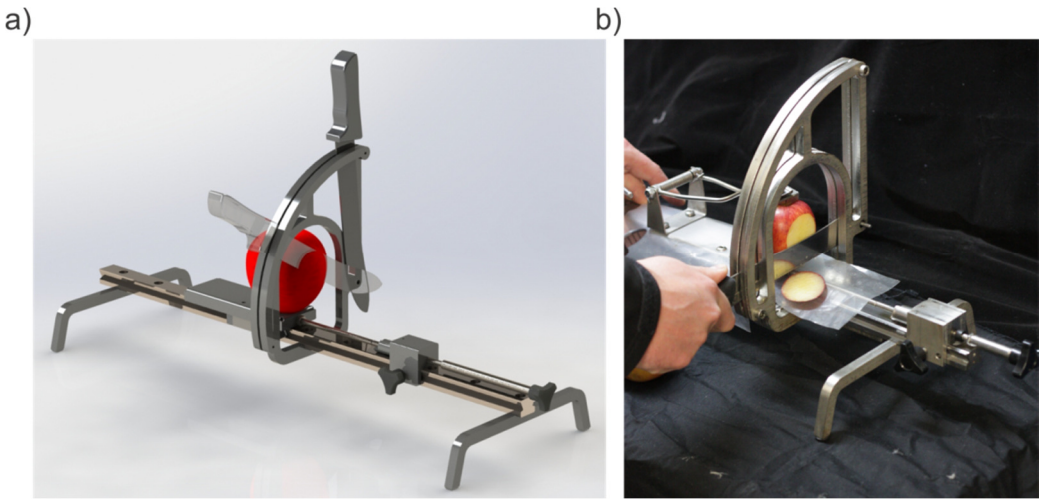

Figure 7-17. (a) CAD model for a custom 'guillotine' fruit slicing system. (b) Actual implementation used to slice a 'Royal Gala' apple.

Figure 7-18 shows the fruit mounted rigidly using spikes that enter both through the top and bottom of the fruit. The spikes help keep the fruits location fixed and also allow us to relocate the fruit in between slices. The fruit mount is attached securely to a linear guide that allows the fruit to slide towards the cutting section of the system until it hits the adjustable end-stop. Once in position the mount is prevented from further movement by engaging the locking bolt (left side of Figure 7-18).

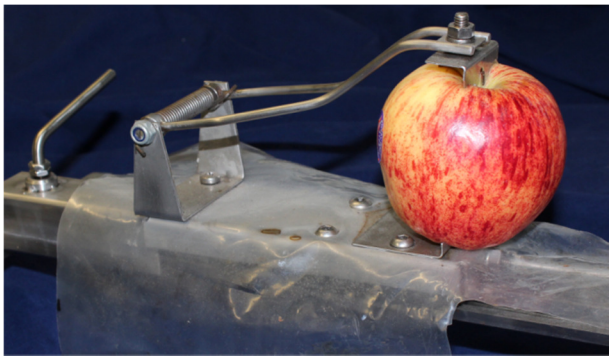

Figure 7-18. Rigid fruit mount used on the fruit slicing system.

Figure 7-19a shows a close up of the adjustable end-stop. This has four pre-defined end stop positions relative to where the end-stop carriage is locked in place (using the black knob). Figure 7-19b shows the four end stop positions indicated in blue, green, red, and yellow. The first position (blue) defines the start location. The second end-stop (green) defines the first 6 mm slice removed from the fruit to expose a flat surface for the

multispectral imaging system. The third end-stop (red) provides a thin 2 mm slice used to square up a samples surface. This is because the fruit was removed for the multispectral imaging measurement and re-mounting it on the guillotine may have introduced some positioning error. The final end-stop (purple) provides a nominally 5 mm thick slice for use with the IAD system. Figure 7-19c illustrates each of the three slices. In no cases did the final slice reach into the core tissue of the 'Royal Gala' apples. Multispectral images are collected on the flat surface created by the first slice, the second slice is usually discarded, and the final slice is then taken and measured with the IAD sytem.

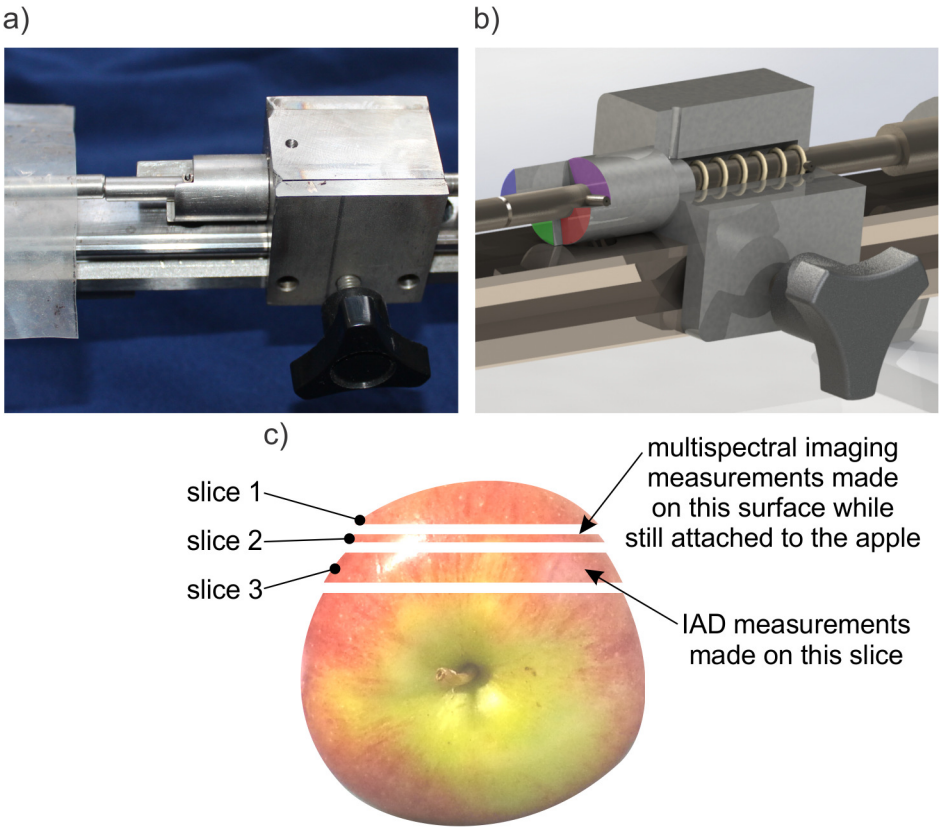

Figure 7-19. (a) Adjustable end-stop used to get repeatable, uniform fruit slices. (b) Three settings (green, red, and purple) allow for three different thickness slices. (c) Outline of the three slices removed from the fruit.

8. Static System Validations

8.1. Introduction

The semi-automated inverse adding-doubling (IAD) and the static multispectral imaging (MSI) systems were validated using optical phantoms made up of filtered water and different concentrations of Intralipid® (Fresenius Kabi, Bad Homburg, Germany). Four optical phantoms were used each with an increasing reduced scattering coefficient covering a range from 0.6 mm^{-1} to 2.4 mm^{-1} at 685 nm. This range exceeds or is comparable to those seen in the literature for a number of apple varieties (Qin et al., 2007; Cen et al., 2011, 2013).

8.2. Method

8.2.1 Intralipid Optical Phantoms

To validate the IAD and static MSI systems, 0.5, 1.0, 1.5, and 2% standard solutions of Intralipid (Fresenius Kabi, Bad Homburg, Germany) were prepared from a 20% stock solution, by dilution with type-1 filtered water (ASTM D1193-91, Milli-Q Integral, Millipore, USA). Intralipid is a fatty emulsion originally used for parenteral (non-oral) nutrition in patients who are unable to get nutrition from an oral diet. It contains small fat droplets (average diameter of 97 nm), consisting of soy bean oil encapsulated in a lecithin layer, which are suspended in water. The refractive index mismatch between these droplets and water lead to high levels of light scattering (van Staveren et al., 1991). This scattering, as well as Intralipid's availability, low price, and well controlled manufacturing process makes it useful as a scattering agent in optical phantoms for diffuse optical measurements (Ninni et al., 2011). Phantoms containing Intralipid have been used as calibration standards or as models for the development of new systems (Michels et al., 2008).

Table 8-1 shows the composition of the Intralipid phantoms used in this study. Each phantom has an increasing concentration of scattering particles (due to the increased concentration of Intralipid). This leads to a proportional increase in the reduced scattering coefficient. The absorption coefficient of each phantom is the sum of the absorption coefficients for the individual components (Michels et al., 2008). In the phantoms used in this study, the main absorbers are the water used to dilute the stock

Intralipid, and the soy bean oil contained within the Intralipid itself (Flock et al., 1992). Water absorption is well known from the literature (Kou et al., 1993; Hale & Querry, 1973). The absorption of soy bean oil in Intralipid is provided by Flock et al. (1992). Figure 8-1 shows the absorption of pure water and that of a 2% Intralipid solution. The additional absorption remains low from 400 to 650 nm and becomes negligible above that.

Intralipid 20% Stock Solution [mL]	Total Lipids [mL]	Type-1 Filtered Water [mL]	Intralipid Phantom %
75	15	2925	0.5
150	30	2850	1.0
225	45	2775	1.5
300	60	2700	2.0

Table 8-1. Intralipid optical phantom composition.

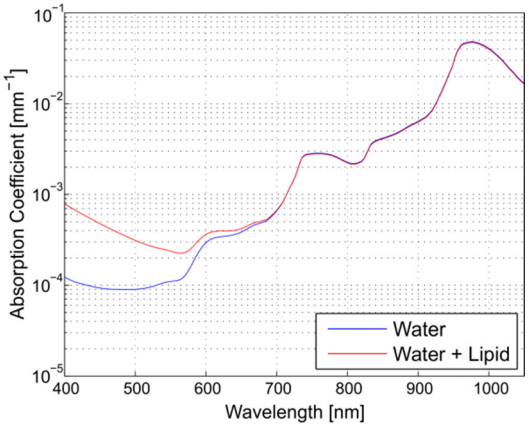

Figure 8-1. Absorption coefficient of pure water and the combination of pure water and Intralipid for a 2% solution (Kou et al., 1993; Hale & Querry, 1973; Flock et al., 1992).

8.2.2 Inverse Adding-Doubling

For the IAD system, the optical phantoms were measured in custom cuvettes fabricated from 1.12 mm thick borosilicate glass. These consisted of an open slot with two glass walls measuring 100 x 100 mm separated by 4.83 mm using a glass spacer (Figure 8-2). Each sample was mounted on the IAD system in a similar way to the fruit samples using the magnetic mounting system (Chapter 7).

Each of the Intralipid samples is measured following the process described in Chapter 7. The data collection and analysis was managed by Matlab (The Mathworks Inc., Massachusetts, USA). The total reflectance and total transmittance values were fed into version 3.9.10 of the IAD program (Prahl, 2013). The IAD program requires a number of parameters that are used during calculation. Table 8-2 shows the values used for each

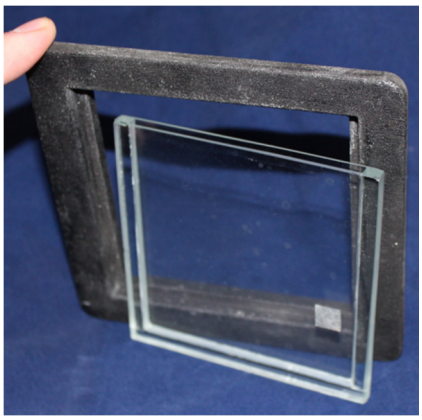

Figure 8-2. Glass cuvette for holding liquid samples while they are measured using the IAD system.

of the parameters. The refractive index used for the Intralipid sample was calculated using the Cauchy equation:

$$n(\lambda) = I_{water} + \frac{J}{\lambda^2} + \frac{K}{\lambda^4} \quad ,$$

where $I_{water} = 1.311$, $J = 1.154 \times 10^4$, and $K = -1.132 \times 10^9$. The wavelength of light (λ) should be in nanometers (Michels et al., 2008). The anisotropy factor was calculated using the empirical model developed for Intralipid by van Staveren et al. (1991):

$$g(\lambda) = 1.1 - 0.58\lambda \quad ,$$

where λ is the wavelength of light in micrometers. The IAD program also features a Monte Carlo simulation which attempts to correct for light loss out the edges of the sample. This was enabled for all fruit and Intralipid measurements.

IAD Program Parameters	Total Lipids [mL]
Refractive Index Sample	Cauchy Equation (Michels et al., 2008)
Refractive Index Glass Slides	1.52 (Parker et al., 2009)
Sample Thickness	4.83 mm
Glass Slide Thickness	1.12 mm
Beam Diameter	6.2 mm
Reflectance of Standard	99%
Monte Carlo Light loss Correction	Enabled

Table 8-2. IAD program parameters used to calculate the optical properties of the sample.

8.2.3 Static Multispectral Imaging System

For the MSI system, 1.4 L of each Intralipid standard solution was poured carefully (to minimize bubbles) into a plastic cylindrical container with a diameter of 150 mm and a height of 92 mm. This container was sufficiently large ensure the smallest dimension of

the phantom was always greater than 40 transport mean free paths. This minimises edge effects from the container as suggested by Farrell et al. (1992). The sample was centred on the fruit location system described in Chapter 7 and adjusted so that the surface was 160 mm from the camera (working distance).

With the Intralipid sample correctly positioned, 49 replicate images were captured (1 ms exposure time). This was replicated 9 times, with the sample removed and replaced each time. At the end of each replicate sequence, a dark image was collected. During this validation stage, the 980 nm laser (Chapter 7) was not available so only measurements at 685, 850, and 904 nm were carried out.

Images were analysed by first correcting for dark current, then the intensity profile was extracted using the radial averaging technique described in Chapter 6 and logarithmically transformed. This is a common variance stabilising transformation that has been shown to improve the curve fit results by Cen et al. (2010). The diffusion theory model (Chapter 6) was fitted to the experimental data using the Matlab Curve Fitting Toolbox (Mathworks, Massachusetts, United States). It was configured to use a Levenberg-Marquardt non-linear least squares algorithm. The data used in the fit was limited to measurements below 3500 ADC counts to exclude the saturated region and extended out to a distance of 10 mm. The outer displacement of 10 mm was chosen because the diffusion model fitted the data well, the signal is above the background level, and it is consistent with the outer displacement used in earlier studies (Cen et al., 2013, 2011; Lu et al., 2009).

8.3. Results and Discussion

8.3.1 Inverse Adding-Doubling

Figure 8-3a shows the reduced scattering coefficients at four concentrations of Intralipid. The grey lines indicate the measured reduced scattering coefficient and the black lines show the expected results based on the model provided by van Staveren et al. (1991). Each of the reduced scattering coefficient profiles shows a monotonically decreasing curve from 400 to 1000 nm, typical of previously reported results (McGlone et al., 2007). Comparing the measured (red) and modelled (blue) results shows a consistently greater slope across the wavelength range. The largest discrepancy was at 400 nm; it then reduced until crossing near 800 nm and then began to increase again, equating to a worst case average error of 11.1% (0.5% solution). This discrepancy is not

uncommon, with similar profiles seen in earlier studies. Qin & Lu (2007) used their hyperspectral imaging system to measure the optical properties of Intralipid and dye samples over a wavelength range from 500 to 900 nm. They found a similar average error of 11% with their reduced scattering coefficient spectra. Zhang et al. (2010) presented reduced scatting coefficient spectra from 400 to 800 nm for Intralipid and blue dye liquid solutions, also measured, using the inverse adding-doubling technique. They found that it overestimated the reduced scattering coefficient by 5% at 400 nm, and underestimated by 5% at 800 nm.

Above 900 nm (Figure 8-3b), crosstalk can be seen. Crosstalk, also known as absorption-to-scattering coupling, is a term given to regions of the reduced scatting coefficient spectra which depart from the expected monotonic decreasing profile (Figure 8-3b) (Pifferi et al., 2007; Svensson et al., 2008). This occurs in regions with elevated absorption, in this case at the 980 nm water absorption peak and has been observed in earlier studies (Saeys et al., 2008; Bashkatov et al., 2005). Zamora-Rojas et al. (2013) suggest that this could also be attributed to insufficient separation of the absorption and scattering effects, leading to errors in both. They suggest this might be caused by ill conditioning of the input parameters such as the refractive index of the sample and glass slides.

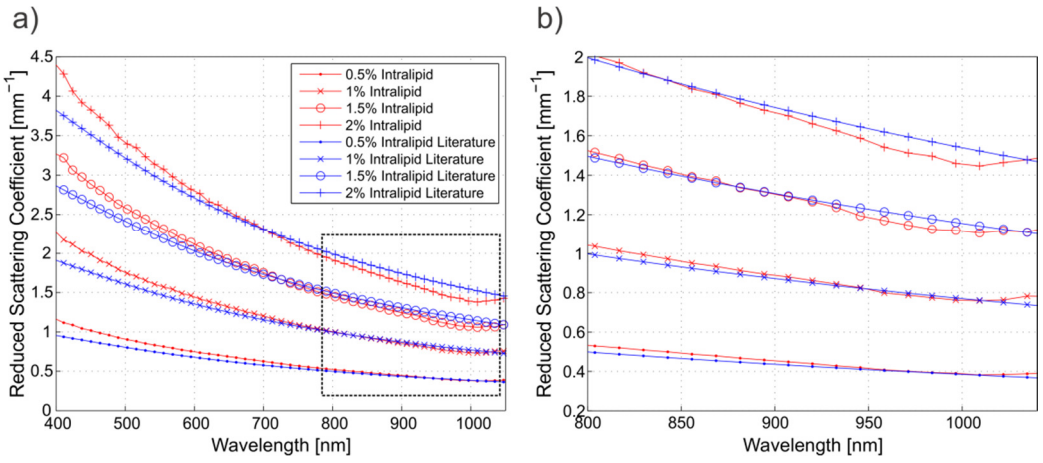

Figure 8-3. Reduced scattering coefficient at four concentrations of Intralipid. Blue lines indicate the reduced scattering based on the model by van Staveren et al. (1991). The blown up view demonstrates crosstalk in the 980 nm water absorption region.

Figure 8-4 demonstrates the correlation between Intralipid concentration and the reduced scattering coefficient at three typical wavelengths. From 400 nm to 1000 nm, the linear correlation was greater than 0.99 with a zero intercept (95% confidence interval). This demonstrates that the reduced scattering coefficient was linear over a

range much larger than typically seen in apple tissue (Cen et al., 2013; Qin et al., 2007; Lu et al., 2009).

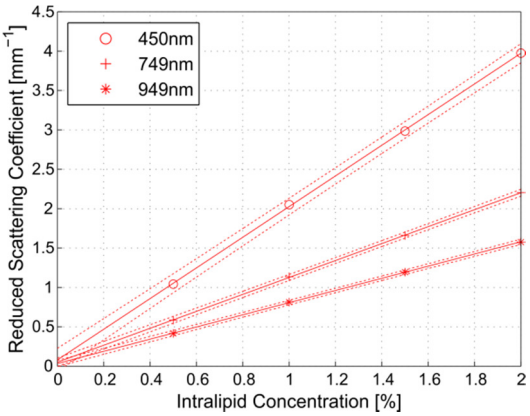

Figure 8-4. The reduced scattering coefficient at each concentration for three wavelengths, demonstrating a strong linear relationship. Dashed lines indicate a 95% confidence interval.

Figure 8-5a shows the absorption coefficient for the four Intralipid concentrations measured (blue). The black dashed line shows the absorption from the combination of water and Intralipid (2%) (Kou et al., 1993; Hale & Querry, 1973; Flock et al., 1992). The measured spectral profiles were consistent with that of water absorption: there was a large absorption peak at 980 nm followed by smaller absorption at 840 nm and 740 nm. Absorption due to the soy bean oil also becomes visible in the region from 400 to 600 nm as the Intralipid concentration increases.

There is a considerable baseline offset at each concentration. Figure 8-5b shows the absorption coefficient at 602, 700, and 801 nm as the concentration of Intralipid increases. The expected behaviour is a linear reduction in the absorption coefficient as water is substituted for Intralipid. This was not the case; instead there was a non-linear relationship between the concentration of Intralipid and the absorption coefficient, as well as a broad baseline offset. This baseline offset is consistent with reports in the literature also using the inverse adding-doubling technique (Cen & Lu, 2010; Saeys et al., 2008). It is believed to be caused by direct and diffuse light loss (Figure 8-6a). Direct light loss occurs when light escapes out the edges of the sample without ever reaching the integrating sphere. Diffuse light loss occurs when light, diffusely reflecting off the surface of the integrating sphere, travels back through the sample and out it's edges. A further possible mechanism for light loss is through total internal reflection at the boundary between the glass slide and air (Figure 8-6b). This could allow light to "walk" down the inside of the glass slides and escape out the end (Prahl, 2011). This

combined light loss is assumed by the IAD program to be attributed to absorption and leads to erroneously high absorption coefficients (Moffitt, 2007). The IAD program does include a Monte Carlo simulation component which attempts to correct for these light loss effects, however, it appears to be ineffective in this study.

The relative error of the absorption coefficient decreases as the absorption due to pure water increases to a peak at 980 nm. At this peak, the measured absorption coefficients are 5 to 15% higher than expected, depending on Intralipid concentration. At 685 nm, this dramatically increases to an overestimation ranging from 87 to 97%. At every wavelength, the error reduces as Intralipid concentration increases. This increased scattering likely confines the light reducing the amount that gets lost by travelling out the edges of the sample.

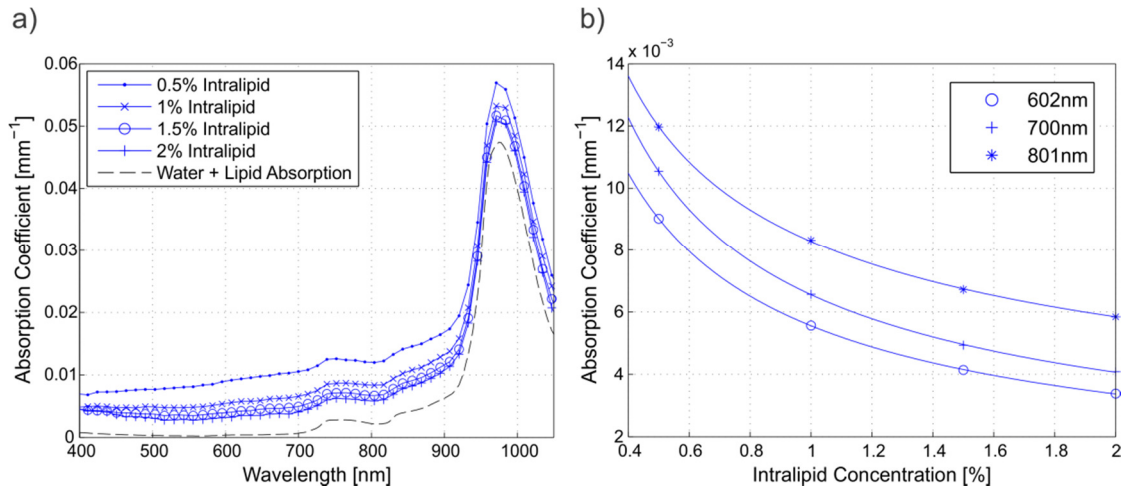

Figure 8-5. Absorption coefficient for the four concentrations of Intralipid; dashed line illustrates the combination pure water and Intralipid (2%) absorption (Kou et al., 1993; Hale & Querry, 1973; Flock et al., 1992).

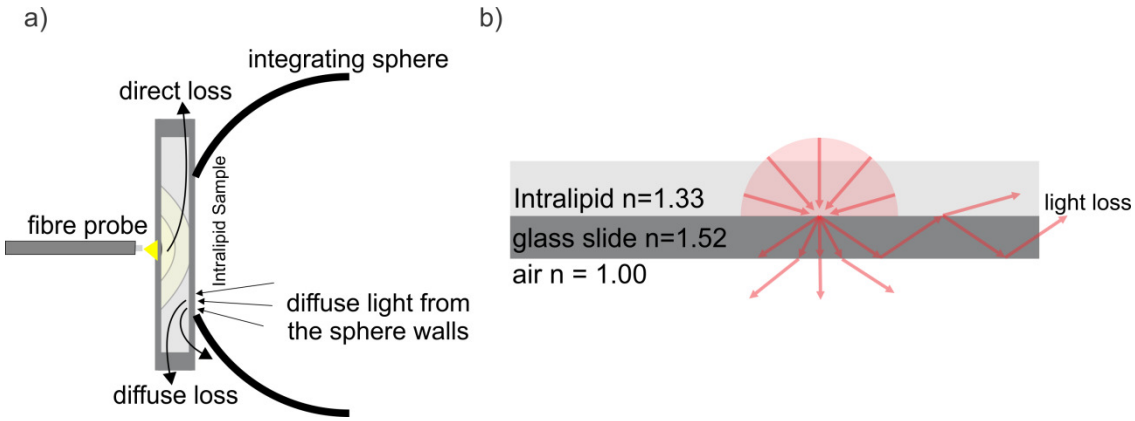

Figure 8-6. (a) Direct and diffuse light loss while the sphere is in transmittance mode. (b) Light loss due to reflections on and within the glass slides.

8.3.2 Static Multispectral Imaging System

Figure 8-7 shows the reduced scattering coefficients extracted from the multispectral images on Intralipid optical phantoms at four concentrations (0.5, 1, 1.5, and 2%). The blue circles indicate the experimental measurements, the blue line indicates a linear fit to the data, and the red circles show the expected results based on the empirical model provided by van Staveren et al. (1991). Each data point corresponds to the average of the nine replicates and the error bars indicate the standard deviation of those replicates.

At 685 nm the reduced scattering values, as measured using the diffusion model, are underestimated by 6, 12, 16, and 21% at the 0.5, 1, 1.5, and 2% concentrations, respectively. At 850 and 904 nm the reduced scattering coefficients are similarly underestimated at 1, 1.5, and 2% concentrations (11, 11, 12% and 7, 13, 14% at 850 and 904 nm, respectively). At 0.5% the situation reverses and the reduced scattering

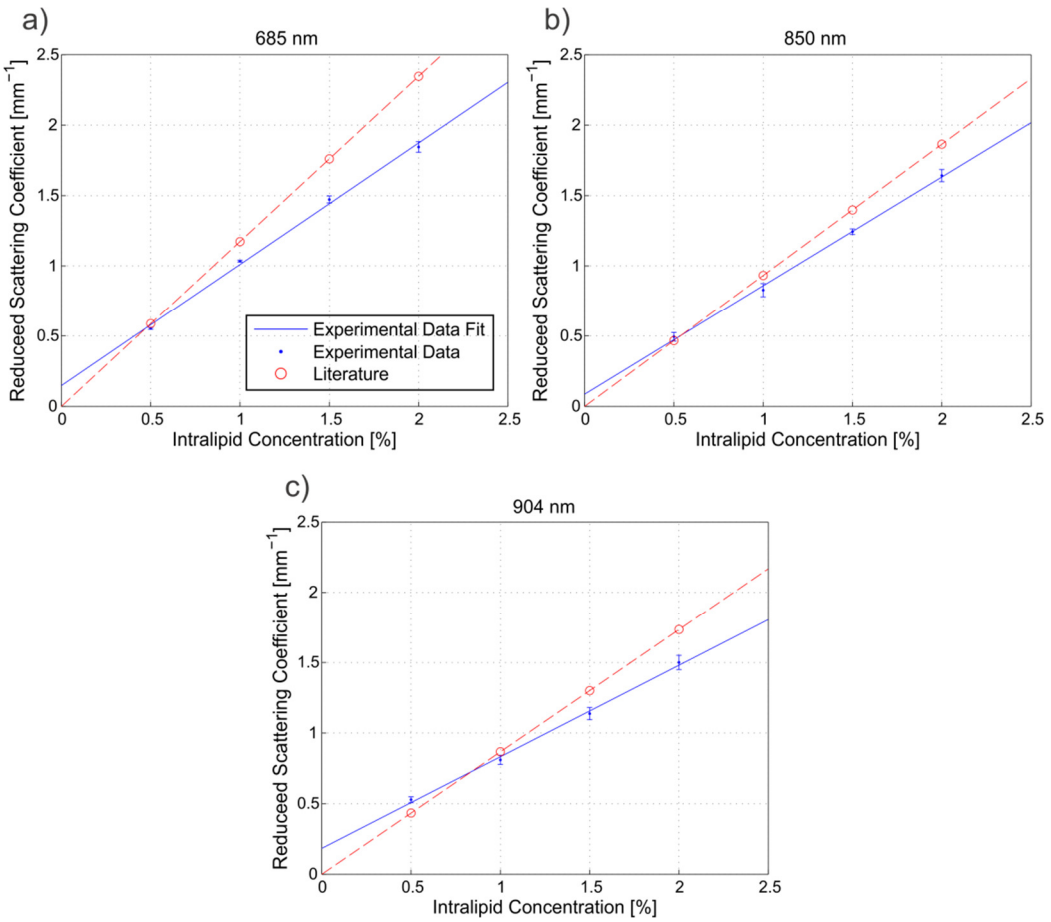

Figure 8-7. The reduced scattering coefficient at (a) 680, (b) 850, and (c) 904 nm as the concentration of Intralipid increases.

coefficient is overestimated (5% and 21% at 850 and 904 nm, respectively).

These results are similar to other studies. Zhang et al. (2010) measured the optical properties of Intralipid and dye solutions using an inverse adding-doubling system. They showed that at the wavelengths covered by the lasers used in this study, there was an increasing underestimation of the reduced scattering coefficient as the concentration of Intralipid increased. They also show this becomes non-linear above concentrations of about 2% due to the Intralipid solution no-longer satisfying the independent scattering assumption, where scatters are assumed to be uncorrelated (Zaccanti et al., 2003). Qin & Lu (2005) measured the optical properties of Intralipid and dye mixtures using a hyperspectral imaging system and diffusion theory model. They found errors in the reduced scattering coefficient ranging from about -30 to +30% with the majority below what they expected from their reference data. While the reduced scattering coefficients in the present study show largely underestimation, increasingly so at higher concentrations, the relationship with concentration is nonetheless highly linear and covers a reduced scattering coefficient range in excess of those typically seen in apple tissue (Cen et al., 2013; Qin et al., 2007; Lu et al., 2009). This indicates that the method will provide at least relative information on the behaviour of the reduced scatting coefficient in apple tissue and its possible relationship with fruit firmness.

Figure 8-8 shows the absorption coefficients extracted from the 685, 850, and 904 nm multispectral images (blue) and the expected absorption coefficient from the literature (red) as the Intralipid concentration increases. The error bars indicate the standard deviation of the nine replicate measurements. At the laser wavelengths used in this study, the absorption due to the Intralipid component is negligible (>650 nm, Figure 8-1). This means the expected absorption is that of the remaining fraction of water, so, as the Intralipid concentration increased there should be a slight negative slope (difficult to seen in the reference data of Figure 8-8).

At 685 nm (Figure 8-8a), the average absorption coefficient values found using the diffusion theory model were effectively zero ($2.3 \cdot 10^{-14}$ mm^{-1}). At the concentrations of Intralipid used in this study the expected absorption coefficient at 685 nm is $5.5 \cdot 10^{-4}$ mm^{-1}. This indicates that the diffusion theory model and curve fitting approach may be unable to correctly estimate the absorption coefficients at such a low level.

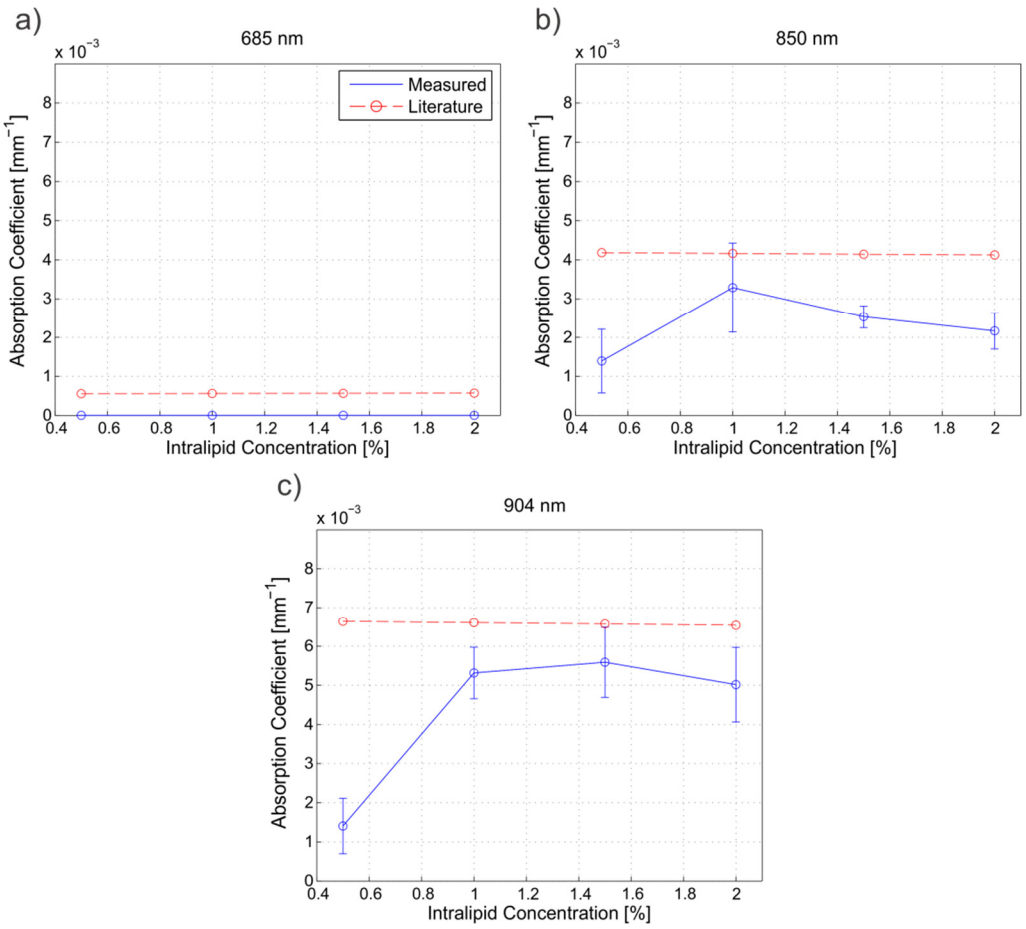

Figure 8-8. The absorption coefficient at (a) 680, (b) 850, and (c) 904 nm as the concentration of Intralipid increases.

At 850 and 904 nm, the curve fitting procedure finds higher levels of absorption, as is expected from pure water at these wavelengths (Figure 8-8b and c). At the lowest concentration and, therefore, lowest reduced scattering coefficient, the absorption coefficients deviate the most from the expected absorption. This is consistent with the requirement of diffusion theory, that, for the models to apply, scattering must be much higher than absorption. Figure 8-9 shows the ratio of the reduced scattering and absorption coefficients from the literature at the relevant laser wavelengths. Aydin et al. (2004) investigated the influence of this ratio on the accuracy of the diffusion approximation suggesting a factor of at least 100 be used for diffusion theory to provide accurate results (Figure 8-9, grey dashed line). At the lowest concentration of Intralipid, this condition is the least satisfied with a ratio of 112 and 65 at 850 and 904 nm respectively. As scattering increases and this condition is further satisfied, the absorption values increase and plateau. Even with this increase in scattering, the absorption coefficient at 850 nm and 904 nm is underestimated on average by 35% and 19% respectively (the averages exclude the 0.5% concentration). It appears, as the

wavelength dependent absorption increases in the phantoms, the diffusion model curve fitting procedure is better able to extract the absorption signal from the intensity profiles.

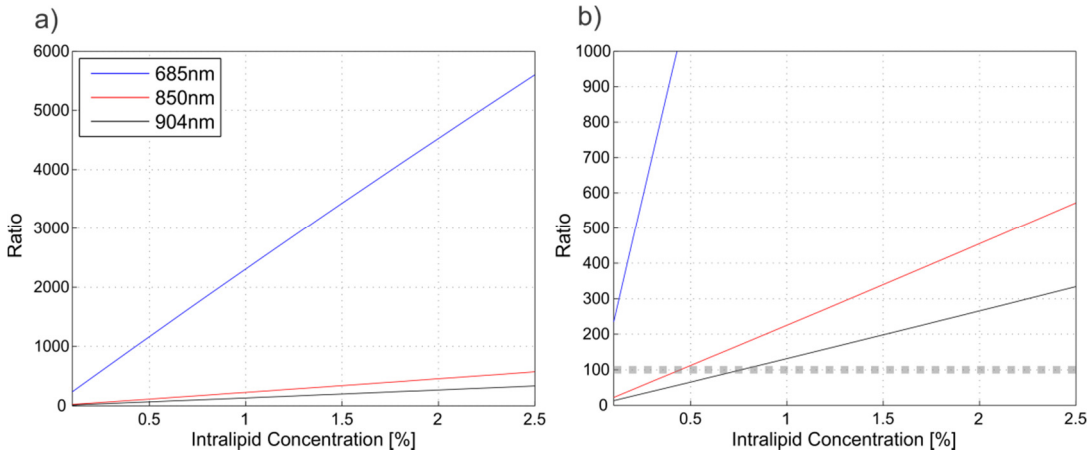

Figure 8-9. Ratio of scattering and absorption coefficients using the values found in the literature (Kou et al., 1993; Hale & Querry, 1973; Flock et al., 1992). Both plots show the same data but (b) has a reduced range of ratios to show the detail at 850 and 904 nm. The grey dashed line indicates a factor of 100 suggested as a minimum by Aydin et al. (2004).

Qin & Lu (2007) had similar issues when measuring the optical properties of milk and various fruit juices. Both of which have low absorption, similar to water. They suggest that the nonlinear curve fitting algorithm, used to fit the diffusion theory model, will not be accurate at determining absorption coefficients at such low levels. This indicates that the absorption coefficient may be more accurate at 980 nm, due to the increased absorption by water, and 685 nm in fruit, due to an increase in absorption by chlorophyll.

8.3.3 System Comparison

Figure 8-10 compares the reduced scattering coefficient measured by the inverse adding-doubling and multispectral imaging systems at 685, 850, and 904 nm for the four intralipid concentrations (blue dots). A one to one line is shown in red illustrating what is expected from two perfect measurement systems. The reduced scattering coefficients measured using the two systems are highly correlated (black line, R = 0.99) over the range investigated, indicating that the two systems are both measuring similar phenomena inside the Intralipid. They do not, however, provide the same quantitative result as illustrated by the deviation from the one to one line. The inverse adding-doubling system consistently gave higher reduced scattering coefficients compared to the multispectral imaging system.

A useful comparison between the absorption coefficients found using the two systems was not possible. The inverse adding-doubling system suffered from erroneously high absorption coefficients consistent with direct and diffuse light loss common in inverse adding-doubling measurements. The MSI system, on the other hand, showed an inability to measure the low absorption coefficient of water at 685 nm and underestimated the absorption coefficients at 850 and 904 nm, especially at the lowest concentrations of Intralipid where the diffusion approximation is least satisfied.

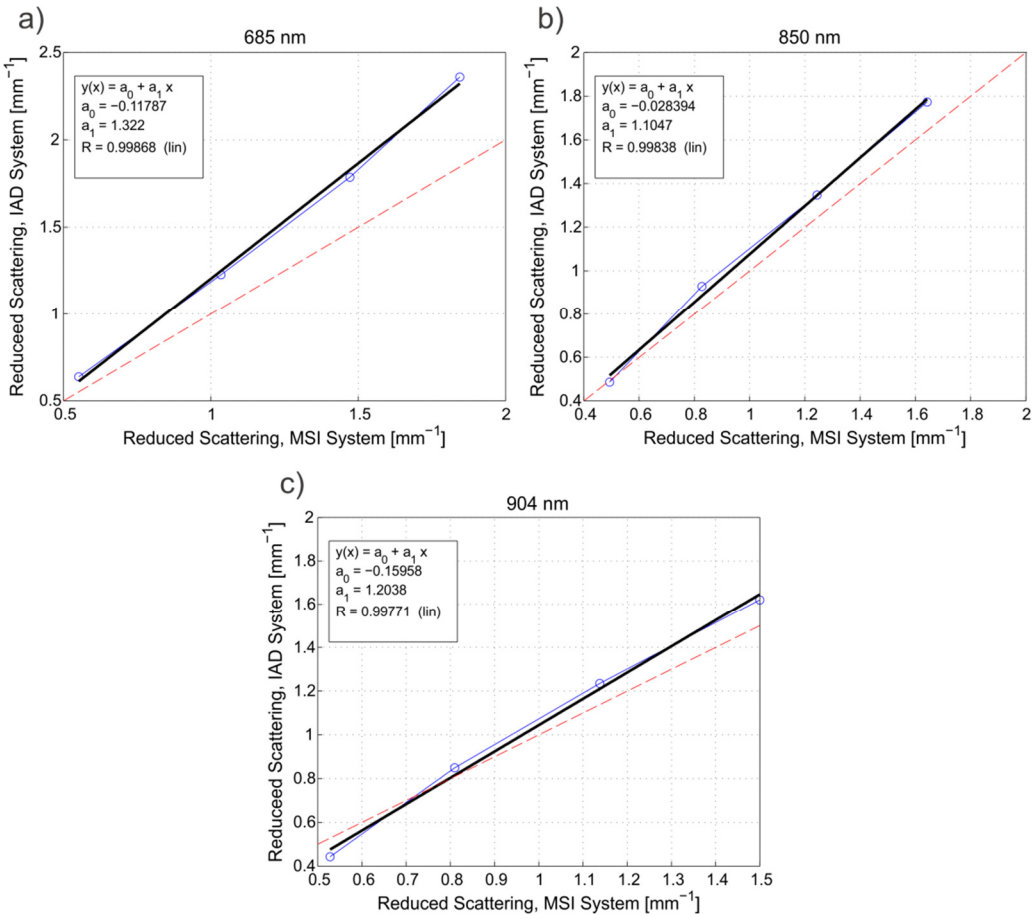

Figure 8-10. Comparison between the reduced scattering coefficient measured using the inverse adding-doubling (IAD) and multispectral imaging systems (MSI) at (a) 685, (b) 850, and (c) 904 nm. The red lines indicate a 1 to 1 relationship, the blue dots indicate the reduced scattering coefficient at each concentration, and the black lines show the results of a simple linear fit.

8.4. Conclusion

The optical properties of four liquid phantoms, with a reduced scattering coefficient range similar to those seen in apples, were measured using the inverse adding-doubling and static multispectral imaging systems. The reduced scattering coefficient measured on both systems was consistent with other studies increasing linearly as

concentration increased over a range of reduced scattering coefficients in excess of those from typical fruit.

The values measured by the inverse adding-doubling system were more accurate with an 11% average error when compared with the published empirical scattering model. The reduced scattering spectra showed signs of crosstalk near the main water absorption peak where the absorption and reduced scattering are not fully decoupled. The absorption spectra suffered from a light loss issue, especially at low scattering concentrations, leading to erroneously high absorption values (87 to 97% higher at 685 nm and 5 to 15% higher at 980 nm).

The multispectral imaging system showed increasing underestimation of the reduced scattering coefficients as Intralipid concentration increased (6 to 21% at 685 nm, 11 to 12% at 850 nm and 7 to 14% at 904 nm). The accuracy of the absorption coefficients was poor, no absorption was measured at 685 nm and the absorption coefficient at 850 and 904 nm was 35 and 19% lower than expected, respectively. The biggest discrepancies between the expected and measured absorption occurred at the lowest Intralipid concentration. This is consistent with the requirement of diffusion theory that scattering must be much greater than absorption (factor of 100).

Both the inverse adding-doubling and multispectral imaging systems provide useful information on the behaviour of the reduced scatting coefficient over a range consistent with apple tissue. This enables measurements on apples to be carried out to see if the reduced scattering coefficient can predict fruit firmness. The absorption coefficient was difficult to measure using either system. The inverse adding-doubling system provided erroneously high absorption coefficients consistent with light loss, and the multispectral imaging system appeared to have trouble extracting the absorption coefficients at the low levels expected from pure water. This indicates that care needs to be taken when interpreting the absorption coefficient results from the two systems.

9. Static and Inverse Adding Doubling Experiment on 'Royal Gala' apples

9.1. Introduction

In Chapter 6, the results from an experiment on 'Royal Gala' apples using the high-speed multispectral imaging system was discussed. The intensity profiles were extracted from each image and parameterised using the modified Lorentzian and diffusion theory models, two approaches used in the literature. The parameters extracted from the profiles correlated poorly to both penetrometer and acoustic firmness. Multiple linear regression was used to predict penetrometer firmness. However, the correlation was low (R = 0.42) and the standard error high (8.79 N) compared to other studies (Peng & Lu, 2006a, 2007; Lu et al., 2009).

Following the high-speed experiment, work was carried out to refine the multispectral imaging system. It was transitioned from a high-speed conveyor based measurement to one where the fruit is static throughout the measurement. Other refinements included precise location control of the fruit relative to the camera, a fourth laser added to interrogate water absorption (980 nm), laser stability improvements, and elimination of a polarization effect. More detail on these refinements can be found in Chapter 7. As well as these refinements to the multispectral imaging system, an integrating sphere system was developed. This, along with the inverse adding-doubling algorithm, allowed for an independent measurement of the optical properties over a broad range of wavelengths (400-1000 nm). The inverse adding-doubling system enabled us to identify if there are more suitable wavelength choices for estimating 'Royal Gala' firmness and compare the optical properties measured by the two systems.

This section reports the relationships between the optical properties/parameters and fruit firmness on 92 'Royal Gala' apples using the static multispectral imaging (MSI) and inverse adding-doubling (IAD) systems. Fruit samples were carefully prepared so that the systems interrogated just the flesh of each sample. For the MSI system, this meant that each apple sample had a slice removed exposing a flat measurement surface. The removal of this slice eliminates the variation caused by the fruits curved surface, and the skin structure and pigments. For the IAD system, this was achieved by

measuring a thin slice taken from flesh adjacent to where the MSI measurement was made.

The multispectral imaging data was processed using the same approaches discussed in Chapter 6. The intensity profiles were extracted using a radial averaging technique and parameterised using the modified Lorentzian and diffusion theory models. Unlike the high-speed experiment, a single treatment was used in this study to produce a wide firmness range and to reduce variation from other causes which might not necessarily relate to firmness. Reference measurements in this study include penetrometer and acoustic firmness.

An additional aim of the work was to explore the spectral range below 500 nm using the IAD technique. Most work published on the optical measurement of fruit firmness to date has explored wavelengths above 500 nm. However, Gross (1987) reported a breakdown of chlorophyll and a synthesis of carotenoid pigments as apples mature, while Merzlyak et al. (2003) found carotenoids have a strong absorption below 500 nm. Together these suggest that optical measurements characterising the parallel process of pigment synthesis or breakdown below 500 nm may offer insight on tissue firmness.

9.2. Method

92 'Royal Gala' apples were measured using the refined static MSI system and the newly constructed IAD system (Chapter 7). The measurements were completed in nine separate daily sessions spread across 24 days. Measurements started on the 10th of April 2013 (day zero) and continued on days 1, 2, 5, 7, 9, 13, 20, and 23. The timing between measurements was guided by each previous session's penetrometer measurements to produce a data set with a wide range of firmness.

Figure 9-1 illustrates the experimental sequence. At the beginning of each measurement cycle, AWETA acoustic firmness is measured (AFS, AWETA, Netherlands). Following this each fruit is measured using the GUSS fruit texture analyser (Fruit Texture Analyser GS-20, GUSS Manufacturing Limited, South Africa), MSI system, and IAD system. The following sections will describe the method in more detail.

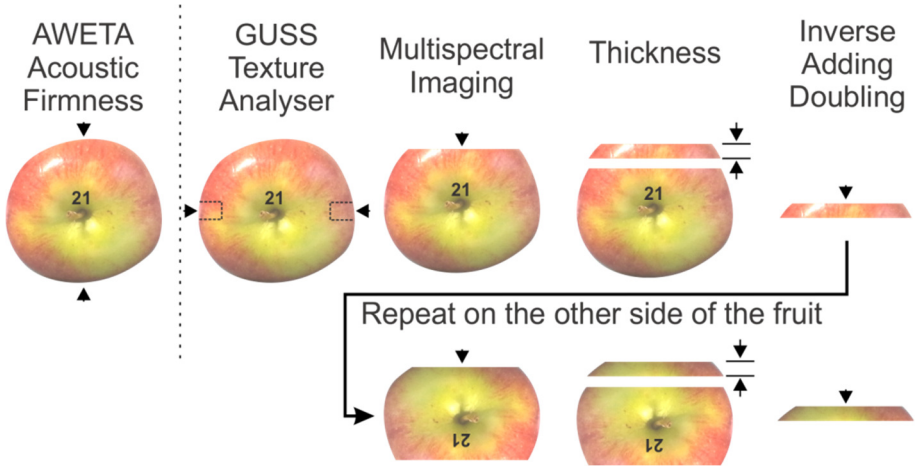

Figure 9-1. Overview of the different measurements used in this study and the positions on the fruit where they occur. Measurement orientation is indicated by the position of the fruit number and was chosen to avoid any visible defects.

9.2.1 Fruit Samples

'Royal Gala' apples were harvested, at commercial maturity, in February 2013 from an orchard in Hawke's Bay, New Zealand. Any fruit with obvious visible defects, which might lead to rots, were discarded. The fruit were stored at 5 °C for 2 months prior to measurement. At the start of the experiment, approximately 200 fruit were placed in chambers where the temperature (20 °C) and relative humidity (greater than 94%) were controlled to limit water loss as the fruit were ripened and to produce a wide distribution in firmness. 12 of these 200 fruit in storage were removed each measurement day. Due to human error and time constraints not all 12 fruit were successfully measured every day. This gave a total of 92 fruit over the experimental period, after which the remaining fruit were too soft to continue, and were discarded.

9.2.2 Acoustic Firmness

Acoustic firmness was measured on all 12 fruit at the beginning of each measurement day using a commercial desktop sensing system (AFS, AWETA, Netherlands). This system measures the resonant frequency, related to the elastic mechanical properties of the fruit tissue. A detailed description of the measurement can be found in Chapter 6.

Two acoustic firmness measurements were made on each fruit and averaged. The measurements were made on flesh directly adjacent to the slice used for the optical measurements (Figure 9-1).

9.2.3 Texture Analysis

Texture analysis was performed in a similar way to the high-speed experiment (Chapter 6). This time, however, a GUSS fruit texture analyser was used (GS-20, GUSS Manufacturing Ltd, South Africa). The GUSS fruit texture analyser (Figure 9-2b) operates in a similar fashion to the TA.XTplus system measuring the force required to drive an 11 mm diameter metal probe 9.5 mm into the sample's flesh at 10 mm s^{-1} (Abbott, 1999). The force profiles were recorded as the probe penetrated the apple flesh. Penetrometer firmness was taken to be the maximum force at any point in the displacement cycle (including after the rupture point), and the measurements from opposite sides of the fruit were averaged (Figure 9-1). Care was taken to avoid visible defects, such as localised soft spots, that could affect the firmness measurement.

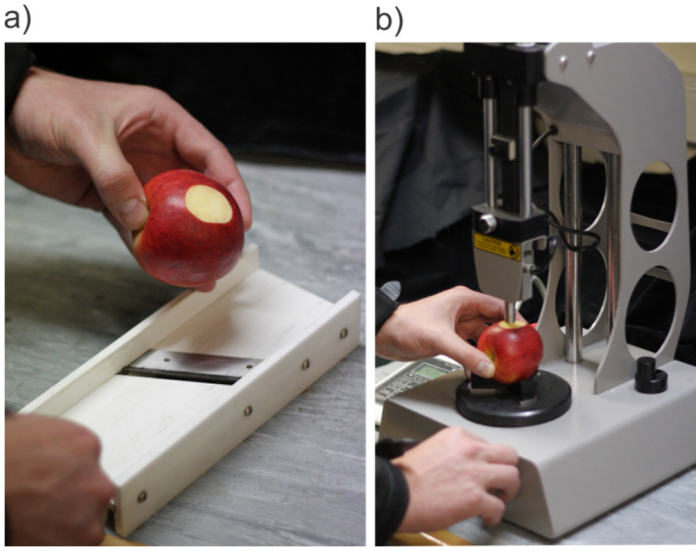

Figure 9-2. (a) Fruit skin is removed using a mounted razor blade. (b) A GUSS fruit texture analyser (GS-20, GUSS Manufacturing Ltd, South Africa) is used to measure penetrometer firmness.

9.2.4 Inverse Adding-Doubling

Inverse adding-doubling measurements on thin apple samples were carried out using the system described in Chapter 7. Samples were sliced from the fruit using a custom 'guillotine' (Figure 9-3) and had a nominal thickness of 5 mm with faces parallel to closer than 0.5 mm over a slice diameter of approximately 40 mm. The actual thickness of each slice was recorded as the average across four measurements, one in each quadrant, using digital callipers. The fruit slices were sandwiched between two borosilicate glass slides (1.12 mm thick). Three drops of water were placed on each face of the slice both to help to match the refractive index of the sample and glass slides and to remove any air bubbles. The sandwiched sample was held in front of the 38.1 mm

port on the integrating sphere using a customised holder fabricated in-house. The sphere's baffle was oriented between the sample and measurement ports to exclude direct specular reflections from the glass and sample. Light from a quartz-halogen lamp, delivered through a 1000 µm optical fibre, was used for illumination. The fibre was held rigidly inside a stainless steel tube (painted white, 2.25 mm external diameter), which was mounted on a motorized translation stage.

Figure 9-3. In-house designed 'guillotine' for making parallel slices on the fruit.

The system was operated in two modes, reflectance and transmission, both of which are needed for measuring the optical properties. In reflectance mode (Figure 9-4a), a lamp measurement was made by placing a 99% Spectralon® standard (SRS-99, Labsphere, New Hampshire, USA) over the sample port. A background measurement was made with the port open to a distant black velour cloth. The fruit measurement is made with the sample mounted on the sphere with the probe 8 mm from the glass slide. In transmission mode (Figure 9-4b), the reflectance of the sphere, with no sample, was used for the lamp reference, while the background signal was obtained with the sample port of the integrating sphere completely blocked by a black metal cap. The fruit measurement was made with the probe positioned inside the sphere again 8 mm from the glass slides surface. This gave a beam size of 6.8 mm at the samples surface in both modes.

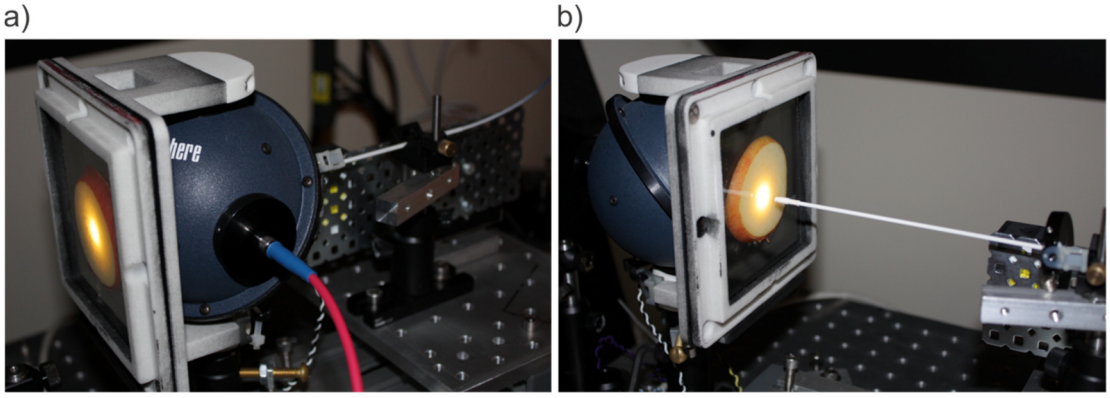

Figure 9-4. IAD system in (a) reflectance mode, and (b) transmittance mode.

All data collection was managed by Matlab (The Mathworks Inc., Massachusetts, USA). The optical properties were calculated using version 3.9.10 of the IAD program (Prahl, 2013). An anisotropy of 0.66 and a refractive index of 1.37, calculated in previous studies (Saeys et al., 2008), were used to solve the radiative transport equations for fruit tissue. Measurements on slices from the two orientations were averaged to give an overall fruit measurement.

9.2.5 Multispectral Imaging

Multispectral images were collected using the refined static system described in Chapter 7. A 6 mm slice is removed from the measurement location (Figure 9-1) of the fruit using the 'guillotine' shown in Figure 9-3. This created a flat surface on the sample removing any variation caused by fruit skin and curvature. In the first orientation (when the other side of the fruit is still intact) fruit are placed in a plastic cup (Figure 9-5) atop a vertical scissor labjack. The surface of the fruit is then levelled using a spirit level and the height of the fruit is adjusted using the scissor labjack until the displacement sensor read zero. This indicated that the fruit sample was located 160 mm from the camera. A similar process is repeated on the opposite side of the fruit, however, this time, a spiked mount (Figure 9-5) is used because the plastic cup was no longer able to hold the fruit securely.

Figure 9-5. In the first position a black plastic cup was used to mount fruit. In the second position, when fruit had been sliced, a spiked mount was required.

Image collection was managed by the Matlab script (Mathworks, Massachusetts, United States) described in Chapter 7. At each wavelength, 49 replicate images were collected. An exposure time of 1 ms was used. This was kept the same as for the high-speed system to remain compatible with moving fruit. Once complete the fruit sample is then removed and repositioned to gather a replicate set of images. The level and height are rechecked and adjusted if necessary. This measurement cycle is repeated four times.

Images were first corrected for dark current, then the intensity profiles from each were extracted using the same radial averaging technique described in the high-speed experiment (Chapter 6). The intensity profiles were parameterized using the modified Lorentzian function, and the optical properties were extracted using the diffusion theory model (Chapter 6). Both approaches used the Matlab Curve Fitting Toolbox (Mathworks, Massachusetts, United States) to fit their respective models to the intensity profiles. The fitting was configured to use a Levenberg-Marquardt non-linear least squares algorithm. The modified Lorentzian function was fitted to intensity profiles ranging from 0 mm to 10 mm which includes the saturated region. For the diffusion theory model, raw data was first logarithmically transformed. As discussed in Chapter 8, this is a variance stabilising transformation which has been shown by Cen et al. (2010) to improve the curve fitting results. The data used to fit the diffusion theory model to was limited to measurements below 3500 ADC counts (to exclude the saturated region) out to a distance of 10 mm. This outer distance was found to be

suitable for the validation measurements (Chapter 8) and is consistent with other studies (Cen et al., 2013, 2011; Lu et al., 2009).

9.3. Results and Discussion

9.3.1 Texture Analysis

The force versus displacement curves are plotted in Figure 9-6, each curve is coloured based on penetrometer firmness using a gradient from blue (soft) to red (firm). The general shape was consistent with reports published on compression-based tests for other apple varieties (Cen et al., 2013). In the elastic deformation region — the initial rise between 0.5 mm and 2 mm — there was a steady slope followed by a rupture point where cell damage occurred and a region where the force fluctuated. The rupture point is clearly visible in some cases and not in others. This behaviour is typical of what others have observed (Cen et al., 2013).

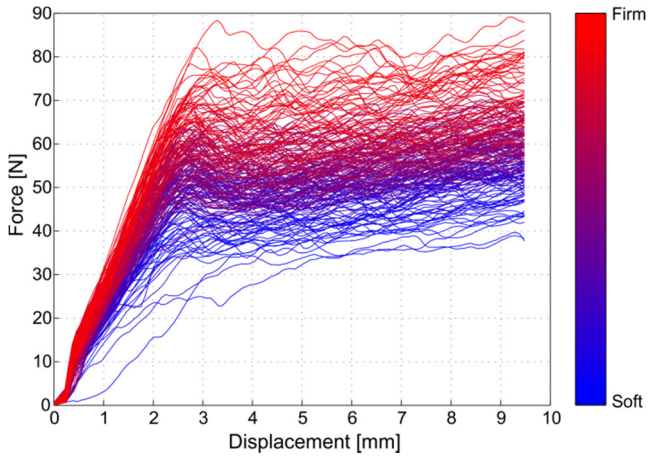

Figure 9-6. Force v. displacement curves for the GUSS firmness measurement system on 'Royal Gala' apples. Colour gradient goes from blue to red representing soft to firm fruit based on the penetrometer firmness.

Figure 9-7a shows the distribution of firmness for all apple samples. The range extended from 43.5 N to 85 N with a mean firmness of 62 N and standard deviation of 9.2 N. The standard deviation of these 'Royal Gala' apples is the same as that of the high-speed experiment (Chapter 6), however the mean firmness in this set is 6 N higher. Like the high-speed data, this range is pertinent to the apple consumer. The top end of the range exceeds the firmness requirement (78.4 N) for the highest maturity grade while the bottom end of the range extends below the outturn specification of 63.7 N, at which the fruit could not be exported (Pipfruit New Zealand, 2005).

Figure 9-7b shows the variation between the penetrometer measurements in the two locations on the fruit. The standard error for a simple linear regression model is used to give a measure for the around fruit and instrument variability. In the high-speed trial on 200 'Royal Gala' apples a standard error of 5.65 N was found using the same approach. In this study, the variability was marginally higher with a standard error of 5.94 N. This indicates that the combined variability is at a similar level in the two studies. For the analysis in this report, the average penetrometer firmness from the two positions is used (Dobrzański et al., 2006).

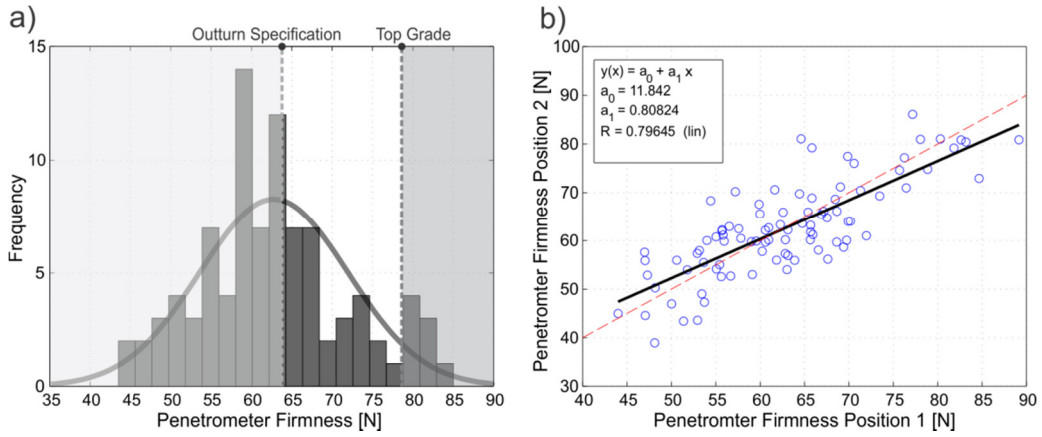

Figure 9-7. (a) Distribution of penetrometer firmness values in 92 'Royal Gala' apples. The shaded regions indicate the outturn specification and the top maturity grades. (b) Relationship between penetrometer firmness measured in the two positions.

9.3.2 Acoustic Firmness

The distribution of AWETA acoustic firmness measurements is shown Figure 9-8a. The range of acoustic firmness extended from 18 to 27 $Hz^2g^{2/3}$, with a mean of 22 $Hz^2g^{2/3}$ and a standard deviation of 1.67 $Hz^2g^{2/3}$. This range is consistent with those found in other studies. Symoneaux et al. (2005) investigated the acoustic firmness of 'Golden Delicious', 'Braeburn', and 'Fuji' apples and its relationship with penetrometer firmness and sensory data. Their acoustic firmness ranged from 11 to 41 $Hz^2g^{2/3}$. De Ketelaere et al. (2006) measured acoustic firmness with a range of 5 to 25 $Hz^2g^{2/3}$ in 'Golden Delicious' apples while comparing acoustic and low mass impact measurements. Cen et al. (2013) investigated the optical properties and acoustic firmness of 'Granny Smith' and 'Golden Delicious' apples. Their acoustic firmness ranged from about 30 to 34 $Hz^2g^{2/3}$ and 14 to 24 $Hz^2g^{2/3}$ for the two cultivars respectively.

The individual storage conditions used in each study appear to affect these acoustic firmness ranges. The fruit used by Symoneaux et al. (2005) and De Ketelaere et al.

(2006) were stored with a lower relative humidity (~80%) compared to the conditions used by Cen et al. (2013) (~95% RH) and in the present study (>94% RH). High humidity environments have been shown to slow the rate at which acoustic firmness decreases explaining the reduced acoustic firmness ranges (Shmulevich et al., 2002; Tu, Nicolaï, et al., 2000).

Figure 9-8b shows the acoustic firmness as measured in the two orientations. There is very good agreement between the two orientations with a correlation coefficient of 0.98. There also appears to be less variation between the two orientations when comparing it to the high-speed experiment. The single outlier (orange circle) is likely the result of a higher vibrational mode, of which there can be many, being incorrectly assigned as the primary fruit resonance and measured by the AWETA system. It was excluded from the regression shown in Figure 9-8b.

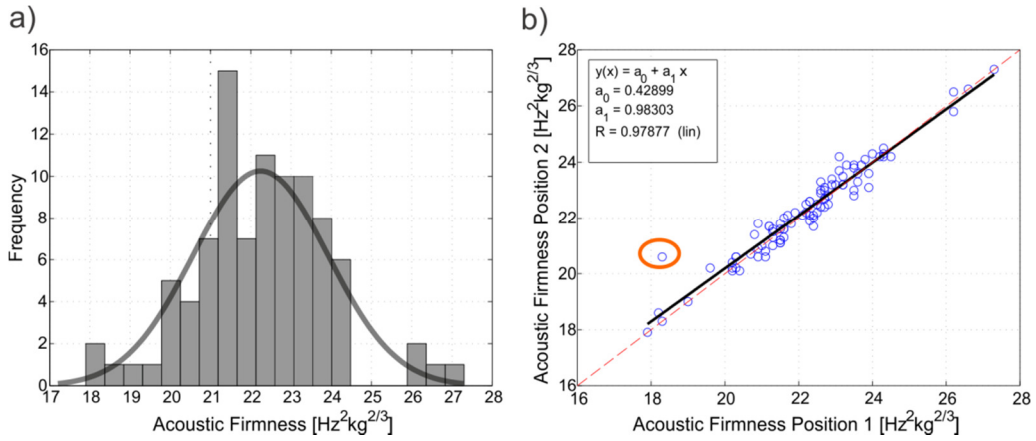

Figure 9-8. (a) Distribution of AWETA acoustic firmness for the 92 'Royal Gala' apples investigated. (b) Relationship between AWETA acoustic firmness measured in the two positions.

9.3.3 Acoustic and Penetrometer Firmness

Figure 9-9a demonstrates that there is no relationship between AWETA acoustic and GUSS penetrometer firmness for the 92 'Royal Gala' apples in this study. This is consistent with the results found in the high-speed experiment (Chapter 6) and is likely a consequence of the storage conditions and the fundamental difference between the measurement principles of the two approaches.

Like the previous experiment, fruit were housed in plastic bins where the humidity was kept high (>90%). This high-humidity storage limited water loss to less than 2%. Shmulevich et al. (2002) found that increasing their humidity from 90% to 95% caused a three times reduction in the acoustic softening rate. The high humidity environment

where the fruit were housed could have reduced the decline of acoustic firmness enough to eliminate a correlation with penetrometer firmness.

Another factor in the disagreement between acoustic and penetrometer firmness could be the fundamental differences between the two approaches. Acoustic firmness measures the stiffness of the fruit flesh. This is an elastic property which does not probe destructive forces. Penetrometer firmness, on the other hand, interrogates both elastic and failure mechanisms. Figure 9-9b illustrates what occurs as the penetrometer probe propagates through fruit tissue. The force measured is a combination of cell shear and compression which is dependent on the fruit cells, the bonding between cells and the extra cellular volume (Abbott, 1999; Abbott et al., 1997).

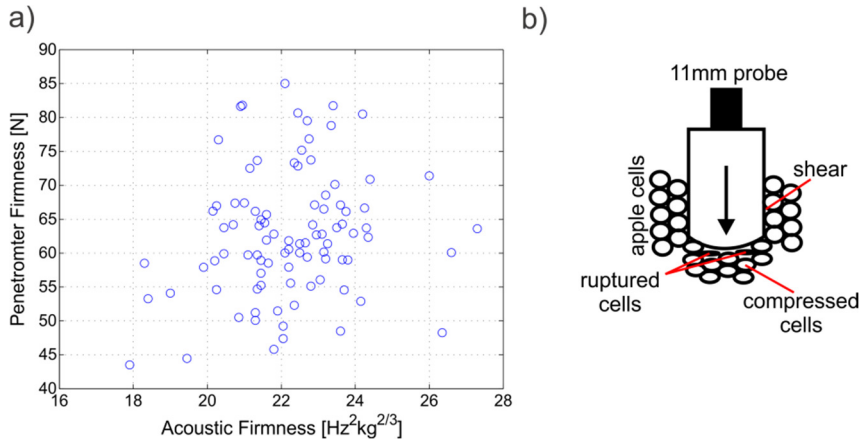

Figure 9-9. (a) Relationship between AWETA acoustic and GUSS penetrometer firmness. (b) Illustrates the different mechanisms taking place during fruit texture analysis.

9.3.4 Inverse Adding-Doubling

9.3.4.1 Optical Properties

Figure 9-10a shows the absorption coefficient calculated using the IAD technique (Chapter 7) on the apple samples over a wavelength range spanning 400 to 1050 nm. The visible peak at 980 nm corresponds to the water absorption peak. The range of absorption coefficients for the water peak extended from 0.046 mm^{-1} to 0.055 mm^{-1}. The black dashed line illustrates the absorption of pure water (Kou et al., 1993). Previous studies have found similar water absorptions in fruit using a variety of techniques. For example, Qin et al. (2009) measured the water absorption on 'Golden Delicious' apples using spatially resolved hyperspectral imaging and found it ranged from 0.025 mm^{-1} to 0.052 mm^{-1}. Saeys et al. (2008), also using the inverse adding-doubling technique, found the water absorption of 'Granny Smith' apples to be approximately 0.05 mm^{-1}. However, apple tissue contains a significant portion (~20%) of intercellular air space

(Mendoza et al., 2007). This should reduce the density of absorbers and hence the absorption coefficient below that of pure water (0.048 mm^{-1} at 980 nm). This was not observed in the results presented, nor consistently in published literature. However, this and the elevated absorption in the region from 550 to 900 nm is consistent with the offset caused by diffuse and direct light loss out the edges of the sample and glass slides, also seen in the Intralipid absorption coefficients during validation of the systems (Chapter 8).

A second, much smaller, absorption peak extending from 0.01 to 0.017 mm^{-1} can be seen at 670 nm corresponding to chlorophyll-a, a green pigment used by plants for photosynthesis. This absorption peak is consistent with reported values in the literature on other apple varieties. Qin et al. (2007) found chlorophyll-a absorptions ranging from 0.003 up to about 0.039 mm^{-1} for 'Golden Delicious' apples using a spatially resolved technique. Cubeddu et al. (2001) found chlorophyll absorptions ranging from 0.013 to 0.017 mm^{-1} for 'Golden Delicious', 'Granny Smith', and 'Starking Delicious' using time resolved reflectance spectroscopy. The other absorption peaks located around 425 nm, 455 nm, and 480 nm form a distinctive spectral pattern corresponding to a combination of chlorophyll-a and carotenoids (Merzlyak et al., 2003). At 450 nm, this absorption extended from 0.09 mm^{-1} to 0.145 mm^{-1}. This region has not been well studied for its relationship with firmness.

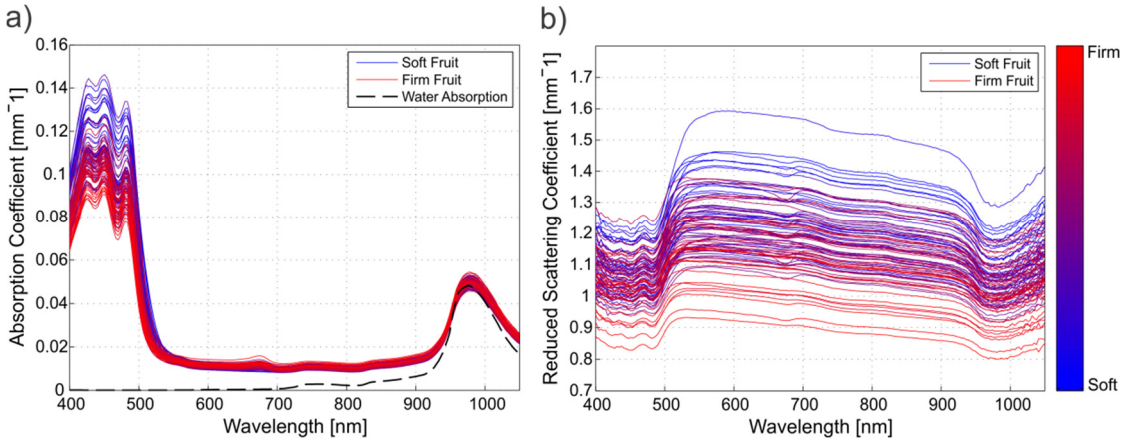

Figure 9-10. (a) Absorption and (b) reduced scattering coefficients from the inverse adding-doubling measurements made on 'Royal Gala' apple slices. Black dashed line shows the absorption coefficient expected for pure water (Kou et al., 1993).

Figure 9-10b shows the measured reduced scattering coefficient, with traces for soft fruit shaded blue and firm fruit shaded red. Softer 'Royal Gala' apples tended to have a higher reduced scattering coefficient than firm fruit. From 550 nm to 900 nm, the profiles followed the behaviour expected from the Mie solution: a monotonic decrease

as wavelength increases. Below 550 nm and above 900 nm there is considerable crosstalk, an effect discussed in Chapter 8, corresponding with the carotenoid, chlorophyll-a, and water absorption peaks. As mentioned in Chapter 8, Zamora-Rojas et al. (2013) suggest crosstalk could in part be due to ill conditioning of the input parameters. In this study no wavelength dependent refractive index and anisotropy factor was measured so a fixed value based on earlier work by Saeys et al. (2008) was used. These fixed values may not have adequately described the behaviour of light inside the samples and may have introduced errors that contributed to this crosstalk. The range of reduced scattering for all fruit samples extended from 0.86 mm^{-1} to 1.48 mm^{-1} at 800 nm. This range was consistent with earlier reports using a hyperspectral imaging technique on 'Golden Delicious' apples, with one report ranging from 1.05 mm^{-1} to 1.15 mm^{-1} at 800 nm and another from 0.9 mm^{-1} to 2.0 mm^{-1} (Cen et al., 2013; Qin et al., 2007).

9.3.4.2 Relationship with Firmness

Figure 9-11 shows the correlation coefficients for AWETA acoustic firmness and the average absorption (a) and reduced scattering (b). Reduced scattering showed a flat, average correlation across the range of 0.13. The absorption coefficient showed two small visible peaks at 522 nm and 955 nm, each with an absolute correlation of 0.2. Earlier reports (Cen et al., 2013; Tu, Jancsok, et al., 2000) have demonstrated correlations between acoustic firmness and optical properties, but this was not apparent in the results presented. However, the earlier work looked at 'Golden Delicious' and 'Granny Smith' apple cultivars and tomato fruit. As previously mentioned, water loss tends to influence acoustic firmness measurements. The fruit in this study were housed in high humidity chambers where weight loss was minimized to less than 2% over the experimental period. Together with the cultivar effects, this may explain the absence of correlation between acoustic firmness and optical measurements that some studies, including ours, have observed.

Figure 9-11b shows the correlation coefficient between penetrometer firmness and the average reduced scattering coefficient. The profile was flat from 550 to 900 nm, with an average correlation coefficient of -0.68. Outside this range, correlation was reduced through crosstalk. In other apple varieties the reduced scattering coefficient increased as penetrometer firmness fell. Negative correlations ranging from -0.70 to -0.75 with penetrometer firmness have been presented for 'Golden Delicious', 'Braeburn', and

'Jonagold' cultivars (Vanoli et al., 2010; Qin & Lu, 2006). Cen et al. (2013), on the other hand, found the opposite for 'Golden Delicious' and 'Granny Smith' varieties: as the fruit softened, the reduced scattering coefficient decreased.

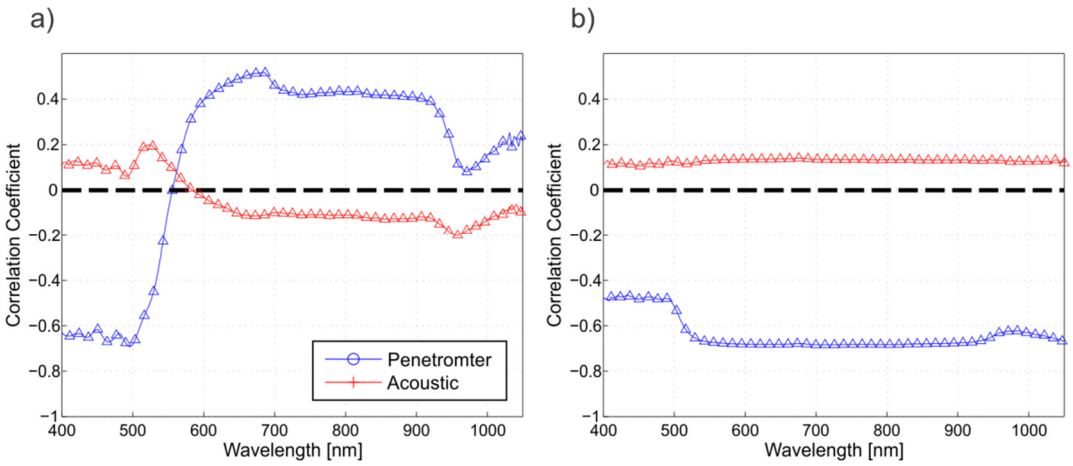

Figure 9-11. Correlation coefficients between the acoustic/penetrometer firmness measurements of 'Royal Gala' apples and the (a) absorption coefficient and (b) reduced scattering coefficient.

Figure 9-11a shows the correlation coefficient between penetrometer firmness and the average absorption coefficient. There were two distinct regions that correlate with firmness. The first region extended from 400 to 500 nm and had a maximum correlation of -0.69 at 500 nm. The second region above 600 nm had a maximum correlation of 0.52 centred on 680 nm. These two correlations corresponded to the carotenoid and the chlorophyll-a pigment absorptions respectively. As fruit ripen, there is a breakdown of chlorophyll and a synthesis of additional carotenoids (Gross, 1987). These pigment changes can be used as an indicator of fruit maturity and firmness (Lu & Peng, 2006). Care needs to be taken, however, as they are secondary effects that occur in parallel with mechanical softening and are likely susceptible to storage and other external conditions.

The broad correlation between absorption and penetrometer firmness from 700 to 900 nm was not expected from the chemistry of the fruit. However, the Intralipid measurements in Chapter 8 showed absorption coefficients are influenced by the scattering behaviour. As the reduced scattering coefficient increases, the light loss reduces. This would lead to a broad positive correlation between penetrometer firmness and the measured absorption coefficient. This suggests that the correlation between 700 and 900 nm, and most of the correlation at 680nm (chlorophyll-a) was not based on absorption but on light losses, which are due to the scattering in the sample.

9.3.5 Multispectral Imaging System

9.3.5.1 Modified Lorentzian

Figure 9-12a shows the extracted intensity profiles for the 904 nm laser. There are two distinct groups that show up in the data. This indicates that a step change occurred that affected the 904 nm laser, reducing its intensity. This occurred between the seventh and eighth experimental sessions effecting the last two measurement days. It may have been caused by a degraded laser or something that effected the alignment of the spatial filter stack. This shift in intensity would cause a step change in the modified Lorentzian full width at half maximum and amplitude parameters. For this reason these samples were removed from the following analysis.

There are clear visible differences in the intensity profiles as the fruit soften. Figure 9-12b shows the intensity profiles extracted from the multispectral images collected at 904 nm (orientation one, replicate one). Each profile is coloured from blue to red representing soft to firm fruit based on penetrometer firmness. A close up view shows that the soft fruit tends to have lower intensities compared to the firm fruit. Comparing these changes to the effects each parameter has in the modified Lorentzian model we should expect to see a significant penetrometer firmness signal from the 'd' parameter as it describes the curvature of the profile. There may also be some correlation with the full width at half maximum (FWHM). Similar behaviour to this was observed at 685, 850, and 980 nm.

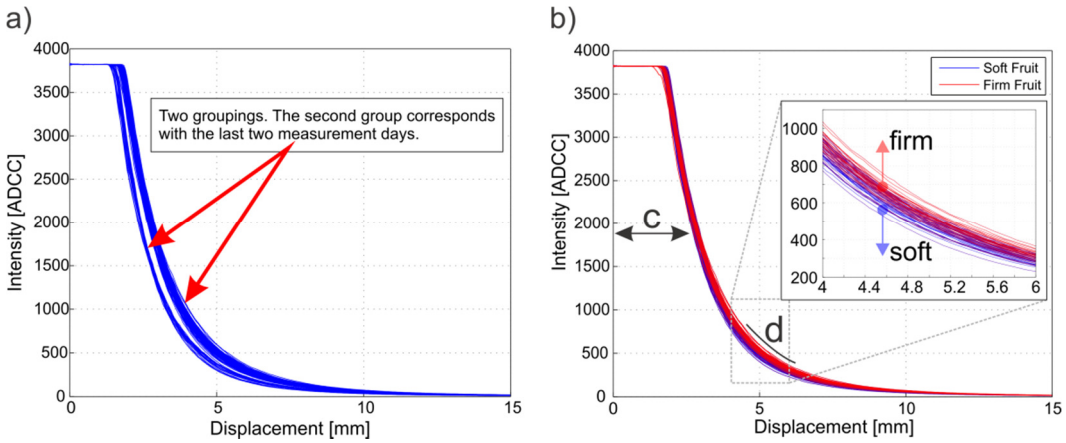

Figure 9-12. a) 904 nm curves show two distinct groupings. This corresponded with the last two days of measurement and indicates an intensity step change with the 904 nm laser. (b) Example intensity profiles at 904 nm coloured from blue to red representing soft to firm fruit (penetrometer).

Modified Lorentzian Parameter Values

The four parameters extracted from the modified Lorentzian curve fits for all 77 'Royal Gala' apples (excluding the eighth and ninth day's fruit) at the four laser wavelengths are shown in Figure 9-13. Each data point is the average of the parameter values found for each replicate measurement from the two orientations. Each data point is shaded from blue to red indicating the penetrometer firmness of the fruit (soft to firm) as measured by the texture analyser.

Figure 9-13a shows the parameters found for the background term ('a' parameter). This is the asymptotic value expected from the decaying intensity profile. The average value of the 'a' parameter at all wavelengths is negative. A background value of about zero is expected if the dark image is measured and subtracted correctly. This indicates that either the dark correction is larger than expected or that the data included in the fit does not contain enough character for the model to correctly converge on the true background term. The variation at each wavelength appeared to be similar unlike the high-speed experiment where the 685 nm laser showed more variation. In this study, the fruit are sliced to remove the skin and expose a flat surface of fruit flesh. The removal of this skin would have reduced the variation at 685 nm because previously the light would have been absorbed by chlorophyll pigments in the skin (Saeys et al., 2008). This absorption would effectively vary the incident intensity based on the skin condition of each fruit. The shading of each data point based on penetrometer firmness indicates that firmer fruit tends to have a lower background value at all four wavelengths. This was consistent with the profiles presented by Peng & Lu (2006a).

Figure 9-13b shows the modified Lorentzian parameter values that represent amplitude ('b' parameter). As discussed in Chapter 6, this should be near the saturation intensity of the camera due to the inclusion of this region in the curve fit. In this study, the 685 nm laser appeared to have higher intensity values compared to the other three wavelengths. The variation at 685 nm is also higher than the other wavelengths. This is due to absorption from chlorophyll pigments inside the fruit flesh that vary between fruit as they mature. At all three wavelengths the firm fruit (red) appear to have a higher intensity value compared to the soft fruit (blue). This is in contrast with the results of Peng & Lu (2006a) who found soft fruit had higher amplitude values.

Figure 9-13c shows the full width at half maximum ('c' parameter) values at each laser wavelength. In the high-speed experiment, there was more variation in the 685 nm values compared to the other wavelengths. This was not observed in the current study and, like the background parameter, is likely the result of removing the fruit skin preventing intensity variations due to chlorophyll absorption. At 685, 850 and 904 nm the soft fruit had higher 'c' parameter values consistent with the results of Peng & Lu (2006a), while at 904 nm firm fruit had higher 'c' parameter values.

Figure 9-13d shows the slope found in the FWHM region of the intensity profiles ('d' parameter). The results show an increase in the slope as wavelength increases. Also, at each wavelength the soft fruit (blue) have steeper profiles compared to the firm fruit (red) consistent with the curves shown in Figure 9-12b. This is consistent with the IAD results where scattering increased as fruit softened. This increase in scattering would constrain the propagation of light increasing the slope of the intensity profile. In the study by Peng & Lu (2006a) the opposite was found. Their soft fruit had lower values compared to firm fruit.

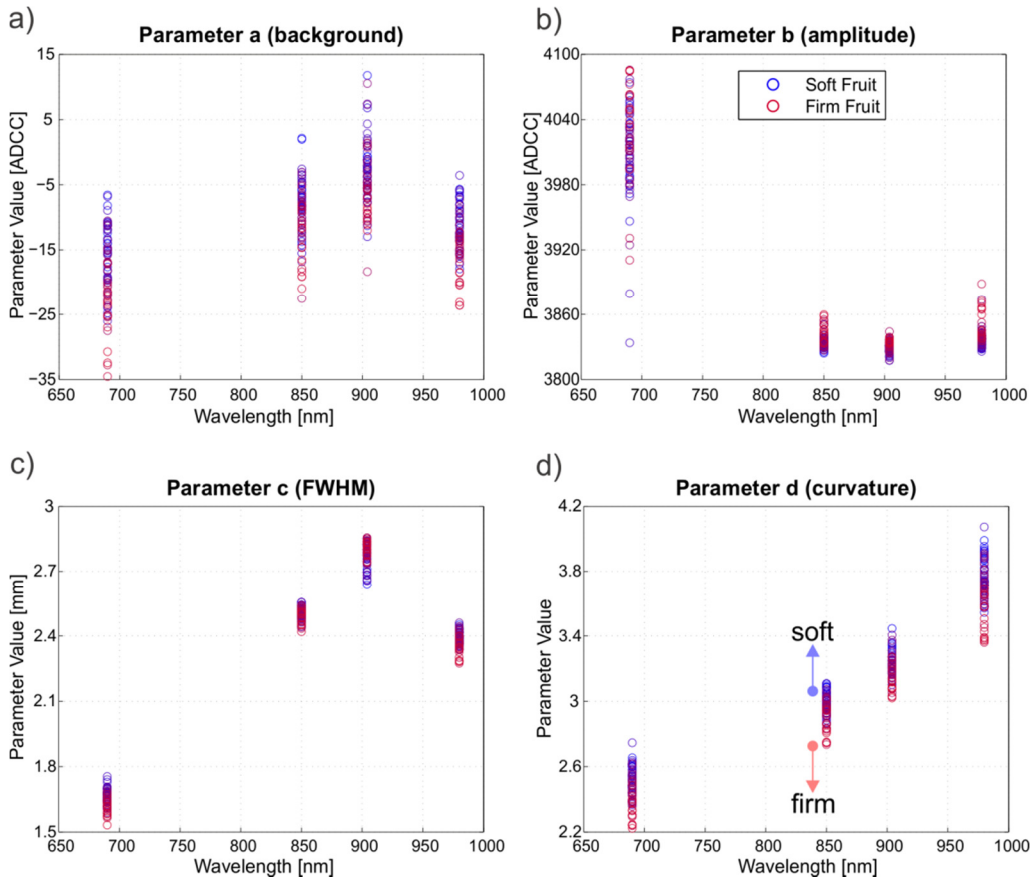

Figure 9-13. Modified Lorentzian parameters for the four laser intensity profiles on 77 'Royal Gala' apples.

Relationship with Fruit Firmness

Figure 9-14 shows the relationships between penetrometer firmness and the slope parameter ('d') at all four laser wavelengths. The slope parameter is shown because it had the highest correlations with penetrometer firmness compared to the other parameters. Each data point consists of averaged parameter values from the four replicates and two orientations. This provided a whole fruit measurement, reduced the noise, and improved the correlations.

The correlations between penetrometer firmness and the slope parameter at all wavelengths are much stronger compared to the high-speed experiment (Chapter 6). In that experiment, the best correlation with penetrometer firmness was the FWHM parameter ('c') at 685 nm (R = -0.33). However, also in the high-speed study the correlation coefficients at 850 and 904 nm were higher for the slope parameter. This suggested that the slope parameter could better describe firmness at those wavelengths. This result is consistent with those in the current study where the slope

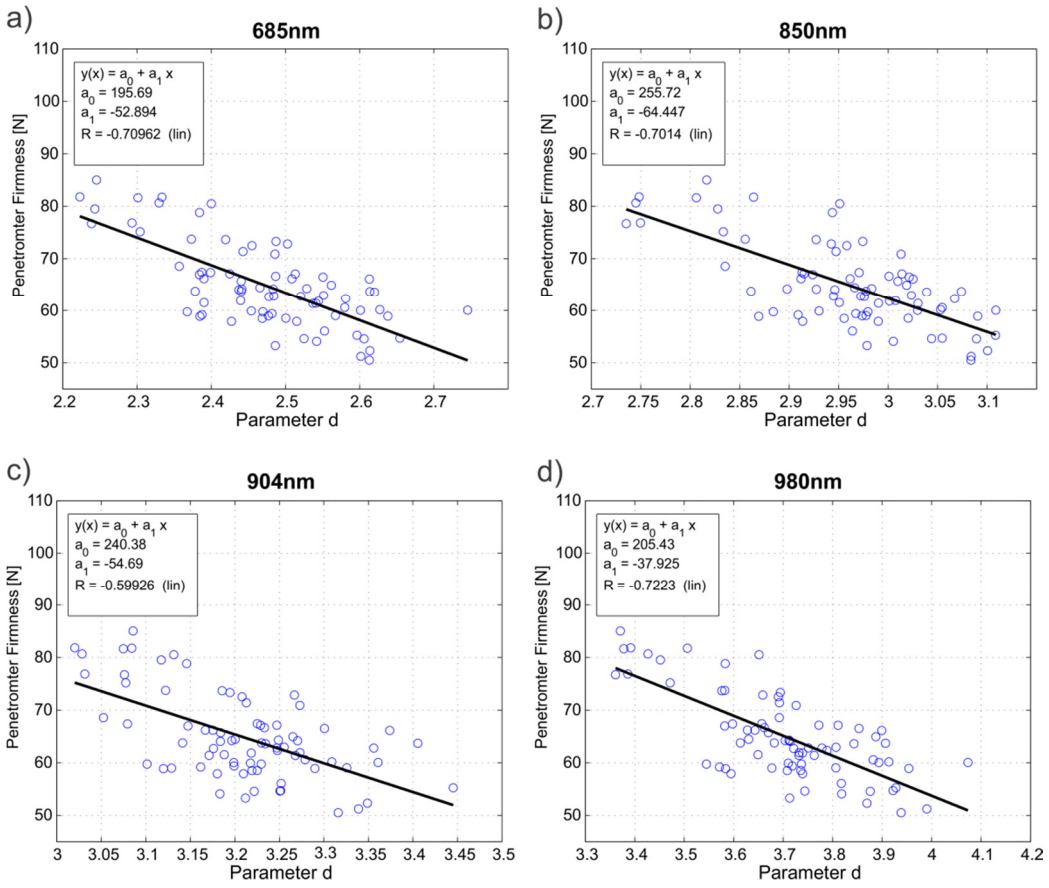

Figure 9-14. Relationship between penetrometer firmness and the slope ('d') parameter from the modified Lorentzian model at (a) 685 nm, (b) 850 nm, (c) 904 nm, and (d) 980 nm.

parameter showed the highest correlation with penetrometer firmness at all wavelengths. The highest overall correlation was between penetrometer firmness and the slope parameter at 980 nm and was closely followed by the slope parameter at 685 nm (R = 0.72 and 0.71 respectively). These two wavelengths correspond to regions of higher absorption, at 980 nm due to water and 685 nm due to chlorophyll. This suggests that the modified Lorentzian model may describe the intensity profiles better when absorption is higher, allowing the curve fit process to extract a stronger firmness signal.

Table 9-1 summarises the correlations and standard errors for simple linear models between each modified Lorentzian parameter and firmness at all four wavelengths. These results compare favourably with other studies. Peng & Lu (2006a) used all four modified Lorentzian parameters in an MLR model at each wavelength to predict penetrometer firmness on 180 'Red Delicious' and 'Golden Delicious' apples. Their best result for 'Red Delicious' apples was at 810 nm with a standard error of 8.81 N and a correlation coefficient of 0.58. For 'Golden Delicious' apples, they found 690 nm performed the best with a standard error of 8.64 N and a correlation coefficient of 0.5. Our single slope parameter ('d') models show a stronger relationship with correlation coefficients ranging from 0.60 to 0.72 and standard errors ranging from 5.54 to 6.42 N.

Peng & Lu (2008) also investigated the relationship at individual wavelengths between the modified Lorentzian parameters and penetrometer firmness. They found correlations outside of the chlorophyll pigment absorption region (450 to 580 nm and 700 nm to 1000 nm) were quite low (R = 0.30). At 675 nm, they found a maximum correlation of 0.60 illustrating that chlorophyll absorption played an important role in their prediction models. Our results do support Peng & Lu's (2006a, 2008) assertion that single wavelength models are not sufficient for accurate prediction alone and that

Modified Lorentzian Parameter	685 nm		850 nm		904 nm		980 nm	
	R	RMSE	R	RMSE	R	RMSE	R	RMSE
a	-0.66	5.99 N	-0.56	6.63 N	-0.42	7.26 N	-0.72	5.60 N
b	0.21	7.83 N	0.60	6.42 N	0.50	6.95 N	0.65	6.12 N
c	-0.61	6.33 N	-0.35	7.52 N	0.37	7.44 N	-0.58	6.52 N
d	-0.71	5.65 N	-0.70	5.71 N	-0.60	6.42 N	-0.72	5.54 N

Table 9-1. Correlation coefficients between penetrometer firmness and the modified Lorentzian parameters at all wavelengths.

combinations should be used to improve predictions.

The relationships between modified Lorentzian parameters and acoustic firmness in this study are all poor with correlation coefficients ranging from 0 to 0.23 (Table 9-2). The highest correlation was found at 980 nm with the slope parameter. This had a similar correlation (R = 0.20) to the slope parameter at 904 nm, in the high-speed experiment, the highest correlation in that study. This is consistent with the acoustic firmness measurement's high sensitivity to water loss and the strong water absorption peak in the 980 nm region (Landahl, 2007; Belie et al., 1999). This relationship is likely weakened by our attempts to limit water loss through high humidity storage.

Modified Lorentzian Parameter	685 nm		850 nm		904 nm		980 nm	
	R	RMSE	R	RMSE	R	RMSE	R	RMSE
a	0.14	1.53	0.16	1.53	0.11	1.54	0.12	1.54
b	-0.05	1.55	-0.13	1.54	-0.14	1.53	-0.16	1.53
c	0.18	1.52	-0.07	1.54	0.00	1.55	0.23	1.51
d	0.19	1.52	0.17	1.53	0.18	1.53	0.15	1.53

Table 9-2. Correlation coefficients between acoustic firmness and the modified Lorentzian parameters at all wavelengths. Standard error values have units of $Hz^2g^{2/3}$.

Multiple Linear Regression Firmness Prediction

Multiple linear regression was used to build models with the modified Lorentzian parameters that could predict firmness. The models were built using a venetian blind cross-validation with 10 data folds on all 16 parameters (four modified Lorentzian terms at the four wavelengths). Figure 9-15 shows the results from the venetian blind cross validation. The resulting correlation coefficient was 0.63 with a standard error of cross validation (RMSECV) equal to 6.4 N. This is an improvement over the model

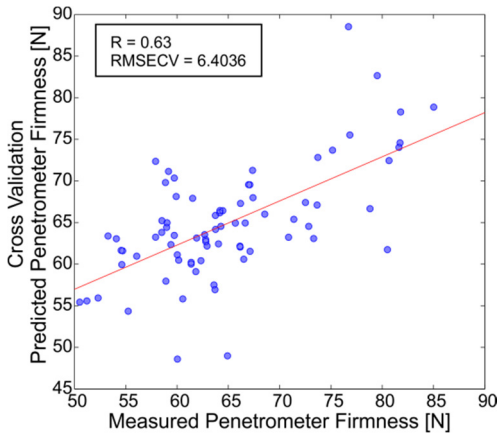

Figure 9-15. Cross-validated multiple linear regression model used to predict penetrometer firmness from the modified Lorentzian parameters.

built using data collected on the high-speed MSI system where the correlation coefficient was 0.42 and the RMSECV 8.79 N.

The loadings from the multiple linear regression model are shown in Figure 9-16. The most heavily loaded parameters are the background ('a') and slope ('d') at 685, 904, and 980 nm. All parameters at 850 nm do not contribute significantly and may introduce noise to the model. These parameters were removed, and the modelling was redone using only the background and slope parameters at 685, 904, and 980 nm (blue stars in Figure 9-16).

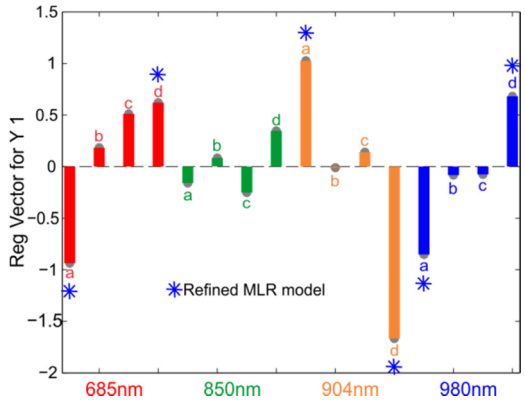

Figure 9-16. Multiple linear regression loadings for the model predicting penetrometer firmness. From this 'a' and 'd' was selected at 685, 904, and 980 nm.

The refined multiple linear regression model showed some improvement (Figure 9-16). The correlation coefficient increased to 0.71 (compared to 0.63) and the standard error decreased 5.65 N (compared to 6.4 N). This indicates that the parameters removed from the model were detrimental to the prediction.

The results from the MLR model are comparable to earlier studies. Peng & Lu (2004) used a liquid crystal tunable filter based multispectral imaging system along with modified Lorentzian parameters to predict firmness on 180 'Red Delicious' apples. They found using an optimized seven wavelength model (28 parameters in total) a correlation coefficient of 0.82 and a SEP of 6.64 N. Lu & Peng (2007) used a discrete four wavelength filter based multispectral imaging system on 547 'Golden Delicious' and 572 'Red Delicious' apples. Images were also parameterised using modified Lorentzian parameters. They found for 'Golden Delicious' apples a correlation coefficient of 0.86 and a SEP of 6.86 N. For 'Red Delicious' apples the correlation was the same (R = 0.86), but the SEP increased to 7.24 N. While the standard error in our model is lower it is important to consider that the sample numbers are higher and the

firmness ranges slightly different in the other studies. Also, the fruit in this study are sliced to eliminate variation caused by skin and fruit shape.

Another useful indicator of merit for the MLR model, commonly used in near-infrared spectroscopy, is the ratio of standard error of prediction to the standard deviation (RDP) (Williams & Norris, 1987). For the model developed in this study using the modified Lorentzian parameters the RDP is 1.5, indicating that the fruit could be separated into roughly 1.5 groups. This is considered quite low and is unlikely to be sufficient for a commercial fruit firmness system.

No suitable MLR models were identified between acoustic firmness and the modified Lorentzian parameters. This was expected as the individual correlations (Table 9-2) were all poor.

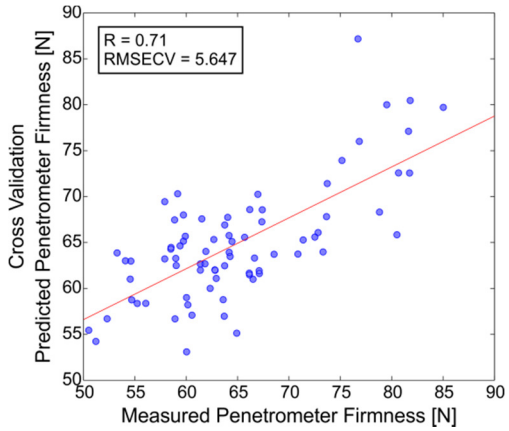

Figure 9-17. Cross-validated multiple linear regression model used to predict penetrometer firmness from a selection of the modified Lorentzian parameters chosen based on the loadings in Figure 9-16. These include 'a' and 'd' at 685 nm, 'a' and 'd' at 904 nm, and 'a' and 'd' at 980 nm.

9.3.5.2 Optical Property Extraction

The optical properties of each fruit sample were extracted by fitting the diffusion theory model to the intensity profiles. In this analysis, all 92 'Royal Gala' fruit were included. The step change problem at 904 nm identified in the modified Lorentzian section should not affect the optical property extraction. The amplitude term in the diffusion theory model will account for the intensity step change in the data and is not used to form predictive models.

Figure 9-18a shows an example curve fit carried out on the extracted intensity profile from one of the fruit illuminated by the 980 nm laser. The diffusion model fits the experimental data very well. Figure 9-18b shows the correlation coefficients for each of the curve fits carried out on all 92 apples. The correlation coefficients at 980 nm appear

lower and fluctuate more than the other wavelengths, however they are still very high. For diffusion theory to be valid, one of the main requirements is that the reduced scattering coefficient must be much larger than the absorption coefficient (Farrell et al., 1992; Martelli et al., 2000). The 980 nm laser corresponds to the highest absorption peak (water). At this wavelength, the IAD system measured average absorption as 0.05 mm^{-1} and averaged reduced scattering as 1.03 mm^{-1}. This means the scattering coefficient is 20 times greater. At 685 nm the average absorption measured was 0.01 mm^{-1} and averaged reduced scattering was 1.19 mm. In this case, the scattering coefficient is 119 times greater. While light transport at 980 nm would still be dominated by scattering, the greater contribution of absorption may explain the slightly poorer fits found at this wavelength.

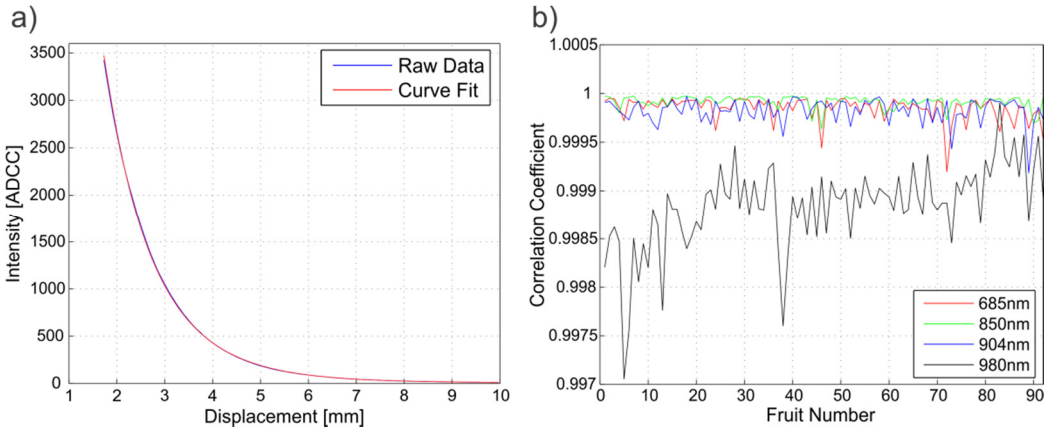

Figure 9-18. (a) An example curve fit from an image collected on one of the 'Royal Gala' apples illuminated with the 980 nm laser. (b) Correlation coefficients for the diffusion model curve fits on all 92 'Royal Gala' apples. Data is from the first orientation and first placement of the fruit.

Extracted Optical Properties

The extracted absorption and reduced scattering coefficients are shown in Figure 9-19. The four replicate measurements at the two orientations are fruit averaged to reduce noise and provide an overall fruit measurement. Seven fruit were removed as outliers because their curve fitting was unstable, and the results were not consistent with the other fruit. The shaded regions indicate results from earlier studies for comparison. The first by Qin et al. (2007) on 'Golden Delicious' apples is shown in gray, the second by Cen, Lu & Mendoza (2011) on 'Golden Delicious' and 'Red Delicious' apples is shown in red, and third is a study again on 'Golden Delicious' apples by Cen et al. (2013) shown in blue. Each data point in the present study is shaded from blue to red indicating soft to firm fruit based on penetrometer firmness.

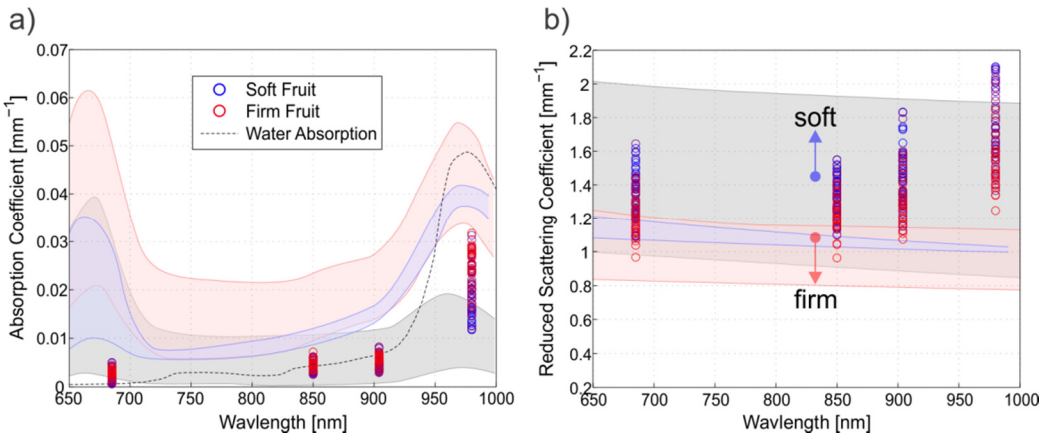

Figure 9-19. Absorption (a) and reduced scattering coefficients (b) plotted at each of the four laser wavelengths. Grey, red, and blue shaded regions represent data from Qin et al. (2007), Cen, Lu & Mendoza (2011), and Cen et al. (2013) respectively. Dashed line indicates the absorption coefficient of pure water (Kou et al., 1993).

At 685, 850, and 904 nm the absorption coefficients (Figure 9-19a) agree with the results obtained by Qin et al. (2007). The other studies by Cen, Lu & Mendoza (2011) and Cen et al. (2013) show higher absorption coefficients across the full wavelength range. The absorption coefficients at 685 nm in these earlier studies show elevated absorption levels due to the chlorophyll pigments. This was not observed in the current study and is consistent with the IAD results (Figure 9-10a) which showed only a small chlorophyll absorption peak. This small absorption, in contrast with other studies, may be due to the removal of apple skin which contains a significant quantity of chlorophyll (Saeys et al., 2008).

At 980 nm the absorption coefficient increases, with the extracted coefficients extending from 0.011 mm^{-1} to 0.031 mm^{-1}. This corresponds to the main water absorption peak in the current spectral region (650 nm to 1000 nm). For reference, the absorption coefficient of pure water is shown by the black dashed line in Figure 9-19a (Kou et al., 1993). The absorption coefficient values for the 'Royal Gala' apples in this study appear higher than those found in the study by Qin et al. (2007) on 'Golden Delicious' apples but lower than those found in the studies by Cen, Lu & Mendoza (2011) and Cen et al. (2013) on 'Golden Delicious' and 'Red Delicious' apples. The absorption in this region should be less than that of pure water due to a significant amount (~20%) of intercellular air space (Mendoza et al., 2007). While this was not observed in the IAD results with water absorption ranging from 0.046 mm^{-1} to 0.055 mm^{-1}, it was observed here with the absorption coefficients measured at 980 nm falling below the absorption coefficient of pure water.

The reduced scattering coefficients (Figure 9-19b) are in agreement with the values presented on 'Golden Delicious' apples found by Qin et al. (2007). There was a consistent pattern in the data where soft fruit (blue) had higher reduced scattering coefficients compared to firm fruit (red). This was consistent with the results found using the IAD system (Figure 9-10b) and with other studies (Vanoli et al., 2010; Qin & Lu, 2006; Cubeddu, D'Andrea, Pifferi, Taroni, Torricelli, Valentini, Dover & Johnson, 2001). The reduced scattering coefficients at 980 nm were higher than expected exceeding the range of the earlier study shown in grey. This may have been a consequence of the poorer curve fit results and reduced satisfaction of the diffusion theory assumptions at 980 nm (Figure 9-18).

Relationship with Fruit Firmness

Figure 9-19b showed firmer fruit had consistently lower reduced scattering coefficients compared to soft fruit across all four laser wavelengths. Figure 9-20 shows the quantitative relationships between these reduced scattering coefficients and penetrometer firmness. The correlation coefficients range from -0.62 to -0.70 with the highest found at 980 nm. This is in strong contrast to the results found in the high-speed experiment where no relationships were found. These correlations support the hypothesis that scattering properties relate to the firmness characteristics of fruit (Qin et al., 2007; Cen et al., 2011).

There is also a strong agreement between these relationships and those found using the IAD system. The correlation coefficients between penetrometer firmness and the reduced scattering coefficient measured using the IAD system were -0.68 at 685, 850, and 904 nm, and reduced to -0.6 at 980 nm. The weaker correlation at 980 nm for the IAD system is likely a result of the crosstalk issue described in section 9.3.4.

Similar correlations have also been found between optical properties and penetrometer firmness using other optical systems on different apple varieties. Vanoli et al. (2010) investigated 'Braeburn' apples using time resolved reflectance spectroscopy (TRS). They found correlation coefficients of -0.75 and -0.742 between sensory firmness and the reduced scattering coefficients at 790 and 912 nm. Vanoli et al. (2013), again using their TRS system, found similar results on another set of 'Braeburn' apples with a correlation coefficient of -0.52 between reduced scattering, and this time, penetrometer firmness but were unable to get a significant correlation for 'Cripps Pink' apples ($R = 0.21$). Qin & Lu (2006) found a peak negative correlation of -0.70 at 780 nm

between the reduced scattering coefficient and penetrometer firmness. Their study looked at 'Golden Delicious' apples and used a hyperspectral imaging system. More recently Cen et al. (2013) found the opposite. As their 'Golden Delicious' and 'Granny Smith' apples softened, the reduced scattering coefficient decreased.

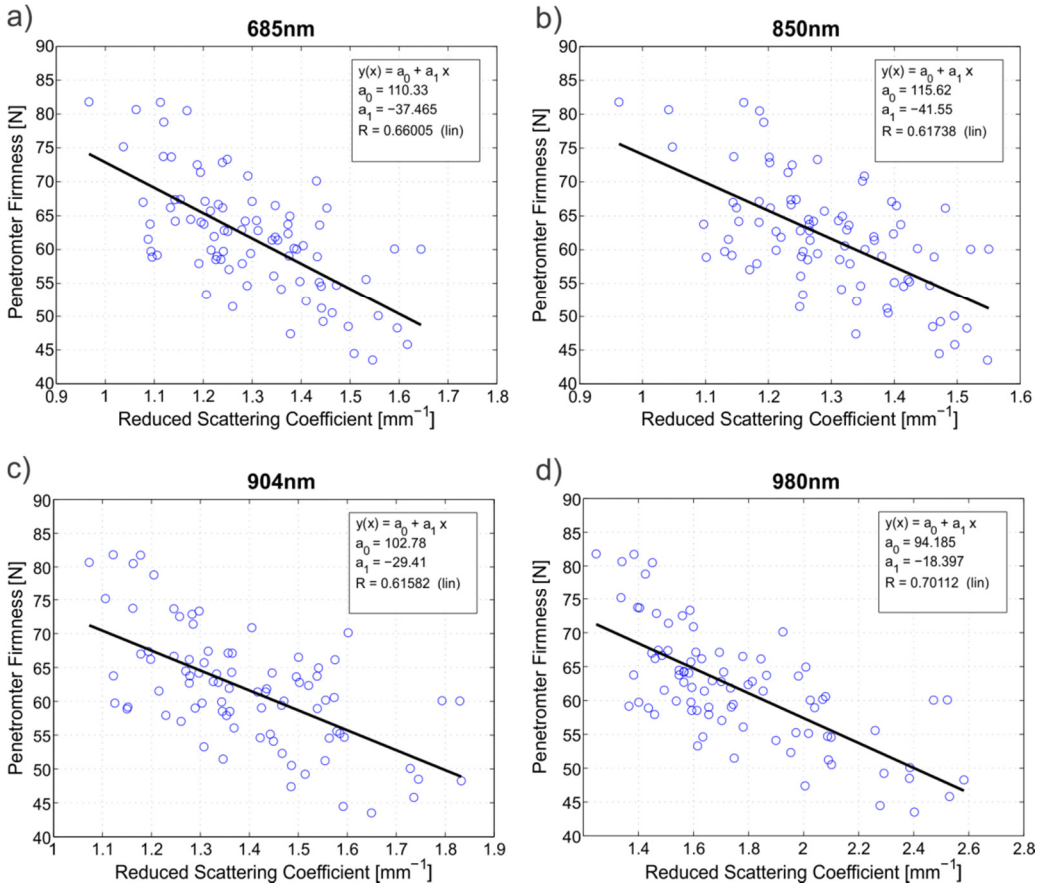

Figure 9-20. Relationships between penetrometer firmness and the reduced scattering coefficient at (a) 685 nm, (b) 904 nm, (c) 904 nm, and (d) 980 nm.

Hertog et al. (2004) found that the enzymatic breakdown of the cell walls and water loss significantly affect fruit firmness. These two effects would alter the behaviour of light inside the fruit tissue. Water loss leads to an increase in air filled pores and a reduction in the average cell size (Bobelyn et al., 2010). These air spaces provide strong refractive index mismatches, increasing light scattering. In contrast, enzymatic breakdown of the cell walls will weaken cell to cell bonding and diminish the complex structure inside the tissue. This will result in a reduction of the number of scattering boundaries and hence reduce the scattering coefficient (Bobelyn et al., 2010). This may explain why Cen et al. (2013) found their reduced scattering coefficient decreased as fruit softened, in contrast to results from other studies, where it increased. Enzymatic breakdown may also open new intercellular spaces as adhesion between cell walls

weakens, creating new boundaries and scattering surfaces (Mohr, 1979; Tu et al., 1996). Harker & Hallett (1992) demonstrated such cell separation with fracture surfaces on soft and firm 'Braeburn' apples when they captured cryo-transmission electron microscopy images (Cryo-TEM). The TEM images suggested a greater tendency for soft fruit to tear in the middle lamella region. This creates additional air spaces (refractive boundaries), increasing light scattering. Our results are consistent with this hypothesis: water loss was minimized to less than 2% over the course of the experiment, yet the reduced scattering coefficient still increased as fruit softened.

The relationships between absorption coefficient and penetrometer firmness found using the MSI system are shown in Figure 9-21. The correlations are all positive indicating that as fruit softened the absorption coefficients decreased. This is consistent with the relationships found using the IAD system. The drop in absorption at 685 nm as fruit soften (R = 0.44) corresponds to the breakdown of chlorophyll expected as the fruit mature (Gross, 1987; Zude et al., 2006). This relationship is weaker than those

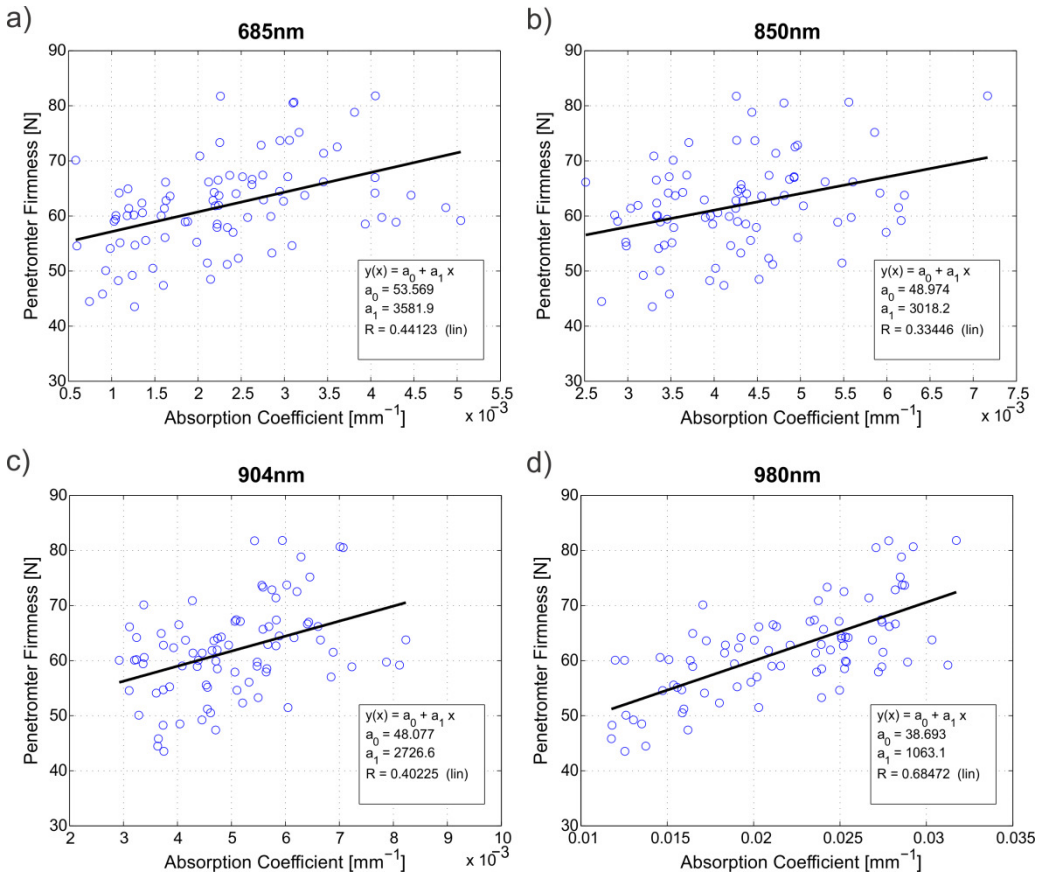

Figure 9-21. Relationships between penetrometer firmness and the absorption coefficient at (a) 685 nm, (b) 904 nm, (c) 904 nm, and (d) 980 nm.

found in other studies. McGlone et al. (2002), for example, found a correlation coefficient (R = 0.69) between absorbance at 680 nm and penetrometer firmness. Their measurements were made on 'Royal Gala' apples using a visible/near-infrared spectroscopic system. One significant difference is that the skin was present in that study which likely increased the chlorophyll signal (Saeys et al., 2008). As discussed in the adding-doubling results section (9.3.4), chlorophyll breakdown is a secondary effect which has not been directly linked to the mechanical softening of fruit. It also varies significantly with harvest date (McGlone et al., 2002) and suffers from seasonal variability (Zude et al., 2006).

The highest correlation between absorption and penetrometer firmness was found at 980 nm (R = 0.68) corresponding to water absorption. While the fruit were housed in high humidity chambers to limit water loss, preventing it completely was not realistic. We were left with, on average, 2% mass loss over the experimental period. This parallel process would have reduced the absorption coefficient and may explain why this relationship with firmness exists.

The relationships between optical properties and acoustic firmness were similar to those of the modified Lorentzian parameters (Table 9-3). There was no clear relationship at any of the wavelengths with low correlation coefficients ranging from 0.08 to 0.18. This is also consistent with the poor relationship found using the IAD system and suggests, for the storage conditions used in our experiment, there is no relationship between the optical properties of 'Royal Gala' apples and its acoustic firmness.

	685 nm		850 nm		904 nm		980 nm	
	R	**RMSE**	**R**	**RMSE**	**R**	**RMSE**	**R**	**RMSE**
Absorption Coefficient	-0.12	1.69	-0.08	1.70	-0.11	1.69	-0.08	1.70
Reduced Scattering Coefficient	0.18	1.67	0.16	1.68	0.18	1.67	0.11	1.69

Table 9-3. Correlation coefficients between acoustic and either the measured absorption or reduced scattering coefficients. Standard error values have units of $Hz^2g^{2/3}$.

Multiple Linear Regression Firmness Prediction

In a similar way to the modified Lorentzian parameters, the optical properties were used to build multiple linear regression models that could predict penetrometer firmness. The same venetian blind cross-validation was used with 10 data folds. The model was constructed using both the absorption and reduced scattering coefficients (total of 8 factors) as this has been shown to provide the best prediction models (Vanoli

et al., 2011; Rizzolo et al., 2010; Vanoli et al., 2010). Figure 9-22 shows the results of the venetian blind cross-validation. The final model has a correlation coefficient of 0.79 and a standard error of cross validation equal to 5.98 N.

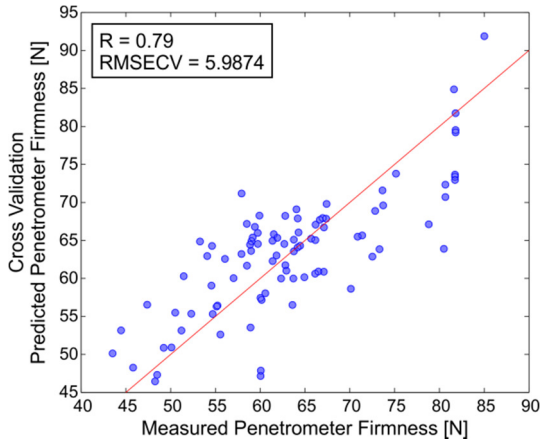

Figure 9-22. Cross-validated multiple linear regression model used to predict penetrometer firmness from the combined absorption and reduced scattering coefficients.

Figure 9-23 shows the loadings used by the multiple linear regression model. The model appears to utilise all of the absorption coefficients (green) but only the reduced scattering coefficient at 685 nm and 904 nm. This suggests that the reduced scattering coefficients at 850 and 980 nm may be redundant. These parameters were removed, and a new MLR model was developed.

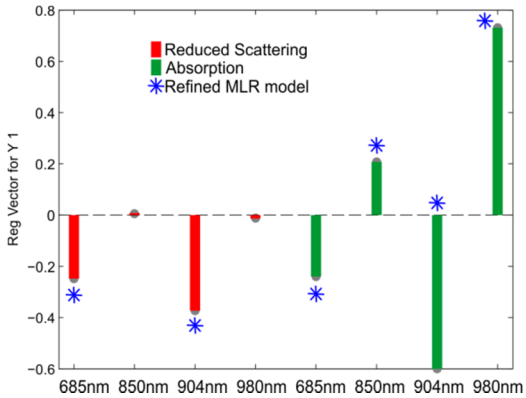

Figure 9-23. Loadings for the MLR model used to predict penetromter firmness.

Figure 9-24 shows the MLR model generated using the reduced scattering at 685 and 904 nm and the absorption coefficients at all four wavelengths (blue stars in Figure 9-23). In this case, the cross validation (Figure 9-24b) had a higher correlation coefficient of 0.8 and a smaller standard error of 5.87N. The removal of redundant parameters from the MLR model has helped reduce noise and make it more robust.

The performance of the models is similar to other studies. Vanoli et al. (2011), for example, investigated models to predict firmness in 60 'Pink Lady' apples using combinations of absorption and reduced scattering coefficients from their TRS system. They used a partial least-squares regression analysis (PLS) to construct prediction models. The best performing model had a correlation coefficient of 0.91 and a standard error of validation equal to 5.44 N. Qin et al. (2009) used a hyperspectral imaging system to measure the optical properties of 600 'Golden Delicious' apples. They formed MLR models to predict penetrometer firmness and found the best result when combining absorption and reduced scattering spectra. Their model had a correlation coefficient of 0.857 and a standard error of prediction equal to 6.07 N. Cen et al. (2011) also used a hyperspectral imaging system to make optical property measurements on 1039 'Golden Delicious' and 1040 'Red Delicious' apples. They then used PLS to form prediction models for penetrometer firmness. For 'Golden Delicious' apples, they found a model with a correlation coefficient of 0.89 and a SEP of 7.89 N, and for 'Red Delcicious' apples a correlation coefficient of 0.86 and a SEP of 8.94 N. The same caution must be taken here as with the modified Lorentzian models. The studies by Qin et al. (2009) and Cen et al. (2011) use significantly more fruit and have a different firmness ranges which will likely affect the performance of their regression models. They are also investigating whole fruit, correcting for fruit shape using mathematical models and ignoring skin effects.

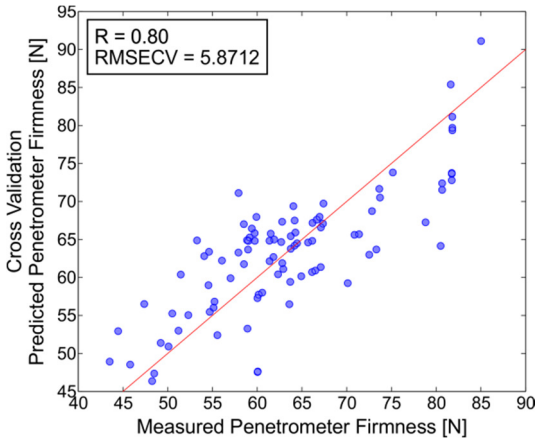

Figure 9-24. MLR model excluding scattering at 850 and 904 nm.

Similar to the modified Lorentzian results, no suitable MLR models were identified between acoustic firmness and the optical properties. This was expected as the relationships between the individual optical properties and acoustic firmness were weak.

9.3.6 Optical Properties Comparison

Figure 9-25 and Figure 9-26 compare the reduced scattering and absorption coefficients measured by the MSI and IAD systems at 685, 850, 904, and 980 nm. The red line shows the one-to-one relationship. The reduced scattering coefficient measured by the IAD system is consistently lower compared to the MSI system (Figure 9-25). This underestimation increases both as the reduced scattering coefficient and wavelength increases. This is not consistent with the validation measurements made with Intralipid where the reduced scattering coefficients measured using the IAD system were typically higher than those measured using the MSI system and there was no obvious trend with wavelength (Chapter 8). However, like the validation measurements, there is a good correlation between the two measurement systems with correlation coefficients of 0.73, 0.74, and 0.71 at 685, 850, and 904 nm, respectively. At 980 nm the correlation is lower at 0.68 and the results from the IAD system are almost flat. This reduced correlation and apparent inability to measure the scattering in the 980 nm

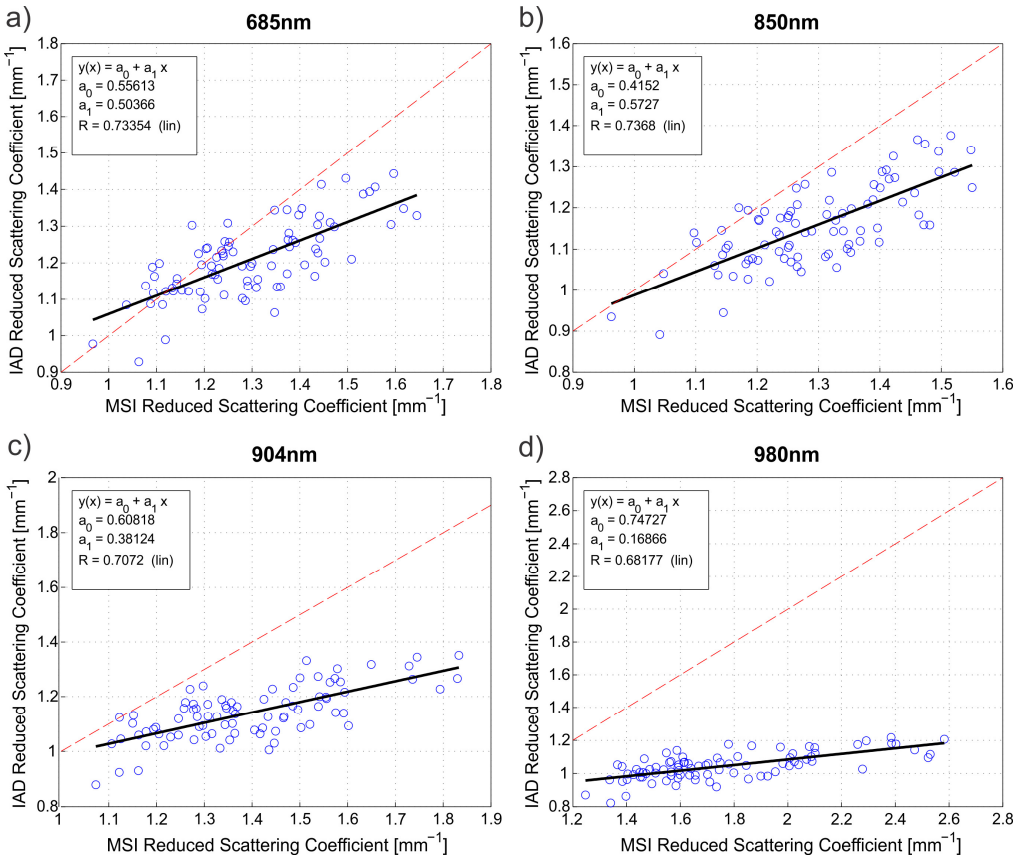

Figure 9-25. Comparison between the reduced scattering coefficient found using the IAD and MSI systems at (a) 685 nm, (b) 850 nm, (c) 904 nm, and (d) 980 nm.

region is likely due to crosstalk, most significant in the regions where absorption is high such as the 980 nm water peak.

The absorption coefficients had lower correlations of 0.51, 0.45, and 0.31 at 685, 850, and 904 nm respectively. While at 980 nm, there was no correlation at all (R = 0.07). The absorption coefficient measured by the IAD system shows a considerable offset, overestimating the absorption coefficient compared to the measurement using the MSI system. Like with the validation results on Intralipid this offset was the result of the light loss (Chapter 8). Light loss occurs out the edges of the fruit sample and glass slides. This loss is assumed by the algorithm to be due to absorption causing an overestimation. Cen & Lu (2010) saw similar absorption coefficient overestimation when comparing their hyperspectral measurement system to the inverse adding-doubling approach. These issues need to be resolved before a fair comparison of the absorption coefficients measured with the two systems can be made.

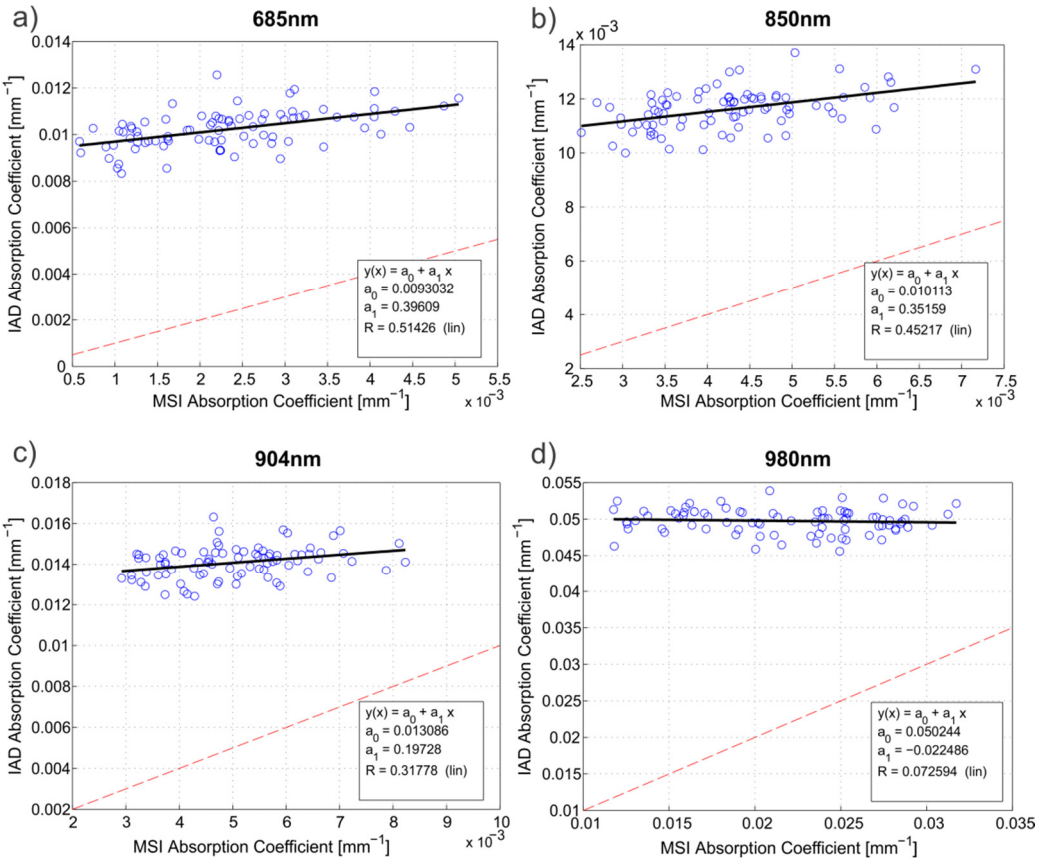

Figure 9-26. Comparison between the absorption coefficient found using the IAD and MSI systems at (a) 685 nm, (b) 850 nm, (c) 904 nm, and (d) 980 nm.

9.3.7 Discussion

The 'Royal Gala' apples used in this study covered a wide firmness range measured both acoustically and using the industry standard penetrometer. Fruit measured using

the penetrometer fell both above and below the outturn specification of 63.7 N relevant to both industry and the consumers. Measurements using the GUSS texture analyser were comparable to the TA.XTplus texture analyser used in the high-speed trial (Chapter 6) both showing similar standard errors. There was no clear relationship between acoustic and penetrometer firmness consistent with the results from the high-speed experiment. The two approaches measure fundamentally different properties with non-destructive acoustic firmness only interrogating elastic properties compared to the destructive compression and rupture properties measured by the penetrometer.

There were two major changes to the MSI component of this study compared to the high-speed experiment. The first was physical refinements made to the MSI system reducing variation caused by fruit positioning, improving laser stability, removing polarisation effects, and increasing the spatial resolution. The second was to prepare the fruit in a way that removes fruit shape and skin effects. Other researchers have used mathematical correction schemes which introduce unknown errors due to assumptions, for example, assuming fruit are perfect spheres and that the average diameter of a set can be used to correct each individual fruit (Peng & Lu, 2007, 2006b). In this study shape and skin effects were eliminated by carefully slicing the fruit, so that flat measurement surfaces were exposed. While this approach is far from the non-destructive measurement required by industry, it did provide the best opportunity to measure the basic optical properties of 'Royal Gala' apples and identify the relationships between these properties and firmness.

In addition to these changes, a fourth laser was added to interrogate the prominent water absorption peak at 980 nm. This provided complementary information useful when developing firmness prediction models. The strongest relationship with penetrometer firmness both in terms of the scattering and absorption coefficients was found at the 980 nm wavelength. Also, the optimised MLR model used to predict penetrometer firmness put a high weighting on the 980 nm absorption coefficient. While these results support the use of the 980 nm laser, further work is required to prove that this information is a genuine indicator of fruit softening and is not just another parallel process such as water loss.

The combination of these refinements and the addition of the IAD system as an independent measurement of the optical properties provided greater confidence in the MSI system and allowed for the identification of relationships not observed in the

high-speed experiment. The absorption coefficient measured using the IAD system showed clear peaks in the carotenoid (<500 nm) and water (980 nm) absorption regions and a smaller absorption peak in the chlorophyll (680 nm) region. However, the absorption spectra did suffer from a broad positive offset consistent with light loss. The absorption coefficients measured by the MSI system were consistent with those measured by Qin et al. (2007) but lower than those measured by Cen, Lu & Mendoza (2011) and Cen et al. (2013). The removal of skin, which contains a significant quantity of chlorophyll, may have reduced the absorption effect at 685 nm. At 980 nm, absorption increased as expected due to the apples water content. This was below that that of pure water due to a significant portion of the fruit consisting of other constituents such as cell walls, sugars, and a large portion of air space.

The absorption coefficients measured by the IAD system showed positive correlation (R = 0.52) at the chlorophyll absorption and a stronger negative correlation (R = -0.69) in the carotenoid absorption region. As fruit soften there is a synthesis of carotenoid and a breakdown of chlorophyll pigments consistent with these results. This occurs in parallel with mechanical softening and although it provides useful complementary information it may be susceptible to external factors such as storage treatments. The relationships between firmness and the absorption coefficients measured by the MSI system showed weak correlations at 685, 850, and 904 nm (on average R = 0.39) and a stronger correlation at 980 nm (R = 0.68). The relationship with chlorophyll at 685 nm although weaker than the IAD result was consistent with a breakdown in softer fruit.

The reduced scattering spectra measured by the IAD system showed smooth decreasing profiles from 550 nm to 900 nm. This behaviour is expected based on the Mie solution. However, below 550 nm and above 900 nm where absorption was higher there was significant crosstalk a common problem seen in results using the inverse adding-doubling algorithm. The reduced scattering coefficient measured using the MSI system fell mostly within the bounds of the earlier study by Qin et al. (2007). However, at the 980 nm wavelength the reduced scattering coefficient deviated from the expected decreasing profile. Further work is required to identify the reasons for this. One possible cause is the increased absorption in this region which may have invalidated the condition of the diffusion theory that scattering is much larger than absorption.

The relationships between penetrometer firmness and the measured reduced scattering coefficients were consistent between the two measurement systems. As fruit softened

scattering tended to increase with an average correlation coefficient of -0.68 and -0.65 for the IAD and MSI systems respectively. This result was consistent with some studies while others found the opposite relationship occurred. Enzymatic breakdown of cell walls and water loss are key factors in fruit softening (Hertog et al., 2004). Water loss reduces cell size and opens up air spaces which provide strong refractive index mismatches increasing scattering. Enzymatic breakdown weakens cell walls and can diminish structure reducing scattering. There is also evidence that this weakening may allow further cell separation, increasing intercellular air space, and again increase scattering. The combination of these effects may lead to situations where scattering could increase or decrease as fruit soften. Further work is needed to establish if these effects are related to the fruit cultivar or external factors such as storage condition.

9.4. Conclusion

In this study 92 'Royal Gala' apples were measured using the static MSI and IAD systems. All fruit were stored using a single high humidity treatment to minimize any uncertainty due to storage conditions. Apple curvature and skin variation was eliminated from the multispectral images by removing a section of each apple to exposure a flat surface where measurements were made. Multispectral images were processed to extract intensity profiles and these were parameterised using a modified Lorentzian model and the optical properties extracted using the diffusion theory model. The IAD system provided an independent measurement for the optical properties between 400 and 1050 nm. The relationships between the optical properties or modified Lorentzian parameters and either penetrometer firmness or acoustic firmness were investigated.

The optical properties of 'Royal Gala' apples measured using the IAD system were consistent with the literature on other apple varieties. The absorption spectra showed all the expected features including prominent carotenoid (<500 nm) and water peaks (980 nm), and a subtle chlorophyll absorption peak (675 nn). The reduced scattering coefficient spectra followed a smooth monotonic decrease as wavelength increased, expected from the Mie solution. The carotenoid (400 to 500 nm) and to a lesser extent the chlorophyll-a (680 nm) absorption coefficients were found to correlate with penetrometer firmness, with correlations coefficients of -0.69 and 0.52 respectively. The reduced scattering coefficient across all wavelengths increased as fruit softened with an average correlation between the reduced scattering coefficient and penetrometer

firmness of -0.68 (550 – 900 nm). There was no clear relationship between the AWETA acoustic firmness measurement and either of the optical properties.

The IAD optical properties also showed clear signs of crosstalk and light loss in the absorption and reduced scattering coefficient spectra, respectively, issues common to the method and similar to what was observed during validation measurements (Chapter 8). Better separation of absorption and reduced scattering coefficients, specifically to reduce crosstalk and the impact of light loss, will likely strengthen the relationships identified.

The background and FWHM modified Lorentzian parameters measured using the MSI system were consistent with previous studies, the background term decreasing, and the FWHM term increasing with firmness. On the other hand, the amplitude and slope parameters did not agree with the earlier work, the amplitude term increasing, and the slope term decreasing with firmness. The relationship between the modified Lorentzian parameters and acoustic firmness remained poor with a maximum correlation coefficient of 0.23. The relationship between the modified Lorentzian parameters and penetrometer firmness increased significantly. The slope term ('d') gave strongest relationships with penetrometer firmness, found at the absorbing wavelengths, 685, and 980 nm, with correlation coefficients of 0.71 and 0.72 respectively. A multiple linear regression was used to predict penetrometer firmness from a reduced set of 6 modified Lorentzian parameters. The correlation coefficient for this model was 0.71 and the standard error of cross validation was 5.64 N.

The optical properties measured by the MSI system were within the expected range found in other studies on different apple varieties. At 980 nm the reduced scattering coefficient was higher than expected. The relationship with penetrometer firmness showed that firmer fruit had lower reduced scattering coefficients compared to soft fruit at all four wavelengths. The correlations between firmness and the reduced scattering coefficient ranged from -0.62 to -0.70. These were in agreement with the optical properties found using the IAD system. This may be due to the enzymatic break down of cell walls which weakens the cell to cell bonds increasing intercellular air space and strong refractive index boundaries which in turn increase the scattering. The absorption coefficient showed the strongest relationship with penetrometer firmness at 980 nm followed by 685 nm. The first was consistent with the fruit losing water and the second with the breakdown of chlorophyll as fruit mature. There was no

clear relationship at any of the wavelengths between the absorption or reduced scattering coefficients and acoustic firmness. A multiple linear regression model was constructed to predict penetrometer firmness. The cross validated results had a correlation coefficient of 0.80 and a standard error of cross validation equal to 5.87 N.

Comparing the optical properties found using the MSI and IAD systems showed correlations ranging from 0.68 to 0.74 for the reduced scattering coefficients and 0.07 to 0.51 for the absorption coefficients. The lower correlations for absorption may be due to the inability of the MSI system to accurately measure low levels of absorption and the significant offset in the IAD absorption coefficients caused by light loss.

The results of this study although improved show that it is no surprise that performance was poor in the high-speed experiment discussed in Chapter 6. The concessions made to get the current level of performance such as slicing the fruit and making measurements on stationary fruit show that there is significant challenges to overcome before a practical high-speed system can be developed.

10. Conclusion and Future Work

Non-destructive fruit grading technologies have become an invaluable tool in post-harvest management allowing fruit to be sorted based on numerous external and internal attributes. This gives marketers the ability to differentiate their produce and fruit processors the ability to maximize the performance of fruit in storage. Together this minimizes waste and maximizes market returns and the period of availability.

Through the evolution of grading technology, fruit firmness has remained a difficult quality parameter to measure non-destructively at high speed. The industry standard penetrometer measurement is destructive, limiting its application to small samples. Mechanical non-destructive approaches require physical contact with the fruit, limiting grading speed and risking fruit damage. A number of promising optical approaches have been presented in the literature. They typically characterise the behaviour of light in fruit tissue building models to predict penetrometer firmness. The purpose of this thesis was to design and develop a high-speed multispectral imaging system building on this literature.

Two multi-spectral imaging systems capable of measuring spatially resolved spectra for the purpose of assessing fruit firmness were developed. The first was a high-speed system capable of making optical measurements of apples travelling at more than 1 m/s (10 fruit/s) on a commercial high-speed fruit grading line. Previous work presented in the literature had only made measurements on stationary or slow (2 fruit/s) moving fruit. The design used a high-resolution complementary metal–oxide–semiconductor (CMOS) camera coupled with a 12.5 mm lens and discrete laser sources operating at 685, 850, and 904 nm. The laser wavelengths were selected based on spectral features and past performance documented in the literature. Each laser illuminated a separate fruit and the camera captured the interaction of light with fruit tissue for all three lasers in a single frame. The high-resolution camera coupled with a 12.5 mm lens provided a spatial resolution ranging from 0.15 to 0.22 mm/pixel depending on fruit size.

The second multispectral system was a refinement of the first. The purpose of this was to reduce variability and better understand the performance limits a commercial system will encounter in measuring fruit firmness. With this system the fruit were kept

stationary (static) throughout measurements and several modifications were made to improve the quality of the results. These modifications included the addition of a 980 nm laser, the elimination of an asymmetry caused by laser polarisation, improved laser stability, an electronic shutter system, and precise location control of the fruit. The system retained the CMOS camera but captured only a single fruit in each image with a 25 mm lens, increasing the spatial resolution to 0.057mm/pixel. Both the high-speed and static multispectral imaging systems were used to capture images of 'Royal Gala' apples along with reference penetrometer and acoustic firmness measurements. Multispectral images were analysed using diffusion theory and modified Lorentzian models. The diffusion theory model enabled the extraction of the sample's optical properties — the absorption and reduced scattering coefficient — while the modified Lorentzian curve characterised the data using a four parameter model.

A semi-automated inverse adding-doubling system was also developed to provide an independent measurement of fruit optical properties. Measurements were made on thin (5mm) fruit samples from 400 to 1050 nm to calculate the absorption and reduced scattering coefficients.

High-speed multispectral images were captured and acoustic and penetrometer firmness measured on 200 'Royal Gala' apples. While the extracted modified Lorentzian parameters and the absorption and reduced scattering coefficients were consistent with earlier studies the relationships between these and both acoustic or penetrometer firmness were poor. A maximum correlation coefficient of 0.33 was found between the full-width at half-maximum parameter and penetrometer firmness. Multiple linear regression was used to build a variety of models to predict firmness. The best result was found using the modified Lorentzian parameters. A correlation coefficient of 0.42 and a standard error of 8.79 N were obtained. This correlation was low compared to published studies where fruit were stationary (R = 0.82, 6.64 N, for example).

A second study was carried out on 92 'Royal Gala' apples using the static multispectral imaging system. The purpose of this study was to investigate the relationships between firmness measurements and the behaviour of light as it interacts with apple tissue. Measurements were made using the static multispectral imaging and inverse adding-doubling measurement systems along with acoustic and penetrometer firmness. To isolate flesh firmness from confounding factors, such as natural variation in skin

pigments and fruit curvature, the fruit were sliced using a 'Guillotine' to expose a uniformly flat surface. The use of the inverse adding-doubling system also allowed for the exploration of optical properties below 500 nm, a region of the spectrum that is not well explored for firmness assessment in apples.

The results from the inverse adding-doubling measurements showed that the optical properties of 'Royal Gala' apples are consistent with other apple varieties. Visible in the absorption coefficient spectra were clear carotenoid, chlorophyll and water peaks. The reduced scattering coefficient spectra showed a smooth decrease with wavelength expected from the Mie solution to the light transport equation. The carotenoid (400 to 500 nm) and chlorophyll (680 nm) absorption coefficients were found to correlate with penetrometer firmness, with correlation coefficients of -0.69 and 0.52 respectively. This was due to a breakdown of chlorophyll and the synthesis of carotenoid pigments expected as fruit mature. The reduced scattering coefficient increased as fruit softened with an average correlation coefficient of -0.68 (550–900 nm). There was no clear relationship between acoustic firmness and either of the optical properties.

The results of the static multispectral imaging system showed a marked improvement over the results from the high-speed system. The optical properties were within the expected ranges of those found in other studies on different apple varieties and the relationships with firmness were consistent with those identified using the inverse adding-doubling system. As fruit softened the reduced scattering coefficient increased with a correlation coefficient ranging from -0.62 to -0.70 depending on wavelength. This was consistent with the enzymatic breakdown of cell walls weakening the cell-to-cell bonds and increasing the intercellular air-space. This creates strong refractive index boundaries which, in turn, increases scattering. The absorption coefficients at 980 nm and 685 nm were positively correlated with firmness, which is explained by a small amount of water loss and the breakdown of chlorophyll respectively. Again, there was no correlation found between the optical properties and acoustic firmness. A model was developed from the optical properties to predict penetrometer firmness using multiple linear regression. The results from cross-validation showed a correlation coefficient of 0.80 and a standard error of 5.87 N, a significant improvement over the model built using data from the high-speed multispectral imaging system and comparable to those found in the literature on other apple varieties. The modified Lorentzian parameters also showed correlations with penetrometer firmness. The

strongest relationships were with the slope ('d') parameter at 685 nm (R = 0.71) and 980 nm (R = 0.72) where absorption is strongest. A multiple linear regression model was also built using the modified Lorentzian parameters. The optimised model had a correlation coefficient of 0.71 with a standard error of 5.64 N. This model, for example, could allow separation of the data into roughly 1.5 groups (based on the ratio of standard error of prediction to sample standard deviation). This is unlikely to be sufficient to justify the development of a commercial fruit firmness system, however.

These results suggest that further work is needed to improve the measurement before revisiting the complications of skin pigment, fruit curvature, and high-speed collection. This could involve further optimisation of the hardware to identify and minimize individual sources of noise. It would also be worth putting some focus on the fruit itself: the natural variability in 'Royal Gala' apples optical properties may be too large for an effective firmness measurement. There may be opportunities to assess other types of fruit and apple varieties which are more uniform and provide larger changes in their optical properties as they soften. This would reduce noise, increase the strength of the relationships measured, and improve the performance of predictive models.

11. Appendices

11.1. Appendix 1 - Thermal Stability of Intralipid

11.1.1 Introduction

Intralipid® is a fatty emulsion commonly used as a component in optical phantoms, simulating the light-scattering and absorption properties of biological tissues (Ninni et al., 2011; Olsen & Sager, 1995; Pogue & Patterson, 2006). It has been shown that Intralipid has high temporal stability and negligible batch-to-batch variations (Ninni et al., 2011). Intralipid based phantoms have also been used in the development of optical temperature measurement systems (Kakuta et al., 2008; Chung et al., 2010; Cletus et al., 2010; Yang et al., 2012; McGlone et al., 2007). For these phantoms to be useful, it is important to understand how temperature affects their stability.

While studying the optical temperature coefficients of Intralipid in the biologically relevant temperature range (30 – 40 °C), we discovered instability in spectral measurements carried out at 35 °C and above. Over several hours, transmitted light intensity below 700 nm generally decreased, yet it remained steady above 700 nm. Soya oil, an ingredient in Intralipid, contains linoleic, oleic, linolenic and other fatty acids. These fatty acids oxidise rapidly, often causing a yellow tint (Mallégol et al., 2001; Privett et al., 1961; Stenberg et al., 2005), indicative of increasing absorption around 450 nm. Mallégol et al. (2001) suggested that higher temperatures would increase the oxidation rate of oils. To establish a link between oxidation and the stability of Intralipid as an optical phantom below 700 nm, transmission spectra were collected at 70 °C, a convenient temperature high enough to accentuate the thermal instability.

11.1.1 Method

Figure 11-1 illustrates two of the experiments discussed in this work where Intralipid was heated to explore thermal stability. In both cases a feedback-stabilized quartz-halogen lamp (Newport Oriel Instruments, US) was used to illuminate the sample through a 600 µm optical fibre. The lamp (Model 68951) uses a feedback system to provide a stable source of 'white' light with less than 1 out of 18000 ADC counts in intensity drift per hour. A second 600 µm fibre, 15 mm away from the source, was used

to collect light. The spectrum, from 300–1100 nm, was measured by a MMS-1 spectrometer (Carl Zeiss, Germany) and corrected for dark current.

In the first experiment a 1% Intralipid solution was diluted from a 10% stock solution with grade three filtered water (ISO 3696, 1987). This sample was housed in a 10 L stainless steel vessel and placed on a heating magnetic stirrer (ARE Heating Magnetic Stirrer, Velp Scientific, Italy). A sealed cover trapped room air in the headspace to minimize evaporation. The sample was heated to 35 °C then the temperature held constant while spectra were collected every 10 minutes for 60 hours.

For the second experiment the 1% Intralipid solution was diluted from a 20% stock solution using type one filtered water (ASTM D1193-91; Milli-Q® Integral, Millipore, USA). In this case the sample was housed in a three-necked round-bottom flask, heated to 70 °C using a temperature controlled water bath (GR150, Grant Instruments, UK), and stirred to maintain homogeneity. The heated magnetic stirrer used in the first experiment controls temperature with a plate that can reach 250 °C. The water bath eliminates this high temperature gradient minimizing the risk of damage to the Intralipid solution. The three-necked flask and a gas bubbler allowed the atmosphere in the headspace to be flushed with either bottled air (21% Oxygen, 78% Nitrogen) or bottled nitrogen (oxygen-free). After flushing, the gas bubbler was used to maintain a positive pressure to prevent oxygen from entering the system. Spectra were collected every 30 seconds for 12 hours.

To understand the effect of temperature on the fundamental optical properties, a third experiment using two fresh 500 ml 1% Intralipid samples was performed. One sample was heated to 70 °C for 12 hours while the other remained at room temperature. The absorption and scattering coefficients for each sample were measured using the inverse adding-doubling technique after the second sample had equilibrated back to room temperature (Prahl, 1999). The reflectance and transmittance measurements were made with a 4 inch integrating sphere (4P-GPS-033-SL, Labsphere, New Hampshire), the MMS-1 spectrometer, and a custom sample holder. The sample holder was made from two 1.1 × 75 × 75 mm glass slides separated by 3.8 mm.

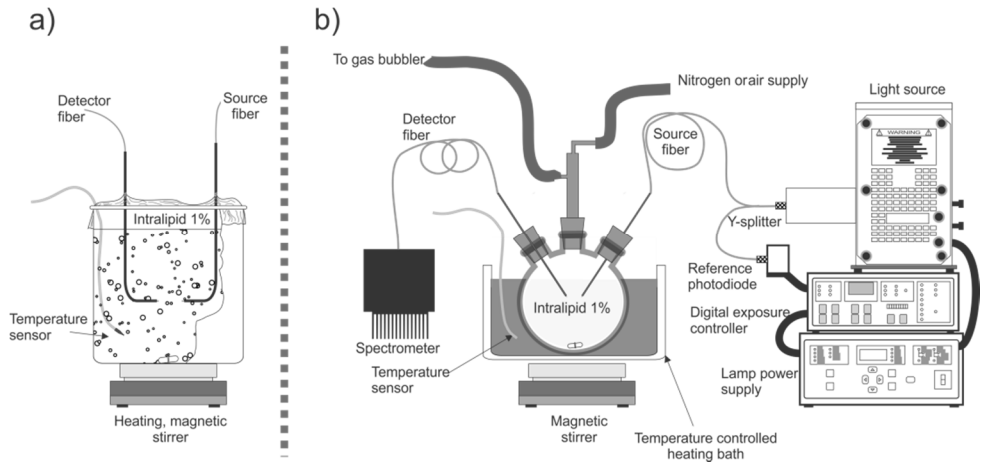

Figure 11-1. Experimental set up to investigate the stability of Intralipid® at elevated temperatures. (a) Initial pot based heating system with curved probes. (b) Controlled atmosphere system with straight probes incident at approximately 45°.

11.1.1 Results and Discussion

Figure 11-2 shows the raw spectra collected for the two experiments (a–c) and the ratio of the first and last measurements collected for each set of data (d). The shape of the spectra is a combination of the spectrometer's efficiency and the spectral radiance of the source. Measurements below 400 nm and above 950 nm are dominated by noise as both the quantum efficiency of the detector and output from the light-source is low. In every case, the intensity above 700 nm changes less than 2% over the duration of the measurements. With room or bottled air in the atmosphere above the Intralipid solution there is a significant decrease in intensity between 400 and 700 nm over the duration of the experiment, with a larger change at the higher temperature. For example at 500 nm the intensity drops 18% for the sample at 35 °C and 39% at 70 °C. In contrast, with an oxygen free nitrogen atmosphere, the intensity between 400 and 700 nm remains relatively stable, decreasing less than 8%. The most significant changes are occurring in the green and blue portions of the spectrum. This gives a yellow tint to the sample, a change in optical absorption, consistent with the oxidation of fatty acids (Privett et al., 1961). Oxidation would also suggest the effect of temperature on the relative change in Figure 11-2d is to increase the reaction rate consuming a greater amount of oxygen from the headspace increasing the absorption from the oxidized species.

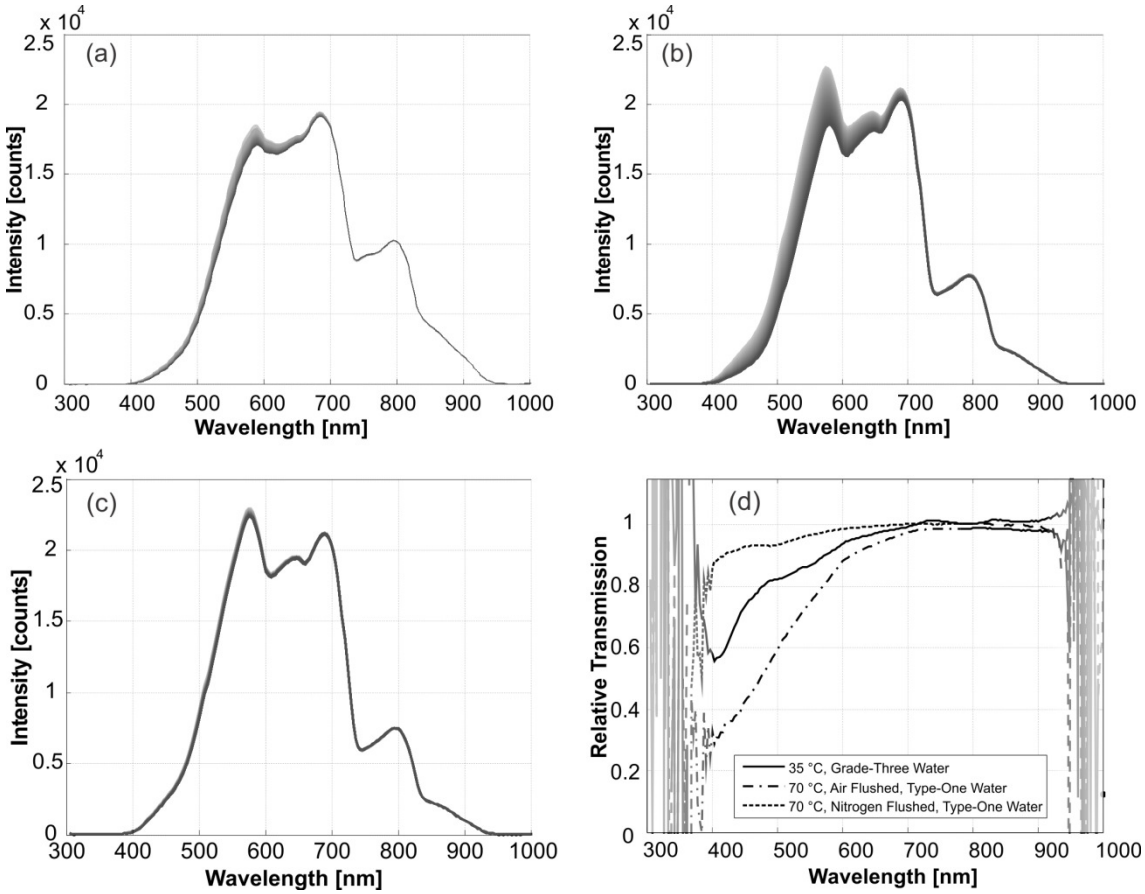

Figure 11-2. Spectra of 1% Intralipid® (a) at 35 °C collected over 60 hours in a stagnant air atmosphere, diluted with grade-three water; (b) at 70 °C over 12 hours in a low velocity air atmosphere, diluted with type-one water; (c) at 70 °C over 12 hours in a nitrogen atmosphere, diluted with type-one water. (d) Intensity ratio of final to first measurement for (a) through (c). Trace colour indicates elapsed time—light grey to black.

In both experimental setups (stainless steel vessel and three-necked flask) the instability was considerably smaller at 35 °C when the Intralipid stock solution was diluted with water from the type-one system (less than 5% at 500 nm; data not shown). The 35 °C data shown here (18% drop at 500 nm) is for Intralipid diluted by water from a grade-three water purification system and demonstrates the instability can occur at temperatures commonly found in biological systems. This may be due to a higher concentration of dissolved oxygen in the original water supply. However the grade-three system was no longer available to test this hypothesis. The 35 °C data shown here is one example from more than a dozen experiments between 35 and 40 °C exhibiting similar instability below 700 nm with water from the grade-three system. In addition the stock solution of Intralipid was from a new batch which may also have contributed to the difference.

To separate the contribution of the absorption and scattering effects on the instability observed, the inverse adding-doubling method was used (Prahl, 1999). Figure 11-3 shows the absorption and reduced scattering coefficients calculated before and after heat treatment. Both samples were measured at room temperature so these results reflect permanent changes to the samples only. Below 400 nm, instrument noise dominated, so this data is not plotted. Both the before and after heat-treatment reduced scattering measurements show smooth monotonically decreasing curves typical of a turbid Intralipid solution (van Staveren et al., 1991). The difference between the scattering coefficient for the heated and unheated sample was uniform and less than 0.5% across the spectrum indicating that the scattering coefficient is thermally stable and is unlikely to be a factor in the intensity reduction observed below 700 nm. After heat treatment the absorption coefficient remained unchanged above 600nm. Below 600nm the absorption tended to increase. At 450nm, for example, absorption increased by 20%. This indicates that the instability observed is dominated by absorption, consistent with a yellowing caused by oxidation of fatty acids in the soybean oil found in Intralipid. Changes in scattering are negligible.

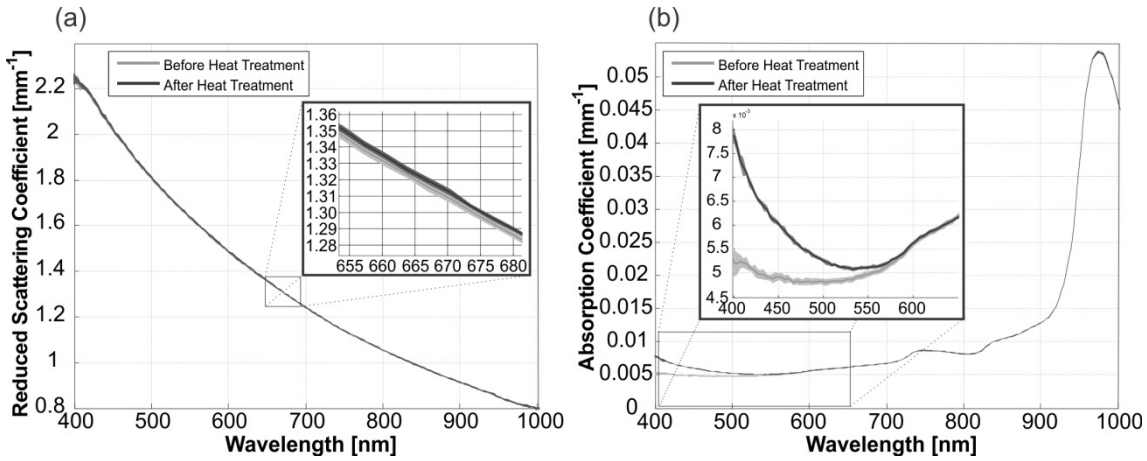

Figure 11-3. (a) Reduced scattering coefficient and (b) absorption coefficient for Intralipid-1% before and after heating. Measurements were made once the samples equilibrated to room temperature. The shaded regions indicate the standard deviation of ten replicate measurements.

11.1.1 Conclusion

We have shown that the scattering coefficient of Intralipid remained stable when the 1% solution was held at temperatures of 70 °C for 12 hours. Scatter properties varied by less than 0.5% over the entire wavelength range of 400 to 950 nm. Changes in absorption were negligible above 700 nm.

Light transmission below 700 nm dropped significantly over time. At 500 nm, for example, transmission through 15 mm of a 1% solution dropped by 18% when heated to 35 °C and 39% when heated to 70 °C. We determined that this was caused by an increase in absorption coefficient most likely due to the oxidation of fatty acids found in Intralipid.

Flushing excess oxygen from the headspace was effective in significantly improving the stability of the solution to better than 8% at 500 nm. Excluding oxygen minimizes the opportunity for the fatty acids to oxidize.

Intralipid is a robust, stable ingredient for tissue phantoms even at elevated temperatures. However, some attention should be paid to the increase in absorption when operating at shorter wavelengths.

11.2. Appendix 2 – Software

11.2.1 High Speed Multispectral Imaging System

The high-speed multispectral imaging system was run by a Windows XP computer with a Dalsa frame-grabber card installed (x64 Xcelera-CL PX4 Camera Link, Teledyne Dalsa, Waterloo, Canada). The frame-grabber card allowed an external hardware trigger to be used which was connected to an opto-interrupt. Dalsa provides a set of library files along with examples which can be used to generate custom Windows applications. Their example program named “Grab Demo” was used as the basis for the custom software we created named “DPF Image Acquisition” (DPF = Dalsa PhotonFocus). This extended the standard Dalsa program also including extra functionality related to the experiment and commands specific to the Photonfocus camera to adjust different settings.

Figure 11-4 illustrates the main user interface for the custom software. The UI consists of a number of elements. The top control gives some extra camera and software options. The first option is crosshairs. These can be used for aligning objects in the frame such as a ruler for the spatial resolution measurement. The second is a review images option; this lets you review the current set of captured images. Clear thumbnails clears the set of collected thumbnails, this is useful because it lets you double check that a complete set of images have been collected and that all of them are new. The fourth option is saturation highlight, this shows the regions in the main image that are saturated (=4095 ADC units). The final option is to enable the status line

in the image, this replaces some of the pixels with digital data such as the frame number and exposure time. This is great for validating that each image is unique and that settings have been successfully changed like exposure time.

Next down in the interface is a histogram which lets you adjust the contrast shown on the computer screen. Because the computer screen can only show a limited number of gray levels it is sometimes useful to rescale those limited levels to different intensify ranges measured by the camera. This control lets you do that by dragging the upper (red bar) and the lower limits (green bar). On the right of the histogram is a control to adjust the exposure time of the camera, and a control to resize the main display in the middle of the screen (Figure 11-5).

Below these is the option to adjust the file name based on serial messages that the program receives. This feature was added because a separate piece of software was used to drive the mechanical fruit grader. This software was used as the central control for naming the files on the multispectral imaging system and other experimental gear. DPF Image Acquisition would use that filename and append image numbers to the end of it for each image collected.

Next are all of the controls related to image acquisition. The first checkbox enables saving triggered images to disk, and the second one allows overwriting. This is disabled during experimental runs to avoid accidentally overwriting images but is very useful when testing. Next are options to select the image format, either tiff or binary images are available. Below that are options to select the image path and the number of images you want to collect in a set. In the case of the high-speed system we have 10 fruit but want to collect a total of 12 images. This is because each frame captures three fruit at once. As the first fruit moves into the frame it is captured without any neighbours. This means two extra images are needed to complete the set. The next option is a filename mask. This is what the serial port sets if that option is enabled. It precedes the current frame number and is useful for identifying the types of samples being measured and the experimental conditions. Finally are a couple of buttons, one to reset the counter so a new set of images is collected, and the second for manually snapping an image rather than relying on the hardware trigger.

The final control at the bottom indicates the next image number and the next image file name. In this case the file name is “Run13.bin” and the image number is 13.

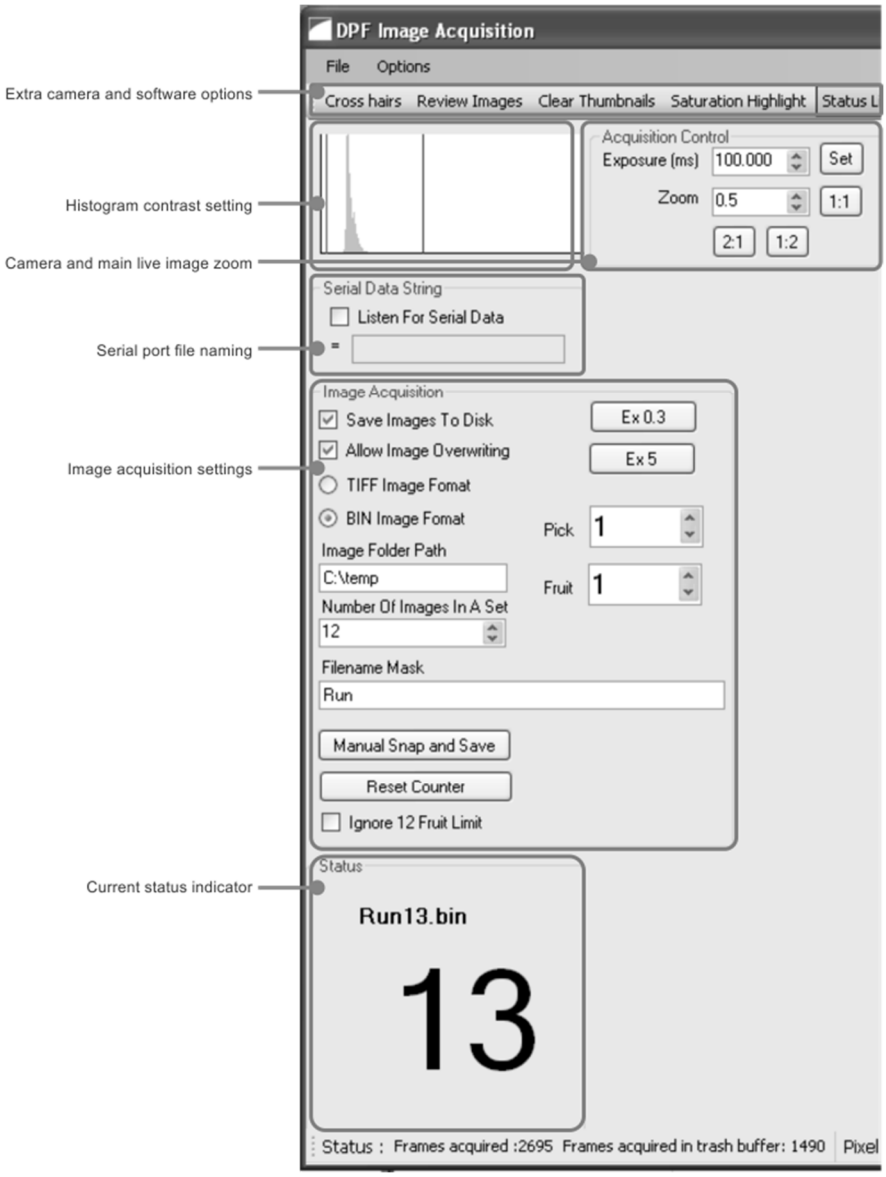

Figure 11-4. Custom software for capturing images using the high-speed multispectral imaging system. Images are captured based on a hardware trigger.

As images are collected they are displayed on the interface shown in Figure 11-5. In the middle shows the last image captured. This is updated each time the opto-interrupt trigger signals the camera. Above this main image are a series of thumbnails. The interface was designed to allow 12 thumbnails to be shown. This allowed manual inspection to insure the images look correct and that the all twelve were collected just in case the triggering or acquisition system fails. If the review images option discussed earlier is enabled then these thumbnails become clickable, as each one is clicked it takes over the main display for a simple way to review images.

Figure 11-5. Software displaying thumbnails of images collected at the top and an example image in the main display. Note the three bright spots corresponding with the three lasers illuminating three different apples.

11.2.2 Static Shutter System

The following code is used on the Arduino Mega to control each of the laser shutters. The software is contained in 3 main sections. The fist is ShutterController.cpp. This contains the main program loop. The second is Shutter.h and Shutter.cpp. These files contain the functions and properties which control each shutter. The final section is contained in SerialHandler.h and SerialHandler.cpp. These deal with serial messages sent from the computer and execute different commands depending on what content is found in each serial message.

ShutterController.cpp

```
/*
   ************************************************************
   ********
** Arduino program to control a shutter.
**
   ************************************************************
   ******** */

#ifdef _MSC_VER
```

```
#include "../Shared/BuildTools/ArduinoIntellisense.h"
#endif

#include <Arduino.h>
#include <Streaming.h>

#include "SerialHandler.h"
#include "Shutter.h"

/* ------------------------------------------------------------------
   --------
** Configuration.
** ------------------------------------------------------------------
   -------- */
#define SHUTTER_COUNT 4

#define SHTR_1_CHANNEL          1
#define SHTR_1_SERVO            10 // arduino green.
#define SHTR_1_SENSOR_POWER     25 // arduino red.
#define SHTR_1_SENSOR_LOW       23 // arduino white
#define SHTR_1_SENSOR_HIGH      24 // arduino orange
#define SHTR_1_SENSOR_DIRECTION 22 // arduino purple.


#define SHTR_2_CHANNEL          2
#define SHTR_2_SERVO            11 // arduino green.
#define SHTR_2_SENSOR_POWER     29 // arduino red.
#define SHTR_2_SENSOR_LOW       27 // arduino white
#define SHTR_2_SENSOR_HIGH      28 // arduino orange
#define SHTR_2_SENSOR_DIRECTION 30 // arduino purple.

#define SHTR_3_CHANNEL          3
#define SHTR_3_SERVO            12 // arduino green.
#define SHTR_3_SENSOR_POWER     33 // arduino red.
#define SHTR_3_SENSOR_LOW       31 // arduino white
#define SHTR_3_SENSOR_HIGH      32 // arduino orange
#define SHTR_3_SENSOR_DIRECTION 34 // arduino purple.

#define SHTR_4_CHANNEL          4
#define SHTR_4_SERVO            13 // arduino green.
#define SHTR_4_SENSOR_POWER     37 // arduino red.
#define SHTR_4_SENSOR_LOW       35 // arduino white
#define SHTR_4_SENSOR_HIGH      36 // arduino orange
#define SHTR_4_SENSOR_DIRECTION 34 // arduino purple.

/* ------------------------------------------------------------------
   --------
** Prototypes
** ------------------------------------------------------------------
   -------- */
void ProcessSystemMessage(CMessageHeader *pMessage);
void ProcessServoMessage(CMessageHeader *pMessage);
void SaveSettings();
void RestoreSettings();
void DumpConfiguration();

/* ------------------------------------------------------------------
   --------
** Global objects
** ------------------------------------------------------------------
   -------- */
```

```
CSerialHandler g_SerialHandler(&Serial);
CShutter g_Shutters[SHUTTER_COUNT];

void setup()
{
  int nShutter = 0;

  g_SerialHandler.Setup();
  g_Shutters[nShutter++].Setup(SHTR_1_CHANNEL, SHTR_1_SERVO,
   SHTR_1_SENSOR_POWER, SHTR_1_SENSOR_HIGH, SHTR_1_SENSOR_LOW);
  g_Shutters[nShutter++].Setup(SHTR_2_CHANNEL, SHTR_2_SERVO,
   SHTR_2_SENSOR_POWER, SHTR_2_SENSOR_HIGH, SHTR_2_SENSOR_LOW);
  g_Shutters[nShutter++].Setup(SHTR_3_CHANNEL, SHTR_3_SERVO,
   SHTR_3_SENSOR_POWER, SHTR_3_SENSOR_HIGH, SHTR_3_SENSOR_LOW);
  g_Shutters[nShutter++].Setup(SHTR_4_CHANNEL, SHTR_4_SERVO,
   SHTR_4_SENSOR_POWER, SHTR_4_SENSOR_HIGH, SHTR_4_SENSOR_LOW);

  Serial << "Servo Controller\r\n";
  Serial << "(c) Plant and Food Research 2013\r\n";
  Serial << "P. Martinsen & P. Rowe\r\n";
  Serial << "Restoring configuration...\r\n";
  RestoreSettings();
  DumpConfiguration();
  Serial << "Ready.\r\n\r\n";
}

void loop()
{
  CMessageHeader *pMessage;
  int nShutter;

  pMessage = g_SerialHandler.ProcessData();
  if (pMessage != NULL)
  {
    switch (pMessage->Channel)
    {
    case 's': // s is the system channel.
      ProcessSystemMessage(pMessage);
      break;

    case '1':
    case '2':
    case '3':
    case '4':
      ProcessServoMessage(pMessage);
      break;

    default:
      Serial.println("Unknown channel");
      break;
    }
  }

  for (nShutter = 0; nShutter < SHUTTER_COUNT; ++nShutter)
    g_Shutters[nShutter].Process(&g_SerialHandler);
}

void ProcessSystemMessage(CMessageHeader *pMessage)
{
  switch (pMessage->Command)
  {
```

```
    case MAKE_COMMAND('HL'):
      Serial.println("Servo controller");
      Serial.println("Help is on its way");
      break;

    case MAKE_COMMAND('SE'): // Save state to eeprom.
      SaveSettings();
      break;

    case MAKE_COMMAND('RS'): // Restore state from eeprom.
      RestoreSettings();
      break;

    case MAKE_COMMAND('GC'): // Report the current configuration.
      DumpConfiguration();
      break;
  }
}

void ProcessServoMessage(CMessageHeader *pMessage)
{
  int nChannel;

  nChannel = pMessage->Channel - '1';
  if (nChannel >= 0 && nChannel < SHUTTER_COUNT)
    g_Shutters[nChannel].ProcessCommand(&g_SerialHandler,
   pMessage);
  else
    g_SerialHandler.ReplyError("invalid shutter channel");
}

void SaveSettings()
{
  int nChannel;

  for (nChannel = 0; nChannel < SHUTTER_COUNT; ++nChannel)
    g_Shutters[nChannel].SaveToEEPROM(&g_SerialHandler);
}

void RestoreSettings()
{
  int nChannel;

  for (nChannel = 0; nChannel < SHUTTER_COUNT; ++nChannel)
    g_Shutters[nChannel].LoadFromEEPROM(&g_SerialHandler);
}

void DumpConfiguration()
{
  int nChannel;

  for (nChannel = 0; nChannel < SHUTTER_COUNT; ++nChannel)
    g_Shutters[nChannel].DumpConfiguration(&g_SerialHandler);
}
```

ShutterData.cpp

```
#pragma once
#ifdef _MSC_VER
#include "../Shared/BuildTools/ArduinoIntellisense.h"
#endif
```

```
#include <Arduino.h>

/* Data that gets persisted to the eeprom. */
struct CShutterData
{
  // The position to use for the servo when open or closed and the
  // opto sensor to use to confirm the position.
  enum EConfirmation { CNFRM_None, CNFRM_High, CNFRM_Low }
   __attribute__((__packed__));

  uint8_t m_nChannelId, m_nPositionClosed, m_nPositionOpen;
  EConfirmation m_ConfirmClosed, m_ConfirmOpen;

} __attribute__((__packed__));
```

Shutter.h

```
#pragma once

#include "Message.h"
#include "SerialHandler.h"
#include <Servo.h>
#include "ShutterData.h"
#include "PString.h"

class CShutter
{
  // Pin mapping for the shutter. Each shutter has a servo output
   signal,
  // a power signal for the sensors (connected to opto LEDs) and
   two inputs.
  // One input for the 'high' opto and one for the 'low' opto.
   High/ low
  // refers to the height of the optos relative to the shutter
   arm.
  int m_nPinServo, m_nPinSensorPower, m_nPinHighSensor,
   m_nPinLowSensor;

  CShutterData m_Configuration;

  bool m_bReportSensorState; // True=> sensor state is reported to
   serial stream
  uint32_t m_uLastReportTime; // Millisecond timer for last time
   state was reported.

  enum EConstants { ConfirmationTimeout = 1000 }; // time to wait
   for sensor confirmation [ms].

  Servo m_ShutterServo;

public:
  CShutter();
  void Setup(int nChannelId, int nPinServo, int nPinSensorPower,
   int nPinHighSensor, int nPinLowSensor);

  void Process(CSerialHandler *pSerialHandler);
  void ProcessCommand(CSerialHandler *pSerialHander,
   CMessageHeader *pMessage);

  void SaveToEEPROM(CSerialHandler *pSerialHander);
  void LoadFromEEPROM(CSerialHandler *pSerialHander);
  void DumpConfiguration(CSerialHandler *pSerialHander);
```

```
protected:
  bool GetHighSensorState();
  bool GetLowSensorState();
  void SensorPower(bool bOn);
  void ParsePosition(CSerialHandler *pSerialHander, CMessageHeader
   *pMessage, uint8_t *pPosition, CShutterData::EConfirmation
   *pConfirmation);
  void SetPosition(CSerialHandler *pSerialHander, CMessageHeader
   *pMessage, int nPosition, CShutterData::EConfirmation
   Confirmation);
  void SetPosition(CSerialHandler *pSerialHander, CMessageHeader
   *pMessage);
  void ReportPosition(CSerialHandler *pSerialHander,
   CMessageHeader *pMessage, int nPosition,
   CShutterData::EConfirmation Confirmation);
  bool ConfirmPosition(CShutterData::EConfirmation Confirm,
   uint32_t uTimeout = 0);

  bool ValidPosition(int nPosition);
  bool ValidConformation(CShutterData::EConfirmation Confirm);

  void WriteConfirm(PString &strOut, CShutterData::EConfirmation
   Confirm);
};
```

Shutter.cpp

```
#include "Shutter.h"
#include "EEPROM.h"

CShutter::CShutter()
{
  m_bReportSensorState = false;
  m_uLastReportTime = 0;
  m_Configuration.m_nChannelId = -1; // signals unitialized
   channel.

  m_Configuration.m_ConfirmClosed = CShutterData::CNFRM_None;
  m_Configuration.m_ConfirmOpen = CShutterData::CNFRM_None;
  m_Configuration.m_nPositionClosed = 80; // degrees.
  m_Configuration.m_nPositionOpen = 100; // degrees.
}

void CShutter::Setup(int nChannelId, int nPinServo, int
   nPinSensorPower, int nPinHighSensor, int nPinLowSensor)
{
  m_Configuration.m_nChannelId = nChannelId;
  m_nPinServo = nPinServo;
  m_nPinSensorPower = nPinSensorPower;
  m_nPinHighSensor = nPinHighSensor;
  m_nPinLowSensor = nPinLowSensor;

  pinMode(m_nPinHighSensor, INPUT_PULLUP);
  pinMode(m_nPinLowSensor, INPUT_PULLUP);
  pinMode(m_nPinSensorPower, OUTPUT);
  pinMode(m_nPinServo, OUTPUT);
}
```

```
void CShutter::Process(CSerialHandler *pSerialHandler)
{
  if (m_bReportSensorState && (millis() - m_uLastReportTime >
  300))
  {
    char chBuffer[20];
    PString strOut(chBuffer, sizeof(chBuffer));

    SensorPower(true);

    strOut.print(m_Configuration.m_nChannelId);
    strOut.print(": H=");
    strOut.print(GetHighSensorState());
    strOut.print(", L=");
    strOut.println(GetLowSensorState());
    pSerialHandler->Send(strOut);
    m_uLastReportTime = millis();

    SensorPower(false);
  }
}

void CShutter::ProcessCommand(CSerialHandler *pSerialHander,
  CMessageHeader *pMessage)
{

  switch (pMessage->Command)
  {
  case MAKE_COMMAND('SO'):  // Set the open position &
  confirmation indicator.
    ParsePosition(pSerialHander, pMessage,
  &m_Configuration.m_nPositionOpen,
  &m_Configuration.m_ConfirmOpen);
    break;

  case MAKE_COMMAND('SC'):  // Set the close position &
  confirmation indicator.
    ParsePosition(pSerialHander, pMessage,
  &m_Configuration.m_nPositionClosed,
  &m_Configuration.m_ConfirmClosed);
    break;

  case MAKE_COMMAND('OP'):  // Move the servo to the open
  position.
    SetPosition(pSerialHander, pMessage,
  m_Configuration.m_nPositionOpen,
  m_Configuration.m_ConfirmOpen);
    break;

  case MAKE_COMMAND('GO'): // Report the current open position and
  indicator.
    ReportPosition(pSerialHander, pMessage,
  m_Configuration.m_nPositionOpen,
  m_Configuration.m_ConfirmOpen);
    break;

  case MAKE_COMMAND('GC'): // Report the current open position and
  indicator.
    ReportPosition(pSerialHander, pMessage,
  m_Configuration.m_nPositionClosed,
  m_Configuration.m_ConfirmClosed);
```

```
    break;

  case MAKE_COMMAND('CL'):  // Move the servo the close position &
  confirm.
    SetPosition(pSerialHander, pMessage,
  m_Configuration.m_nPositionClosed,m_Configuration.m_ConfirmClos
  ed);
    break;

  case MAKE_COMMAND('SS'):  // start/ stop writing the current
  state of the sensor channel to the serial stream.
    m_bReportSensorState = pMessage->Data[0] == '1';
    pSerialHander->ReplyOK(pMessage);
    break;

  case MAKE_COMMAND('SP'): // set position.
    SetPosition(pSerialHander, pMessage);
    break;

  default:
    break;
  }

}

bool CShutter::GetHighSensorState()
{
  return digitalRead(m_nPinHighSensor);
}

bool CShutter::GetLowSensorState()
{
  return digitalRead(m_nPinLowSensor);
}

void CShutter::SensorPower(bool bOn)
{
  //bOn = HIGH;
  digitalWrite(m_nPinSensorPower, bOn ? LOW : HIGH);
  delay(10);//give the leds time to turn on. Otherwise the uC
  detects the servo of already being in place.
}

void CShutter::ParsePosition(CSerialHandler *pSerialHander,
  CMessageHeader *pMessage, uint8_t *pPosition,
  CShutterData::EConfirmation *pConfirmation)
{
  int nValue;
  CShutterData::EConfirmation ConfirmationValue;

  switch (pMessage->Data[0])
  {
  case 'H':
    ConfirmationValue = CShutterData::CNFRM_High;
    break;
  case 'L':
    ConfirmationValue = CShutterData::CNFRM_Low;
    break;
  case 'N':
    ConfirmationValue = CShutterData::CNFRM_None;
    break;
```

```
  default:
    pSerialHander->ReplyError("invalid confirmation position {H,
   L, N} permitted");
    return;
    break;
  }

  nValue = atoi(pMessage->Data + 1); // First character is the
   confirmation position.
  if (!ValidPosition(nValue))
  {
    pSerialHander->ReplyError("invalid position; [0, 180]
   permitted");
    return;
  }

  // If we get this far, both confirmation & angle are valid.
   Update them.
  *pPosition = nValue;
  *pConfirmation = ConfirmationValue;

  pSerialHander->ReplyOK(pMessage);
}

void CShutter::ReportPosition(CSerialHandler *pSerialHander,
   CMessageHeader *pMessage, int nPosition,
   CShutterData::EConfirmation Confirmation)
{
  char achBuffer[20];
  PString strOut(achBuffer, sizeof(achBuffer));

  strOut.print('@');
  strOut.print(m_Configuration.m_nChannelId);
  strOut.print(": ");
  strOut.print(nPosition);
  switch (Confirmation)
  {
  case CShutterData::CNFRM_None:
    strOut.println(", none");
    break;
  case CShutterData::CNFRM_High:
    strOut.println(", high");
    break;

  case CShutterData::CNFRM_Low:
    strOut.println(", low");
    break;

  default:
    break;
  }

  pSerialHander->Send(strOut);
}

void CShutter::SetPosition(CSerialHandler *pSerialHander,
   CMessageHeader *pMessage)
{
  int nValue;

  nValue = atoi(pMessage->Data); // First character is the
```

```
    confirmation position.
    if (!ValidPosition(nValue))
    {
      pSerialHander->ReplyError("invalid position; [0, 180]
    permitted");
      return;
    }

    SetPosition(pSerialHander, pMessage, nValue,
    CShutterData::CNFRM_None);
    pSerialHander->ReplyOK(pMessage);
  }

  void CShutter::SetPosition(CSerialHandler *pSerialHander,
    CMessageHeader *pMessage, int nPosition,
    CShutterData::EConfirmation Confirmation)
  {
    // Check if the servo is already in position.
    if (Confirmation != CShutterData::CNFRM_None &&
    ConfirmPosition(Confirmation))
    {
      pSerialHander->ReplyOK(pMessage);
      return;
    }

    // Position the servo.
    m_ShutterServo.attach(m_nPinServo);
    m_ShutterServo.write(nPosition);
    //Serial.print("servo moved to-");
    //Serial.println(nPosition);
    if (Confirmation == CShutterData::CNFRM_None)
    {
      delay(ConfirmationTimeout); // give the servo a littel time to
    move.
      Serial.println("no confirm");
      pSerialHander->ReplyOK(pMessage);
    }
    else if (ConfirmPosition(Confirmation, ConfirmationTimeout))
      pSerialHander->ReplyOK(pMessage);
    else
      pSerialHander->ReplyError("timeout positioning servo");

    m_ShutterServo.detach();
  }

  bool CShutter::ConfirmPosition(CShutterData::EConfirmation
    Confirm, uint32_t uTimeout)
  {
    //Serial.print("confirm level= ");
    //Serial.println(Confirm);

    uint32_t uStart;
    bool bConfirmed = false;
    //  Serial.print("bconfirmed before= ");
    //Serial.println(bConfirmed);

    if (Confirm == CShutterData::CNFRM_None)
      return true;

    uStart = millis();
    SensorPower(true);
```

```
  do
  {
    switch (Confirm)
    {
    case CShutterData::CNFRM_High:
      {
      bool highstate = GetHighSensorState();
      //Serial.println("highstate-");
      //Serial.println(highstate);
      if (highstate)
      {
        bConfirmed = true;
      //      Serial.println("bconfirmchanged");
      }
      //delay(1000);
      break;
      }

    case CShutterData::CNFRM_Low:
      {
      bool lowstate = GetLowSensorState();
      //Serial.println("lowstate-");
      //Serial.println(lowstate);
      if (lowstate)
      {
        bConfirmed = true;
     // Serial.println("bconfirmchanged");
      }
      //delay(1000);
      break;
      }

    }
  } while (!bConfirmed && (millis() - uStart < uTimeout));


  //    Serial.print("bconfirmed after= ");
  //Serial.println(bConfirmed);

  SensorPower(false);
  return bConfirmed;
}

void CShutter::SaveToEEPROM(CSerialHandler *pSerialHander)
{
  int nDestination;
  uint8_t *pSource;
  char achBuffer[20];
  PString strOut(achBuffer, sizeof(achBuffer));
  int nByte;

  // Calculate address. Assume channels are numbered from 1, and
   that data gets stored
  // starting from the start of the eeprom.
  nDestination =(m_Configuration.m_nChannelId - 1) *
   sizeof(CShutterData);
  pSource = (uint8_t*)&m_Configuration;

  for (nByte = 0; nByte < sizeof(CShutterData); ++nByte)
    EEPROM.write(nDestination++, *pSource++);
```

```
  strOut.print(m_Configuration.m_nChannelId);
  strOut.println(" saved");
  DumpConfiguration(pSerialHander);

  pSerialHander->Send(strOut);
}

void CShutter::LoadFromEEPROM(CSerialHandler *pSerialHander)
{
  CShutterData SensorData;
  uint8_t *pDestination;
  int nSource, nByte;
  char achBuffer[20];
  PString strOut(achBuffer, sizeof(achBuffer));

  // Calculate address. Assume channels are numbered from 1, and
   that data gets stored
  // starting from the start of the eeprom.
  nSource =(m_Configuration.m_nChannelId - 1) *
   sizeof(CShutterData);
  pDestination = (uint8_t*)&SensorData;

  for (nByte = 0; nByte < sizeof(CShutterData); ++nByte)
    *pDestination++ = EEPROM.read(nSource++);

  // Check what we read back is okay.
  if (SensorData.m_nChannelId == m_Configuration.m_nChannelId &&
    ValidPosition(SensorData.m_nPositionClosed) &&
    ValidPosition(SensorData.m_nPositionOpen) &&
    ValidConformation(SensorData.m_ConfirmClosed) &&
    ValidConformation(SensorData.m_ConfirmOpen))
  {
    m_Configuration.m_ConfirmClosed = SensorData.m_ConfirmClosed;
    m_Configuration.m_ConfirmOpen = SensorData.m_ConfirmOpen;
    m_Configuration.m_nPositionClosed =
   SensorData.m_nPositionClosed;
    m_Configuration.m_nPositionOpen = SensorData.m_nPositionOpen;

    strOut.print(m_Configuration.m_nChannelId);
    strOut.println(" loaded");
  }
  else
  {
    strOut.print(m_Configuration.m_nChannelId);
    strOut.println(" load error");
  }

  pSerialHander->Send(strOut);
}

/* Determines if the given position is within the valid range for
   the servo. */
bool CShutter::ValidPosition(int nPosition)
{
  return nPosition >= 0 && nPosition <= 180;
}

bool CShutter::ValidConformation(CShutterData::EConfirmation
   Confirm)
{
  return Confirm == CShutterData::CNFRM_High || Confirm ==
```

```
    CShutterData::CNFRM_Low || Confirm == CShutterData::CNFRM_None;
}

void CShutter::DumpConfiguration(CSerialHandler *pSerialHander)
{
  char achBuffer[100];
  PString strOut(achBuffer, sizeof(achBuffer));

  strOut.print("Channel ");
  strOut.print(m_Configuration.m_nChannelId);
  strOut.print(": open = ");
  strOut.print(m_Configuration.m_nPositionOpen);
  strOut.print(", ");
  WriteConfirm(strOut, m_Configuration.m_ConfirmOpen);

  strOut.print(": closed = ");
  strOut.print(m_Configuration.m_nPositionClosed);
  strOut.print(", ");
  WriteConfirm(strOut, m_Configuration.m_ConfirmClosed);
  strOut.println();

  pSerialHander->Send(strOut);
}

void CShutter::WriteConfirm(PString &strOut,
   CShutterData::EConfirmation Confirm)
{
  switch (Confirm)
  {
  case CShutterData::CNFRM_None:
    strOut.print("none");
    break;
  case CShutterData::CNFRM_High:
    strOut.print("high");
    break;
  case CShutterData::CNFRM_Low:
    strOut.print("low");
    break;
  default:
    strOut.print("unknown");
    break;
  }
}
```

SerialHandler.h

```
#pragma once

#ifdef _MSC_VER
#include "../Shared/BuildTools/ArduinoIntellisense.h"
#endif

#include <Arduino.h>
#include "Message.h"

class CSerialHandler
{
  HardwareSerial *m_pPort;
  uint8_t m_RawReceiveBuffer[sizeof(CMessageHeader)];

  enum EConstants
  {
```

```
    StartOfMessage = '!', // Character to signal start of message.
    EndOfMessage = '\n',   // Character to signal end of message.
    CharacterTimeout = 10, // Timeout for character.
    BaudRate = 9600,       // Baud rate for serial communications.
  };

  bool m_bOverflow, m_bReceivingMessage, m_bInvalidData;
  int m_nNextChar;

public:
  CSerialHandler(HardwareSerial *pPort);
  void Setup();

  CMessageHeader *ProcessData();

  void Send(const char *pchMessage);
  void ReplyOK(CMessageHeader *pMessage);
  void ReplyError(const char *pchDescription);
protected:
  void ReplyOverflowError();
  void ReplyInvalidMessageError();
};
```

SerialHandler.cpp

```
#include "SerialHandler.h"


CSerialHandler::CSerialHandler(HardwareSerial *pPort)
{
  m_bOverflow = false;
  m_nNextChar = 0;
  m_pPort = pPort;
}

void CSerialHandler::Setup()
{
  m_pPort->begin(BaudRate);
}

/* Process serial data as it comes in, filling the buffer. Return
   complete, decoded
** messages. If no message available, returns null.
** Looks for messages like: !1SOT1234\n */
CMessageHeader *CSerialHandler::ProcessData()
{
  // Track the time stamp of the last character received.
  // if it takes too long to receive the next character, the
  // buffer is reset.
  static uint32_t uLastReceiveTime;
  uint32_t uNow;

  char chReceived;

  uNow = millis();
  chReceived = m_pPort->read();

  if (chReceived != -1)
  {
    // Record time that the this character is received.
```

```
    uLastReceiveTime = uNow;

    if (chReceived == StartOfMessage)
    {
      m_nNextChar = 0;
      m_RawReceiveBuffer[m_nNextChar++] = chReceived;
      m_bReceivingMessage = true;
      m_bInvalidData = false;
      m_bOverflow = false;
    }

    if (m_bReceivingMessage && chReceived != StartOfMessage)
      if (chReceived == EndOfMessage)
      {
        m_RawReceiveBuffer[m_nNextChar] = '\0';
        m_bReceivingMessage = false;

        if (m_bOverflow)
          ReplyOverflowError();
        if (m_bInvalidData)
          ReplyInvalidMessageError();
        else
        {
          CMessageHeader *pMessage;
          pMessage = (CMessageHeader*)m_RawReceiveBuffer;
          if (pMessage->Type != CMessageHeader::TYPE_Command)
          {
            ReplyError("Unk type");
            return NULL;
          } else if (m_nNextChar < (sizeof(CMessageHeader) -
  CMessageHeader::MAX_DATA_LENGTH))
          {
            ReplyError("Msg too small");
            return NULL;
          }

          return pMessage;
        }
      }
      else
      {
        if (!m_bOverflow && chReceived != '\r' && chReceived !=
  '\n')
        {
          m_RawReceiveBuffer[m_nNextChar++] = chReceived;
          if (m_nNextChar >= sizeof(m_RawReceiveBuffer) - 1)
            m_bOverflow = true;
        }
      }
  } else if (m_bReceivingMessage && uNow - uLastReceiveTime >
  CharacterTimeout)
  {
    m_bReceivingMessage = false; // we timed out.
  }

  return NULL;
}

void CSerialHandler::Send(const char *pchMessage)
{
  m_pPort->print(pchMessage);
```

```
}

void CSerialHandler::ReplyOK(CMessageHeader *pMessage)
{
  m_pPort->println("@OK");
}

void CSerialHandler::ReplyError(const char *pchDescription)
{
  m_pPort->print("@ERR: ");
  m_pPort->println(pchDescription);
}

void CSerialHandler::ReplyOverflowError()
{
  ReplyError("overflow");
}

void CSerialHandler::ReplyInvalidMessageError()
{
  ReplyError("invalid message");
}
```

11.2.3 Static Multispectral Imaging System Matlab Script

The following Matlab code was used to drive the multispectral imaging system.

```
function CollectLaserLightScatterMeasurements_V3(FruitNumber,
  Orientation)

%% Setup Configuration
tic
addpath('L:\Matlab Library\Hardware\Arduino Shutter Controller
  V2');%shutter controller


config.Waves = [690 850 904 980];
config.ShutterNumbers = [2 1 4 3];
config.ExpTimes = [1 10];
config.RepImages = 49;
config.PickPlaces = 4;
config.PickPlaces = 1;
config.RepDarkImages = 9;
config.RepReferenceImages = 9;
config.StartTime = datestr(now);
config.ShutterPort = 'COM15';
config.RefTstagePort = 'COM18';


% Reference Tile Translation Positions
config.ReferencePosition = 55;
config.SamplePosition = 28;

savepath = ['F:\Collect'];
savepath = ['G:\2013 04 10 Gala Firmness Trial 1\Raw Data\Fruit '
  num2str(FruitNumber)];
savepath = ['E:\2013 04 10 Gala Firmness Timeseries 1\Raw
  Data1\Fruit ' num2str(FruitNumber)];
%savepath = ['E:\Pear Firmness Trial 1\Raw Data\Fruit '
  num2str(FruitNumber)];
```

```
% finalpath = ['E:\2013 04 03 Skin on Skin Off Trial 1\Raw
  Data\Fruit ' num2str(FruitNumber)];
% finalpath = ['E:\2013 04 08 Cox Firmness Trial 1\Raw Data\Fruit
  ' num2str(FruitNumber)];
mkdir(savepath);
% mkdir(finalpath)

save([savepath '\config.mat'],'config');% Save the config data for
  reference
%%


%Create file in folder with same number as pick place, use this as
  a
%check that you are not overwriting already gathered data
if(exist([savepath '\' num2str(Orientation) '.txt'],'file'))
  h=msgbox('have you already done this rep?');
  uiwait(h);
  error('have you already done this rep?');
else
  hF = fopen([savepath '\' num2str(Orientation) '.txt'],'w');
  fclose(hF);
end



% Setup Camera
% Load photon focus camera software
NET.addAssembly('C:\Documents and Settings\hrrpjm\Desktop\DPF
  Image Acquisition V3 FreeRunning\Tunnel Cam\bin\Debug\DPF Image
  Acquisition.exe');
hCamera = PAF.TunnelCam.MatlabInterface.Start('C:\Documents and
  Settings\hrrpjm\Desktop\DPF Image Acquisition V3
  FreeRunning\Tunnel Cam\bin\Debug\P_MV1-D1312(I)-
  160_Time_FreeRunning.ccf');
hCamera.ExposureTime = config.ExpTimes(1);

%Reset Figures
for i=1:length(config.ExpTimes)
  figstr([num2str(config.ExpTimes(i)) 'ms']);clf;
end


% Check that whent he shutters are closed the images are dark, and
  when open the images contain peaks
TmpImgPath = 'C:\tmpimg.bin';
EnableLaserRangeFinder(false);
CheckLasersAndShutters(hCamera,config.ShutterPort,TmpImgPath,confi
  g)

% Load sound to notify user
gong = load ('gong.mat');

for iPickPlace = 1:config.PickPlaces


  %Enable rangefinder, show red laser for positioning and move
  reference tile out of way
  EnableLaserRangeFinder(true);
  ShowLaser(config.ShutterPort,2);
  MoveTo(config.RefTstagePort,config.SamplePosition);
```

```
%Notify user to prepare for replicate
if(iPickPlace>1)
  sound(gong.y,gong.Fs);
  h=msgbox(sprintf('Prepare for replicate %d', iPickPlace));
  uiwait(h);
end

%Reset Figures
for i=1:length(config.ExpTimes)
  figstr([num2str(config.ExpTimes(i)) 'ms']);clf;
end

%Disable range finder to avoid stray light
EnableLaserRangeFinder(false)


%
% Collect Laser Measurements On Sample
%
for iLaser = 1:length(config.Waves)

  %Check that the laser is visible
  hCamera.ExposureTime = 5; %so that there is saturation
  MaxSignal = 0;
  while MaxSignal < 1500
    ShowLaser(config.ShutterPort,config.ShutterNumbers(iLaser));
    for i=1:2
      trash = double(hCamera.GetFrame(200));
      pause(1);
    end
    MaxSignal = max(trash(:));
    if (MaxSignal < 1500)
      %input('Check the shutter opened correctly. ');
      sound(gong.y, gong.Fs);
      h=msgbox('Check the shutter opened correctly. ');
      uiwait(h);
    end
  end

  % Collect the measurements for each exposure.
  for iExposure = 1:length(config.ExpTimes)
    hCamera.ExposureTime = config.ExpTimes(iExposure);
    pause(0.5);
    figstr([num2str(config.ExpTimes(iExposure)) 'ms']);

    % Setup filename
    strFilename = sprintf('Apple,f=%d,o=%d,e=%d,r=%d,w=%d nm-
{0}.bin',...
      FruitNumber, Orientation, ...
      round(config.ExpTimes(iExposure)*10), ...
      iPickPlace, config.Waves(iLaser));

    % Save Images
    SavePFImages(hCamera,[savepath '\'
strFilename],config.RepImages,300); %save rep images to
directory


    fprintf(sprintf('Saved %s\n', strFilename));
    strFilename = strrep(strFilename, '{0}', '0');
```

```
    img = LoadBinImage([savepath '\' strFilename]);

    imgexptime = GetExposureFromImage(img);
    if(imgexptime*1000 ~= config.ExpTimes(iExposure))
      error('exposure time of the images does not match the
target exposure time');
    end
    valid = IsLLSImage(img);
    if(valid~=1)
      error('laser error: invalid LLS image : check shutters and
lasers');
    end

    subplot(2,3,iLaser);
    imagesc(img);
  end
end


%
% Collect laser measurements on reference
%
MoveTo(config.RefTstagePort, config.ReferencePosition);
pause(1.5); % A little time for the reference to stop shaking.
for iLaser = 1:length(config.Waves)

  %Check that the laser is visible
  hCamera.ExposureTime = 5; %so that there is saturation
  MaxSignal = 0;
  while MaxSignal < 1500
    ShowLaser(config.ShutterPort,config.ShutterNumbers(iLaser));
    for i=1:2
      trash = double(hCamera.GetFrame(200));
      pause(1);
    end
    MaxSignal = max(trash(:));
    if (MaxSignal < 1500)
      %input('Check the shutter opened correctly. ');
      sound(gong.y, gong.Fs);
      h=msgbox('Check the shutter opened correctly. ');
      uiwait(h);
    end
  end

  % Collect the measurements for each exposure.
  for iExposure = 1:length(config.ExpTimes)
    hCamera.ExposureTime = config.ExpTimes(iExposure);
    pause(0.5);
    figstr([num2str(config.ExpTimes(iExposure)) 'ms']);

    % Setup filename
    strFilename = sprintf('Reference,f=%d,o=%d,e=%d,r=%d,w=%d
nm-{0}.bin',...
      FruitNumber, Orientation, ...
      round(config.ExpTimes(iExposure)*10), ...
      iPickPlace, config.Waves(iLaser));

    % Save Images
    SavePFImages(hCamera,[savepath '\'
strFilename],config.RepReferenceImages,300); %save rep images
to directory
```

```
    fprintf(sprintf('Saved %s\n', strFilename));
    strFilename = strrep(strFilename, '{0}', '0');
    img = LoadBinImage([savepath '\' strFilename]);

    imgexptime = GetExposureFromImage(img);
    if(imgexptime*1000 ~= config.ExpTimes(iExposure))
      error('exposure time of the images does not match the
target exposure time');
    end
    valid = IsLLSImage(img);
    if(valid~=1)
      error('laser error: invalid LLS image : check shutters and
lasers');
    end

    subplot(2,3,iLaser);
    imagesc(img);
  end
end


%
% Now dark measurements for each exposure.
%
for iExposure = 1:length(config.ExpTimes)
  hCamera.ExposureTime = config.ExpTimes(iExposure);
  pause(0.5);
  figstr([num2str(config.ExpTimes(iExposure)) 'ms']);

  ShowLaser(config.ShutterPort, 0);
  strFilename = sprintf('Dark,f=%d,o=%d,e=%d,r=%d-{0}.bin',...
    FruitNumber, Orientation, ...
    round(config.ExpTimes(iExposure)*10), ...
    iPickPlace);

  % Save Images
  SavePFImages(hCamera,[savepath '\'
strFilename],config.RepDarkImages,300); %save rep images to
directory

  strFilename = strrep(strFilename, '{0}', '0');
  img = LoadBinImage([savepath '\' strFilename]);

  imgexptime = GetExposureFromImage(img);
  if(imgexptime*1000 ~= config.ExpTimes(iExposure))
    error('exposure time of the images does not match the target
exposure time');
  end
  valid = IsDarkImage(img);
  if(valid~=1)
    error('laser error: invalid Dark image : check shutters and
lasers');
  end

  subplot(2,3,iLaser+1);
  imagesc(img);
  fprintf('Saved dark\n');
end
```

```
  MoveTo(config.RefTstagePort, config.SamplePosition,false);
  toc
end

sound(gong.y, gong.Fs);
EnableLaserRangeFinder(true);
ShowLaser(config.ShutterPort, 2);



%% Write Bat File To Move Images
% hF = fopen('E:\Cox Pre Trial Data Collection\test.bat','w');
% string = ['move "f:\\collect\\*.*" "E:\\2013 04 03 Skin on Skin
   Off Trial 1\\Raw Data\\Fruit ' num2str(FruitNumber) '"'];
% %string = 'hello my \\ name is';
% fprintf(hF,string);
% fclose(hF);
%
% msgbox('run bat file to move all images!');
```

12. References

Abbott, JA 1994, "Firmness Measurement of Freshly Harvested ' Delicious ' Apples by Sensory Methods , Sonic Transmission , Magness-Taylor , and Compression," *Journal of the American Society for Horticultural Science*, vol. 119, no. 3, pp. 510–515.

Abbott, JA 1999, "Quality measurement of fruits and vegetables," *Postharvest Biology and Technology*, vol. 15, no. 3, pp. 207–225.

Abbott, JA & Harker, FR 2004, *Texture - Agriculture Handbook Number 66 - The Commercial Storage of Fruits, Vegetables, and Florist and Nursery Stocks*, United States Department of Agriculture, Beltsville, MD.

Abbott, JA, Lu, R, Upchurch, BL & Stroshine, RL 1997, "Technologies for nondestructive quality evaluation of fruits and vegetables," *Horticultural Reviews*, vol. 20, pp. 1–120.

Alamar, MC, Vanstreels, E, Oey, ML, Moltó, E & Nicolaï, BM 2008, "Micromechanical behaviour of apple tissue in tensile and compression tests: Storage conditions and cultivar effect," *Journal of Food Engineering*, vol. 86, no. 3, pp. 324–333.

Anderson, ER, Cuccia, DJ & Durkin, AJ 2007, "Detection of bruises on golden delicious apples using spatial- frequency-domain imaging," *Proceedings of SPIE*, vol. 6430, pp. 1–11.

Anderson, ER, You, JS, Cuccia, DJ, Tromberg, BJ & Durkin, AJ 2006, "Spatial-Frequency-Domain Imaging for quality assessment of apples," *2006 Conference on Lasers and Electro-Optics and 2006 Quantum Electronics and Laser Science Conference*, vol. 1, pp. 1–2.

Atkinson, RG, Sutherland, PW, Johnston, SL, Gunaseelan, K, Hallett, IC, Mitra, D, Brummell, D a, Schröder, R, Johnston, JW & Schaffer, RJ 2012, "Down-regulation of POLYGALACTURONASE1 alters firmness, tensile strength and water loss in apple (Malus x domestica) fruit," *BMC Plant Biology*, vol. 12, no. 1, p. 129.

AWETA America 2013, "Powervision-3D,", accessed September 18, 2013, from <http://www.powervision3d.com/>.

Aydin, ED, de Oliveira, CRE & Goddard, a. JH 2004, "A finite element-spherical harmonics radiation transport model for photon migration in turbid media," *Journal of Quantitative Spectroscopy and Radiative Transfer*, vol. 84, no. 3, pp. 247–260.

Baerdemaeker, J De, Lemaitre, L & Meire, R 1982, "Quality Detection by Frequency Spectrum Analysis of the Fruit Impact Force," *Transactions of the ASABE*, vol. 25, no. 1, pp. 0175–0178.

Bain, J & Robertson, R 1951, "The physiology of growth in apple fruits I. Cell size, cell number, and fruit development," *Australian Journal of Biological Sciences*, vol. 4, no. 2, pp. 75–91.

Baker, G 1998, "Strategic implications of consumer food safety preferences," *The International Food and Agribusiness Management Review*, vol. 1, no. 4, pp. 451–463.

Bashkatov, AN, Genina, EA, Kochubey, VI & Tuchin, V V 2005, "Optical properties of human skin, subcutaneous and mucous tissues in the wavelength range from 400 to 2000 nm," *Journal of Physics D: Applied Physics*, vol. 38, no. 15, pp. 2543–2555.

Batt, PJ & Sadler, C 1998, "Consumer attitudes towards the labelling of apples," *Food Australia: Official Journal of CAFTA and AIFST*, vol. 50, no. 9, pp. 449–451.

Belie, N De, Tu, K, Jancsók, P & De Baerdemaeker, J 1999, "Preliminary study on the influence of turgor pressure on body reflectance of red laser light as a ripeness indicator for apples," *Postharvest Biology and Technology*, vol. 16, no. 3, pp. 279–284.

Blue Leaf Software 2012, "Dagra: Digitize graphical data," *BlueLeafSoftware.com*, accessed May 7, 2014, from <http://www.blueleafsoftware.com>.

Boas, DA, Pitris, C & Ramanujam, N 2012, *Handbook of Biomedical Optics*, CRC Press, Boca Raton, FL.

Bobelyn, E, Serban, A-S, Nicu, M, Lammertyn, J, Nicolai, BM & Saeys, W 2010, "Postharvest quality of apple predicted by NIR-spectroscopy: Study of the effect of biological variability on spectra and model performance," *Postharvest Biology and Technology*, vol. 55, no. 3, pp. 133–143.

Bouguet, J-Y 2013, "Camera Calibration Toolbox for Matlab,", accessed August 5, 2011, from <http://www.vision.caltech.edu/bouguetj/calib_doc/>.

Burdon, J, McLeod, D, Lallu, N, Gamble, J, Petley, M & Gunson, a. 2004, "Consumer evaluation of 'Hayward' kiwifruit of different at-harvest dry matter contents," *Postharvest Biology and Technology*, vol. 34, no. 3, pp. 245–255.

Calavo 2013, "ProRipe,", accessed February 17, 2014, from <http://www.calavo.com/store/pro_ripe_vip.html>.

Campbell, BL, Nelson, RG, Ebel, RC, Dozier, WA, Adrian, JL & Hockema, BR 2004, "Fruit Quality Characteristics That Affect Consumer Preferences for Satsuma Mandarins," *HortScience*, vol. 39, no. 7, pp. 1664–1669.

Cen, H & Lu, R 2010, "Optimization of the hyperspectral imaging-based spatially-resolved system for measuring the optical properties of biological materials," *Optics Express*, vol. 18, no. 16, pp. 17412–32.

Cen, H, Lu, R & Dolan, K 2010, "Optimization of inverse algorithm for estimating the optical properties of biological materials using spatially-resolved diffuse reflectance," *Inverse Problems in Science and Engineering*, vol. 18, no. 6, pp. 853–872.

Cen, H, Lu, R, Mendoza, F a. & Ariana, DP 2011, "Peach maturity/quality assessment using hyperspectral imaging-based spatially resolved technique," *Proceedings of SPIE*, vol. 8027, pp. 1–15.

Cen, H, Lu, R, Mendoza, F & Ariana, D 2012, "Assessing Multiple Quality Attributes of Peaches Using Optical Absorption and Scattering Properties," *Transactions of the ASABE*, vol. 55, no. 2, pp. 647–657.

Cen, H, Lu, R, Mendoza, F & Beaudry, RM 2013, "Relationship of the optical absorption and scattering properties with mechanical and structural properties of apple tissue," *Postharvest Biology and Technology*, vol. 85, pp. 30–38.

Cen, H, Lu, R & Mendoza, FA 2011, "Analysis of Absorption and Scattering Spectra for Assessing the Internal Quality of Apple Fruit," in *Proceedings of the 4th International Conference Postharvest Unlimited*, Leavenworth, Washington, 22-06-2011, pp. 181–188.

Chen, H & DeBaerdemaeker, J 1993, "Effect of apple shape on acoustic measurements of firmness," *Journal of Agricultural Engineering Research*, vol. 56, no. 3, pp. 253–266.

Chen, P, McCarthy, M & Kauten, R 1989, "NMR for internal quality evaluation of fruits and vegetables," *Transactions of the ASABE*, vol. 32, no. 5, pp. 1747–1753.

Chen, P & Ruiz-Altisent, M 1996, "A low-mass impact sensor for high-speed firmness sensing of fruits," in *International Conference on Agricultural Engineering. Paper. No. 96F-003*, Madrid, Spain, pp. 1–8.

Cho, Y & Han, YJ 1999, "Nondestructive characterization of apple firmness by quantitation of laser scatter," *Journal of Texture Studies*, vol. 30, pp. 625–638.

Chung, SH, Cerussi, a E, Merritt, SI, Ruth, J & Tromberg, BJ 2010, "Non-invasive tissue temperature measurements based on quantitative diffuse optical spectroscopy (DOS) of water," *Physics in Medicine and Biology*, vol. 55, no. 13, pp. 3753–65.

Clark, CJ, McGlone, V a. & Jordan, RB 2003, "Detection of Brownheart in 'Braeburn' apple by transmission NIR spectroscopy," *Postharvest Biology and Technology*, vol. 28, no. 1, pp. 87–96.

Cletus, B, Künnemeyer, R, Martinsen, P & McGlone, VA 2010, "Temperature-dependent optical properties of Intralipid measured with frequency-domain photon-migration spectroscopy," *Journal of Biomedical Optics*, vol. 15, no. 1, p. 017003.

Compac Sorting Equipment 2013, "Weight Sorting,", accessed September 18, 2013, from <http://www.compacsort.com/wa.asp?idWebPage=14832&idDetails=106>.

Cook, NC, Rabe, E, Keulemans, J & Jacobs, G 1998, "The Expression of Acrotony in Deciduous Fruit Trees: A Study of the Apple Rootstock M.9," *Journal of the American Society for Horticultural Science*, vol. 123, no. 1, pp. 30–34.

Coriolis Research 2006, "Overview of the New Zealand Apple Industry in a Global Context," *Pipfruit New Zealand*, pp. 1–31.

Cubeddu, R, D'Andrea, C, Pifferi, A, Taroni, P, Torricelli, A, Valentini, G, Dover, C & Johnson, D 2001, "Time-Resolved Reflectance Spectroscopy Applied to the Nondestructive Monitoring of the Internal Optical Properties in Apples," *Applied Spectroscopy*, vol. 55, no. 10, pp. 1368–1374.

Cubeddu, R, D'Andrea, C, Pifferi, A, Taroni, P, Torricelli, A, Valentini, G, Dover, C, Johnson, D, Ruiz-Altisent, M & Valero, C 2001, "Nondestructive quantification of chemical and physical properties of fruits by time-resolved reflectance spectroscopy in the wavelength range 650-1000 nm," *Applied Optics*, vol. 40, no. 4, pp. 538–43.

Cubeddu, R, Pifferi, A, Taroni, P, Torricelli, A, Valentini, G, Ruiz-altisent, M, Valero, C, Ortiz, C, Dover, C & Johnson, D 2000, "Non-destructive measurements of the optical properties of apples by means of time-resolved reflectance," *Applied Spectroscopy*, vol. 55, no. 10, pp. 1368–1374.

Dallmeier 2014, "CCD vs. CMOS Technology,", accessed February 14, 2014, from <http://www.dallmeier.com/fr/produits-electronic/cameras/bon-a-savoir/ccd-vs-cmos.html>.

Delong, JM, Prange, RK, Harrison, PA, Schofield, RA & DeEll, JR 1999, "Using the Streif Index as a Final Harvest Window for Controlled-atmosphere Storage of Apples," *HortScience*, vol. 34, no. 7, pp. 1251–1255.

Derya, Ş & Ilan, B 2013, "Radiative transport theory for light propagation in luminescent media," *Journal of the Optical Society of America*, vol. 30, no. 5, pp. 813–820.

Dobrzański, B, Rabcewicz, J & Rybczyński, R 2006, *Handling of apple: transport techniques and efficiency vibration, damage and bruising texture, firmness and quality*, Institute of Agrophysics Polish Academy of Sciences, Lublin, Poland.

Duprat, F, Chen, H, Grotte, M, Loonis, D & Pietri, E 1995, "Laser light based machine vision system for nondestructive ripness sensing of golden apples," in *Proceedings of the 1st IFAC Workshop: Control Applications in Post-harvest and Processing Technology*, Ostend, Belgium, 01-06-1995, pp. 85–91.

Duprat, F, Grotte, M, Pietri, E, Loonis, D & Studman, CJ 1997, "The acoustic impulse response method for measuring the overall firmness of fruit," *Journal of Agricultural Engineering Research*, vol. 66, no. 4, pp. 251–259.

Elzebroek, A & Wind, K 2008, *Guide to Cultivated Plants*, CAB International, Boston, MA.

Esau, K 1993, *Plant Anatomy*, John Wiley & Sons, Milton, Queensland.

Farrell, T, Patterson, MSM & Wilson, B 1992, "A diffusion theory model of spatially resolved, steady-state diffuse reflectance for the noninvasive determination of tissue optical properties in vivo," *Medical Physics*, vol. 19, no. 4, pp. 879–888.

Ferguson, I, Volz, R & Woolf, A 1999, "Preharvest factors affecting physiological disorders of fruit," *Postharvest Biology and Technology*, vol. 15, no. June 1998, pp. 255–262.

Flock, ST, Jacques, SL, Wilson, BC, Star, WM & van Gemert, MJ 1992, "Optical properties of Intralipid: a phantom medium for light propagation studies," *Lasers in surgery and medicine*, vol. 12, no. 5, pp. 510–9.

Fraser, DG, Künnemeyer, R, McGlone, VA & Jordan, RB 2001, "Near infra-red (NIR) light penetration into an apple," *Postharvest Biology and Technology*, vol. 22, no. 3, pp. 191–195.

García-Ramos, FJ, Valero, C, Homer, I, Ortiz-Cañavate, J & Ruiz-Altisent, M 2005, "Non destructive fruit firmness sensors: A review," *Spanish Journal of Agricultural Research*, vol. 3, no. 1, pp. 61–73.

Greefa 2014, "Greefa Homepage,", accessed May 6, 2014, from <http://www.greefa.nl/UK/default.htm>.

Grigoropoulos, CP 2009, *Transport in Laser Microfabrication: Fundamentals and Applications*, Cambridge University Press.

Groenhuis, RAJ, Ten Bosch, JJ & Ferwerda, HA 1983, "Scattering and absorption of turbid materials determined from reflection measurements. 1: Theory," *Applied Optics*, vol. 22, no. 16, pp. 2456–2462.

Gross, J 1987, *Pigments in fruits*, Academic Press, London, United Kingdom.

Gu, M 1999, *Advanced Optical Imaging Theory*, Springer.

Hale, GM & Querry, MR 1973, "Optical Constants of Water in the 200-nm to 200-microm Wavelength Region," *Applied Optics*, vol. 12, no. 3, pp. 555–63.

Han, D, Tu, R, Lu, C, Liu, X & Wen, Z 2006, "Nondestructive detection of brown core in the Chinese pear 'Yali' by transmission visible–NIR spectroscopy," *Food Control*, vol. 17, no. 8, pp. 604–608.

Harker, F & Hallett, I 1992, "Physiological changes associated with development of mealiness of apple fruit during cool storage," *HortScience*, vol. 27, no. 12, pp. 1291–1294.

Harker, FRF, Maindonald, J, Murray, SH, Gunson, F a., Hallett, IC & Walker, SB 2002, "Sensory interpretation of instrumental measurements 1: texture of apple fruit," *Postharvest Biology and Technology*, vol. 24, no. 3, pp. 225–239.

Harker, R 2001, "Consumer Response to Apples," in *Washington Tree Fruit Postharvest Conference*, Wenatchee, Washington, pp. 1–7.

Haskell, RC, Svaasand, LO, Tsay, TT, Feng, TC, McAdams, MS & Tromberg, BJ 1994, "Boundary conditions for the diffusion equation in radiative transfer," *Journal of the Optical Society of America*, vol. 11, no. 10, pp. 2727–41.

Hertog, MLAT., Ben-Arie, R, Róth, E & Nicolaï, BM 2004, "Humidity and temperature effects on invasive and non-invasive firmness measures," *Postharvest Biology and Technology*, vol. 33, no. 1, pp. 79–91.

Hoehn, E, Gasser, F, Guggenbühl, B & Künsch, U 2003, "Efficacy of instrumental measurements for determination of minimum requirements of firmness, soluble solids, and acidity of several apple varieties in comparison to consumer expectations," *Postharvest Biology and Technology*, vol. 27, pp. 27–37.

Howarth, M & Ioannides, Y 2002, "Sinclair IQ-firmness tester," in *Proceedings of the International Conference of Agricultural Engineering: Paper 02-IE-0006*, Budapest,Hungary, 30-06-2002.

Howell, SB 2000, *Handbook of CCD Astronomy*, Cambridge University Press.

Huang, M & Lu, R 2010, "Apple mealiness detection using hyperspectral scattering technique," *Postharvest Biology and Technology*, vol. 58, no. 3, pp. 168–175.

Huang, M, Zhu, Q, Wang, B & Lu, R 2012, "Analysis of hyperspectral scattering images using locally linear embedding algorithm for apple mealiness classification," *Computers and Electronics in Agriculture*, vol. 89, pp. 175–181.

Institute of Food Research 2009, "Apple Facts,", accessed February 15, 2014, from <http://www.ifr.ac.uk/info/society/spotlight/apples.htm>.

Jacques, S 2007, "SC029: Tissue Optics," in *Short Course Notes*, Photonics West, San Jose, CA.

Jacques, SL & Pogue, BW 2008, "Tutorial on diffuse light transport," *Journal of Biomedical Optics*, vol. 13, no. 4, pp. 041302–1–19.

Johnson, DS & Dover, DJ 2005, "Does `Acoustic Firmness' Relate to Sensory Perception of Apple Texture?," *Acta Horticulturae (ISHS)*, vol. 682, pp. 1395–1402.

Kader, A 1997, "Fruit maturity, ripening, and quality relationships," *Acta Horticulturae*, vol. 485, pp. 203–208.

Kakuta, N, Arimoto, H, Momoki, H, Li, F & Yamada, Y 2008, "Temperature measurements of turbid aqueous solutions using near-infrared spectroscopy," *Applied Optics*, vol. 47, no. 13, pp. 2227–33.

Katz, M 2002, *Introduction to Geometrical Optics*, World Scientific.

Kavdir, I, Lu, R, Ariana, D & Ngouajio, M 2007, "Visible and near-infrared spectroscopy for nondestructive quality assessment of pickling cucumbers," *Postharvest Biology and Technology*, vol. 44, no. 2, pp. 165–174.

De Ketelaere, B, Howarth, MS, Crezee, L, Lammertyn, J, Viaene, K, Bulens, I & De Baerdemaeker, J 2006, "Postharvest firmness changes as measured by acoustic and low-mass impact devices: a comparison of techniques," *Postharvest Biology and Technology*, vol. 41, no. 3, pp. 275–284.

Kienle, A & Patterson, MSM 1997, "Improved solutions of the steady-state and the time-resolved diffusion equations for reflectance from a semi-infinite turbid medium," *The Journal of the Optical Society of America*, vol. 14, no. 1, pp. 246–254.

Kiessling, F & Pichler, BJ 2010, *Small Animal Imaging: Basics and Practical Guide*, Springer.

Kilcast, D 2013, *Instrumental Assessment of Food Sensory Quality: A Practical Guide*, Elsevier.

Kim, MS, Chen, YR & Mehl, PM 2001, "Hyperspectral reflectance and fluorescence imaging system for food quality and safety," *Transactions of the ASAE*, vol. 44, no. 3, pp. 721–729.

Kingston, C 1992, "Maturity indices for apple and pear," in *Horticultural Reviews: Volume 13*, John Wiley & Sons, Inc., Oxford, UK.

Klinger, T 2003, *Image Processing with LabVIEW and IMAQ Vision*, Prentice Hall Professional.

Kou, L, Labrie, D & Chylek, P 1993, "Refractive indices of water and ice in the 0.65- to 2.5-μm spectral range," *Applied Optics*, vol. 32, no. 19, pp. 3531–40.

Kruegle, H 2011, *CCTV Surveillance: Video Practices and Technology*, Butterworth-Heinemann.

Kupferman, E 2007, "Non-Destructive Firmness Instrument Testing: Apples and Pears," *Post Harvest Information Network*, vol. 1, no. 1, pp. 1–19.

Kviklienė, N & Valiuškaitė, A 2009, "Influence of maturity stage on fruit quality during storage of 'Shampion'apples," *Sodininkystė ir Daržininkystė*, vol. 28, no. 3, pp. 117–124.

Lakso, AN & Goffinet, MC 2013, "Apple Fruit Growth," *New York Fruit Quarterly*, vol. 21, no. 1, pp. 11–14.

Lammertyn, J, Nicolaï, B, Ooms, K, Smedt, V De & Baerdemaeker, J De 1998, "Non-destructive measurement of acidity, soluble solids, and firmness of Jonagold apples using NIR-spectroscopy," *Transactions of the ASAE*, vol. 41, no. 4, pp. 1089–1094.

Landahl, S 2007, "Comprehensive evaluation of the acoustic impulse-response of apples as a measure of fruit quality," *PhD Thesis, University of Leuven*, pp. 1–193.

Levetin, E & McMahon, K 2008, *Plants and Society*, McGraw-Hill Education, Columbus, OH.

Lien, C-C, Ay, C & Ting, C-H 2009, "Non-destructive impact test for assessment of tomato maturity," *Journal of Food Engineering*, vol. 91, no. 3, pp. 402–407.

Litwiller, D 2001, "CCD vs . CMOS: Facts and Fiction," *Photonics Spectra*, vol. 35, no. 1, pp. 154–158.

Liu, Y, Chen, X & Ouyang, A 2008, "Nondestructive determination of pear internal quality indices by visible and near-infrared spectrometry," *LWT-Food science and Technology*, vol. 41, pp. 1720–1725.

Lleó, L, Barreiro, P, Ruiz-Altisent, M & Herrero, A 2009, "Multispectral images of peach related to firmness and maturity at harvest," *Journal of Food Engineering*, vol. 93, no. 2, pp. 229–235.

Londhe, D, Nalawade, S, Pawar, G, Atkari, V & Wandkar, S 2013, "Grader: A review of different methods of grading for fruits and vegetables," *Agricultural Engineering International: CIGR Journal*, vol. 15, no. 3, pp. 217–230.

Lu, R 2003, "Multispectral imaging for predicting firmness and soluble solids content of apple fruit," *Postharvest Biology and Technology*, vol. 31, no. 2, pp. 147–157.

Lu, R 2004, "Near-infrared multispectral scattering for assessing internal quality of apple fruit," *Proceedings of SPIE*, vol. 5271, pp. 313–320.

Lu, R 2007, "Nondestructive measurement of firmness and soluble solids content for apple fruit using hyperspectral scattering images," *Sensing and Instrumentation for Food Quality and Safety*, vol. 1, no. 1, pp. 19–27.

Lu, R & Abbott, JA 1996, "Finite element analysis of modes of vibration in apples," *Journal of Texture Studies*, vol. 27, no. 3, pp. 265–286.

Lu, R & Chen, Y 1999, "Hyperspectral imaging for safety inspection of food and agricultural products," *Proceedings of SPIE*, vol. 3544, pp. 121–133.

Lu, R, Huang, M & Qin, J 2009, "Analysis of hyperspectral scattering characteristics for predicting apple fruit firmness and soluble solids content," *Proceedings of SPIE*, vol. 7315, pp. 1–11.

Lu, R & Peng, Y 2005, "A laser-based multispectral imaging system for real-time detection of apple fruit firmness," *Proceedings of SPIE*, vol. 5996, pp. 1–10.

Lu, R & Peng, Y 2006, "Hyperspectral Scattering for assessing Peach Fruit Firmness," *Biosystems Engineering*, vol. 93, no. 2, pp. 161–171.

Lu, R & Peng, Y 2007, "Development of a multispectral imaging prototype for real-time detection of apple fruit firmness," *Optical Engineering*, vol. 46, no. 12, p. 123201.

Lu, R, Qin, J & Peng, Y 2006, "Measurement of the Optical Properties of Apples by Hyperspectral Imaging for Assessing Fruit Quality," *Transactions of the ASAE: Paper No 053068*, pp. 1–11.

Macnish, A, Joyce, D & Shorter, A 1997, "A simple non-destructive method for laboratory evaluation of fruit firmness," *Australian Journal of Experimental Agriculture*, vol. 37, no. 709, p. 713.

Magness, J & Taylor, G 1925, "An improved type of pressure tester for the determination of fruit maturity," *United States Department of Agriculture Department Circular*, vol. 350, pp. 1–8.

Maini 2013, *Lasers and Optoelectronics: Fundamentals, Devices and Applications*, John Wiley & Sons.

Mainzatnight 2011, "Polarizers - Principles and Usage," *Mainzatnight.de*, accessed April 20, 2014, from <http://mainzatnight.de/2011/10/polarizers-principles-and-usage/>.

Mallégol, J, Lemaire, J & Gardette, JL 2001, "Yellowing of oil-based paints," *Studies in Conservation*, vol. 46, no. 2, pp. 121–131.

Manalo, A 1990, "Assessing the importance of apple attributes: an agricultural application of conjoint analysis," *Northeastern Journal of Agricultural and Resource Economics*, vol. 19, no. 2, pp. 118–124.

Marshall, GF & Stutz, GE 2011, *Handbook of Optical and Laser Scanning, Second Edition*, CRC Press.

Martelli, F, Bassani, M, Alianelli, L, Zangheri, L & Zaccanti, G 2000, "Accuracy of the diffusion equation to describe photon migration through an infinite medium: numerical and experimental investigation," *Physics in Medicine and Biology*, vol. 45, no. 5, pp. 1359–1373.

Martelli, F, Bianco, S Del, Ismaelli, A & Zaccanti, G 2009, *Light propagation through biological tissue and other diffusive media: theory, solutions, and software*, SPIE Press.

Martinsen, P & Schaare, P 1998, "Measuring soluble solids distribution in kiwifruit using near-infrared imaging spectroscopy," *Postharvest Biology and Technology*, vol. 14, no. 3, pp. 271–281.

Matlab 2014, "Matlab Curve Fitting Toolbox," *Matlab.com*, accessed May 7, 2014, from <http://www.mathworks.com.au/help/curvefit/fit.html>.

McGlone, VA, Jordan, RB & Martinsen, PJ 2002, "Vis/NIR estimation at harvest of pre- and post-storage quality indices for 'Royal Gala' apple," *Postharvest Biology and Technology*, vol. 25, no. 2, pp. 135–144.

McGlone, VA, Jordan, RB, Seelye, R & Martinsen, PJ 2002, "Comparing density and NIR methods for measurement of Kiwifruit dry matter and soluble solids content," *Postharvest Biology and Technology*, vol. 26, no. 2, pp. 191–198.

McGlone, VA & Kawano, S 1998, "Firmness, dry-matter and soluble-solids assessment of postharvest kiwifruit by NIR spectroscopy," *Postharvest Biology and Technology*, vol. 13, no. 2, pp. 131–141.

McGlone, VA, Martinsen, P, Künnemeyer, R, Jordan, B & Cletus, B 2007, "Measuring optical temperature coefficients of Intralipid," *Physics in Medicine and Biology*, vol. 52, no. 9, pp. 2367–78.

Mehinagic, E, Royer, G, Symoneaux, R, Bertrand, D & Jourjon, F 2004, "Prediction of the sensory quality of apples by physical measurements," *Postharvest Biology and Technology*, vol. 34, no. 3, pp. 257–269.

Mendoza, F, Lu, R, Ariana, D, Cen, H & Bailey, B 2011, "Integrated spectral and image analysis of hyperspectral scattering data for prediction of apple fruit firmness and soluble solids content," *Postharvest Biology and Technology*, vol. 62, no. 2, pp. 149–160.

Mendoza, F, Verboven, P, Mebatsion, HK, Kerckhofs, G, Wevers, M & Nicolaï, B 2007, "Three-dimensional pore space quantification of apple tissue using X-ray computed microtomography," *Planta*, vol. 226, no. 3, pp. 559–70.

Merzlyak, M, Solovchenko, A & Gitelson, A 2003, "Reflectance spectral features and non-destructive estimation of chlorophyll, carotenoid and anthocyanin content in apple fruit," *Postharvest Biology and Technology*, vol. 27, no. 2, pp. 197–211.

Michels, R, Foschum, F & Kienle, A 2008, "Optical properties of fat emulsions," *Optics express*, vol. 16, no. 8, pp. 2304–2314.

Mie, G 1976, "Contributions to the optics of turbid media, particularly of colloidal metal solutions," *Annals of Physics*, vol. 25, no. 3, pp. 377–445.

Miller, JC & Haglund, RF 1997, *Laser Ablation and Desorption*, Academic Press.

Moffitt, TP 2007, "Compact Fiber-Optic Diffuse Reflection Probes for Medical Diagnostics," *PhD Thesis, Western Washington University*, pp. 1–73.

Mohr, W 1979, "Silver proteinate staining of neutral polysaccharides in apple cell walls: implications relative to fruit firmness," *International Journal of Food Science & Technology*, vol. 14, no. 5, pp. 521–526.

Mohsenin, NN 1986, *Physical Properties of Plant and Animal Materials: Structure, Physical Characteristics, and Mechanical Properties*, Gordon and Breach.

Molina-Delgado, D, Alegre, S, Puy, J & Recasens, I 2009, "Relationship between Acoustic Firmness and Magness Taylor Firmness in Royal Gala and Golden Smoothee Apples," *Food Science and Technology International*, vol. 15, no. 1, pp. 31–40.

Mollazade, K, Omid, M, Akhlaghian Tab, F, Kalaj, YR, Mohtasebi, SS & Zude, M 2013, "Analysis of texture-based features for predicting mechanical properties of horticultural products by laser light backscattering imaging," *Computers and Electronics in Agriculture*, vol. 98, pp. 34–45.

Mollazade, K, Omid, M, Tab, FA & Mohtasebi, SS 2012, "Principles and Applications of Light Backscattering Imaging in Quality Evaluation of Agro-food Products: a Review," *Food and Bioprocess Technology*, vol. 5, no. 5, pp. 1465–1485.

Muhua, L, Peng, F & Renfa, C 2007, "Non destructive estimation peach SSC and firmness by mutispectral reflectance imaging," *New Zealand Journal of Agricultural Research*, vol. 50, pp. 601–608.

Nicolaï, BM, Beullens, K, Bobelyn, E, Hertog, MLATM, Schenk, A, Vermeir, S & Lammertyn, J 2006, "Systems to Characterise Internal Quality of Fruit and Vegetables," *Acta Horticulturae*, vol. 712, pp. 59–66.

Nicolaï, BM, Beullens, K, Bobelyn, E, Peirs, A, Saeys, W, Theron, KI & Lammertyn, J 2007, "Nondestructive measurement of fruit and vegetable quality by means of NIR spectroscopy: A review," *Postharvest Biology and Technology*, vol. 46, no. 2, pp. 99–118.

Nicolaï, BM, Defraeye, T, De Ketelaere, B, Herremans, E, Hertog, ML a TM, Saeys, W, Torricelli, A, Vandendriessche, T & Verboven, P 2014, "Nondestructive measurement of fruit and vegetable quality," *Annual Review of Food Science and Technology*, vol. 5, pp. 285–312.

Nicolaï, BM, Verlinden, BE, Desmet, M, Saevels, S, Saeys, W, Theron, K, Cubeddu, R, Pifferi, A & Torricelli, A 2008, "Time-resolved and continuous wave NIR reflectance spectroscopy to predict soluble solids content and firmness of pear," *Postharvest Biology and Technology*, vol. 47, no. 1, pp. 68–74.

Ninni, P Di, Martelli, F & Zaccanti, G 2011, "Intralipid: towards a diffusive reference standard for optical tissue phantoms," *Physics in Medicine and Biology*, vol. 56, no. 2, pp. 21–28.

Nixon, M & Aguado, AS 2008, *Feature Extraction & Image Processing*, Academic Press.

Noh, HK & Lu, R 2007, "Hyperspectral laser-induced fluorescence imaging for assessing apple fruit quality," *Postharvest Biology and Technology*, vol. 43, no. 2, pp. 193–201.

Olsen, JB & Sager, EM 1995, "Subjective evaluation of image quality based on images obtained with a breast tissue phantom: comparison with a conventional image quality phantom," *British Journal of Radiology*, vol. 68, no. 806, pp. 160–164.

Ozaki, Y, McClure, WF & Christy, AA 2006, *Near-Infrared Spectroscopy in Food Science and Technology*, John Wiley & Sons.

Palmer, JW, Harker, FR, Tustin, DS & Johnston, J 2010, "Fruit dry matter concentration: a new quality metric for apples," *Journal of the Science of Food and Agriculture*, vol. 90, no. 15, pp. 2586–94.

Park, B, Abbott, J, Lee, K, Choi, C & Choi, K 2003, "Near-infrared diffuse reflectance for quantitative and qualitative measurement of soluble solids and firmness of Delicious and Gala apples," *Transactions of the ASAE*, vol. 46, no. 6, pp. 1721–1731.

Parker, ST, Domachuk, P, Amsden, J, Bressner, J, Lewis, J a., Kaplan, DL & Omenetto, FG 2009, "Biocompatible Silk Printed Optical Waveguides," *Advanced Materials*, vol. 21, no. 23, pp. 2411–2415.

Patterson, M, Chance, B & Wilson, B 1989, "Time resolved reflectance and transmittance for the non-invasive measurement of tissue optical properties," *Applied Optics*, vol. 28, no. 12, pp. 2331–2336.

Peirs, A, Lammertyn, J, Ooms, K & Nicolaı, BM 2001, "Prediction of the optimal picking date of different apple cultivars by means of VIS / NIR-spectroscopy," *Postharvest Biology and Technology*, vol. 21, pp. 189–199.

Peirs, A, Scheerlinck, N, Touchant, K & Nicolaï, BM 2002, "Comparison of Fourier Transform and Dispersive Near-Infrared Reflectance Spectroscopy for Apple Quality Measurements," *Biosystems Engineering*, vol. 81, no. 3, pp. 305–311.

Peirs, A, Schenk, A & Nicolaï, BM 2005, "Effect of natural variability among apples on the accuracy of VIS-NIR calibration models for optimal harvest date predictions," *Postharvest Biology and Technology*, vol. 35, no. 1, pp. 1–13.

Peng, Y & Lu, R 2004, "A liquid crystal tunable filter based multispectral imaging system for prediction of apple fruit firmness," *Proceedings of SPIE*, vol. 5587, pp. 91–100.

Peng, Y & Lu, R 2005, "Modeling multispectral scattering profiles for prediction of apple fruit firmness," *Transactions of the ASAE*, vol. 48, no. 1, pp. 235–242.

Peng, Y & Lu, R 2006a, "Improving apple fruit firmness predictions by effective correction of multispectral scattering images," *Postharvest Biology and Technology*, vol. 41, no. 3, pp. 266–274.

Peng, Y & Lu, R 2006b, "An LCTF-based multispectral imaging system for estimation of apple fruit firmness: Part I. Acquisition and characterization of scattering images," *Transactions of the ASABE*, vol. 49, no. 1, pp. 259–268.

Peng, Y & Lu, R 2006c, "An LCTF-based multispectral imaging system for estimation of apple fruit firmness: Part II. Selection of optimal wavelengths and development of prediction models," *Transactions of the ASAE*, vol. 49, no. 1, pp. 269–276.

Peng, Y & Lu, R 2007, "Prediction of apple fruit firmness and soluble solids content using characteristics of multispectral scattering images," *Journal of Food Engineering*, vol. 82, no. 2, pp. 142–152.

Peng, Y & Lu, R 2008, "Analysis of spatially resolved hyperspectral scattering images for assessing apple fruit firmness and soluble solids content," *Postharvest Biology and Technology*, vol. 48, no. 1, pp. 52–62.

Photonfocus 2010, "Photonfocus MV1-D1312I-160-CL Manual," *Public Datasheet*, pp. 1–2.

Pifferi, A, Torricelli, A, Taroni, P, Comelli, D, Bassi, A & Cubeddu, R 2007, "Fully automated time domain spectrometer for the absorption and scattering characterization of diffusive media.," *The Review of scientific instruments*, vol. 78, no. 5, p. 053103.

Pipfruit New Zealand 2005, "Best Practice Guidelines for Production , Harvest , Cool-chain and Packing of NZ pipfruit Industry Quality Recommendations," *Industry Report*, vol. 1, no. 1, pp. 1–54.

Plocharski, WJ & Konopacka, D 1999, "The Relation Between Mechanical and Sensory Parameters of Apples and Pears," *Acta Horticulturae*, vol. 485, pp. 309–318.

Pogue, BW & Patterson, MS 2006, "Review of tissue simulating phantoms for optical spectroscopy, imaging and dosimetry," *Journal of Biomedical Optics*, vol. 11, no. 4, p. 041102.

Prahl, SA 1999, "Optical property measurements using the inverse adding-doubling program," *Oregon Medical Laser Center, St. Vincent Hospital*, vol. 2197, no. January.

Prahl, SA 2011, "Everything I think you should know about inverse adding-doubling," *Oregon Medical Laser Center, St. Vincent Hospital*, pp. 1–74.

Prahl, SA 2012, "Personal Correspondence,".

Prahl, SA 2013, "Inverse Adding-Doubling Program," *Omlc.ogi.edu*, accessed February 1, 2013, from <http://omlc.ogi.edu/software/iad/>.

Prahl, SA, Gemert, MJC Van, Welch, AJ & Van Gemert, MJC 1993, "Determining the Optical Properties of Turbid Media Using the Adding-Doubling Method," *Applied Optics*, vol. 32, no. 4, pp. 559–568.

Privett, OS, Blank, ML, Covell, JB & Lundberg, WO 1961, "Yellowing of oil films," *Journal of the American Oil Chemists' Society*, vol. 38, no. 1, pp. 22–27.

Qin, J & Lu, R 2005, "Determination of the optical properties of turbid materials by hyperspectral diffuse reflectance," *Transactions of the ASAE: Paper No 053068*, pp. 1–12.

Qin, J & Lu, R 2006, "Measurement of the optical properties of apples using hyperspectral diffuse reflectance imaging," *Transactions of the ASABE: Paper No 63037*, pp. 1–16.

Qin, J & Lu, R 2007, "Measurement of the absorption and scattering properties of turbid liquid foods using hyperspectral imaging," *Applied Spectroscopy*, vol. 61, no. 4, pp. 388–96.

Qin, J & Lu, R 2008, "Measurement of the optical properties of fruits and vegetables using spatially resolved hyperspectral diffuse reflectance imaging technique," *Postharvest Biology and Technology*, vol. 49, no. 3, pp. 355–365.

Qin, J, Lu, R & Peng, Y 2007, "Internal quality evaluation of apples using spectral absorption and scattering properties," *Proceedings of SPIE*, vol. 6761, pp. 1–11.

Qin, J, Lu, R & Peng, Y 2009, "Prediction of apple internal quality using spectral absorption and scattering properties," *Transactions of the ASABE*, vol. 52, no. 2, pp. 499–507.

Qing, Z, Ji, B & Zude, M 2007, "Predicting soluble solid content and firmness in apple fruit by means of laser light backscattering image analysis," *Journal of Food Engineering*, vol. 82, no. 1, pp. 58–67.

Qing, Z, Ji, B & Zude, M 2008, "Non-destructive analyses of apple quality parameters by means of laser-induced light backscattering imaging," *Postharvest Biology and Technology*, vol. 48, no. 2, pp. 215–222.

Ramella-Roman, JC, Prahl, SA & Jacques, SL 2005, "Three Monte Carlo programs of polarized light transport into scattering media: part I," *Optics Express*, vol. 13, no. 12, p. 4420.

Renk, KF 2012, *Basics of Laser Physics: For Students of Science and Engineering*, Springer.

Rizzolo, A, Vanoli, M, Spinelli, L & Torricelli, A 2010, "Sensory characteristics, quality and optical properties measured by time-resolved reflectance spectroscopy in stored apples," *Postharvest Biology and Technology*, vol. 58, no. 1, pp. 1–12.

Romano, G, Nagle, M, Argyropoulos, D & Müller, J 2011, "Laser light backscattering to monitor moisture content, soluble solid content and hardness of apple tissue during drying," *Journal of Food Engineering*, vol. 104, no. 4, pp. 657–662.

Ruiz-Altisent, M, Ruiz-Garcia, L, Moreda, GP, Lu, R, Hernandez-Sanchez, N, Correa, EC, Diezma, B, Nicolaï, B & García-Ramos, J 2010, "Sensors for product characterization and quality of specialty crops—A review," *Computers and Electronics in Agriculture*, vol. 74, no. 2, pp. 176–194.

Russ, JC 2011, *The Image Processing Handbook, Sixth Edition*, CRC Press.

Saeys, W, Velazco-Roa, M a, Thennadil, SN, Ramon, H & Nicolaï, BM 2008, "Optical properties of apple skin and flesh in the wavelength range from 350 to 2200 nm," *Applied Optics*, vol. 47, no. 7, pp. 908–19.

Saftner, RA, Abbott, JA, Conway, WS, Barden, CL & Vinyard, BT 2002, "Instrumental and sensory quality characteristics of 'Gala' apples in response to prestorage heat, controlled atmosphere,and air storage," *Journal of the American Society for Horticultural Science*, vol. 127, no. 6, pp. 1006–1012.

Schmidt, F 1999, "Development of a Time-Resolved Optical Tomography System for Neonatal Brain Imaging," *PhD Thesis, University College London*, pp. 19–55.

Schubert, EF 2002, *Light-Emitting Diodes*, Cambridge University Press.

Shmulevich, I, Ben-Arie, R, Sendler, N & Carmi, Y 2002, "Sensing technology for quality assessment in controlled atmospheres," *Postharvest Biology and Technology*, vol. 29, no. 2, pp. 145–154.

Shmulevich, I, Galili, N & Rosenfeld, D 1996, "Detection of fruit firmness by frequency analysis," *Transactions of the ASAE*, vol. 39, no. 3, pp. 1047–1055.

Simpson, CR, Kohl, M, Essenpreis, M & Cope, M 1998, "Near-infrared optical properties of ex vivo human skin and subcutaneous tissues measured using the Monte Carlo inversion technique," *Physics in Medicine and Biology*, vol. 43, no. 9, pp. 2465–78.

Sinclair 2007, "An Even Higher iQ,", accessed February 17, 2014, from <http://www.sinclairintl.com/newsletter_pages/summer_2012/iQ_even_higher.html >.

Sirisomboon, P, Tanaka, M, Kojima, T & Williams, P 2012, "Nondestructive estimation of maturity and textural properties on tomato 'Momotaro' by near infrared spectroscopy," *Journal of Food Engineering*, vol. 112, no. 3, pp. 218–226.

Song, J, Deng, W, Beaudry, RM & Armstrong, PR 1997, "Changes in chlorophyll fluorescence of apple fruit during maturation, ripening, and senescence," *HortScience*, vol. 32, no. 5, pp. 891–896.

Van Staveren, HJ, Moes, CJ, van Marie, J, Prahl, SA & van Gemert, MJ 1991, "Light scattering in Intralipid-10% in the wavelength range of 400-1100 nm," *Applied Optics*, vol. 30, no. 31, pp. 4507–14.

Steinmetz, V, Crochon, M, Bellon Maurel, V, Garcia Fernandez, JL, Barreiro Elorza, P & Verstreken, L 1996, "Sensors for Fruit Firmness Assessment: Comparison and Fusion," *Journal of Agricultural Engineering Research*, vol. 64, no. 1, pp. 15–27.

Stenberg, C, Svensson, M & Johansson, M 2005, "A study of the drying of linseed oils with different fatty acid patterns using RTIR-spectroscopy and chemiluminescence (CL)," *Industrial Crops and Products*, vol. 21, no. 2, pp. 263–272.

Studman, CJ 2001, "Computers and electronics in postharvest technology — a review," *Computers and Electronics in Agriculture*, vol. 30, no. 1-3, pp. 109–124.

Sun, H 2012, *Laser diode beam basics, manipulations and characterizations*, Springer Netherlands, Dordrecht.

Suzaki, Y & Tachibana, A 1975, "Measurement of the um sized radius of Gaussian laser beam using the scanning knife-edge," *Applied Optics*, vol. 14, no. 12, pp. 2809–2810.

Svensson, T, Alerstam, E, Einarsdóttír, M, Svanberg, K & Andersson-Engels, S 2008, "Towards accurate in vivo spectroscopy of the human prostate.," *Journal of Biophotonics*, vol. 1, no. 3, pp. 10434–10448.

Symoneaux, R, Royer, G, Madieta, E & Jourjon, F 2005, "Acoustic and Sensory Measurements of Different Ripeness of Apples," *Acta Horticulturae*, vol. 682, pp. 1475–1480.

Taste Technologies 2013, "T1 Technology,", accessed September 18, 2013, from <http://www.taste-technologies.com/t1>.

Taste Technologies Ltd 2013, "Produce,", accessed February 16, 2014, from <http://www.taste-technologies.com/fruit>.

The New Zealand Institute for Plant and Food Research 2013, "Fresh Facts 2013," *Annual Industry Summary*, pp. 1–7.

Thorlabs 2010, "904nm 30mW Laser Diode L904P030," *Thorlabs.com*, p. 11919, accessed March 5, 2014, from <http://www.thorlabs.com/thorcat/11900/L904P030-SpecSheet.pdf>.

Thorlabs 2013, "Laser Diodes by Wavelength," *Thorlabs.com*, accessed January 20, 2014, from <http://www.thorlabs.com/navigation.cfm?guide_id=2164>.

Tollner, EW, Hung, YC, Upchurch, BL & Prussia, SE 1992, "Relating X-ray absorption to density and water content in apples," *Transactions of the ASABE*, vol. 35, no. 6, pp. 1921–1928.

Tu, K, De Baerdemaeker, J, Deltour, R & de Barsy, T 1996, "Monitoring post-harvest quality of Granny Smith apple under simulated shelf-life conditions: destructive, non-destructive and analytical measurements," *International Journal of Food Science and Technology*, vol. 31, no. 3, pp. 267–276.

Tu, K, Chen, YY, Ren, K, Shao, XF, Dong, QL & Pan, LQ 2006, "Modeling Apple Quality Changes Based on Laser Scattering Image Analysis under Simulated Shelf Life Conditions," *Acta Horticulturae*, vol. 712, pp. 371–380.

Tu, K, Jancsok, P, Nicolai, B & De Baerdemaeker, J 2000, "Use of laser-scattering imaging to study tomato-fruit quality in relation to acoustic and compression measurements," *International Journal of Food Science and Technology*, vol. 35, no. 5, pp. 503–510.

Tu, K, Jancsók, P, Nicolaï, B & De Baerdemaeker, J 1995, "Using laser beam as light source to study tomato and apple quality non-destructively," in *Proceedings of the FPAC IV Conference*, Chicago, Illinois, 03-11-1995, pp. 528–536.

Tu, K, Nicolaï, B & De Baerdemaeker, J 2000, "Effects of relative humidity on apple quality under simulated shelf temperature storage," *Scientia Horticulturae*, vol. 85, no. 3, pp. 217–229.

University of Illinois Extension 2007, "Apple Facts,", accessed February 15, 2014, from <http://urbanext.illinois.edu/apples/facts.cfm>.

Valero, C 2004, "Selection Models for the Internal Quality of Fruit, based on Time Domain Laser Reflectance Spectroscopy," *Biosystems Engineering*, vol. 88, pp. 313–323.

Valero, C & Barreiro, P 2005, "Mealiness detection in apples using time resolved reflectance spectroscopy," *Journal of Texture Studies*, vol. 36, no. 2005, pp. 439–458.

Vanoli, M, Rizzolo, A, Grassi, M, Farina, A, Pifferi, A, Spinelli, L & Torricelli, A 2011, "Time-resolved reflectance spectroscopy nondestructively reveals structural changes in 'Pink Lady®' apples during storage," *Procedia Food Science*, vol. 1, pp. 81–89.

Vanoli, M, Rizzolo, A, Zanella, A, Grassi, M, Spinelli, L, Cubeddu, R & Torricelli, A 2013, "Apple texture in relation to optical, physical and sensory properties," in *CD-ROM Proceedings Inside Food Symposium*, Leuven, Belgium, 09-04-2013, pp. 9–12.

Vanoli, M, Rizzolo, A, Zerbini, PE, Spinelli, L & Torricelli, A 2010, "Non-destructive detection of internal defects in apple fruit by time-resolved reflectance spectrscopy," in C Nunes (ed), *Environmentally Friendly and Safe Technologies for Quality of Fruits and Vegetables*, University of the Algarve, Faro, Portugal, pp. 22–28.

Varela, P, Salvador, A & Fiszman, S 2007, "Changes in apple tissue with storage time: Rheological, textural and microstructural analyses," *Journal of Food Engineering*, vol. 78, no. 2, pp. 622–629.

Ventura, M, de Jager, A, de Putter, H & Roelofs, FPM. 1998, "Non-destructive determination of soluble solids in apple fruit by near infrared spectroscopy (NIRS)," *Postharvest Biology and Technology*, vol. 14, no. 1, pp. 21–27.

Vo-Dinh, T 2010, *Biomedical Photonics Handbook*, CRC Press, Boca Raton, FL.

Walsh, K, Golic, M & Greensill, C 2004, "Sorting of fruit using near infrared spectroscopy: application to a range of fruit and vegetables for soluble solids and dry matter content," *Journal of Near Infrared Spectroscopy*, vol. 12, p. 141.

Wang, S, Huang, M & Zhu, Q 2012, "Model fusion for prediction of apple firmness using hyperspectral scattering image," *Computers and Electronics in Agriculture*, vol. 80, pp. 1–7.

Watkins, CB, Kupferman, E & Rosenberger, DA 2004, "Apple," *Agriculture Handbook Number 66 - The Commercial Storage of Fruits, Vegetables, and Florist and Nursery Stocks*.

Welch, A & Gemert, M Van 2010, *Optical-thermal response of laser-irradiated tissue*, Plenum, New York.

Williams, P & Norris, KH 1987, *Near-infrared technology in the agricultural and food industries*, American Association of Cereal Chemists, St. Paul, MN.

Workman, J, Jr. & Weyer, L 2007, *Practical Guide to Interpretive Near-Infrared Spectroscopy*, CRC Press.

Yamamoto, H, Iwamoto, M & Haginuma, S 1980, "Acoustic impulse response method for measuring natural frequency of intact fruits and preliminary applications to internal quality evaluation of apples and watermelons," *Journal of Texture Studies*, vol. 11, no. 2, pp. 117–136.

Yang, L, Sun, JH & Wu, AQ 2012, "Measurements of Optical Parameters of the Fat Emulsion," *Advanced Materials Research*, vol. 510, pp. 822–826.

Ying, Y, Liu, Y & Wang, J 2005, "Fourier transform near-infrared determination of total soluble solids and available acid in intact peaches," *Transactions of the ASAE*, vol. 48, no. 1, pp. 229–234.

Zaccanti, G, Del Bianco, S & Martelli, F 2003, "Measurements of optical properties of high-density media," *Applied Optics*, vol. 42, no. 19, pp. 4023–30.

Zamora-Rojas, E, Aernouts, B, Garrido-Varo, A, Pérez-Marín, D, Guerrero-Ginel, JE & Saeys, W 2013, "Double integrating sphere measurements for estimating optical properties of pig subcutaneous adipose tissue," *Innovative Food Science & Emerging Technologies*, vol. 19, pp. 218–226.

Zappe, H 2003, *Laser Diode Microsystems*, Springer.

Zerbini, PE & Grassi, M 2004, "The Quality and Storability of Apples cv. 'Jonagored' Selected At- Harvest by Time-Resolved Reflectance Spectroscopy," *Acta Horticulturae*, vol. 682, pp. 1481–1488.

Zhang, Y, Wen, X, Xu, Z & Zhu, D 2010, "The accuracy of a commercial spectrophotometer with single integrating sphere for measuring optical properties of turbid sample," *Proceedings of SPIE*, vol. 7562, pp. 1–9.

Zude, M 2010, *Optical Monitoring of Fresh and Processed Agricultural Crops*, CRC Press.

Zude, M, Herold, B, Roger, J-M, Bellon-Maurel, V & Landahl, S 2006, "Non-destructive tests on the prediction of apple fruit flesh firmness and soluble solids content on tree and in shelf life," *Journal of Food Engineering*, vol. 77, no. 2, pp. 254–260.